PREDICTION AND EXPERIMENTAL VALIDATION OF WELD DIMENSIONS IN THIN PLATES USING SUPERIMPOSED LASER SOURCES TECHNIQUE

A Dissertation
Presented to
The Academic Faculty

by

Tsun-Yen Wu

In Partial Fulfillment
of the Requirements for the Degree
Doctor of Philosophy in the
George W. Woodruff School of Mechanical Engineering

Georgia Institute of Technology
August 2011

PREDICTION AND EXPERIMENTAL VALIDATION OF WELD DIMENSIONS IN THIN PLATES USING SUPERIMPOSED LASER SOURCES TECHNIQUE

Approved by:

Dr. I. Charles Ume, Advisor
School of Mechanical Engineering
Georgia Institute of Technology

Dr. Suresh Sitaraman
School of Mechanical Engineering
Georgia Institute of Technology

Dr. J. Rhett Mayor
School of Mechanical Engineering
Georgia Institute of Technology

Dr. Massimo Ruzzene
School of Aerospace Engineering
Georgia Institute of Technology

Dr. Jennifer Michaels
School of Electrical and Computer Engineering
Georgia Institute of Technology

Date Approved: May 18, 2011

ACKNOWLEDGEMENTS

I would like to sincerely thank my advisor, Dr. I. Charles Ume for his guidance, advice, and mentorship throughout this research.

I would like to thank my thesis reading committee: Dr. Suresh Sitaraman, Dr. Rhett Mayor, Dr. Massimo Ruzzene, and Dr. Jennifer Michaels. I sincerely appreciate their time and valuable suggestions to make my research more complete.

I would like to acknowledge the financial support from Toyota Motor Engineering and Manufacturing North America, Inc.

I would like to thank my colleagues in Dr. Ume's group for their support, feedback and collaboration throughout my studies: Dr. Matthew Rogge, Dr. Renfu Li, Dr. Wei Tan, Dr. Jin Yang, Mr. Lei Yang, Ms. Julia Pasternack, Mr. Abel Valdes, Mr. Tyler Randolph, Mr. Jie Gong, and Mr. Sungbum Kang.

I would also like to express my appreciation to Mr. Chien-Chiang Chen for preparing the etching solution for the cutcheck inspection of the welds for me.

Last but not least, I would like to thank my family for their encouragement and support, and my wife, Yungwen, for her love, understanding and sacrifices.

TABLE OF CONTENTS

LIST OF TABLES

LIST OF FIGURES

SUMMARY

Gas Metal Arc Welding (GMAW) is one of the primary techniques used to join thin structures together. The quality of the weld plays an important role in structure integrity and product safety. Weld dimensions such as penetration depth, leg length, throat thickness, and reinforcement height are key to the quality of welds. Therefore, it is crucial to accurately measure them. Previous research has shown that non-destructive evaluation using laser generated bulk waves and electromagnetic acoustic transducer (EMAT) reception is an efficient and effective way to monitor weld quality in thick structures. Laser generated Lamb waves have the potential to be used to monitor weld quality in thin structures. However, due to the fact that laser generated Lamb waves in thin structures are broadband and dispersive, the complexity of ultrasonic signals is greatly increased.

The objective of this research is to develop a method to measure important weld dimensions in thin plates by using laser generated ultrasound. This research comprises three aspects: First, to develop a technique that can generate narrowband Lamb waves in thin plates. Secondly, to develop a signal processing procedure to extract useful information from the ultrasonic signals to evaluate weld dimensions. Thirdly, to develop prediction models to predict weld dimensions by using the reflection coefficients of narrowband Lamb waves.

The technique named superimposed laser sources (SLS) technique is developed to generate narrowband Lamb waves in thin plates. By using the superimposed laser

sources, one has the flexibility to generate desired wavelengths of Lamb waves. The advantage of generating narrowband Lamb waves with fixed wavelengths is that the dominant frequency content and traveling speeds of different wave modes can be determined from the dispersion curves.

The signal processing procedure developed in this research is used to reduce the complexity of the signals of Lamb waves in thin structures. It includes wavenumber-frequency (k-ω) domain filtering and synthetic phase tuning (SPT). The k-ω domain filtering technique helps to filter out the unwanted wave components traveling at the direction that are irrelevant to our analysis and the SPT technique is used to amplify and isolate a particular Lamb wave mode. The signal processing procedure facilitates the calculation of reflection coefficients of Lamb waves that result from the presence of weld joints.

Reflection coefficients that result from the welds can be calculated for A0 and S0 Lamb wave modes for ten discrete wavelengths of interest. Two methods, the direct method and the indirect method, are used to develop models that use reflection coefficients as predictors to measure these weld dimensions. The assumptions made in these two methods are intrinsically different. In the direct method, weld dimensions are assumed to be functions of the reflection coefficients. But in the indirect method, it is assumed that the reflection coefficients are functions of the weld dimensions. Different approaches are taken to identify significant predictors that are used in the prediction models. Both models are shown to effectively predict weld dimensions in thin plates and they are complementary to each other. Furthermore, from the model developed by the indirect method, the response of each reflection coefficient to the change of weld dimensions can be shown. The results provide us a way to investigate the interaction between Lamb waves and geometry of welds. The advantages and disadvantages of these two methods are discussed, and the detailed discussion about the sources of errors is presented.

The weld dimensions measurement techniques and procedures developed in this research have resulted in a new nondestructive and noncontact method for measuring important weld dimensions in thin plates. The techniques and procedures have great potential. They can be applied to other types of thin structures such as curved thin plates. They can also be applied to evaluate welds made by other types of welding processes such as friction stir welding. They will help to improve the quality and efficiency of the welding process on thin structures and reduce costs, material waste and human injury.

CHAPTER 1

INTRODUCTION

Welding is an essential process for joining parts in almost all industries. The quality of the weld plays an important role in structural integrity and product safety. Common defects in welds such as cracks, voids, porosity, and undercut are potential threats. They can decrease the load bearing capability of structures and compromise their static, dynamic and fatigue strength. Apart from these types of defects, weld dimensions also play important roles in weld quality. Insufficient penetration depths, leg lengths, or throat thicknesses are treated as defects as well and they are much harder to assess. This research focuses on evaluation of these important weld dimensions in thin plates. With the realization of the fact that the weld could be the weakest link in a structure, more and more emphasis has been given on fabricating welded components with high quality and ensuring their performance reliability in service. Therefore, it is crucial to accurately measure important weld dimensions. In practice, welded structures are cut and inspected to monitor weld quality in industries. However, the cutcheck method is not only time-consuming, but also destructive and wasteful, and automated inspection by using cutcheck method is not possible. Also, the sample being inspected may not be representative of the whole batch, which results in a low confidence level of quality control. As a result, a lot of research effort has been invested to develop nondestructive evaluation methods such as radiography, thermography, eddy current inspection, etc.

1.1 Gas Metal Arc Welding

Gas metal arc welding (GMAW) is an arc welding process in which an electric arc is formed and maintained between a continuously fed filler metal electrode wire and the weld pool [1-2]. Two work pieces are joined through the addition of heat and the addition of filler material. In the arc heat, the consumable electrode in GMAW is fed towards the work piece and melted, and the molten metal is transferred across the arc into the weld pool. A shielding gas flows through the torch and forms a cover over the weld pool to protect it from atmospheric contamination. The externally supplied shield gas can be argon, carbon dioxide or a gas mixture of the two. The important feature of gas metal arc welding is the production of high quality welds at high welding speeds.

1.2 Defects in Welded Joints

When two samples are welded together, defects can be introduced. Illustration of cross sections of a butt weld and a lap weld are shown in Fig. 1-1 and Fig. 1-2 in which some defects are drawn and critical dimensions are labeled. Some of the common defects are introduced in the following sections.

1.2.1 Cracks

Cracks pose very serious problems when the welded structure is under stress since they can propagate and make the structure break. Care must be taken to avoid or at least detect the presence of cracks in weld joints.

1.2.2 Porosities and Voids

Porosities and voids happen when gases are trapped in the weld while the weld bead cools down and solidifies. Sometimes a through hole can form if a void reaches the surface of weld bead.

1.2.3 Undercut

Undercut is a defect that appears as a groove melted into the base material that is adjacent to the edges of the weld. It is most common in lap welds, but can also be encountered in butt welds. This type of defect is most commonly caused by improper welding parameters, particularly the travel speed and arc voltage.

1.2.4 Lack of Penetration, Lack of Reinforcement, Insufficient Bead Width, Short Legs, and Short Throat

Penetration depth, reinforcement height, bead width, throat thickness and leg length are the most important dimensions related to the quality of the weld [3]. Penetration depth (PD) is a very crucial dimension in both butt welds and lap welds. Lack-of-penetration occurs when there is incomplete penetration of the weld through the thickness of a joint. The incomplete penetration reduces the cross section of the weld, which compromises the load bearing capability of the structure. PD is defined as the depth at which the weld bead (fusion portion) actually extends into the base material. Depending on manufacturers or applications, PD needs to be greater than a certain percentage of the thickness of the base material or a lack-of-penetration defect occurs. In butt welds, the reinforcement height (RH) is defined as the distance at which the weld bead extrudes above the base materials. And the bead width (BW) is simply the width of the extruded bead. These dimensions need to be greater than a specified percentage of the thickness of the material.

In lap welds, the throat thickness is shown as TH in Fig. 1-2. To measure the TH, a line is drawn from the root of the joint to the surface of the weld bead in a 45 degree angle with respect to the edge of the base materials. The legs of a lap weld are shown as S1 and S2 in Fig. 1-2. They are defined as the projected lengths of the interfaces between the weld bead and the base materials on the material edges. A defect of short leg or short throat occurs if their amount is under the specification.

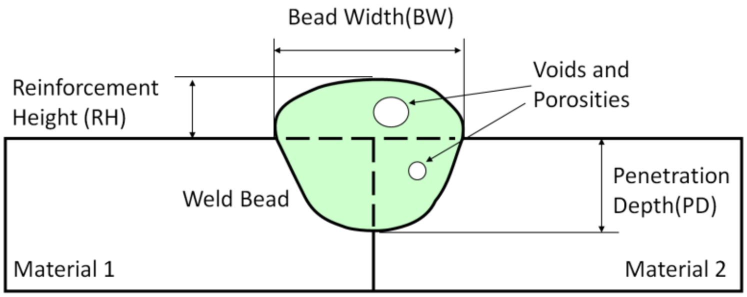

Fig. 1-1: Cross section of a butt weld

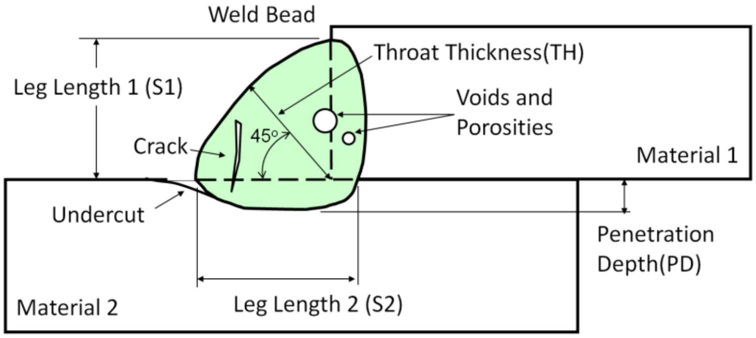

Fig. 1-2: Cross section of a lap weld

1.2 Nondestructive Testing of Welds

Many nondestructive weld evaluation techniques and technologies have been investigated and developed over the past years. In the following sections, several nondestructive testing methods for evaluating quality of welds are discussed.

1.2.1 Thermography Inspection

Thermography inspection techniques include the measurement or mapping of surface temperature as heat flows to, from, or through an object. It makes use of the infrared spectral band of the electromagnetic radiation. During welding, the high temperature and thermal gradients can be used to infer weld geometry. By measuring temperature distributions on the top and bottom surfaces of the workpiece, information regarding the penetration depth, weld pool width and shape can be inferred. Lankalapalli et el. [4] developed a model which uses the information of weld width, temperature distribution and a theoretical 2D heat conduction model to predict penetration depth of a laser weld in real time. They used an infrared sensor to measure the temperature distribution and this provides an indirect measurement of the penetration depth. Menaka et al. [5] used infrared thermal imaging to sense and monitor the welding process by mapping and analyzing the surface temperature distribution. They estimated bead width and penetration depth by using infrared thermal imaging. Fig. 1-3 shows their experimental results. The major disadvantages of this method are its inability to measure internal weld defects and the fact that this method is indirect [6-9].

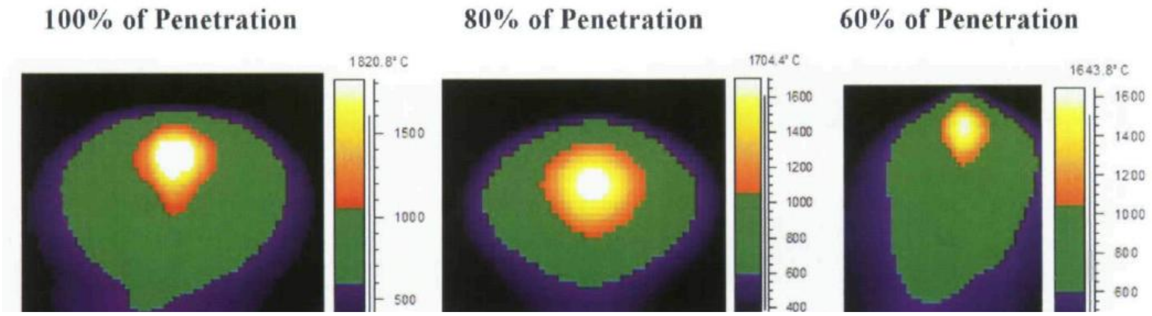

Fig. 1-3: Examples of thermogrphay inspection in butt welding [5]

1.2.2 Eddy Current Inspection

Eddy current testing (ECT) is based on the principle of electromagnetic induction. It employs the use of coils to induce eddy currents on the surface of conductive materials [10-15]. The schematic of eddy current testing method is shown in Fig. 1-4. These eddy currents are generally parallel to the coil winding, and the presence of any defect or discontinuity in the material disturbs the eddy current flow. The disturbed eddy current flow will in turn generate an alternating magnetic field that can be detected by a second pickup coil. By monitoring changes of effective impedance of eddy currents, defects can be detected. However, the sensitivity of ECT drops exponentially as the sensing depth increases. It can only detect defects near the surface. Its sensitivity also depends on the orientation of defects. Also, inspected surfaces need to be accessible and uniform in finishing, which is not usually the case for complex structures in industry.

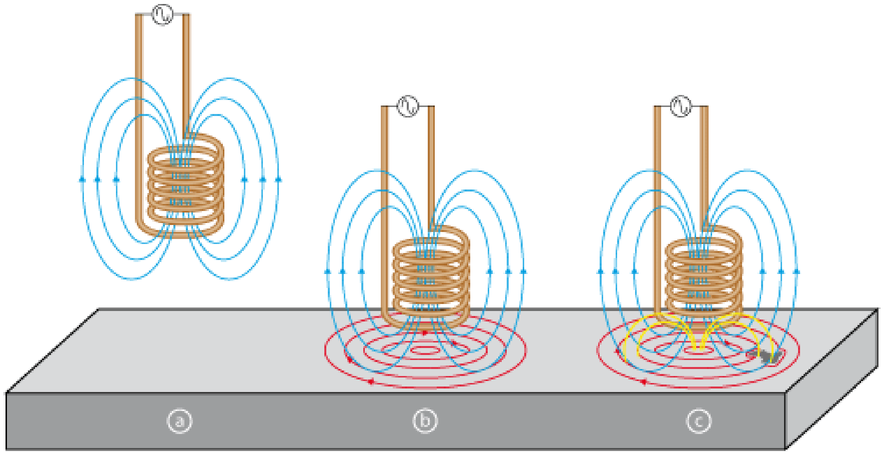

Fig. 1- 4: Schematic of the operation of eddy current inspection [3]

1.2.3 Radiography Inspection

Radiographic inspection evaluates materials through the introduction of electromagnetic radiation of very short wave lengths (X-rays or gamma rays) or particle radiations (alpha, beta or neutron) to penetrate the sample [[16-18]. By utilizing the fact that a defect and its surrounding material have different absorption coefficients to the radiation, one can determine the presence of a defect. While radiography testing is superior in detecting voids and porosities in welds, it is not suitable for detecting defects such as lack-of-penetration or planar cracks in thin structures due to the fact that it is hard to expose the sample with radiation in the direction perpendicular to the thickness. Also, in order to perform radiography testing, one needs to have access to two sides of the sample, which is not always possible. And it can be hazardous to operators if necessary precautions are not properly taken. The safety hazards associated with the use of X-rays and gamma radiation are major concerns of this method. A sample of an X-ray image of a lap weld is shown in Fig. 1-5.

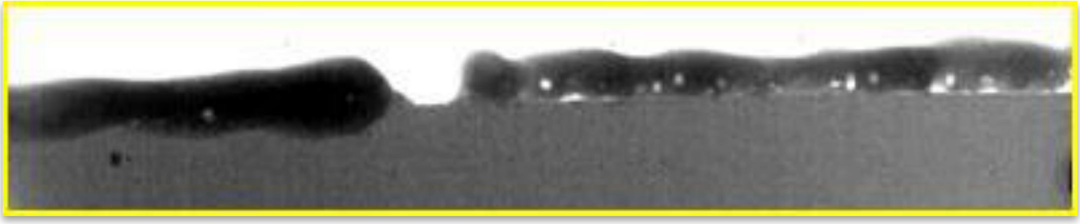

Fig. 1-5: X-ray image of a lap weld

1.2.4 Ultrasound Inspection

Ultrasonic inspection is one of the major techniques used for inspecting welded structures in many areas including building construction, automotive manufacturing, oil platform, pipeline construction, and nuclear, naval or aerospace industries [19-20]. Traditional contact piezoelectric transducers (PZTs) have been used to generate and receive ultrasound during offline weld inspection. While PZTs are easy to use in laboratories, they are not suitable for automated online inspection in industries due to the need for liquid couplants between samples and transducers. Fig. 1-6 shows one possible example of using PZTs to inspect weld penetration depth.

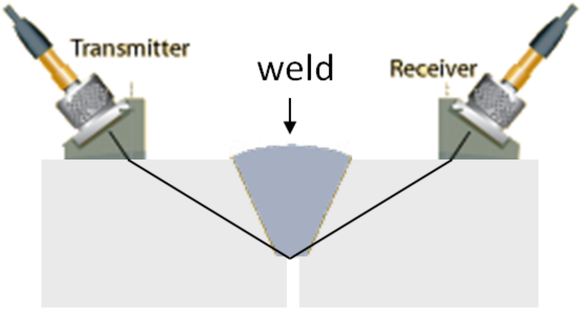

Fig. 1-6: Example of weld inspection by using PZTs

Lots of effort has been put into noncontact ultrasound inspection. A system was first introduced in 1963 by White [21] in which a pulse laser and an interferometer were used to generate and receive ultrasound propagating in the tested sample. While a pulse laser can be an effective broadband ultrasound source, laser interferometry reception systems require reflective and smooth surface finishes on samples, which may not exist in the manufacturing settings.

Nondestructive evaluation using laser generated ultrasound and electromagnetic acoustic transducer (EMAT) receiver is an alternative method for online and offline weld quality monitoring [22-34]. Nanosecond pulse width lasers, such as Q-switched Nd:Yag lasers, can be used to generate ultrasound. The laser pulse is incident onto the surface of a sample and depending on laser energy, thermoelastic or ablative generation can occur and ultrasound can be generated. EMATs can operate at a standoff height to sample surfaces. This noncontact nature makes EMATs suitable for rough surfaces and they are ready for automated inspection.

Mi and Ume [24-26] developed a real-time laser ultrasonics based system for controlling robotic weld quality by monitoring the weld penetration depth of the weld pool. They implemented and optimized a fiber phased array generation system. They also used the transient temperature distribution from finite element simulations to compensate the error of the ultrasound velocity field introduced by the high temperature during welding. In addition, they developed a 3D ray tracing algorithm and successfully correlated the experimental Time-of-Flight (ToF) to the weld penetration depth. Kita and Ume [22-23] utilized the ToF of a new type of wave called the RGLS (Rayleigh Generation Longitudinal to Shear) wave for measuring weld penetration depth. They found the ToF of this particular wave is highly correlated to the penetration depth of the weld. The RGLS TOF method for measuring weld penetration depth has proven to be highly accurate, precise, and repeatable. The method has been demonstrated to work both off-line after welding and real-time during welding. Rogge and Ume [27] utilized a wave called the longitudinal diffracted longitudinal to shear (LdLS) wave to measure the penetration depth of a butt weld. In order to improve the in-process penetration depth measurement, they developed a neuro-fuzzy error compensation model that can correct ToF measurement error induced by high temperatures during welding. The model produced an estimate of the room temperature ToF from the in-process ToF and the time history of the wire feed rate. The estimated ToF was used to measure the penetration depth. The error of the penetration depth measurement was comparable to that obtained after welding at room temperature. By reducing the error caused by the temperature present during welding, the accuracy of this laser ultrasonic technique has been increased significantly.

The aforementioned ultrasonic measurement techniques work well for relatively thick samples where bulk waves are the main waves that travel inside. However, when the sample thickness decreases, all the waves start to interact with the boundaries through reflections, refraction, and mode conversions, and Lamb waves become prevalent in the structure [35]. Because of the dispersion nature of Lamb waves, ToF based techniques are not applicable anymore. Currently, there are no good methods to measure some of the critical dimensions of welds in thin structures. In this research, a new method called superimposed laser sources technique and a signal processing procedure are studied. They can simplify ultrasonic signals in thin plates so that one can extract useful information from the signals that can be correlated with the important dimensions of the welds in thin structures.

CHAPTER 2

BACKGROUND

2. 1 Elastic Waves

In a homogeneous, isotropic, and linearly elastic medium, when an element of the medium is deformed, the disturbance is transmitted from one point to the next, and thus propagating through the medium. As the disturbance propagates through the medium, it carries with it kinetic and potential energy. Energy can be transmitted over considerable distances by the wave motion. In the absence of body forces, the components of the displacement vector are governed by the following system of partial differential equations:

$$\mu\nabla^2\mathbf{u} + (\lambda + \mu)\boldsymbol{\nabla\nabla} \cdot \mathbf{u} = \rho\ddot{\mathbf{u}} \qquad (2\text{-}1)$$

where λ and μ are Lame's constants, ρ is the mass density, **u** is the displacement vector, and ∇^2 is the Laplacian operator. To solve Eq. 2-1, the displacement vector **u** can be expressed via Helmholtz decompostition as the gradient of a scalar and the curl of the zero divergence vector [36]:

$$\mathbf{u} = \nabla\varphi + \nabla \times \boldsymbol{\psi} \qquad (2\text{-}2)$$

where φ and $\boldsymbol{\Psi}$ are scalar and vector potentials, respectively. By substituting Eq. 2-2 into Eq. 2-1 and rearranging, it can be shown that the displacement vector can be obtained by solving two uncoupled wave equations:

$$\nabla^2\varphi = \frac{1}{C_L^2}\ddot{\varphi} \qquad (2\text{-}3)$$

$$\nabla^2\psi = \frac{1}{C_T^2}\ddot{\psi} \qquad (2\text{-}4)$$

where C_L and C_T are longitudinal and shear velocities, respectively.

2.1.1 Bulk Waves

In an isotropic, homogeneous and elastic solid, two kinds of bulk waves can propagate. The movement of particles can either be parallel or perpendicular to the direction of wave propagation. These propagation modes are called longitudinal and shear waves, respectively. The wave speeds of these two modes (C_L and C_T) depend only on material properties and can be expressed as:

$$C_L^2 = \frac{\lambda + 2\mu}{\rho} \qquad (2\text{-}5)$$

$$C_T^2 = \frac{\mu}{\rho} \qquad (2\text{-}6)$$

where ρ is the mass density.

2.1.2 Lamb Waves

The Lamb wave problem is associated with wave motion in a homogeneous and isotropic plate with two traction-free boundaries. Unlike bulk waves, which travel in the bulk of the material and away from the boundaries, Lamb waves, which travel in thin plates, always interact with boundaries by means of reflection, refraction, and mode conversion between longitudinal and shear waves. The superposition of these waves causes the formation of guided wave modes traveling in the direction of the plate and a standing wave across the thickness of the plate. Mathematically, bulk waves and Lamb waves are governed by the same set of partial differential equations. However, for bulk waves, there are no boundary conditions that need to be satisfied. On the other hand, the solution to a Lamb wave problem must satisfy the governing equations as well as some physical boundary conditions. Lamb waves are dispersive, which means the phase and group velocities of Lamb waves are dependent on frequency. In addition, many modes of propagation may be present at a particular frequency. According to the particle movement, all these modes can be further categorized into symmetric and antisymmetric modes. The illustrations of the particle motions of the symmetric and antisymmetric modes in the cross section of a thin plate are shown in Fig. 2-1(a) and (b), respectively.

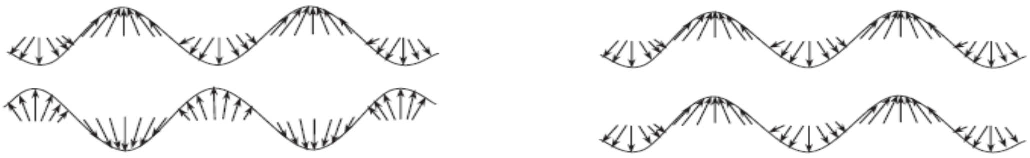
(a) (b)

Fig. 2-1: Illustrations of the particle motions of (a) symmetric and (b) antisymmetric modes in the cross section of a thin plate [37]

To determine phase and group velocities of a given mode, the Rayleigh-Lamb equations need to be solved for the corresponding pair of frequencies and wavenumbers. These combinations of wavenumbers and frequencies define the dispersive relationship for each Lamb wave mode. The Rayleigh-Lamb equations for symmetric and antisymmetric modes can be expressed as in Eq. 2-7 and Eq. 2-8, respectively [35, 37]:

$$\frac{\tan(\mathrm{qh})}{\tan(\mathrm{ph})} = -\frac{4\mathrm{k}^2\mathrm{pq}}{(\mathrm{q}^2-\mathrm{k}^2)^2} \tag{2-7}$$

$$\frac{\tan(qh)}{\tan(ph)} = -\frac{(q^2 - k^2)^2}{4k^2pq} \tag{2-8}$$

where,

$$p^2 = \frac{\omega^2}{C_L^2} - k^2, q^2 = \frac{\omega^2}{C_T^2} - k^2 \tag{2-9}$$

and ω is angular frequency, k is wavenumber defined as $k = 2\pi/\lambda$, h is the plate half-thickness, C_L is longitudinal wave speed, and C_T is shear wave speed. Eqs. 2-7 and 2-8 can only be solved numerically. Fig. 2-2 shows dispersion spectrum between frequency and wavenumber for a 2 mm thick steel plate. After determining the dispersion relationship, the phase, C_p, and group velocities, C_g, can be calculated by Eqs. 2-10 and 2-11. The phase velocity determines the instantaneous phase of the wave, while the group velocity is the velocity at which the energy travels.

$$C_p = \frac{\omega}{k} \tag{2-10}$$

$$C_g = \frac{d\omega}{dk} \tag{2-11}$$

The dispersion curves of phase and group velocities for a 2 mm steel plate are shown in Fig. 2-3 and Fig. 2-4. It is clear that for a given frequency, multiple modes can exist.

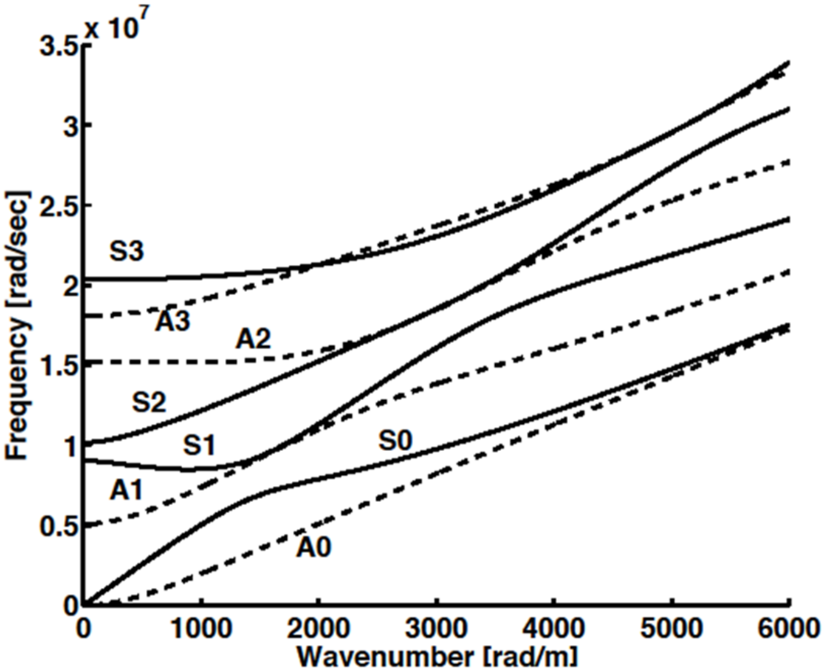

Fig. 2-2: Dispersion spectrum between frequency and wavenumber of a 2 mm steel plate

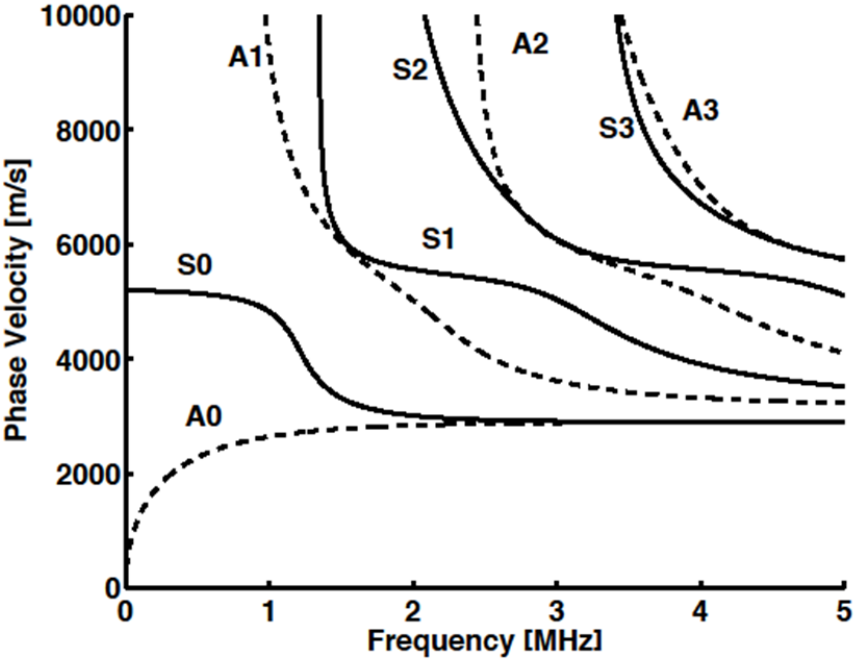

Fig. 2-3: Dispersion curves of phase velocities of a 2 mm steel plate

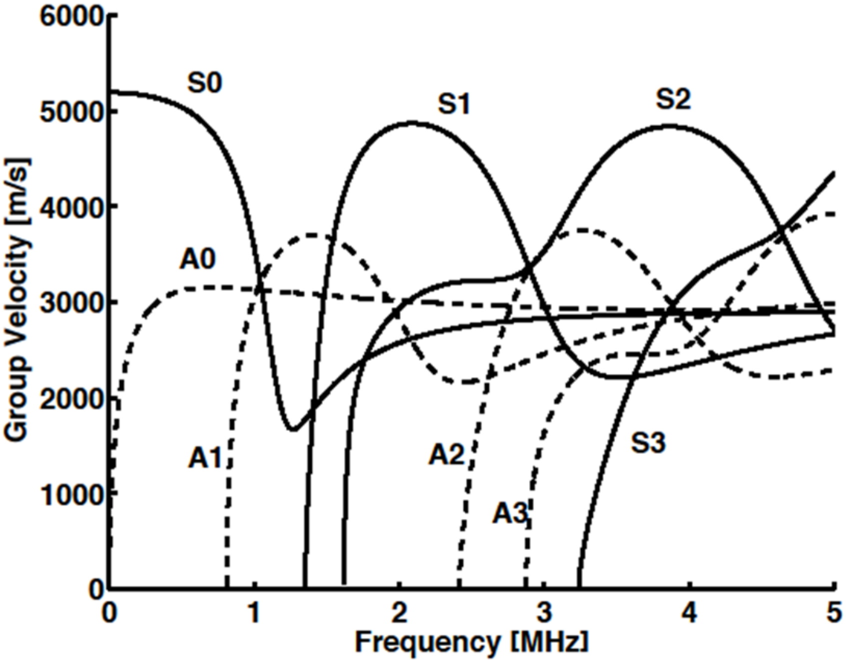

Fig. 2-4: Dispersion curves of group velocities of a 2 mm steel plate

2.2 Review of Narrowband Lamb Waves

Lamb waves are widely used in structural integrity inspection and defect detection in thin structures because of their potential to inspect large areas and their ability to detect various kinds of defects. The key characteristic of Lamb waves is their dispersive nature. One consequence of this characteristic is that their phase and group velocities vary with frequency. The use of lasers to generate Lamb waves is beneficial due to its noncontact nature, but since the laser generated ultrasound is broadband, for a given mode, different frequency components would travel at different speeds. Different modes interfere and present a difficulty to signal interpretation.

The advantage of generating narrowband Lamb waves with a single wavelength is that the dominant frequency content and the traveling speeds for different modes can be determined from the dispersion curves. For illustration, Fig. 2-5 shows the dispersion curves of phase velocity, C_p, versus frequency for an aluminum plate with thickness equal to 2 mm. In the graph, wavelengths can be represented as a straight line passing through the origin with a slope equal to the wavelength. When the wavelength of the narrowband Lamb waves is pre-determined by the investigator, the frequency of each mode can be determined by the x-coordinate of the intersection between the line and the dispersion curves. For example, in Fig. 2-5, the x coordinate of the intersection between the straight line of 2 mm wavelength and S0 dispersion curve is at frequency 1.57 MHz and are 1.36, 2.66 and 2.23 MHz for A0, S1, A1 respectively. Once the dominant frequency of each mode is determined, the traveling speed can be determined by dispersion curves of group velocity versus frequency as shown in Fig. 2-6. In Fig. 2-6, the traveling speeds, C_g, of S0, A0, S1, A1 modes are 2255.75, 3053.65, 3565.23, and 2252.13 m/s respectively.

To create laser generated narrowband Lamb waves, some investigators used spatial array illumination sources produced by several means, which include the use of shadow masks [38-40], optical diffraction gratings [41], multiple lasers [42], interference patterns [43-44] and lenticular arrays [45-47]. Among them, shadow masks are economical, effective and easy to implement (referred as pattern source hereafter), but they are not flexible and have some disadvantages. First, different masks need to be fabricated for different desired wavelengths. Second, a substantial amount of energy is blocked by the mask. Third, depending on manufacturing methods, masks for very small spacing may not be feasible. Furthermore, experimental setup for masks for large wavelengths can be impractical.

In order to overcome the drawbacks of the shadow mask while retaining the advantages of arrayed line sources, the superimposed line sources (SLS) technique is developed. The details of SLS technique will be presented in chapter 5.

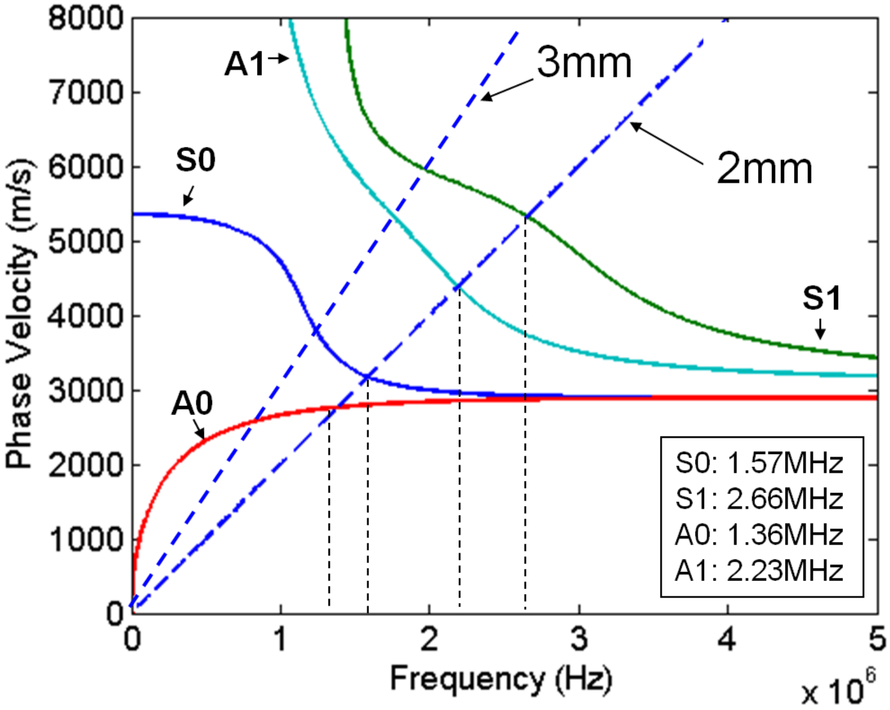

Fig. 2-5: Phase velocities for 2 mm thick aluminum plate

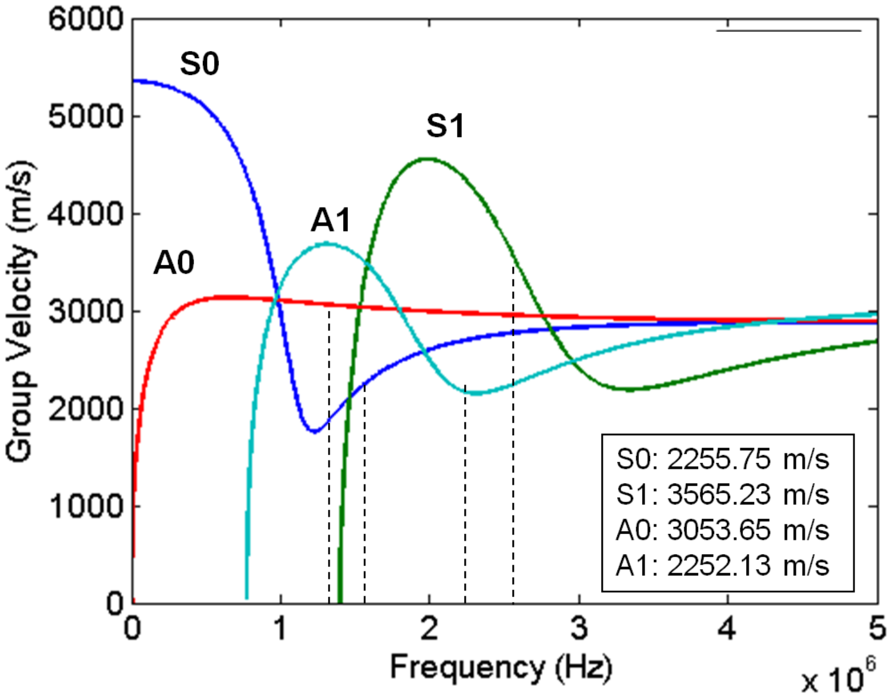

Fig. 2-6: Group velocities for 2 mm thick aluminum plate

2.3 Review of Laser Generation of Ultrasound

Using pulsed lasers to generate ultrasound is beneficial due to its noncontact nature. Unlike traditional contact piezoelectric transducers (PZTs), it does not require couplants on the surfaces of samples. This makes it convenient and suitable for automated inspection. Ultrasound can be generated by different mechanisms depending on the power density of lasers. The high energy and very short duration pulse induces a quick increase of the local temperature due to partial absorption of the radiation. The laser generated ultrasound is broadband in nature. They contain a wide range of frequency contents. There are two main regimes of laser generation of ultrasound: thermoelastic and ablation regimes.

2.2.1 Thermoelastic Regime

When the incident power density on the area illuminated by the laser is relatively low and the local temperature is below the melting point of the material, ultrasound is generated through thermoelastic mechanism [48]. The incident laser beam rapidly heats up a thin layer of material on the top surface. The heated region expands through thermoelastic effect and axially symmetric tensile stresses are generated. Along any vector on the surface that originates from the middle of excitation, the resulting forces can be modeled as a force dipole acting in the surface plane as shown in Fig. 2-7. The heated portion is then followed by a slower contraction as the laser pulse is momentarily shut off. The rapid expansion and contraction create ultrasound which propagates through the sample.

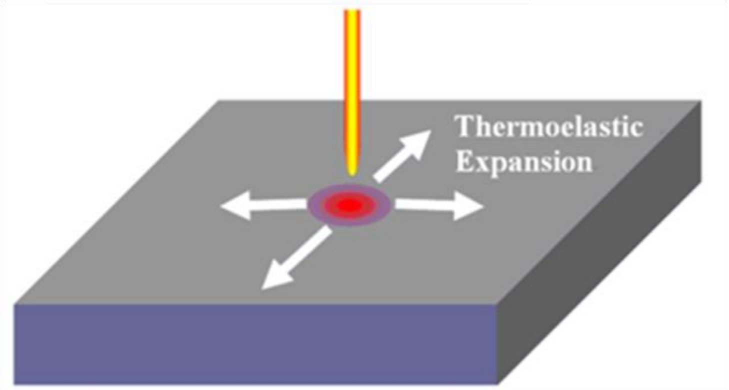

Fig. 2-7: Illustration of laser generation ultrasound in thermoelastic regime

2.2.2 Ablation Regime

When the power density on the illuminated area is high enough to vaporize a small amount of the material, ultrasound is generated through ablative mechanism. In addition to the stresses created by the thermoelastic effect, a normal reaction stress is created by a small amount of material being ejected from the surface [49]. The amplitude of ultrasound generated in the ablative regime is usually higher than that in the thermoelastic regime.

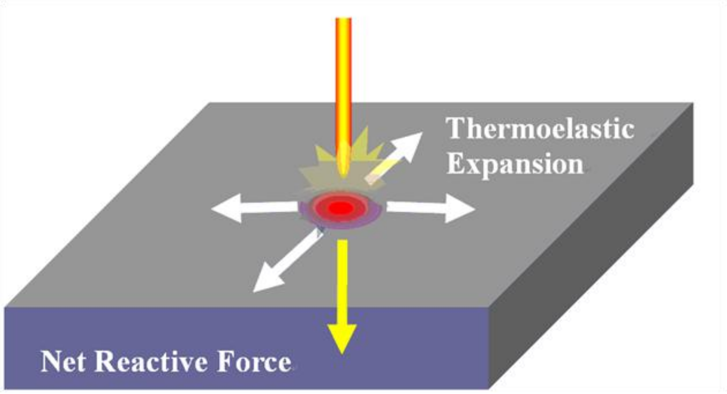

Fig. 2-8: Illustration of laser generation ultrasound in ablation regime

2.4 Electromagnetic Acoustic Transducer (EMAT)

An EMAT is used as a receiver for ultrasonic signals in this research. EMATs are non-contact sensors. They can be moved without application of couplants and the non-contact nature of the device is suitable for automated inspection systems that require various testing points within a part. They are excellent receivers in a harsh industrial environment. EMATs can be tuned to different frequencies and ultrasonic wave types. However, EMATs can only be used to measure ultrasonic signals within conductive materials. The schematic of the operation of EMATs is shown in Fig. 2-9. An EMAT is composed of a permanent magnet and a pickup coil. When a particle with conductivity vibrates in the magnetic field **B** created by the magnet due to the propagation of ultrasound, the velocity, v, of the particle interacts with the magnetic field and eddy currents, J, are created in the material. The resulting eddy currents will then induce an alternating magnetic field which then induces currents on the pickup coil. The relation between eddy currents J, electrical conductivity σ, particle velocity v, and magnetic field B is expressed in Eq. 2-12 [50-51].

$$J = \sigma v \times B \tag{2-12}$$

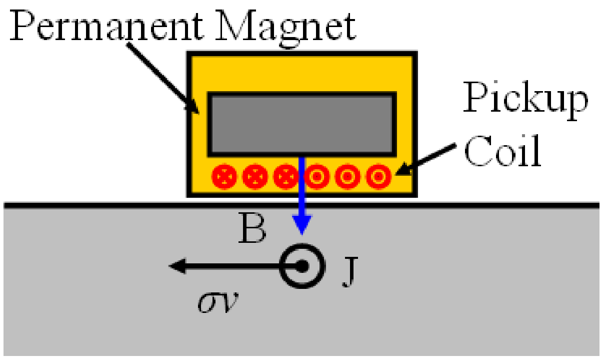

Fig. 2-9: Schematic of operation of EMAT

CHAPTER 3

EXPERIMENTAL SYSTEMS

This chapter introduces the experimental systems used in this research. Two separate systems are used to perform sample welding and inspection. The welding system can make butt welds or lap welds from two pieces of steel. By changing the welding parameters such as wire feed rate or arc voltage during welding, different weld dimensions, i.e. penetration depth, leg length, throat thickness or reinforcement height ,can be produced. The samples welded by the welding system are then inspected by the inspection system.

3.1 Welding System

The welding system is composed of a welder, a microcontroller module and a positioning system. When it welds, the welding torch is stationary and the samples are moved by the positioning system. This configuration eliminates the need for an industrial welding robot that could introduce errors in torch position. The schematic of the welding system is shown in Fig. 3-1 in which the torch is in the upright position for the butt joint welding. The photos of parts of the system are shown in Fig. 3-2. For welding a lap joint, the torch is set up with a 45 degree angle. For welding a butt joint, the torch is perpendicular to the samples. The details of each component in the welding system are introduced in this section.

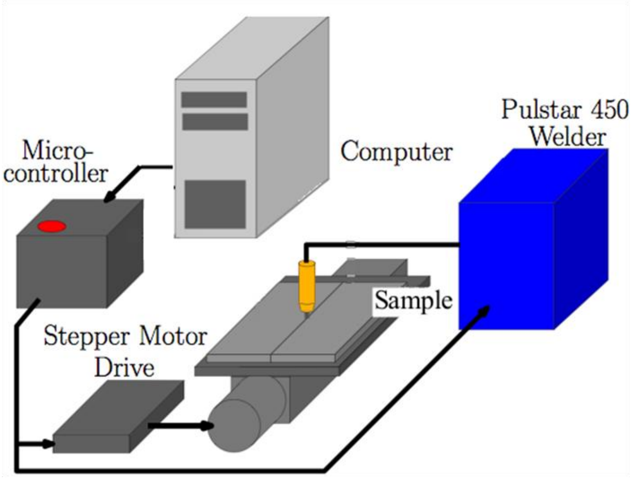

Fig. 3-1: Schematics of the welding system

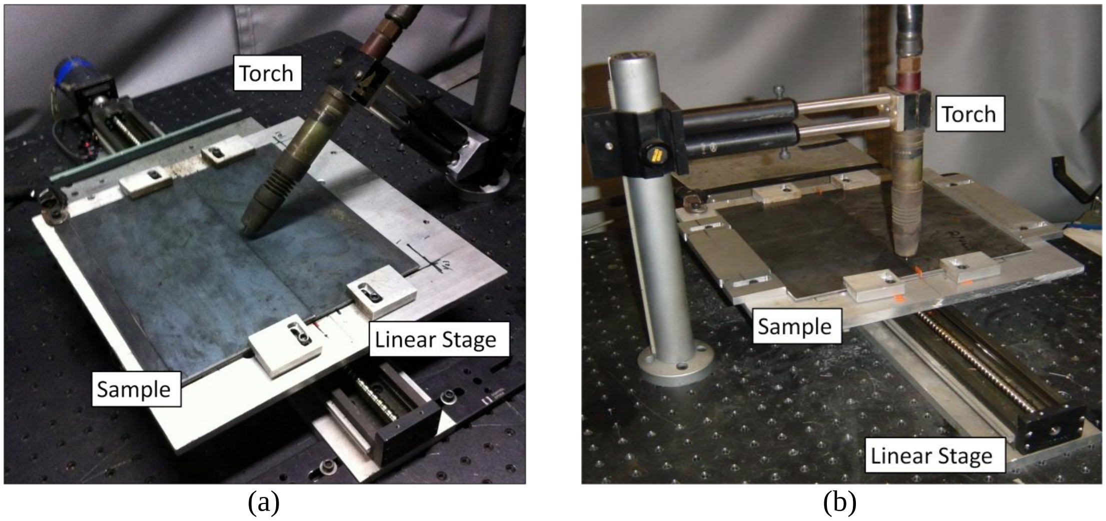

(a) (b)

Fig. 3-2: Photos of the welding setup for (a) Lap joint (b) Butt joint welding

3.1.1 Welder

A Miller Pulstar 450 welder is used to perform welding. The welder has an interface for remote control of the welding parameters and actions (such as start/stop and gas flow). Two 24 V digital signals control shielding gas flow and the welding arc. Two analog signals determine the arc voltage and wire feed rate (WFR) during welding. The signals range from 0-8 V and 0-10 V, which corresponds to 0-800 in/min wire feed rate and 0-50 V arc voltage, respectively.

3.1.2 Microcontroller Module

The microcontroller module was designed and built by the previous student, Matthew Rogge. A microcontroller is used to control the automatic aspects of the experiment. It communicates with the welder through the digital and analog signals already mentioned and with a PC through an RS-232 interface. The role of the microcontroller module is not only to interface with the equipment, but to ensure the process is controlled at a consistent rate.

At the heart of the microcontroller module is a Freescale Semiconductor 68HC11E9 microprocessor operating at a system clock rate of 2 MHz. Custom circuitry was designed and created in order to interface with other equipment. An Analog Devices AD7327 dual 12-bit Digital to Analog Converter (DAC) is used to generate analog control signals sent to the welder. The module also controls the firing of laser and data acquisition in the inspection system. Digital control of the drive of the positioning system is also implemented in this microcontroller module.

3.1.3 Positioning System

In this research, the welding torch does not move along the weld seam. Instead, the work piece is moved underneath the torch via a positioning system. The positioning system consists of a ball screw stage driven by a stepper motor, an optical limit switch and the sample holding table. An Oriental Motor 5-phase stepper motor with a resolution of 0.78 degrees per step is used. Given the lead of the ball screw, this corresponds to a linear resolution of 6 μm per step. Calibration of the table position is achieved by means of an optical switch. Welding samples are placed on the table and located by means of fixtures, which allows for repeatable placement of the samples. The welding torch is positioned using optical bench equipment. A custom made fixture is used to hold the torch with an angle to the sample that is necessary for different types of welding.

3.2 Inspection System

The inspection system is composed of a laser, an EMAT, an EMAT holder, a microcontroller module, a positioning system, lens holders and a user interface and data acquisition program. Parts of the inspection system are shown in Fig. 3-3.

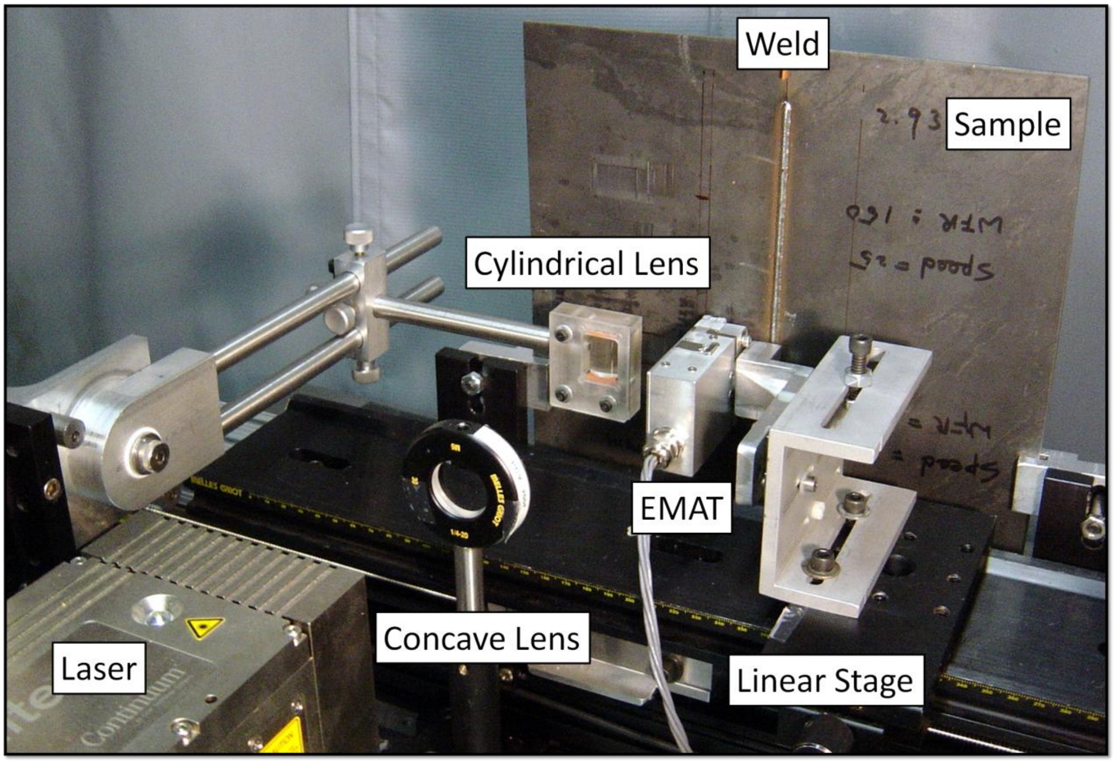

Fig. 3-3: Photo of inspection system

3.2.1 Laser

The laser used in this research is a Continuum Lasers Inlite II-20 pulsed Nd:YAG laser. The wavelength of the output laser is 1064 nm. It has an external trigger which allows laser firing to be controlled by a TTL signal generated by the microcontroller. The photo of the laser is shown in Fig. 3-4 and key specifications are listed in Table 3-1.

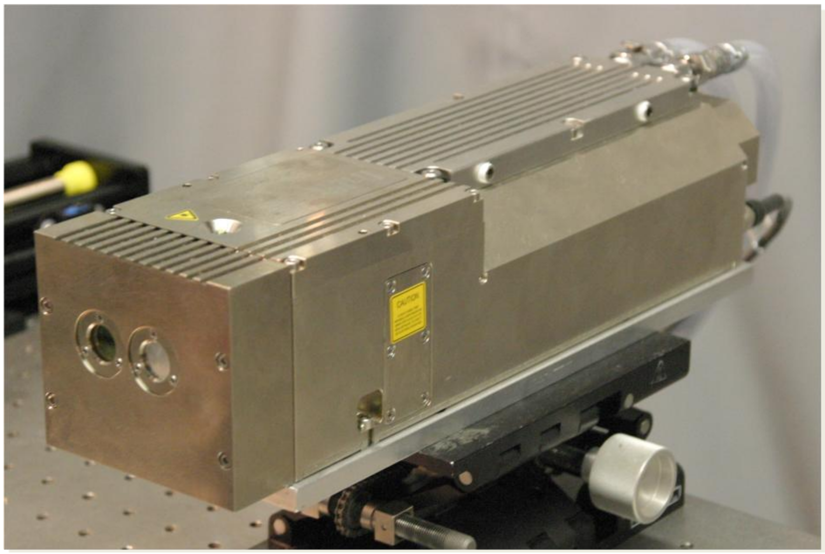

Fig. 3-4: Photo of the laser

Table 3-1: Specifications of the laser

Repetition Rate:	20 pulses/sec	Divergence:	0.6 mrads
Maximal Output Energy:	450 mJ/pulse	Energy Stability:	0.5 %
Pulsewidth:	6-8 ns	Power Drift:	3 %

3.2.2 EMAT

The EMAT used in this research is designed and fabricated by the BWXT Corporation. The EMAT has a 0.5 – 2.5 MHz bandwidth. It consists of four independent coils which are connected to a pre-amplifier outside of the EMAT housing. The interval between the centers of the coils is 2 mm. Four separate signals can be acquired at the same time during experiments. The signals are amplified first and then acquired by the data acquisition card installed in the computer. The EMAT housing measures 1 cm x 2 cm x 2 cm. The picture of the EMAT is shown in Fig. 3-5: Photo of the EMAT.

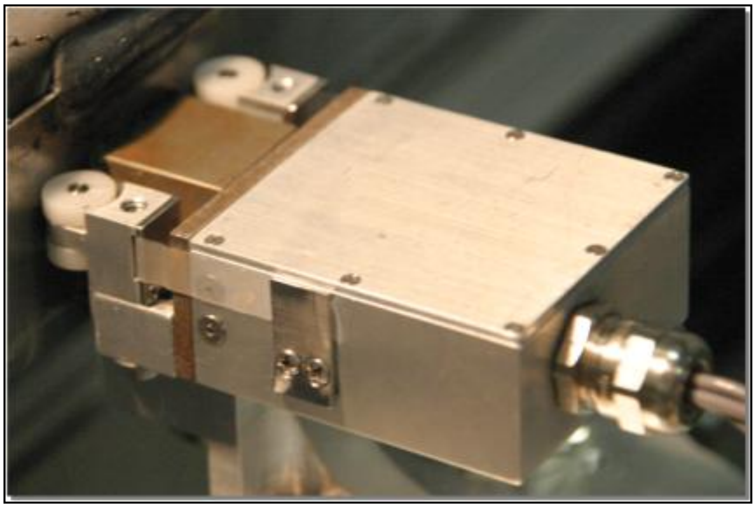

Fig. 3-5: Photo of the EMAT

3.2.3 Data Acquisition System

A Gage Compuscope 8349 PCI/AD card is used to digitize signals. The card is installed on a dual core Xenon based computer system. The specification of the data acquisition card is shown in Table 3-2.

Table 3-2: Specifications of the data acquisition system

Channels:	4	Input Impedance:	50 or 1 M
Amplitude Resolution:	14 bit	Maximum Sample Rate:	125 MHz (8 ns time resolution)
Onboard Memory:	128 MSamples	Gain Setting:	100 mV, 200 mV, 500 mV, 1 V, 2 V, 5 V

3.2.4 Positioning System

The positioning system used in the inspection system is similar to the one used in the welding system. It consists of a ball screw driven by a stepper motor, a mechanical limit switch and a fixture to carry samples. The positioning resolution is 25 μm. During inspection, samples are moved while the EMAT and laser are fixed.

3.2.5 User Interface and Data Acquisition Program

A Matlab Graphical User Interface (GUI) program has been developed by the previous student, Matthew Rogge, to allow the user to control the experiment. The program is capable of acquiring and storing digitized signals at a 125 MHz sample rate. Since the program is developed in MATLAB, signal processing tools can be integrated directly into the application. In addition to data acquisition, the program is capable of communicating with the microcontroller module to determine the experimental parameters. The screenshot of the GUI with four signals is shown in Fig. 3-6.

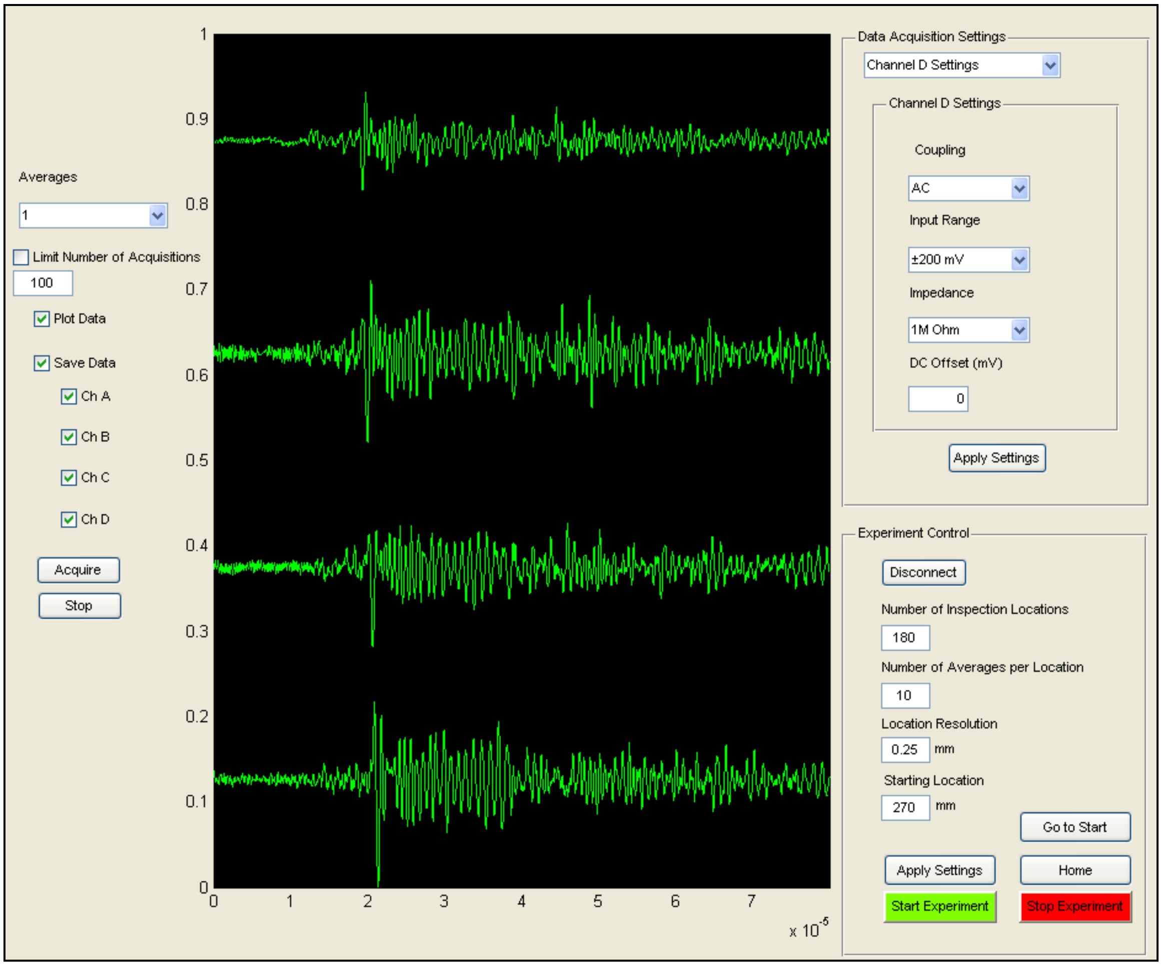

Averages
1

☐ Limit Number of Acquisitions
100

☑ Plot Data

☑ Save Data
- ☑ Ch A
- ☑ Ch B
- ☑ Ch C
- ☑ Ch D

Data Acquisition Settings

Channel D Settings

Channel D Settings

Coupling
AC

Input Range
±200 mV

Impedance
1M Ohm

DC Offset (mV)
0

Experiment Control

Number of Inspection Locations
180

Number of Averages per Location
10

Location Resolution
0.25 mm

Starting Location
270 mm

Fig. 3-6: Screenshot of the graphic user interface

CHAPTER 4

SIGNAL PROCESSING METHODS

The signal processing methods used in this research include three parts: (1) wavenumber-frequency (k-ω) domain filtering, (2) synthetic phase tuning (SPT) and (3) continuous wavelet transform (CWT). The objective of signal processing is to reduce the complexity of signals and identify sources of wave packets to calculate reflection coefficients resulting from the weld.

4.1 Wavenumber-Frequency Domain Filtering

The two-dimensional Fourier transform (2D FT) method is well documented in literatures [49, 52-58]. It is widely used to measure the dispersion curves of Lamb waves and can be used to identify and measure the amplitudes of individual Lamb modes. It is also a critical step in wavenumber-frequency domain filtering technique [53-54]. When full wavefield measurements are transformed into wavenumber and frequency domain by 2D FT, waves traveling in different directions will have different signs in wavenumber. By separating wave components with different signs in wavenumbers, waves traveling in the different directions can be separated.

To illustrate the technique, a simplified model is shown in Fig. 4-1. Referring to Rose [37], it is stated that when a propagating disturbance strikes the interface between two media of different material properties, part of the disturbance is reflected and part is transmitted across the interface.

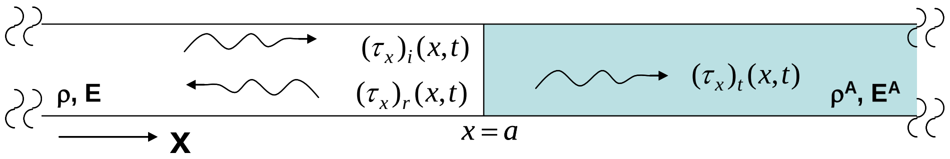

Fig. 4-1: Simplified schematic of one dimensional wave propagation

Assume a harmonic stress input with amplitude A_0 and angular frequency ω_0 is applied in a 1D infinite non-dispersive material. The stress input can be expressed as:

$$(\tau_x)_i|_{x=0} = A_0 e^{i\omega_0 t}\Big|_{x=0} \tag{4-1}$$

And assume there is a discontinuity located at x = a as depicted in Fig. 4-1. The 1D stress in region x < a can be expressed as sum of incident and reflected stress waves as:

$$(\tau_x) = (\tau_x)_i + (\tau_x)_r = A_0 e^{i\omega_0\left(t-\frac{x}{C_L}\right)} + C_r A_0 e^{i\omega_0\left(t+\frac{x}{C_L}-2\frac{a}{C_L}\right)} \tag{4-2}$$

where (τ_x) is 1D stress and subscripts i and r stand for incident and reflected waves. C_L is the phase velocity in region 1 and C_r is the reflection coefficient which can be shown to be determined by the mechanical impedances of materials. The mechanical impedance is defined as the product of density and phase velocity in a material.

$$C_r = \frac{\rho^A C_L^A / \rho C_L - 1}{\rho^A C_L^A / \rho C_L + 1} \tag{4-3}$$

where ρ and ρ^A are densities of materials and C_L and $C_L{}^A$ are phase velocities in region 1 and region 2 respectively. Eq. 4-2 can be further re-written into Eq. 4-4 by introducing wavenumber $k_0 = \omega_0/C_L$.

$$\tau_x(x,t) = A_0 e^{i(\omega_0 t - k_0 x)} + C_r A_0 e^{i(\omega_0 t + k_0 x - 2k_0 a)} \tag{4-4}$$

Since the responses of the whole wave field are known, both spatial and time information is available for the stress distribution in the domain of interest. The two-dimensional Fourier transform (2D FT) of $\tau_x(x,t)$ can be evaluated as:

$$T_x(k,\omega) = \int_{-\infty}^{\infty}\int_{-\infty}^{\infty} \tau_x(x,t)e^{-i(\omega t+kx)}dxdt \tag{4-5}$$

which can be calculated by substituting Eq. 4-4 into Eq. 4-5 and the result is:

$$T_x(k,\omega) = A_0\delta(\omega-\omega_0)\delta(k-k_0) + C_r A_0 e^{2ik_0x_0}\delta(\omega-\omega_0)\delta(k+k_0) \tag{4-6}$$

where δ denotes the delta function. The result of the 2D FT can be represented as a surface plot in wavenumber-frequency domain with two peaks at $\omega = \omega_0$, $k = \pm k_0$, where the positive wavenumber corresponds to incident waves and the negative wavenumber corresponds to reflected waves. The amplitudes at (ω_0, k_0) and $(\omega_0, -k_0)$ are A_0 and C_rA_0 respectively. A simple window function is used to remove the wave components with negative wavenumbers. The wave components with positive wavenumbers left after filtering are transformed back to space-time domain by using inverse 2DFT. Hence the resulting signal will contain wave components travelling in one direction. Similarly the same window function is used to filter out the wave components with positive wavenumbers, and the process described above is repeated to obtain the signals with wave components travelling in the other direction. In some NDT applications, because of the finite sizes of samples under inspection, multiple reflections from the edges of the samples may be present in the signals. Oftentimes, they are irrelevant to the analysis process but by using this technique, they can be filtered out to leave the desired signals, and the resulting less complicated signals can be used for further processing [53-54].

4.2 Synthetic Phase Tuning

Synthetic phase tuning (SPT) technique [59] is similar to the phased array technique in which time delay circuits and multiple generating units are required and the tuned signal is generated and acquired in real time. The SPT technique does not require time delay circuits, and can be implemented by shifting a single general purpose generating unit at a constant interval. At each location, the signals generated are stored independently in memory. These signals are shifted in time and the shifted amount can be calculated by dividing relative distance between sources by the phase velocity of the Lamb wave mode of interest. After shifting, they are superimposed together. The wave mode that propagates with the desired phase velocity will be constructively interfered and amplified. At the same time, for other wave components traveling with different speeds, their amplitudes will tend to be canceled or at least not amplified. Therefore, after applying the SPT technique, the desired wave mode should be dominant in the resulting signal.

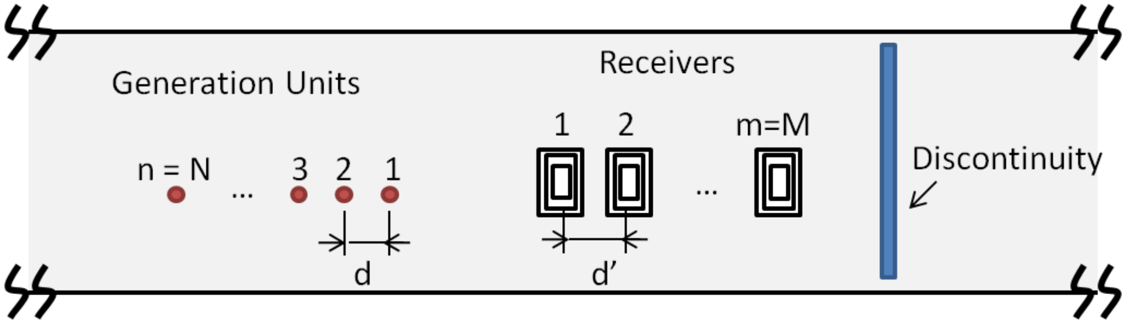

Fig. 4-2: Schematic of the transducer arrangement

To illustrate the SPT technique, a schematic of N sources and M receivers is shown in Fig. 4-2. Waves emitted by each source are captured by each receiver separately. There are N·M signals recorded in memory. Assume that all sources and receivers are identical and the intervals between the sources and receivers are d and d'. If the time domain signal that is generated by the nth source and received by the mth receiver is $h_{nm}(t)$, the mathematical expression of the SPT operation on the source side can be expressed as in Eq. 4-7, which is basically the summation of the shifted versions of $h_{nm}(t)$ for the mth receiver. The shifting is done so that all the signals are shifted to the signal generated by the first source. Fig. 4-3 depicts the operation of the tuning for the wave mode that travels with phase velocity C_p when only two wave modes are present.

$$g_m(t) = \sum_{n=1}^{N} h_{nm}(t + \frac{(n-1)d}{C_p}) \qquad (4\text{-}7)$$

After the SPT operation is done for the source side, there are M synthetic signals left, one for each receiver. By the same fashion, the SPT operation can be applied on the receiver side. Care needs to be given to the direction to shift the signals. In the arrangement shown in Fig. 4-2, as the receiver approaches the discontinuity, the arrival time of the direct incident waves becomes later but that of the reflection waves becomes earlier. The shifting directions for these two waves are opposite. The mathematical expression of the final result $f^{\mp}(t)$ is shown in Eq. 4-8. Here, the shifting is done so that all signals are shifted to the signal received by the first receiver. The minus sign is for the incident wave and the plus sign is for the reflection. Notice that if the arrangement and numbering of the sources and the receivers are different from the one in Fig. 4-2, the signs need to be changed accordingly. One can refer to [59] for more details on SPT technique.

$$f^{\mp}(t) = \sum_{m=1}^{M} g_m\left(t \mp \frac{(m-1)d'}{C_p}\right) = \sum_{n=1}^{N}\sum_{m=1}^{M} h_{nm}(t + \frac{(n-1)d \mp (m-1)d'}{C_p}) \quad (4\text{-}8)$$

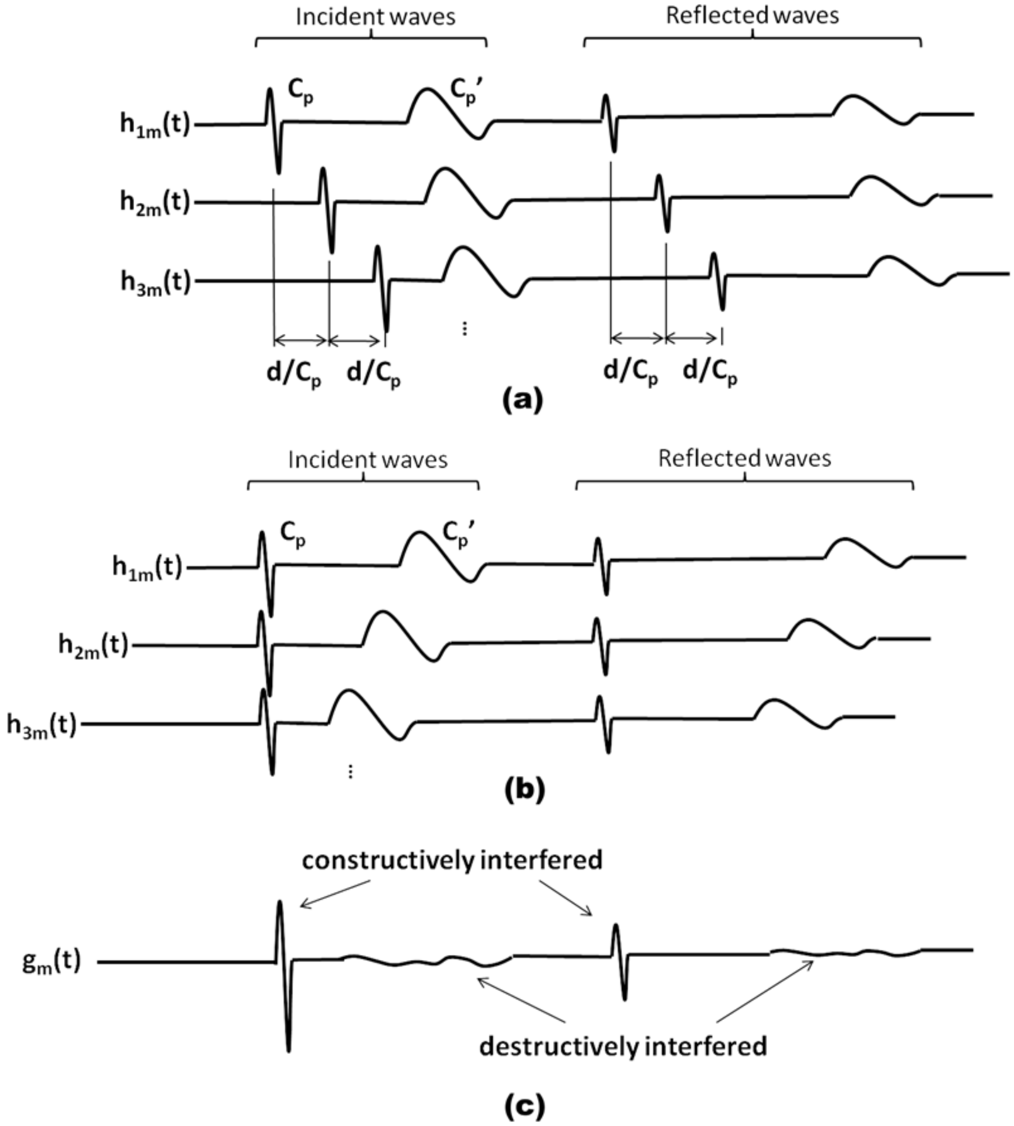

Fig. 4-3: Illustration of operation of SPT

4.3 Continuous Wavelet Transform

Laser generated ultrasonic signals are intrinsically non-stationary, non-periodic and broadband. Although the Fourier transform is widely used to obtain frequency information in signals, it is not suitable for non-stationary signals due to the fact that it cannot retain time information. The continuous wavelet transform (CWT) retains both frequency and time information. Its definition is in Eq. 4-9 [60-61].

$$\mathrm{WS}(s,\tau) = \int f(t)\Psi^*_{s,\tau}(t)dt \qquad (4\text{-}9)$$

where * stands for complex conjugate. The equation shows how a signal f(t) is decomposed into a set of basis functions, $\Psi_{s,\tau}(t)$, which are called wavelets. A set of wavelets is obtained by scaling the mother wavelet $\Psi(t)$ by s and translating it by τ as shown in Eq. 4-10.

$$\Psi_{s,\tau}(t) = \frac{1}{\sqrt{s}}\Psi(\frac{t-\tau}{s}) \qquad (4\text{-}10)$$

Parameters s and τ are the scale and shifting parameters which are the two dimensions after the wavelet transform. The scale parameter is related to frequency. Eq. 4-9, combined with Eq. 4-10, is essentially the inner product of f(t) with scaled and shifted mother wavelet.

Unlike the Fourier transform, different wavelet functions can be used in the wavelet transform depending on the application and signals of interest, and oftentimes they are irregular. This characteristic makes the wavelet transform flexible and powerful. Wavelet analysis approximates a signal with shifted and scaled versions of the mother wavelet. Signals with sharp changes can be better analyzed with an irregular wavelet than with a smooth sinusoid as used in Fourier analysis. All wavelet functions need to satisfy admissibility and regularity conditions. The admissibility condition requires that wavelet functions have zero average in the time domain and makes sure that they can be used to decompose and reconstruct a signal without losing any information. The regularity condition ensures that a wavelet function has limited duration in time. In short, a wavelet is a waveform of effectively limited duration that has an average value of zero [61].

CHAPTER 5

SUPERIMPOSED LASER SOURCES TECHNIQUE

The superimposed laser sources technique is proposed to overcome the drawbacks of the pattern source technique as mentioned in Chapter 2. To create a pattern source, the laser beam is expanded and collimated, and the beam goes through a shadow mask with slits. Pattern sources can be treated as independent line sources illuminating the surface of the sample simultaneously. Because of the constructive interference of ultrasound in space, a narrowband ultrasound sourcewith the designated wavelength can be created. The resulting narrowband signal is then captured by the sensor. On the other hand, for the superimposed laser sources, the laser line source illuminates the sample at discrete locations. To generate narrowband Lamb waves with a dominant wavelength, the signals that are generated by the laser line sources at the interval corresponding to the desired wavelength are superimposed together. The superposition is performed in software so that it permits the flexibility of selecting desired wavelength afterwards. By generating narrowband signals with fixed wavelengths using the SLS technique, the complexity of signals can be reduced and the speeds and frequencies can be estimated from the dispersion curves. The knowledge of speeds and frequencies of narrowband Lamb wave modes permits identification and time-of-flight analysis of each Lamb wave mode.

5.1 Comparison between Pattern Source and SLS

In order to compare the pattern source and the SLS experimentally, two preliminary experiments are conducted on a 300 mm x 200 mm x 2 mm aluminum plate. Fig. 5-1 shows the schematic of the experiment and the placement of the sensors and sources. Fig. 5-1(a) depicts the experiment using a pattern source where the laser beam goes through a mask with 8 slits. Each slit is 1 mm wide and 15 mm long and the pitch between slits is 2 mm. It also shows a laser mark of the pattern source on the laser alignment paper. The width of each stripe is about 1 mm and the pitch is 2 mm. Fig. 5-1(b) shows the experiment using SLS where the laser beam goes through a cylindrical lens and the beam is focused into a line source. Laser marks with 2 mm pitch are shown in the figure as well. Compared with the laser mark in Fig. 5-1(a), the laser line source is more focused and the line is much narrower than the stripe in the pattern source.

The signal induced by the line source is then acquired by the EMAT. After acquisition, a motorized linear stage moves the sample and the EMAT in a 0.5 mm increment while the laser source is fixed and the signals induced by separate line sources are acquired. An example of acquired signals is shown in Fig. 5-2 where each signal is generated with an increment of 0.5 mm in space. In this figure, there are 19 separate signals (portion of the total signals). By superimposing signals generated at the pitch corresponding to the desired wavelength, an artificial pattern source can be created. For example, we can superimpose seven signals together to create narrowband signals. The superposition of signals pointed by the dashed arrows corresponds to 3 mm artificial pattern source (only four of them are shown here) and short solid arrows are for 2 mm source (only five of them are shown here). The long solid arrows indicate another 2 mm source shifted away from the one indicated by short solid arrows by 0.5 mm (five signals are superimposed together). Fig. 5-3 shows an example signal from a 2 mm pattern source, and the 2 mm and 3 mm signals from the SLS technique in the time domain. Here, for the pattern source, the distance between the source (middle of the pattern) and the receiver is 30 mm and for the SLS, seven signals that correspond to 2 mm and 3 mm wavelength are superimposed and the signals are chosen so that the middle one is also 30 mm away from the receiver. In Fig. 5-3, signals are normalized by their own maxima. The comparison shows similarities between a pattern source and the result of the SLS technique. It shows the potential to use the SLS technique to replace a pattern source. The next section mathematically shows the equivalence between a pattern source and the SLS technique under some assumptions.

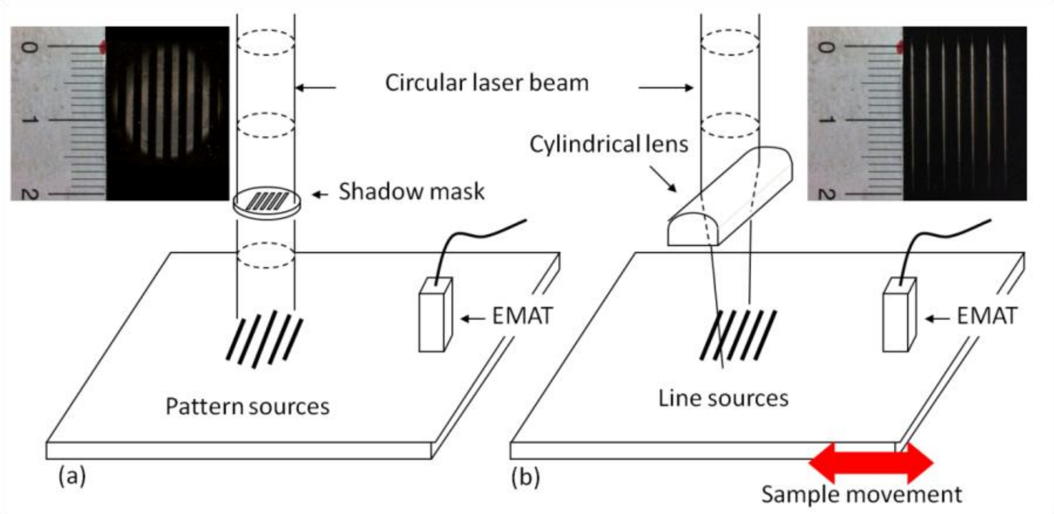

Fig. 5-1: Schematics of experimental setups of the pattern source and superimposed line source

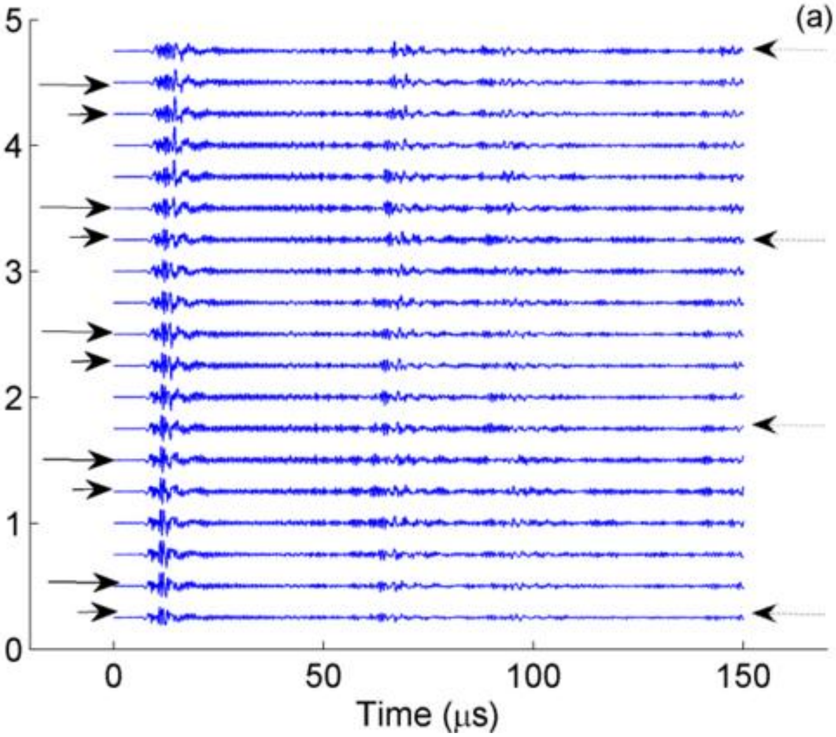

Fig. 5-2: Example of signals acquired from individual line sources

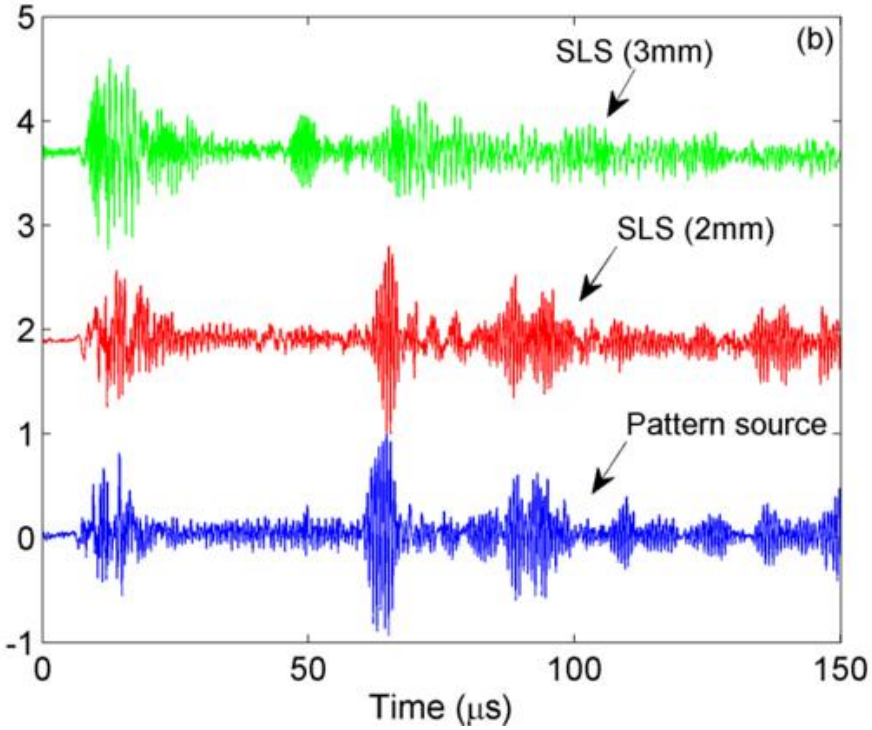

Fig. 5-3: Comparison of time domain signals between superimposed line sources and pattern source

It is informative to show the equivalence between a patter source and SLS technique mathematically. Assume a single line source is infinite long in the y axis and the response of the wave field for it is h(x,t). If the pattern source is made of perfect line sources and linearity holds, then the response of the wave field of the pattern source can be expressed as a convolution integral in space. The mathematical expression is shown in Eq. 5-1:

$$f(x,t) = h(x,t) * g(x) \tag{5-1}$$

where x denotes the distance from the first line source and t denote time; f(x,t) is the response of the pattern source, h(x,t) is the response of a single line source and g(x) is the input sequence for a pattern source which can be expressed as multiple Dirac delta impulses that are separated by the distance corresponding to the wavelength as in Eq. 5-2.

$$g(x) = \sum_{i=0}^{n-1} \delta(x - i\lambda) \tag{5-2}$$

where λ is the distance between line sources and it corresponds to the desired wavelength to be generated, n stands for the total number of line sources that constitute the pattern source, and i is the index of the line source. When i is zero, it denotes the first line source. Substitute Eq. 5-2 into Eq. 5-1 and the response of the pattern source can be derived. The derivation of the convolution is shown in Eq. 5-3:

$$f(x,t) = \int_{-\infty}^{-\infty} h(x-\xi,t)g(\xi)d\xi = \int_{-\infty}^{-\infty} h(x-\xi,t)\sum_{i=0}^{n-1}\delta(\xi - i\lambda)\,d\xi \tag{5-3}$$

Since the first term is independent of i, the summation over i can be moved to the front. Eq. 5-3 becomes Eq. 5-4.

$$\sum_{i=0}^{n-1}\int_{-\infty}^{-\infty} h(x-\xi,t)\delta(\xi - i\lambda)d\xi = \sum_{i=0}^{n-1} h(x - i\lambda, t) \tag{5-4}$$

Eq. 5-3 and Eq. 5-4 show that the wave field of a pattern source that consists of n+1 line sources, with the pitch of λ, is actually the superposition of n shifted replicates of the wave field of a single laser line source and the interval between each replicate is the wavelength, λ. Eq. 5-4 also shows that the superposition can be performed after all signals have been stored in the computer memory.

5.2 Implementation of SLS Technique and Signal Processing Methods

This section presents an example that illustrates the implementation of the superimposed laser sources technique and the signal processing methods described in Chapter 4.

5.2.1 Implementation of Superimposed Laser Sources Technique

An experiment is conducted on a 2 mm aluminum plate. Fig. 5-4 shows the schematic of the experimental setup where the plate is held on a motor driven linear stage and a laser line source is used to generate ultrasound. On the sample, there is an artificial groove which is 0.8 mm wide and 1.75 mm deep. When conducting the experiment, the laser beam is fixed; samples and the EMAT are moved by the linear stage at a 0.5 mm increment. At each location, 32 signals are acquired and averaged to increase signal-to-noise ratio. After all ultrasonic signals have been stored in computer memory, the superimposed laser sources are generated by superimposing every five signals corresponding to 2 mm wavelength together.

Fig. 5-5(a) shows the scan of the original signals, where the X axis denotes time and the Y axis denotes the distance between sources and the EMAT. Fig. 5-5(b) shows the results of the SLS technique. The gray scale of the plots represents relative signal amplitude. However, the contrast and brightness are adjusted for the clarity of the plots. There are some wave fronts featuring positive slopes and some featuring negative slopes indicating waves with increasing or decreasing distance of travel as the laser source is moved away from the defect and the EMAT. The theoretical arrival time for the direct incident waves, the reflections from the groove, and the reflections from the left edge of the sample are also plotted in the figure. The blue solid lines are for A0 mode and the red dashed lines are for S0 mode.

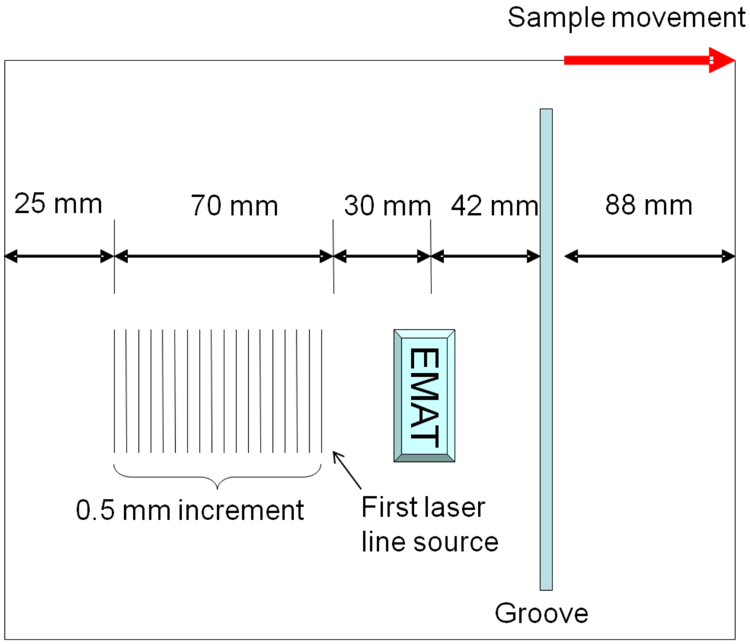

Fig. 5-4: Schematic of the experimental setup

5.2.2 Implementation of Wavenumber-Frequency Domain Filtering Technique

Next, in order to separate waves traveling with increasing and decreasing distance of travel, wavenumber-frequency domain filtering technique is performed. The result of 2D FT of Fig. 5-5(b) is shown in Fig. 5-6 in which X axis denotes frequency, Y axis denotes wavenumber and the brightness represents signal amplitude (the gray scale is reversed for the clarity of the graph). Four bright stripes can be seen in Fig. 5-6. The image is basically symmetrical about the x axis. Two of those stripes center around (1.36 MHz, ±3141 rad/m) and the other two center around (1.57 MHz, ±3141 rad/m). Wavenumber 3141 rad/m corresponds to wavelength 2 mm. To apply k-ω domain filtering, the components with positive wavenumbers and with negative wavenumbers are filtered out separately and then the filtered space-time representation can be obtained by taking the inverse 2D FT on the filtered signals. The results are shown in Fig.

5-7(a) and 5-7(b). Compared with Fig. 5-5(b), it is clear that the wave fronts with positive slopes and negative slopes have been separated successfully and the complexity of signals is greatly reduced. Because the direct incident waves and reflection waves from the defect have increasing distance of travel as the source is moved away from the EMAT, Fig. 5-7(a) contains all the necessary information for calculating reflection coefficients.

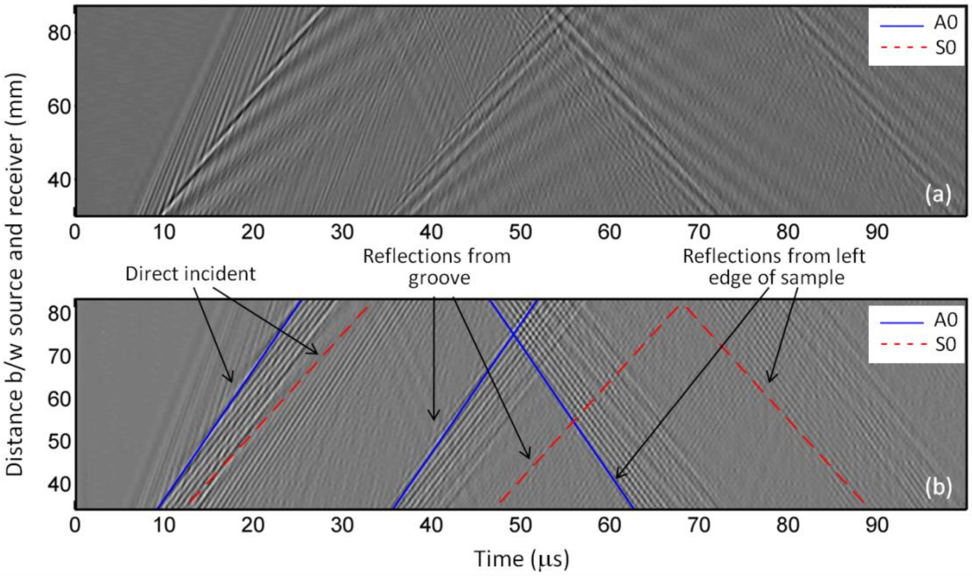

Fig. 5-5: Space-time representation of (a) original signals (b) results of SLS operation (2 mm wavelength)

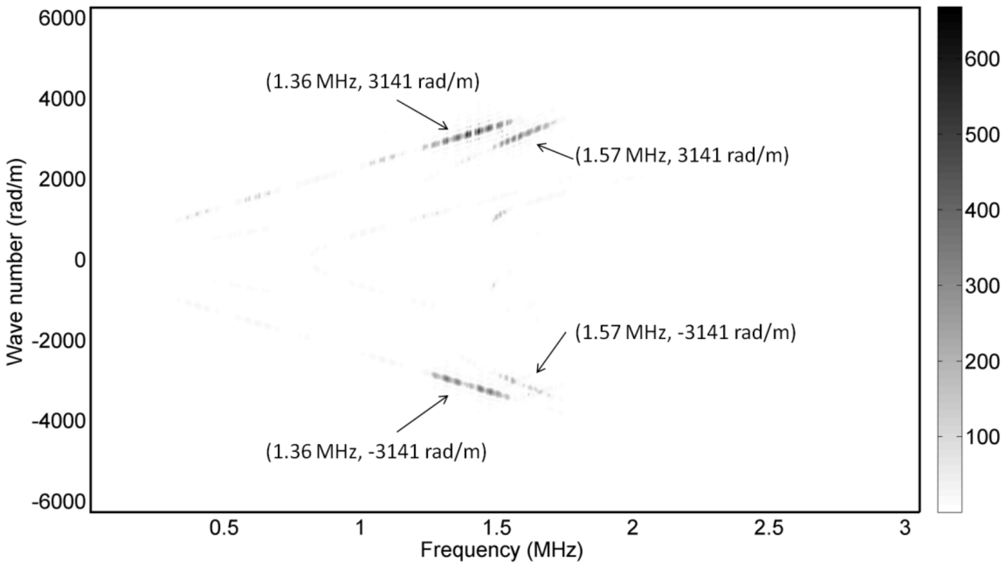

Fig. 5-6: Wavenumber-frequency representation of signals after SLS operation

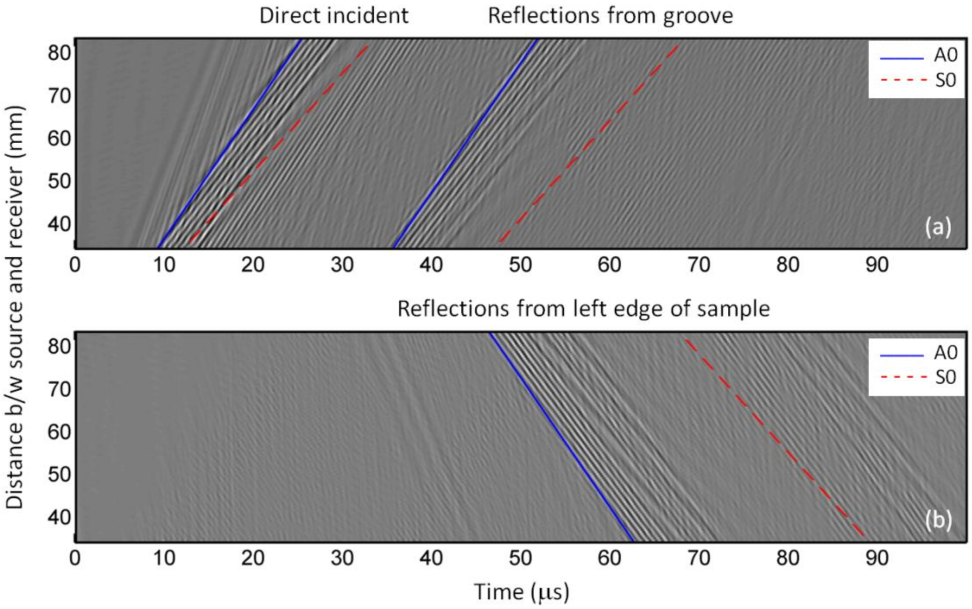

Fig. 5-7: Space-time representation of (a) components with positive wavenumbers (b) components with negative wavenumbers

5.2.3 Implementation of Synthetic Phase Tuning Technique

By applying SLS technique, narrowband Lamb waves can be created. It reduces complexity of the signals by limiting the possible traveling wavelengths in the signals. The k-ω domain filtering technique further simplifies the signals by filtering out the waves that travel at the direction that is not of interest to us. However, the resulting signals after applying the abovementioned two techniques can still be complicated because multiple Lamb wave modes still coexist in the signals. Synthetic phase tuning (SPT) technique can be applied to isolate a particular Lamb wave mode. By properly shifting the signals in Fig. 5-7(a) in time, the desired mode can be isolated. The shifted amount can be calculated by dividing relative distance between sources by the phase velocity of the desired mode. In this case, the relative distance between sources is 0.5 mm. If the modes to be isolated are 2 mm A0 and S0 modes, the shifting amount in time can be calculated as the multiples of 0.5 mm divided by their phase velocities, which are 2760.7 m/s and 3169.4 m/s for 2 mm A0 and S0 modes in a 2 mm thick aluminum plate. Fig. 5-8(a) and 5-9(a) are time domain results of SPT for 2 mm A0 and S0 modes respectively. The effect of isolation is apparent. The incident waves and reflected waves of both modes can be easily identified and reflection coefficients can be calculated. Also in the graphs are envelops for the time domain signals. These envelops are derived by the Hilbert transform [62], which allows us to determine the amplitudes of wave components. The details of the Hilbert transform can be found in the section 5.3.4. Fig. 5-8(b) and 5-9(b) are time frequency representation for these two modes in the frequency range of 1MHz to 2MHz. The transformation is done by using the complex Morlet mother wavelet. The complex Morlet mother wavelet is defined as:

$$\Psi(t) = \frac{1}{\sqrt{\pi f_b}} \exp(2i\pi f_c t) \exp\left(-\frac{t^2}{f_b}\right) \tag{5-5}$$

where f_b is a bandwidth parameter and f_c is the wavelet center frequency. More details about complex Morlet mother wavelets can be found in [61]. Here, f_b and f_c are chosen to be 10 and 1.5 MHz respectively. The frequency components of 2 mm A0 and S0 modes can also be identified as 1.36 and 1.57 MHz respectively, which match the calculation shown in Fig. 2-5 and Fig. 2-6.

The operations of SPT and SLS share a lot of similarities. Both of these techniques require moving the ultrasound generating unit at a constant interval. All signals are generated and stored in computer memory independently and individually. The resulting signal is obtained by manipulating those signals in software. This means that the application of SPT can be easily incorporated in the course of SLS operation.

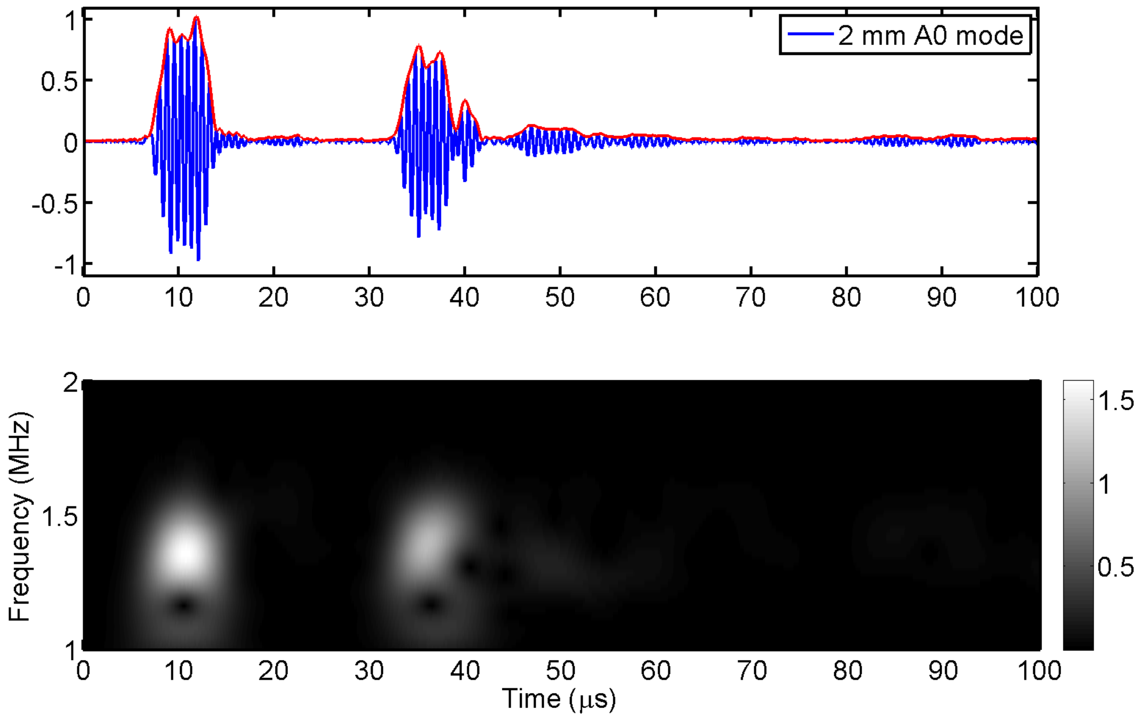

Fig. 5-8: (a) Time domain and (b) CWT results of SPT for 2 mm A0 mode

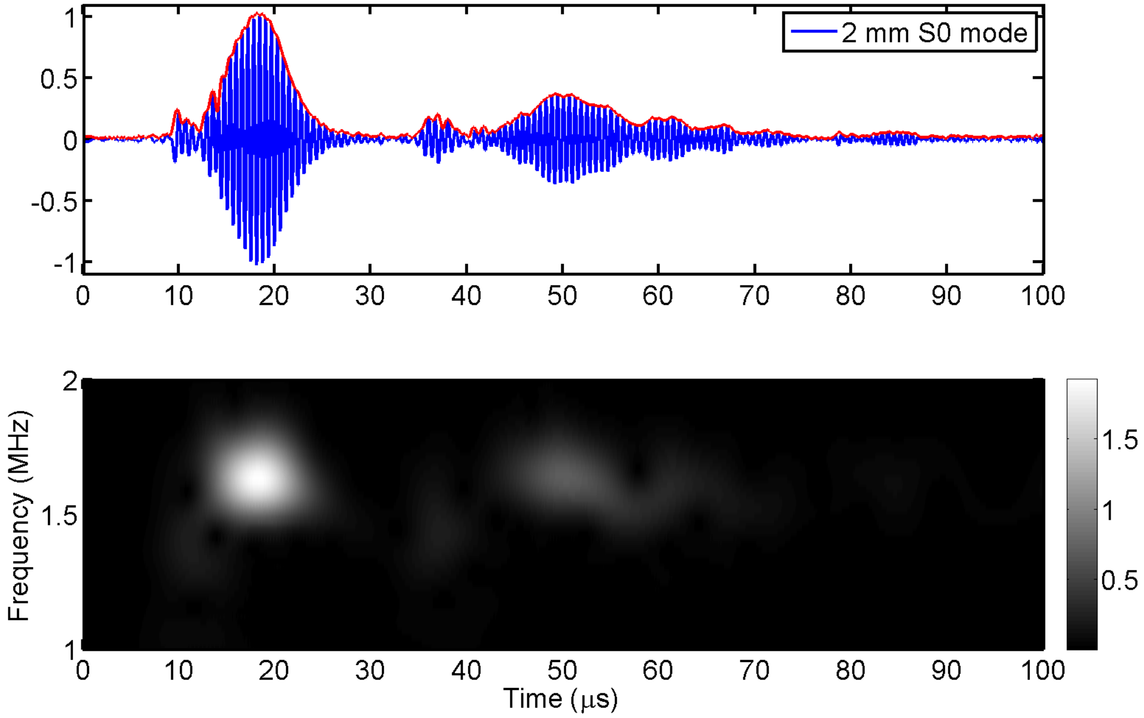

Fig. 5-9: (a) Time domain and (b) CWT results of SPT for 2 mm S0 mode

5.2.4 Calculation of Reflection Coefficients

There are two ways to calculate reflection coefficients. The first way is through the time domain signals. The Hilbert transform can be applied to the time domain signal to get the envelope of it.

For an arbitrary signal X(t), the Hilbert transform is defined as [63]:

$$\mathrm{H}(t) = \frac{1}{\pi}\int_{-\infty}^{\infty} \frac{\mathrm{X(t')}}{\mathrm{t - t'}} \mathrm{dt'} \tag{5-6}$$

The Hilbert transform performs a 90 degree phase shift to construct the so-called analytic signal as:

$$\mathrm{Z(t) = X(t) + iH(t) = e(t)e^{i\phi(t)}} \tag{5-7}$$

whose real part is the original signal X(t) itself and imaginary part is its Hilbert transform H(t). The envelop e(t) and instantaneous phase $\phi(t)$ can be derived as:

$$\mathrm{e(t)} = \sqrt{\mathrm{X^2(t) + H^2(t)}}, \qquad \phi(\mathrm{t}) = \arctan\frac{\mathrm{H(t)}}{\mathrm{X(t)}} \tag{5-8}$$

The Hilbert transform represents the instantaneous characteristics of wave signal. The reflection coefficients can be obtained by dividing the amplitude of the reflection envelope peak by that of the incident envelope peak in the time domain. These envelopes are overlapped with the time domain signals in Fig. 5-8(a) and 5-9(a). In this example, the reflection coefficients for 2 mm A0 mode and S0 mode calculated by the Hilbert transform are 0.776 and 0.368, respectively.

Another way to calculate reflection coefficients is through the continuous wavelet transform. In the examples shown in Fig. 5-8(b) and 5-9(b), amplitudes of the wave components are represented by the brightness. Therefore, the reflection coefficients can be obtained by dividing the amplitude of the reflection component by that of the incident component in the CWT domain. In this example, the reflection coefficients for 2 mm A0 mode and S0 mode calculated by from the signals in the CWT domain are 0.769 and 0.371, respectively. The reflection coefficients calculated by both methods are very close to each other. However, because the signal processing time for the continuous wavelet transform is usually longer. Therefore, the first method is used in this research.

CHAPTER 6

FEASIBILITY STUDY OF THE PROPOSED RESEARCH

In order to show that SLS has practical applications, and that the proposed signal processing procedure can be used to correlate reflection coefficients to defect severity, validation is conducted through both finite element simulations and preliminary experiments on thin plates with surface breaking defects. First, simulations on models with different severities of surface breaking defects are performed. Once achieved, reflection coefficients are then calculated. Following this, a series of experiments similar to the model are conducted. Ultimately, the reflection coefficients obtained from the experiments are compared with those from the simulations to show the applicability of the proposed method.

6.1 Simulation Procedures

To simplify the problem at hand, the laser line sources are assumed to be infinitely long in the direction orthogonal to the plane determined by the wave propagation and thickness directions. In this way, the problem can be simplified to a 2D plane strain problem [64-67]. The material used in the simulation is aluminum, and the material properties, longitudinal (C_L) and shear (C_T) wave speeds are listed in Table 6-1. The simulation of laser generated ultrasound is approached as a sequentially solved transient thermomechanical problem. The temperature field induced by laser input is first solved and the temperature distribution is taken as a thermal nodal load in the transient structural analysis in each time step. The transient displacement field is then solved sequentially. To perform this analysis, two different physical fields of analyses are required to share the same geometry model with the same mesh but with different element types. Furthermore, the element type used in thermal analysis needs to be compatible with the element type used in structural analysis. The commercial software Abaqus 6.8 is used to perform this analysis.

Table 6-1: Material properties and wave speeds

	E (GPa)	ν	λ (GPa)	μ (GPa)	C_L (m/s)	C_T (m/s)
Aluminum	70	0.33	51.1	26.3	6194.4	3120.2

Care needs to be taken to the size of mesh. Due to the large temperature gradient at the location at which the laser illuminates in a very short period of time, considerably fine mesh is needed in that heat-affected region in order to capture the accurate transient temperature field. On the other hand, the element size needed for calculating accurate transient structural field is not that demanding. This means a coarser mesh can be used for the region where ultrasonic waves propagate. Therefore a smooth transition from the fine mesh to the coarse mesh needs to be taken care of. Benmeddour et al. [66-67] suggest the mesh size be smaller than one-sixth of the wavelength. In this model, the mesh size of 100 μm is used in the wave propagation region and the mesh size of 5 μm is used in the laser input region.

Two time steps are used in the analysis. Around the heat input (laser irradiating) stage, which takes place during the first 100 ns, the time step is set to 1 ns to capture the rapid change in temperature distribution. Afterwards, the time step is set to 25 ns for the rest of analysis. According to Xu et al. [64], the appropriate time step is chosen to correspond to the time the fastest possible wave propagates between successive elements in the mesh. Considering that the fastest wave is the longitudinal wave with a speed of around 6000 m/s, the choice of 25 ns is appropriate.

The thermal loading condition in the simulation can be described as follows:

$$-k\frac{\partial T(x,y,t)}{\partial y}\bigg|_{top\_surface} = I_0 A(T) f(x) g(t) \tag{6-1}$$

where k is the thermal conductivity, I_0 is the incident laser energy density and the total energy is set to be 46 mJ, which is the setting used in the experiment. A(T) is the optical absorptivity of the specimen surface. For aluminum, the optical absorptivity is as follows, where T is in Celsius [59].

$$A(T) = 5.2 \times 10^{-2} + 3 \times 10^{-5}(T - 27) \tag{6-2}$$

f(x) and g(t) are the spatial and temporal distributions of the laser pulse, respectively. These two functions can be written as:

$$f(x) = \exp\,(-\frac{x^2}{x_0^2}) \tag{6-3}$$

$$g(t) = \frac{t}{t_0}\exp\,(-\frac{t}{t_0}) \tag{6-4}$$

where x_0 and t_0 are set to be 300 μm and 10 ns in the simulation.

The model of the simulation is shown in Fig. 6-1. The length of the plate is 255 mm and the thickness is 1.5 mm or 2 mm. A surface breaking notch is located at the location 170 mm away from the left end of the plate. The width, w, of the notch is 0.8

mm and the depth, d, increases from 1/8 to 7/8 of the plate thickness with an increment of 1/8 of the thickness. The receiving point shown by an upward arrow is located at 125 mm away from the left side of the plate. For the model with a particular notch depth, ultrasonic signals are generated separately by 20 single line sources located between 51 mm and 70 mm away from the left end of the plate with the interval equal to 0.5 mm. Wavenumber-frequency domain filtering is performed on these signals and waves propagating in different directions are separated. After the ultrasonic signals are simplified, narrowband signals corresponding to 2 mm and 3 mm wavelengths are created by superimposing every five signals together.

The narrowband signals are processed by the above mentioned techniques. The wave packets induced by different sources are identified so that the reflection coefficients due to the notches can be calculated by dividing amplitudes of reflected waves by those of incident waves as shown in Section 5.3.4. The simulation results are shown in Fig. 6-2. Detailed discussion will be given in section 6.3.

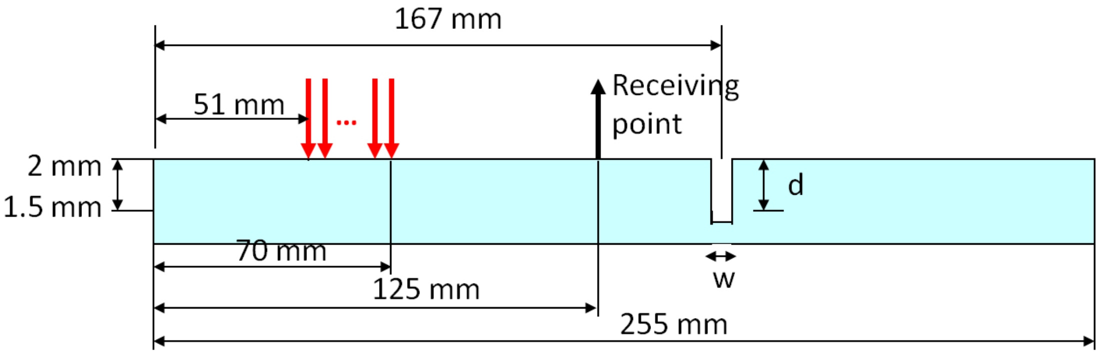

Fig. 6-1: Schematic of finite element analysis model

6.2 Experimental Procedures

In order to validate the simulation results, a set of experiments is conducted. The experimental setup is the same as the setup depicted in Chapter 5 and the testing procedure is the same as the procedure described Chapter 4. On each sample, an artificial groove is made to simulate a surface breaking crack defect. The plate thickness is 2 mm and the grooves are 0.8 mm wide and vary in depth. Seven depths are used in these experiments: 0.25, 0.50, 0.75, 1.00, 1.25, 1.50 and 1.75 mm (1/8, 2/8, 3/8, 4/8, 5/8, 6/8 and 7/8 of the plate thickness). A set of five signals that correspond to 2 mm or 3 mm wavelength are superimposed and followed by the signal processing procedure as discussed earlier. Reflection coefficients are calculated and compared with simulation results. The results and comparison are shown in Fig. 6-3.

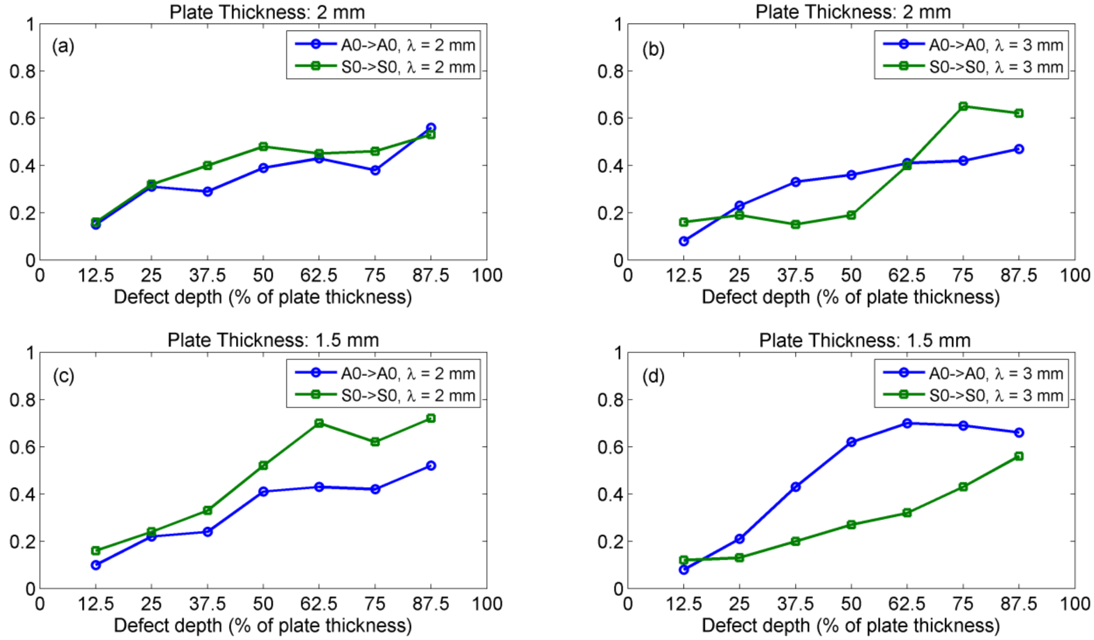

Fig. 6-2: Simulation results of reflection coefficients of mode A0 and S0 in an aluminum plate with different plate thicknesses and wavelengths

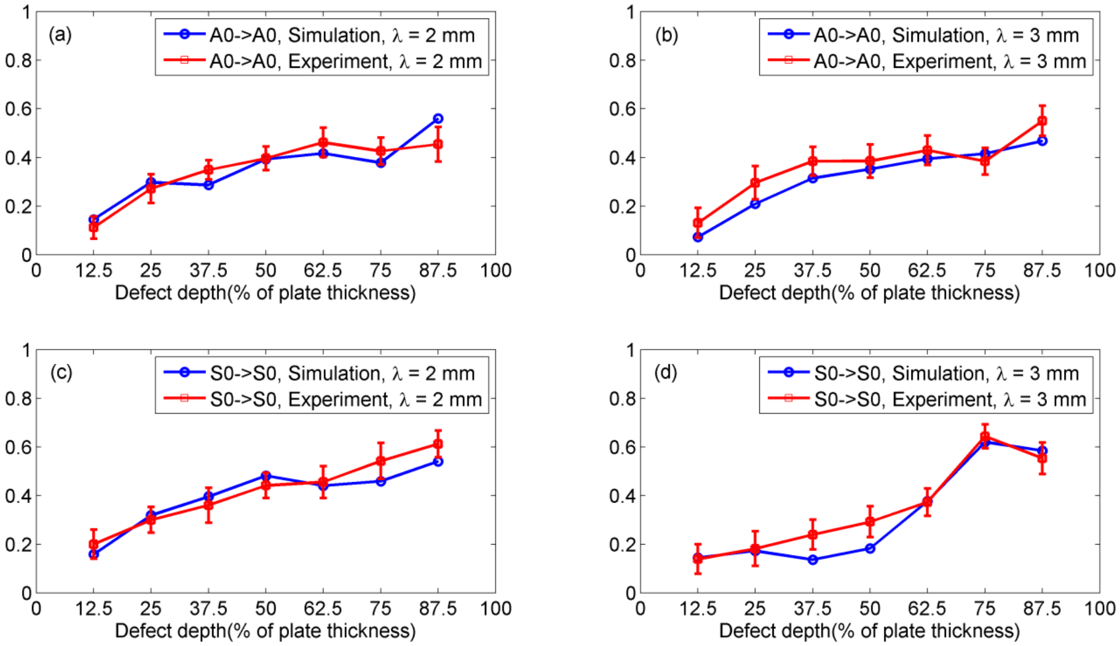

Fig. 6-3: Comparison between simulation and experimental results with 2 mm plate thickness

6.3 Discussion of Simulation and Experimental Results

In Fig. 6-2, the simulation results of the reflection coefficients of modes A0 and S0 with different plate thickness and wavelengths are presented. In the figure, the legend “A0->A0” denotes the coefficients corresponding to incident A0 mode and reflected A0 mode; the legend “S0->S0” denotes the coefficients corresponding to incident S0 mode and reflected S0 mode. As expected, the overall trend for the reflection coefficients increases with severity of defects. However most of them do not increase monotonically.

In Fig. 6-2(a), for the plate thickness equal to 2 mm, the reflection coefficients for A0 mode and S0 mode with 2 mm wavelength show very similar results. The frequency-thickness (f-d) product of A0 mode and S0 mode are 2720 and 3120 Hz-m respectively. Most parts of the reflection coefficients for both cases are between 0.2 and 0.6. In Fig. 6-2(b), the reflection coefficient curves of A0 mode and S0 mode with 3 mm wavelength are very different. The f-d product of A0 mode and S0 mode are 1700 and 2480 Hz-m respectively. For A0 mode, the coefficients gradually rise with the defect depth. The rather linear response between 3 mm A0 mode in 2 mm plate makes it suitable as a calibration curve for quantifying defect depth. For S0 mode, the coefficients are basically constant around 0.2 when the defect depth is below 50% of the plate thickness.

Fig. 6-2(c) and 6-2(d) show reflection coefficients when the plate thickness is 1.5 mm. The f-d product of 2 mm wavelength A0 mode and S0 mode are 2325 and 2880 Hz-m respectively; the f-d product of 3 mm wavelength A0 mode and S0 mode are 1455 and 2325 Hz-m respectively. The profile of reflection coefficients for A0 mode with 2 mm wavelength shows much similarity with the one with plate thickness equal to 2 mm. For 3 mm wavelength, the reflection coefficient of S0 mode increases steadily with defect depth but A0 mode levels off when the defect depth is greater than 50% of the plate.

Fig. 6-3 shows the comparison between the simulation and experimental results with the plate thickness equal to 2 mm. The experimental result agrees with the simulation result very well. Based on the simulation and experimental results, it is observed that the sensitivities of reflection coefficients to defect depth are quite different in different situations. For example, when the plate thickness is 2 mm and the wavelength is 3 mm, the reflection coefficient of S0 is insensitive to the shallow defects when the depth is less than 1 mm. Under the same situation, the reflection coefficient of A0 is insensitive to the defect depths in the middle range between 37.5% and 75% of the plate thickness.

In this study, mode conversion coefficients are not calculated because the mode converted waves cannot be clearly observed in the resulting signals. One possible reason is because the sensor is placed too close to the groove so that the arrival time of the reflected waves and the mode converted waves is very close. Even though the synthetic phase tuning technique can isolate a particular wave mode, there will still be some components of other wave modes that cannot be completely cancelled out. The remaining wave components can create a problem for the identification of mode converted signals if their arrival time is too close. One possible solution is to increase the distance between the groove and the sensor. For example, we can place the laser line sources between the groove and the sensor. The increase of the distance between the groove and the sensor will make the arrival time of reflected waves and mode converted waves from the groove separate further apart.

There is one limitation of the SLS technique. Ideally when SLS technique is performed, only signals with a certain wavelength will be constructively interfered. However, in fact, signal with any other wavelength, which can be calculated by dividing the desired wavelength by any integers, will also be constructively interfered and reserved in the resulting signal. This problem can be easily tackled because these extra signals usually have different frequency contents from the desired signals and can be easily distinguished in the time-frequency representation.

The relationship between the reflection coefficients and the defect depths promises the potential of using the reflection coefficients of different wave modes and wavelengths to quantify the severity of defect. However, from the observation, different modes or wavelengths are sensitive to different ranges of defect depths. Therefore, it is crucial to understand the relationships between wave modes, wavelength, plate thickness and defect.

CHAPTER 7

PREDICTION AND EXPEIMENTAL VALIDATION OF DIMENSIONS OF BUTT WELDS IN THIN PLATES (I)

This chapter and the next chapter are dedicated to the methodology to develop prediction models that can be used to predict dimensions of butt welds in thin plates by using laser generated ultrasound. In this chapter, the details of experimental procedure are discussed. The superimposed line sources (SLS) technique is used to generate narrowband ultrasound in the welded samples. The signal processing procedure that combines wavenumber-frequency (k-ω) domain filtering and synthetic phase tuning (SPT) is used to reduce the complexity of Lamb wave signals. The reflection coefficients for different wavelengths corresponding to each wave mode are calculated. Cutcheck inspection is performed and critical dimensions of each weld such as penetration depth, reinforcement height and bead width are measured.

7.1 Experimental Procedure

The experimental procedure, model development and validation can be described in the following steps: 1. Prepare two sets of samples. One set of samples is used for model development and the other set is used for model validation. 2. Inspect these samples by using the SLS technique. 3. Perform cutcheck inspections on the samples and measure the dimensions of the weld joints. 4. Follow the signal processing procedure and calculate the reflection coefficients of Lamb wave modes A0 and S0 for ten different wavelengths. 5. Develop regression models that correlate the reflection coefficients to weld dimensions with data from one set of samples. 6. Use reflection coefficients from the other set of samples to predict weld dimensions using the regression. These predicted weld dimensions are validated with the cutcheck results. From the validated prediction results, the best prediction model can be chosen. Step 5 and 6 will be discussed in details in Chapter 8.

7.2 Sample Preparation

Weld dimensions are affected by many welding parameters such as electrode extension, arc voltage, welding speed, wire feed rate. In a controlled experiment, a range of weld dimensions can be realized by applying different welding parameters. A sample is made by welding two pieces of A36 steel plates together. The material properties of the steel and the longitudinal and shear wave speeds are shown in Table 7-1. The plate measures 254 x 140 x 2.5 mm. The weld seam is 216 mm long. During welding, the torch is fixed and the samples are moved by a linear stage with a programmable speed. The first set of samples is made by varying four welding parameters to make wide ranges of weld dimensions. These four parameters are contact tip-to-workpiece distance (CTWD), welding speed, arc voltage and wire feed rate (WFR). A four-factor two-level full factorial design of experiment is conducted. The parameters and their levels are shown in Table 7-2 and the design matrices are shown in Table 7-3. There are 16 runs and the run order is randomized to minimize lurking variables that are not identified. The second set of samples is prepared by varying two welding parameters, which are welding speed and WFR. In fact, the second set of samples was not prepared until the cutcheck and measurement of the first set was done. However, in order to make the paragraph flow well, they are presented together in this section. A two-factor three-level full factorial design is implemented. There are nine runs. The levels are shown in Table 7-2 as well. The levels chosen for the second set were based on the cutcheck results of the first set. The CTWD and Arc voltage are held constant for the second set in order to reduce variability of the weld. The other reason for varying just varying the welding speed and wire feed rate is because these factors are easier to be accurately controlled by the computer program.

Table 7-1: Material Properties of A36 Steel

	E (GPa)	ν	λ (GPa)	μ (GPa)	C_L (m/s)	C_T (m/s)
A36 Steel	200.0	0.26	86.0	79.4	5584.3	3180.4

Table 7-2: Welding parameters for two sets of samples

	First Set Levels		Second Set Levels		
Factor	-	+	-	0	+
A. CTWD (inch)	0.5	0.8	0.5		
B. Welding speed (in/min)	17	25	15	20	25
C. Arc voltage (Volt)	18	22	18		
D. Wire feed rate (in/min)	150	200	150	175	200

Table 7-3: Design Matrices for two sets of samples

	First Set				Second Set	
Run	CTWD	Welding speed	Arc voltage	WFR	Welding speed	WFR
1	-	-	-	+	-	-
2	-	-	-	-	-	0
3	-	-	+	+	-	+
4	-	-	+	-	0	-
5	-	+	-	+	0	0
6	-	+	-	-	0	+
7	-	+	+	+	+	-
8	-	+	+	-	+	0
9	+	-	-	+	+	+
10	+	-	-	-		
11	+	-	+	+		
12	+	-	+	-		
13	+	+	-	+		
14	+	+	-	-		
15	+	+	+	+		
16	+	+	+	-		

7.3 Experimental Setup

The experimental setup is the same as the setup shown in Fig. 3-3. The photo presented here in Fig. 7-1. A sample is held vertically on a linear stage. A laser beam is directed through a concave lens and then focused by a cylindrical lens to form a line source which illuminates the surface of the samples to generate ultrasound. The laser is a Continuum Lasers Inlite II-20 pulsed Nd:YAG Q-switched laser. The repetition rate of the laser is 20 Hz and the energy per pulse is 56 mJ. An electromagnetic acoustic transducer (EMAT) is used to receive the ultrasonic signals. The EMAT has a 0.5 - 2.5 MHz bandwidth. The laser and the EMAT are arranged in a reflection mode so that the EMAT can capture both the direct incident wave and its reflection from the weld seam.

A 14 bit data acquisition card samples the signals at 25 MHz sampling frequency and stores the signals in the computer memory.

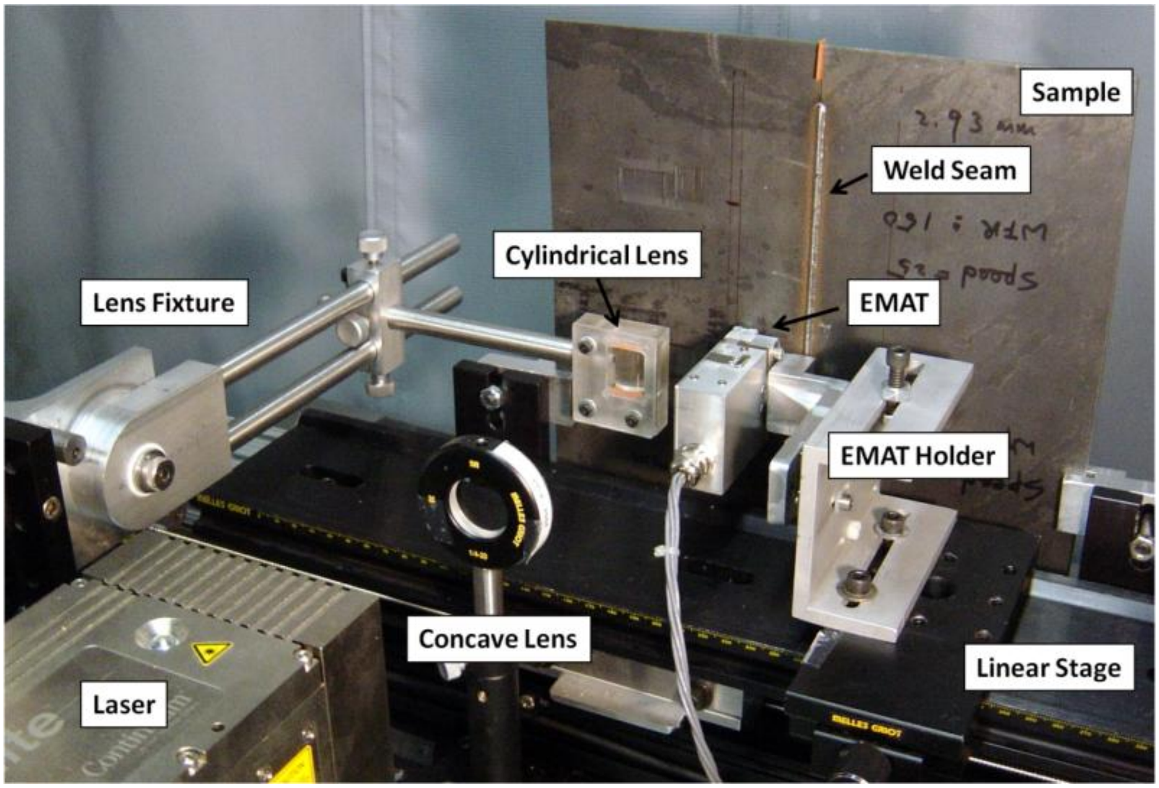

Fig. 7-1: Photo of experimental setup

In this research, ten wavelengths from 1.75 to 4 mm at the step of 0.25 mm are generated. The upper bound and lower bound of the wavelengths of interest are determined by the bandwidth of the EMAT, which is from 0.5 to 2.5 MHz. The wavelengths are chosen so that the frequency of S0 and A0 modes of these wavelengths is within the range of uniform frequency response of the EMAT. The wave speed and frequency content of each Lamb wave mode of the desired wavelength can be estimated from the dispersion curves. The dispersion curves between phase velocity and frequency for S0 and A0 modes in a 2.5 mm A36 steel are shown in Fig. 7-2. Three straight lines that represent 2 mm, 3 mm and 4 mm wavelengths are also shown in the figure as examples. The frequency of narrowband ultrasound of a certain wavelength and wave mode can be determined by looking at the intersection between the straight line of the corresponding wavelength and the curve of the corresponding wave mode. Once the frequency has been determined, one can use Fig. 7-3 to determine group velocity of the wave. This procedure has been described in section 2.2. A computer program has been written to determine the frequencies, phase velocities and group velocities of S0 and A0 modes of the wavelengths of interest, and they are listed in Table 7-4.

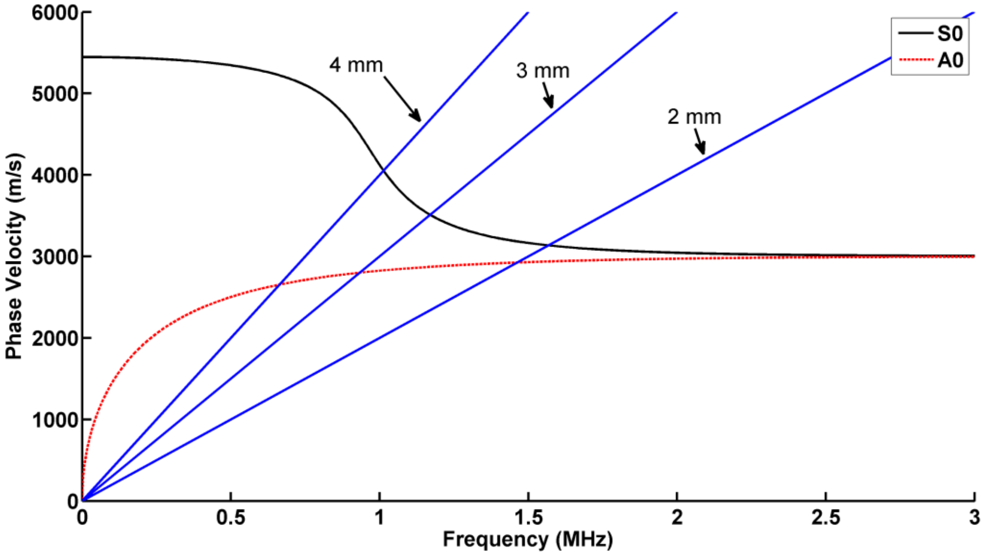

Fig. 7-2: Dispersion curves of phase velocities of a 2.5 mm A36 steel plate

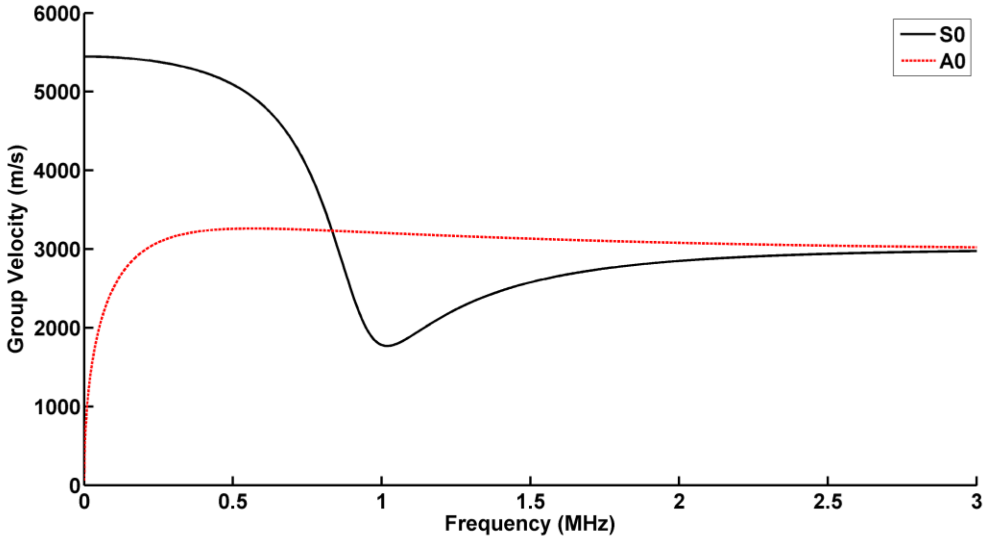

Fig. 7-3: Dispersion curves of group velocities of a 2.5 mm A36 steel plate

Table 7-4: Frequencies, phase and group velocities of S0 and A0 modes of the wavelengths used in this research

λ (mm)	S0			A0		
	f (MHz)	Cp (m/s)	Cg (m/s)	f (MHz)	Cp (m/s)	Cg (m/s)
1.75	1.75	3068.9	2787.0	1.69	2956.1	3102.8
2.00	1.56	3116.7	2675.6	1.47	2933.2	3129.1
2.25	1.41	3179.7	2546.9	1.29	2907.3	3152.8
2.50	1.30	3257.6	2407.5	1.15	2878.8	3174.1
2.75	1.22	3349.9	2264.5	1.04	2848.3	3193.0
3.00	1.15	3455.1	2125.7	0.94	2816.1	3209.6
3.25	1.10	3541.7	1999.2	0.86	2782.7	3223.8
3.50	1.06	3696.8	1892.9	0.79	2748.3	3235.6
3.75	1.02	3828.7	1815.1	0.72	2713.1	3245.2
4.00	0.99	3964.7	1773.8	0.67	2677.4	3252.4

7.4 Optimization of Inspection Parameters

In this section, the procedure to determine some important inspection parameters and component placement that result in stable reflection coefficients is discussed. The placement of inspection components is shown in Fig. 7-4. Four things need to be determined and optimized. First, the number of signals to be superimposed in the SLS technique. Second, the total number of signals generated in the SLS technique. Third, the location of the laser line sources, which is the distance between the center of weld to the first laser line source, and is shown as x in Fig. 7-4. Fourth, the location of EMAT, which is shown as y in Fig. 7-4. Notice that the location of EMAT is measured from the center of weld to the center of coil A of the EMAT. The interval between four coils of EMAT is 2 mm, and coil A is the closest to the laser line sources while coil D is the furriest.

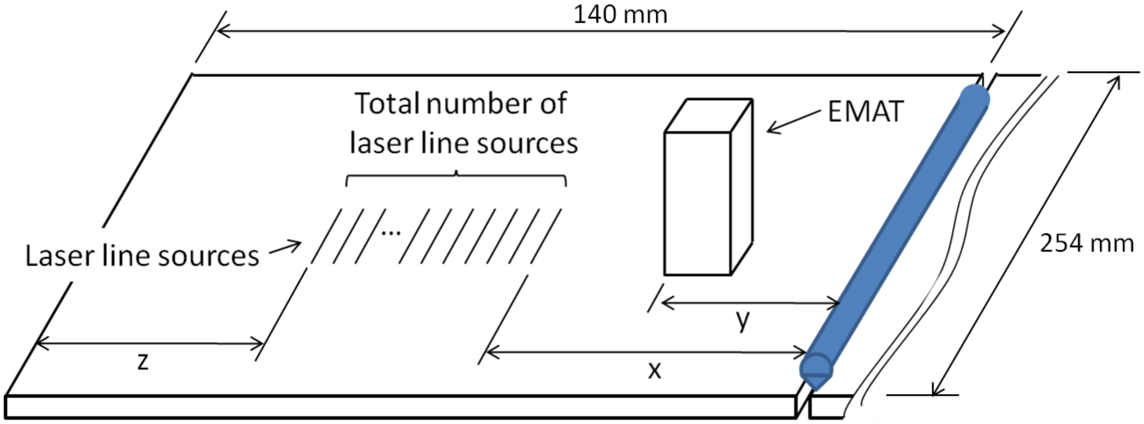

Fig. 7-4: Placement of inspection components

7.4.1 Determination of Number of Signals to Superimpose in SLS Technique

When performing the SLS technique, several signals are superimposed to generate narrowband signals. When more signals are superimposed, the effect of generating single wavelength signals becomes more significant. But it also means that the laser needs to be moved to more locations to generate more signals from a line source and this increases experiment time significantly. In order to decide the optimal number of signals to be superimposed and understand how this number affects the stability of reflection coefficients, the overall relative error E(x), which is defined in Eq. 7-1, can be calculated.

$$\mathrm{E(x)} = \frac{1}{\mathrm{2MN}} \sum_{\mathrm{m=1}}^{\mathrm{M}} \sum_{\mathrm{n=1}}^{\mathrm{N}} \left[\left| \frac{\mathrm{R_{mn}^{A0}(x+1) - R_{mn}^{A0}(x)}}{\mathrm{R_{mn}^{A0}(x)}} \right| + \left| \frac{\mathrm{R_{mn}^{S0}(x+1) - R_{mn}^{S0}(x)}}{\mathrm{R_{mn}^{S0}(x)}} \right| \right] \cdot 100\% \quad \text{(7-1)}$$

E(x) is a function of the number of line sources being superimposed, which is represented by x. R_{mn}^{A0} and R_{mn}^{S0} are reflection coefficients calculated for the n$^{\mathrm{th}}$ wavelength of interest at the m$^{\mathrm{th}}$ test location along the weld seam for A0 and S0 modes, respectively. N and M are total number of wavelengths of interest and total number of test locations. Ten wavelengths ranging from 1.75 mm to 4.00 mm in an increment of 0.25 mm are used. For example, when n equals 1, it represents 1.75 mm wavelength; when n equals 2, it represents 2.00 mm wavelength and so on so forth. The superscripts represent the wave modes. The analysis is performed at 81 different test locations along 9 welds. When performing the analysis, the location of the first laser line source is 70 mm and the location of coil A of the EMAT is 40 mm away from the weld, respectively. The placement of the laser line source and the EMAT will be tested in Section 7.4.3 to see whether this setting is appropriate or not.

This equation evaluates the stability of the reflection coefficients among M test locations. It calculates the averaged relative error between reflection coefficients calculated using x+1 line sources and those calculated using x line sources. The factor 1/2MN is for averaging 2N relative errors from M test locations. When E levels off and is close to zero, it means that the reflection coefficients have converged and using more line sources would not give more advantages to the stability of reflection coefficients. In Fig. 7-5, the X axis represents the number of signals that are superimposed to produce narrowband signals and the Y axis is the averaged relative error, E(x). It shows that the averaged relative error drops below 3 % when x is greater than or equal to seven and it levels off around 2%. Therefore, seven signals are superimposed in the SLS technique in the experiments conducted in this research.

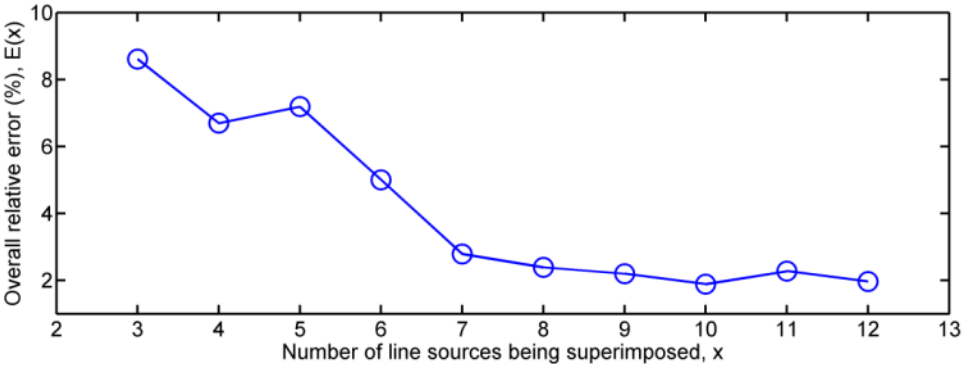

Fig. 7-5: Overall relative error vs. number of line sources being superimposed

7.4.2 Determination of Total Number of Signals Generated in SLS Technique

From the previous section, it is shown that when we superimpose more than seven signals, the measured reflection coefficients converge and become stable. The next step is to determine the total number of signals that are necessary in performing the SLS technique and the signal processing procedure. In other words, we need to determine how many discrete locations we need to move the laser to generate signals. The total number of signals affects the performance of wavenumber-frequency (k-ω) domain filtering and synthetic phase tuning (SPT) in the signal processing procedure.

In k-ω domain filtering, if we move the laser to more discrete locations to increase the total number of signals, we will increase the resolution of signals in the wavenumber axis. For SPT, it essentially superimposes shifted versions of signals together to amplify a particular wave mode. Therefore, as more signals are superimposed together, the effect of amplification becomes more significant.

The disadvantage of generating more signals is obvious. It takes excessive time. There is a lower limit of the total number of signals we need to generate. Because given that the interval of laser sources is fixed, if we want to superimpose signals of larger wavelengths, we will need to move the laser to more locations. For example, if we always move the laser every 0.25 mm and we want to make a single synthetic 4 mm wavelength signal by superimposing 7 signals. In order to cover the whole range of 7 signals with the interval of 4 mm, we need to move the laser to 97 locations and generate 97 signals. In other words, if the number of signals is fewer than 97, we would not have enough signals to synthesize 4 mm wavelength signal. For 1.75 mm wavelength signal, a minimum of 43 signals are needed. On the other hand, there is a higher limit of the total number of signals and it is determined by the physical size of the sample because we only have limited space to move the laser.

To know the minimum number of signals we need, we can investigate how this number affects the stability of the reflection coefficients. The overall relative error defined in Eq. 7-1 can be used again with minor modification. The definitions of the variables used in Eq. 7-1 are all the same except for x, which now stands for the total number of signals generated in the SLS technique. The analysis is performed at 81 different locations along 9 welds. When performing the analysis, the location of the first laser line source is 70 mm and the location of coil A of the EMAT is 40 mm away from the weld, respectively. Since the minimum number of signals is 97, the analysis is performed from 100 to 240. The upper limit is selected based on the size of the sample. When performing the analysis, the location of the first laser line source is 70 mm and the location of coil A of the EMAT is 40 mm away from the weld, respectively. The placement of the laser line source and the EMAT will be tested in Section 7.4.3 to see whether this setting is appropriate or not. The results are shown in Fig. 7-6, in which, the X axis represents the total number of signals generated in the SLS technique and the Y axis is the overall relative error, E(x). It shows that the overall relative error starts to become less than 2% and converge when x is greater than around 130. Therefore, x = 140 is chosen for all the experiments in this research.

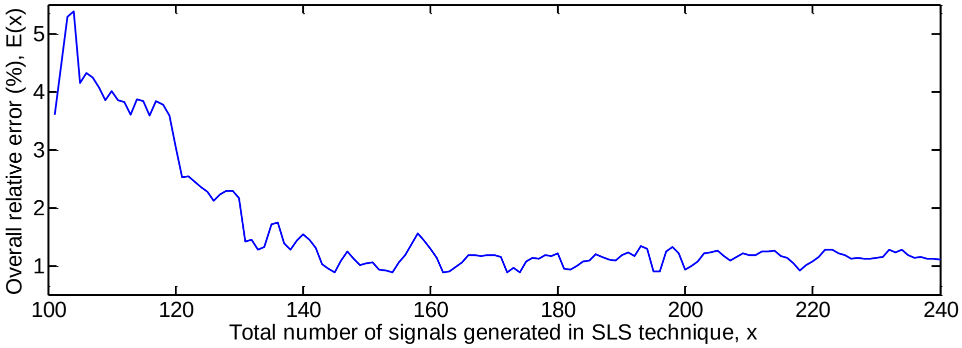

Fig. 7-6: Overall relative error vs. total number of signals generated in SLS technique

7.4.3 Determination of Locations of Laser Line Sources and EMAT

The next step is to determine locations of the EMAT and the laser line sources. We need to investigate how their locations affect the stability of reflection coefficients. The similar approach as mentioned in Sections 7.4.1 and 7.4.2 can be used again. The only difference is that the overall relative error is now a function of two variables, which are the locations of the laser line sources and the EMAT, or x and y as shown in Fig. 7-4. The overall relative error E(x,y) can be define as in Eq. 7-2 :

$$\begin{aligned} E(x,y) = \frac{1}{4KMN}\sum_{k=1}^{K}\sum_{m=1}^{M}\sum_{n=1}^{N}\Bigg[&\frac{\left|R_{mn}^{k}(x+1,y)-R_{mn}^{k}(x,y)\right|}{R_{mn}^{k}(x,y)} \\ &+\frac{\left|R_{mn}^{k}(x-1,y)-R_{mn}^{k}(x,y)\right|}{R_{mn}^{k}(x,y)}+\frac{\left|R_{mn}^{k}(x,y+1)-R_{mn}^{k}(x,y)\right|}{R_{mn}^{k}(x,y)} \\ &+\frac{\left|R_{mn}^{k}(x,y-1)-R_{mn}^{k}(x,y)\right|}{R_{mn}^{k}(x,y)}\Bigg]\cdot 100\% \end{aligned} \tag{7-2}$$

E(x,y) is a function of the locations of the laser sources and the EMAT, which are represented by x and y respectively. R_{mn}^{k} is the reflection coefficient calculated for the n^{th} wavelength of interest at the m^{th} test location for k^{th} mode. N is the total number of wavelengths. M is the total number of test locations. Superscript k represents the wave mode of interest. When k is 1, it represents A0 mode. When k is 2, it represents S0 mode and K is the total number of modes of interest. In our case, K is 2. The analysis is performed at a random test location at a random sample. The analysis is only performed at one test location because it is a very computationally intensive and time consuming analysis. When performing the analysis, a total number of 140 signals are generated in the SLS technique and seven signals are superimposed to generate narrowband signals. The range of the location of the laser line source under investigation is from 60 mm to 90 mm in an increment of 1 mm and the range of the EMAT is chosen from 20 mm to 50 mm in an increment of 1 mm. The ranges are chosen based on the physical dimensions of the sample and the limitation of the experimental hardware. They are chosen so that the holder of cylindrical lens does not interfere with the sample holder and the EMAT, and the EMAT housing does not touch the weld bead.

Eq. 7-2 evaluates the averaged relative error between reflection coefficients calculated at a pair of (x,y) and those calculated when x and y are incremented and decremented by one. The factor 1/4KMN is for averaging 4 relative errors among K modes, M test locations and N wavelengths. In this case, K is 2, M is 1, and N is 10. The result of calculation is shown in Fig. 7-7 in which the x and y axes are locations of laser line source and EMAT. The vertical axis is the overall relative error. It shows that laser line source location does not really affect the stability of reflection coefficients. The overall relative error does not show any trend in the x axis. For the EMAT location, it shows that as long as it is larger than 25, this dimension does not affect the stability of reflection coefficients either. Therefore, we can choose any values for x and y in these ranges. The analysis also shows that the locations of the first laser line source and the EMAT used in the previous two analyses are valid, which are 70 mm and 40 mm away from the weld, respectively. These two values are used for the experiments in this research.

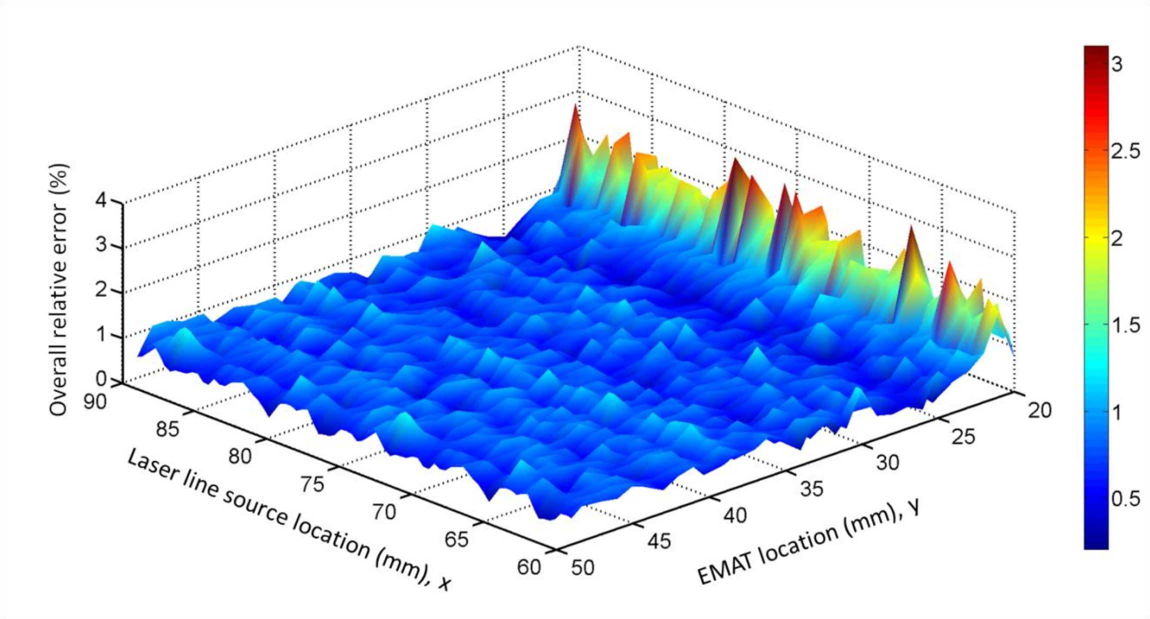

Fig. 7-7: Overall relative error vs. locations of laser line sources and EMAT

7.5 Nondestructive Testing Using SLS Technique

For the first set of samples, sixteen samples are made, and for each sample, five locations along the weld seam are inspected. For the second set of samples, nine samples are made, and for each sample, nine locations along the weld seam are inspected. During the inspection of a particular location, the laser beam is fixed while the samples and the EMAT are moved by the linear stage at 0.25 mm increments. At each laser incident location, 32 signals are acquired and averaged to increase signal-to-noise ratio. A total number of 140 averaged signals are stored for each test location.

7.6 Cutcheck Inspection

After the samples are inspected nondestructively, cutchecks are performed to measure the dimensions of the welds. Cross sections of the inspected locations are cut out and mounted onto acrylic pucks which are then ground and polished. The cross sections of the samples are polished up to grit 800 level. After polishing, the samples must be etched so that the boundaries between the weld beads and the base materials become clear. The etching solution is nital, or the mixture of 5% nitric acid and 95% methanol by volume. After etching, each puck is scanned by an optical scanner with 1200 dpi (dot-per-inch) resolution and important dimensions are measured. The cross sections of samples are shown in Fig. 7-8.

For the first set of the samples, there are 160 cutcheck locations (10 locations on each of the 16 samples); for the second set of the samples, there are 81 cutcheck locations (9 locations on each of the 9 samples). It should be noticed that for the first set of samples, the numbers of locations for cutcheck and for SLS inspection are different. Because the experiment operator was inexperienced with the experimental setup when the first set of sample was inspected, the number of the SLS inspection locations is fewer than that of the cutcheck locations. The summary of the cutcheck and SLS inspection locations for two sets of samples are listed in Table 7-5.

The box plots (box-and-whisker plot) for penetration depth (PD), reinforcement height (RH), and bead width (BW) versus test runs are shown in Fig. 7-9. A box plot encloses the interquartile range of the data in a box that has the median displayed within. The interquartile range has as its extremes, the 75th percentile (upper quartile) and the 25th percentile (low quartile). In addition to the box, “whiskers” extend, showing the maximum and minimum observations in the data set [68]. Outliers are also shown in the box plot. Outliers are observations that are considered to be unusually far from the bulk of the data. Observations are considered as outliers if their distance from the box exceeds 1.5 times the interquartile range (in either direction). Legend for the box plot is shown in Fig. 7-10. The values of weld dimensions in this research are all normalized by the plate thickness. These quantities change with different welding parameters. The effects of the welding parameters on the 8th and 16th samples of the first set of experiments show very high variations and the results also agree with the surface conditions of the welds. The weld beads on the 8th and the 16th samples have very rough surfaces and are the least consistent along the weld seam.

To measure the average effect of a factor, say X, the difference between the average value of all observations in the experiment at the high (+) level of X and the average value of all observations in the experiment at the low level (-) of X is computed. The difference is called the main effect of one factor and represented by,

$$ME(X) = \overline{z}(X+) - \overline{z}(X-) \tag{7-3}$$

Where $\overline{z}$ denotes average of the observations, and X+ and X- represent the high and low levels of X, respectively [69]. The main effects calculation can be displayed graphically in a main effects plot. The main effects plot graphs the averages of all the observations at each level of the factor and connects them by a line.

The main effect plots on PD and its standard deviation are shown in Fig. 7-11 in which the solid line plots represent PDs and the dashed plots represent their standard deviations. The left four plots are for the first set of data and the right two plots are for the second set of data. From the main effect plots for the first set of data, it can be observed that in order to increase PD, CTWD and welding speed should be small while arc voltage and WFR should be large. To reduce variation of PD, welding speed and arc voltage should be minimized while WFR should be increased. CTWD alone has a relatively small effect on the variation of PD. The main effect plots on RH are shown in Fig. 7-12. For the first set of data, the main effect plots of RH are similar to those of PD except for the one for arc voltage. Opposite to the effect on PD, raising arc voltage decreases RH. For BW, the main effect plots are shown in Fig. 7-13. In the main effect plot of WFR, the effect on the standard variation of BW is different from that of PD.

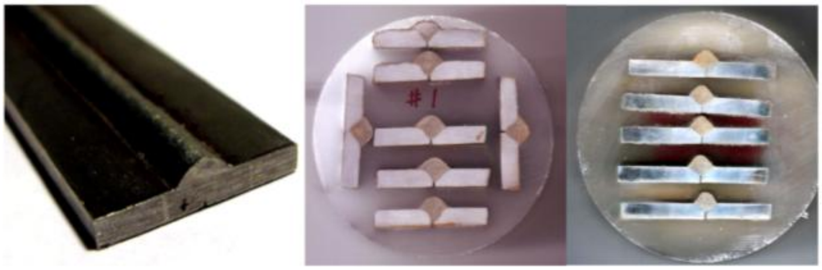

Fig. 7-8: cutcheck cross sections of butt welds

Table 7-5: Summary of cutcheck and SLS inspection locations for two sets of samples

	# of sample	# of cutcheck location on each sample	# of SLS inspection location on each sample	Total # of cutcheck	Total # of SLS inspection location
First set	16	10	5	160	80
Second set	9	9	9	81	81

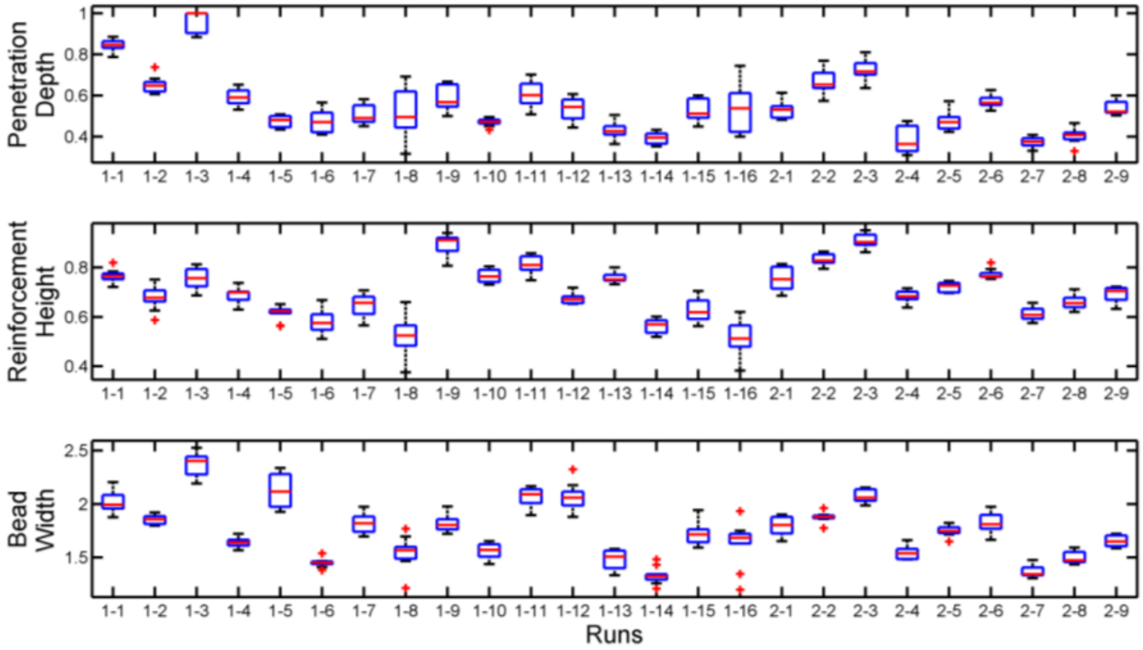

Fig. 7-9: Box plots of PD, RH and BW of both sets of samples

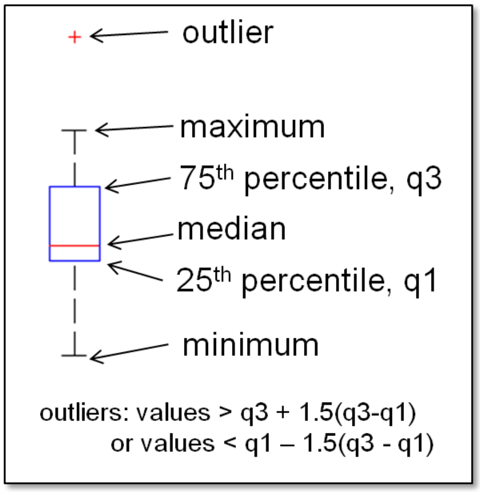

Fig. 7-10: Legend for box plots

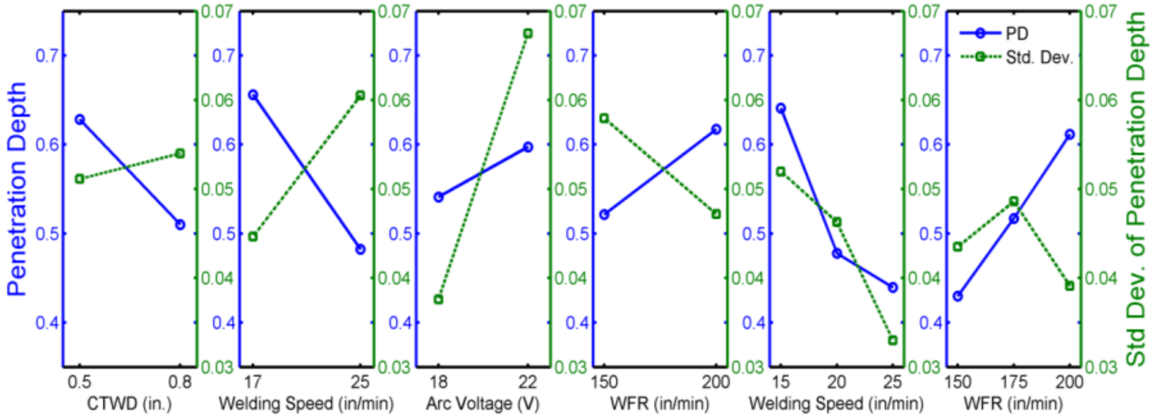

Fig. 7-11: Main effects plots on PD and its standard deviation for both sets of samples

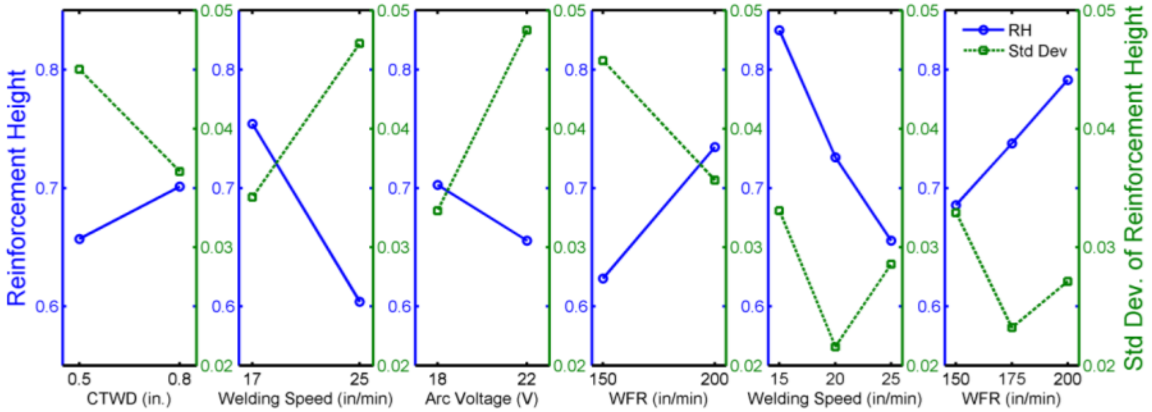

Fig. 7-12: Main effects plots on RH and its standard deviation for both sets of samples

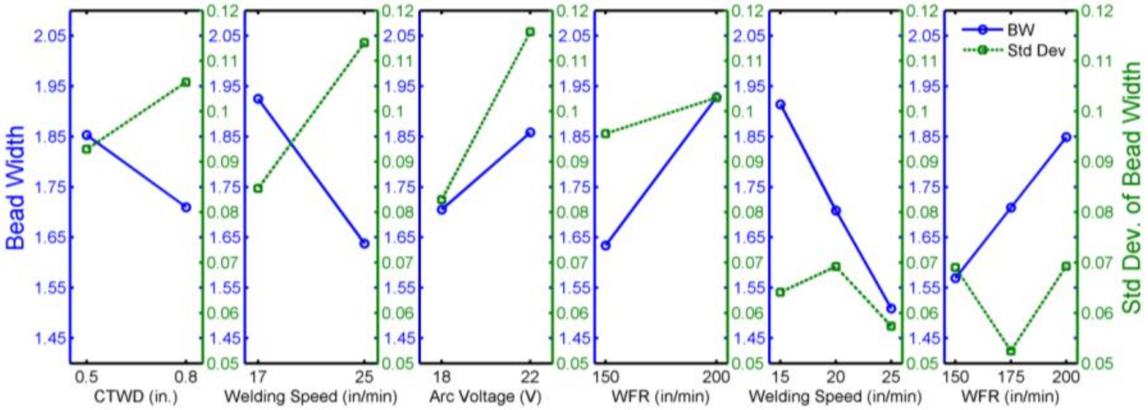

Fig. 7-13: Main effects plots on BW and its standard deviation for both sets of samples

The second set of samples is prepared by holding CTWD and arc voltage constant. The arc voltage is chosen to be 18 V to reduce variability of the weld and the

CTWD is chosen to be 0.5 inch. The WFR and welding speed are varied because they are easier to control. The box plots of PD, RH and BW are also shown in Fig. 7-9 and the main effects plots on PD, RH and BW for the second set of samples are shown in the two plots on the right of Fig. 7-11, 7-8 and 7-9 respectively. The trends of PD, RH and BW are similar. As the welding speed slows down and the WFR increases, the values of PD, RH and BW become larger. The trends of these three dimensions for the second set of data also agree with the trends for the first set of data. However, the variations of these quantities are very complex. They are neither consistent among themselves nor consistent between two sets of data. For example, for the main effects plots of welding speed for the second set of data, as welding speed becomes faster, the variations of PD, RH and BW show three distinct trends. On the other hand, for the main effects plots of welding speed on PD for both sets of data, the variations show completely opposite trends. In the first set of data, the variation of PD increases as welding speed increases; in the second set of data, the variation of PD decreases as welding speed decreases. Similar inconsistency can be observed for other weld dimensions.

The summary of effects of welding parameters on weld dimensions and variation is listed in Table 7-6. It shows how one factor needs to be adjusted to increase a particular weld dimension or decrease the variation of a particular weld dimension. The upper arrow indicates that the welding parameter needs to be increase to achieve the objective listed in the first column in the table, and vice verse. A question mark indicates that there is no clear trend to adjust the welding parameter. From the observations here, it can be seen that the variation of weld dimensions is not consistent among two sets of data. There may be other factors, which are not identified, affecting the variations of weld dimensions. These factors could be temperature, humidity, or simply the variation within the welder signals. Because the welder used in the research has been operated for more than 30 years, drift in controlling signals is likely to happen. Therefore, the inconsistency of the variation of weld dimensions is most likely due to the inconsistency of performance associated with the welder.

Table 7-6: Summary of effects of welding parameters on weld dimensions and variation

	First set				Second set	
	CTWD	Welding Speed	Arc Voltage	WFR	Welding Speed	WFR
Increase PD	↓	↓	↑	↑	↓	↑
Increase RH	↑	↓	↓	↑	↓	↑
Increase BW	↓	↓	↑	↑	↓	↑
Decrease variation of PD	↓	↓	↓	↑	↑	?
Decrease variation of RH	↑	↓	↓	↑	?	?
Decrease variation of BW	↓	↓	↓	↓	?	?

The histograms of PD, RH and BW and their normal probability plots of both sets of data are shown in Fig. 7-14, 7-11 and 7-12. For RH and BW, the results from both sets of data do not deviate from the normal distribution too much. However, for PD, the results show that the second set of data is more normally distributed than the first set of data, in which several data points have values about one. These data points have large leverage and can easily bias the developed model(s). Therefore, the models will be developed by using the second set of data and validated by the first set of data. They are referred to as development data and validation data respectively in this research.

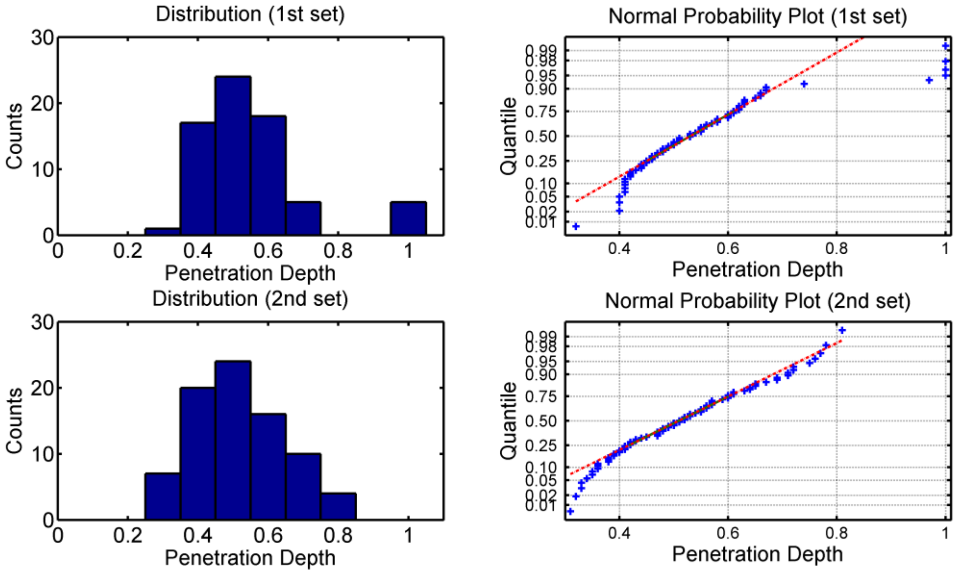
Distribution (1st set)

Normal Probability Plot (1st set)

Distribution (2nd set)

Normal Probability Plot (2nd set)

Fig. 7-14: Histogram of PD and its normal probability plot of both sets of samples

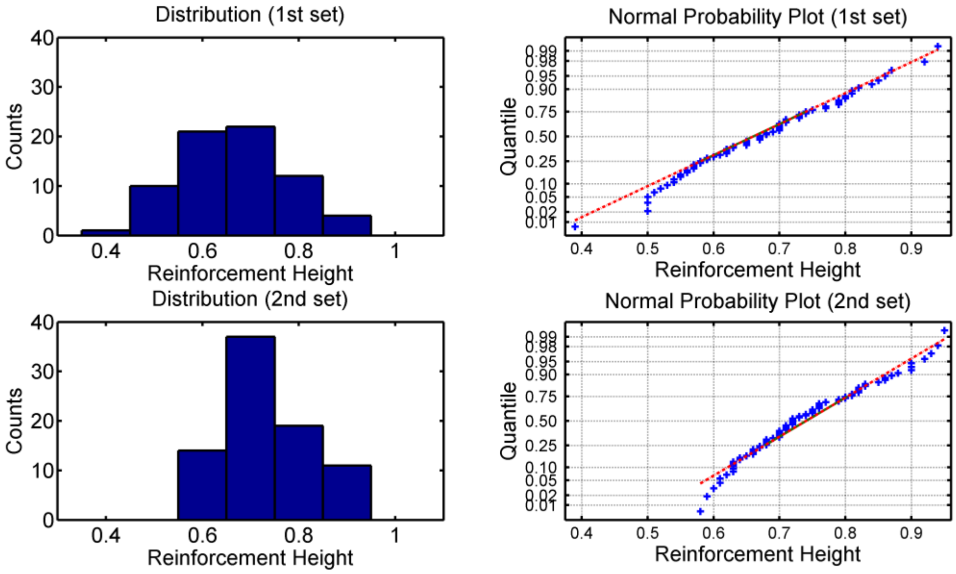
Distribution (1st set)

Normal Probability Plot (1st set)

Distribution (2nd set)

Normal Probability Plot (2nd set)

Fig. 7-15: Histogram of RH and its normal probability plot of both sets of samples

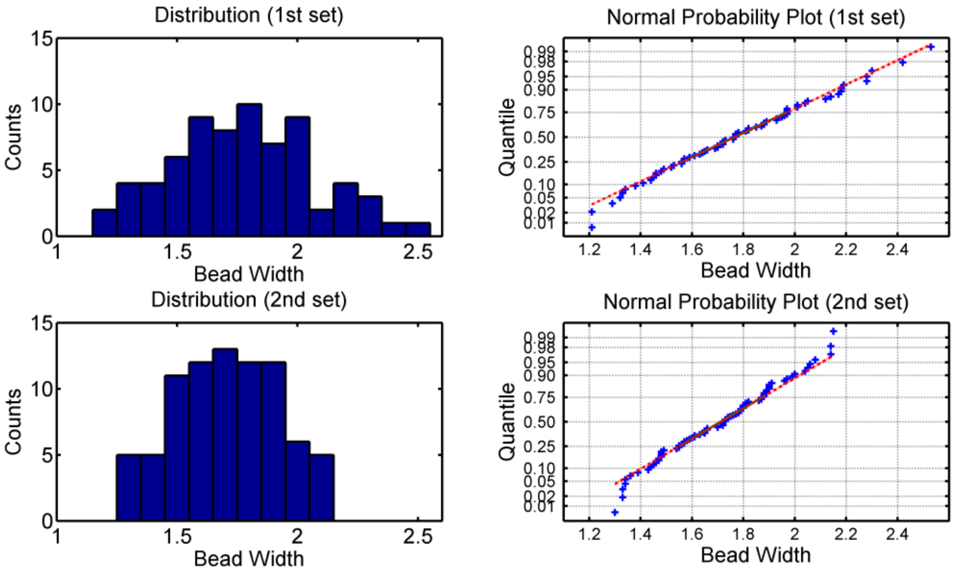

Fig. 7-16: Histogram of BW and its normal probability plot of both sets of samples

7.7 Signal Processing

The ultrasonic signals obtained before cutchecks were performed can be compiled into a scan. The scan captured by the coil A of the EMAT is shown in Fig. 7-17(a) in which X axis is time of flight and the Y axis is the distance between the laser source and the coil A of the EMAT. Wave fronts of different frequencies and slopes can be observed in the figure. The gray scale of the plots represents relative signal amplitude. The contrast and brightness are adjusted for the clarity of the plots. There are some wave fronts featuring positive slopes and some featuring negative slopes indicating waves with increasing or decreasing distance of travel as the laser source is moved away from the weld and the EMAT. The SLS technique is used to produce narrowband ultrasound. Every seven signals are superimposed to produce the desired wavelengths. An example of the superposition operation for 3 mm wavelength is shown in Fig. 7-17(b). In the figure, the Y axis denotes the distance between the sensor and the first line source in every seven line sources that are superimposed line sources. Based on the experimental setup shown in Fig. 7-4, time-of-flight of each wave component can be calculated. The time-of-flight information of the direct incident wave and reflection waves from the weld and the left edge of the sample for both 3 mm A0 and S0 modes are also shown in the figure.

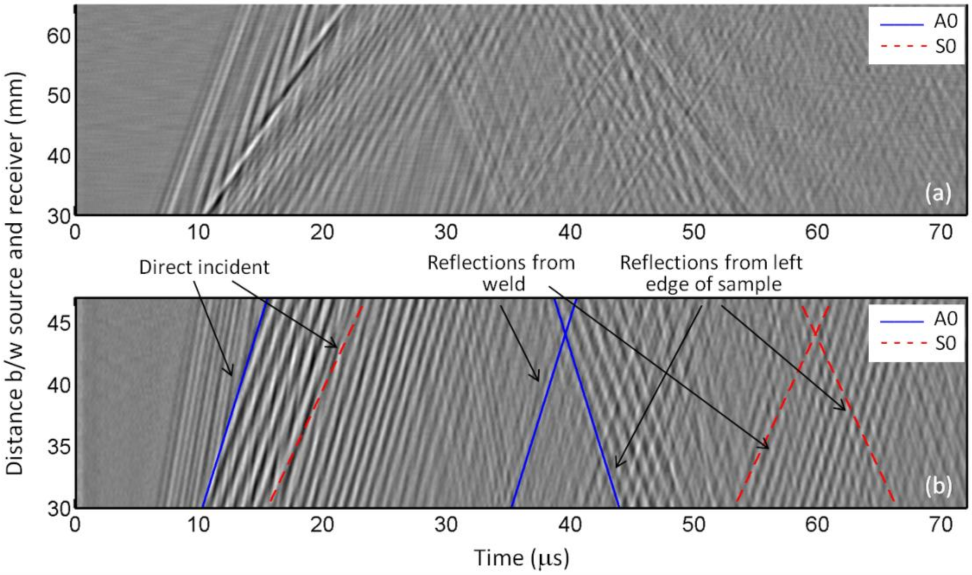

Fig. 7-17: Space-time representation of (a) original signals (b) results of SLS operation (3 mm wavelength) received by the coil A of the EMAT

The next step is to apply k-ω domain filtering to filter out unwanted waves in the signals. The results of 2DFT of Fig. 7-17(a) and Fig. 7-17(b) are shown in Fig. 7-18 in which X axis denotes frequency, Y axis denotes wavenumber and the brightness represents signal amplitude (the gray scale is reversed to give clarity to the graph). The image is basically symmetrical about the X axis. The positive values of the wavenumber are for waves propagating with increasing distance of travel, and the negative values are for the waves with decreasing distance of travel. Fig. 7-18(a) shows the original signals in k-w domain. The broadband and dispersive nature of the laser generated signals is clearly shown in the figure. Fig. 7-18(b) is identical to Fig. 7-18(a) with the theoretical solutions of Lamb wave modes of S0, A0, S1 and S2 modes overlapping the experimental data. The transformed result of the signals after applying SLS technique for 3 mm wavelength is shown in Fig. 7-18(c). The two stripes at the top center around (0.94 MHz, 2094.4 rad/m) and (1.15 MHz, 2094.4 rad/m), and the other stripe at the bottom centers around (0.94 MHz, -2094.4 rad/m). The wavenumber 2094.4 rad/m corresponds to wavelength 3 mm.

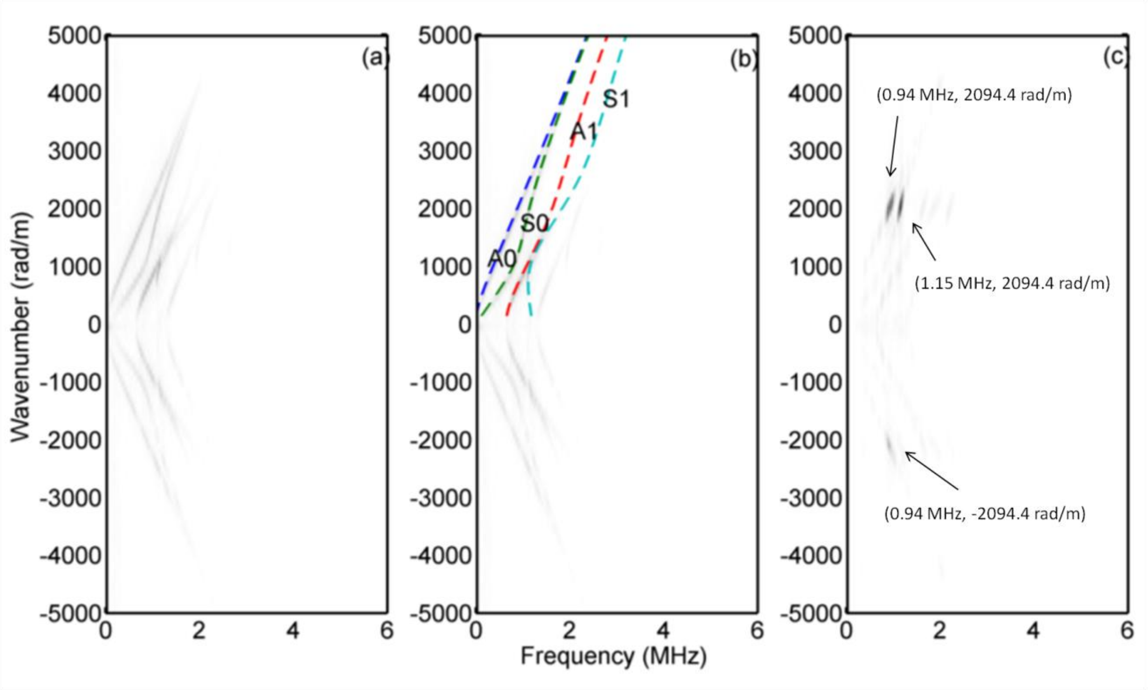

Fig. 7-18: k-ω representations of (a) original signals (b) original signals with theoretical predictions and (c) signals after SLS operation (3 mm wavelength) received by the coil A of the EMAT

The signals with negative wavenumbers are filtered out and leaving the signals with positive wavenumbers. The results are then inversely transformed back to the space-time domain as shown in Fig. 7-19(a). In a similar manner, the signals containing positive wavenumbers can be filtered out, and leaving behind the signals with negative wavenumbers. These signals can be inversely transformed back to space-time domain as shown in Fig. 7-19(b). By looking at Fig. 7-17 (b), Fig. 7-19(a) and (b), it is clear that the wave fronts with positive slopes and negative slopes have been separated successfully and the complexity of the signals is greatly reduced. Because the direct incident waves and reflection waves from the weld seam have increasing distance of travel as the source is moved away from the EMAT, Fig. 7-19(a) contain all the necessary information for calculating reflection coefficients. In Fig. 7-19(b), waves with negative slopes are retained. These are the waves that are reflected from the edge of the sample which are irrelevant in our analysis. The time-of-flight predictions of direct incident waves and reflections from the weld and the left edge of the sample are also shown in both figures.

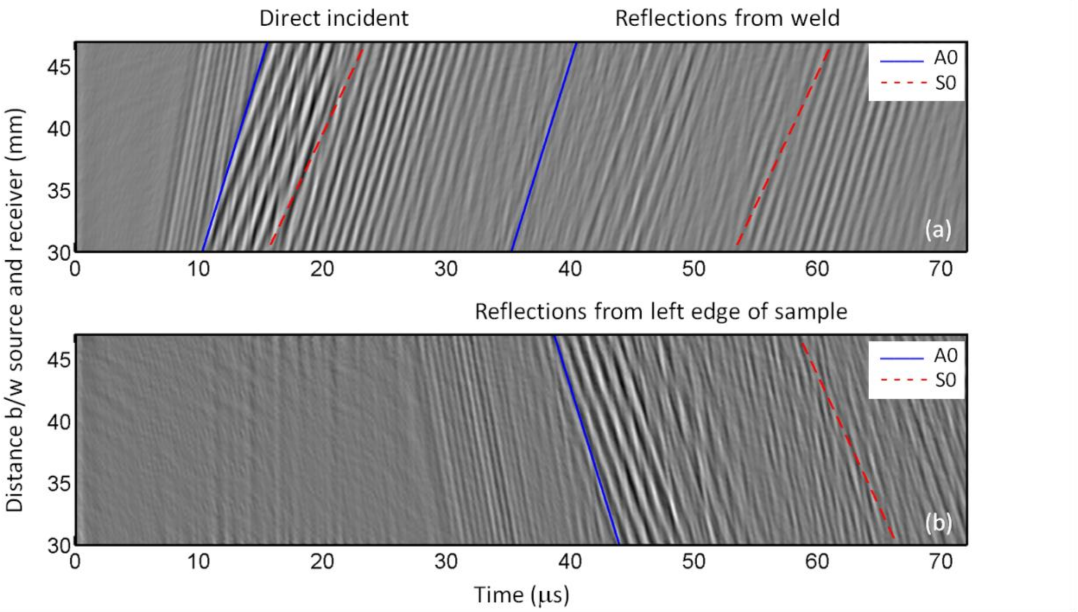

Fig. 7-19: Space-time representation of (a) components with positive wavenumbers (b) components with negative wavenumbers received by the coil A of the EMAT

The same procedure can be applied to the signals received by the other three coils in the EMAT, and three scans similar to Fig. 7-19(a) can be obtained. Synthetic phase tuning technique is then applied to isolate a particular Lamb wave mode in each scan captured by each coil. In each scan, all the signals can be shifted with respect to the signal that is closest to the EMAT. At this stage, four synthetic signals are produced. Examples of the four synthetic signals for 3 mm S0 mode and A0 mode of four coils are shown in Fig. 7-20 and Fig. 7-21, respectively. The difference in arrival time of the wave components can be observed. For example, the direct incident wave in coil A has the earliest arrival time but the reflection from the weld in coil A has the latest arrival time. Furthermore, Fig. 7-20 and Fig. 7-21 also show different shifting directions for different wave components. By shifting these signals properly in time, the desired mode can be isolated. Fig. 7-20(a) shows the result for 3 mm S0 mode and Fig. 7-21(b) shows the result for 3 mm A0 mode. The envelopes that are obtained by the Hilbert transform are also shown in both figures. In both cases, the incident and reflected waves from the weld can be identified by time-of-flight analysis. Thereafter, reflection coefficients can be calculated for both Lamb wave modes for each wavelength of interest. For each test location, 20 reflection coefficients can be calculated for ten wavelengths of two Lamb wave modes.

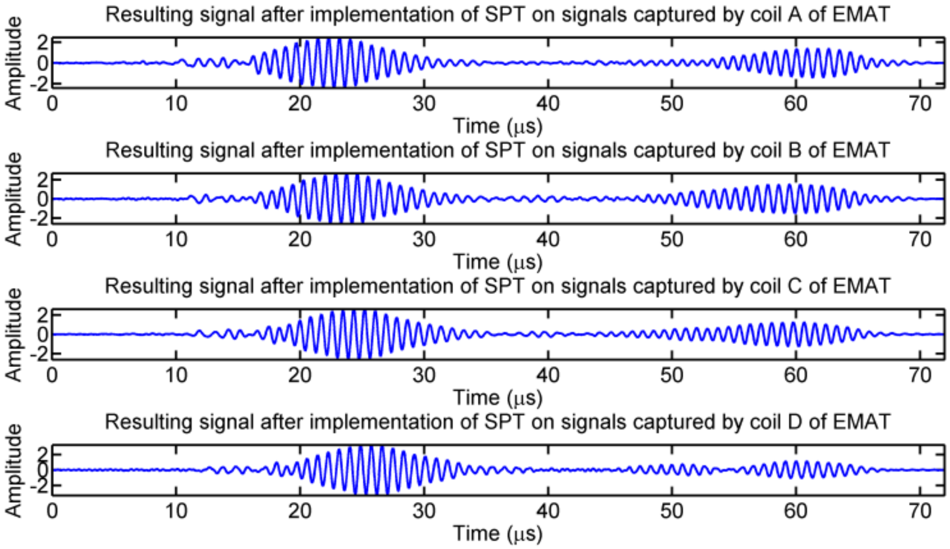

Fig. 7-20: Four synthetic signals for 3 mm S0 mode of four coils of EMAT

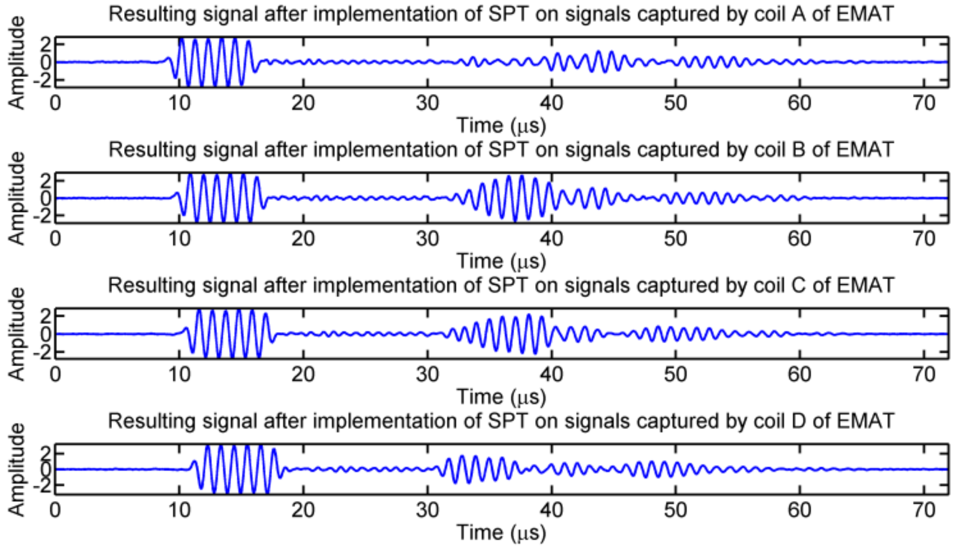

Fig. 7-21: Four synthetic signals for 3 mm A0 mode of four coils of EMAT

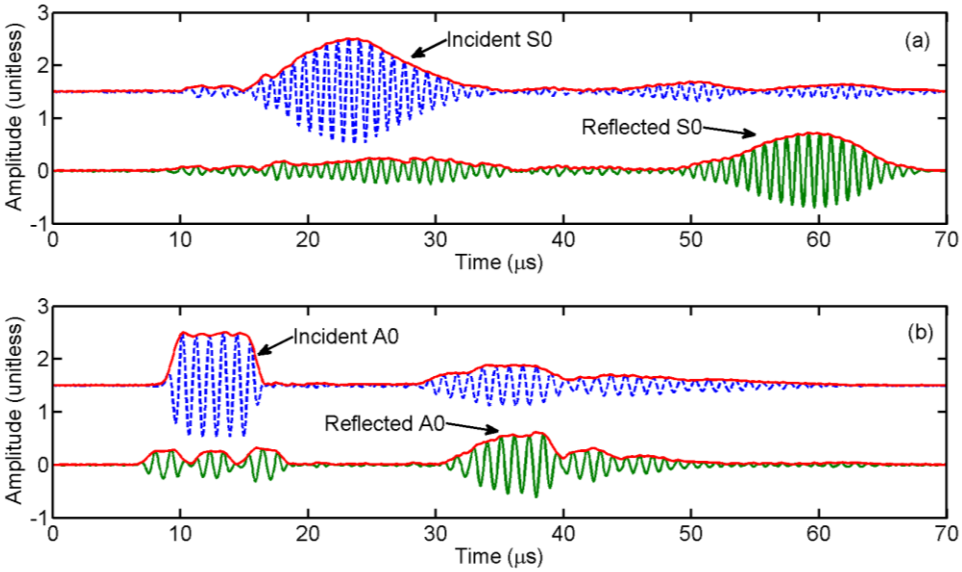

Fig. 7-22: Examples of results of SPT operation for (a) 3 mm S0 (b) 3 mm A0

CHAPTER 8

PREDICTION AND EXPEIMENTAL VALIDATION OF DIMENSIONS OF BUTT WELDS IN THIN PLATES(II)

After reflection coefficients at each test location have been calculated and dimensions of the welds have been measured, models that correlate the reflection coefficients with the weld dimensions can be developed. Since no analytical formulations can be found in the literature to describe the relationship between the weld dimensions and the reflection coefficients of Lamb waves, regression analysis is used here to develop an empirical model(s). In this chapter two methods are introduced and used to develop models for predicting weld dimensions in thin plates. The first method is called the direct method. In the direct method, the weld dimensions are assumed to be functions of the reflection coefficients of two Lamb wave modes of ten wavelengths. Once the model is built, one can calculate weld dimensions by substituting reflection coefficients directly into the model.

The second method, referred to as the indirect method in this research, assumes that each reflection coefficient is a function of weld dimensions and their interactions. A system of equations can be obtained by regression analysis to describe the relationship between all the reflection coefficients and weld dimensions. This system of equations can be represented in a matrix form. The coefficient matrix that links the weld dimensions to the reflection coefficients can be determined. For the weld dimension prediction purposes, once the reflection coefficients of an unknown sample are obtained, one would need to solve this system of equations to predict the weld dimensions. More detailed description will be presented in Section 8.2.

8.1 The Direct Method

In the direct method, weld dimensions are assumed to be functions of the reflection coefficients. In regression analysis, a model with fewer predictors is preferred as long as it can explain the data well. A model that overfits the data may give poor predictions. The stepwise regression method and the Corrected Akaike's Information Criterion (AICc) [68] are used to formulate the models with fewer significant predictors. Notice that the expressions of "terms", "predictors", and "independent variables" mean the same thing and they will be used interchangeably.

8.1.1 Stepwise Regression

The stepwise regression is an automatic model selection algorithm [68]. It identifies statistically significant variables for the model. It adds variables into or deletes them from the model by constantly evaluating the p-value of the variables. In a statistical significance test, the p-value is a measure of how much evidence we have to reject the null hypothesis. The smaller the p-value, the more evidence we have against the null hypothesis. In our case, the null hypothesis is that the variable under evaluation is insignificant. Therefore, variables are more significant when their p-values are smaller. When using the stepwise regression, one assigns a threshold of p-value. When the p-value of a variable is smaller than the threshold, it will be included into the model, and vice versa. Therefore, if one wants to develop a prediction model that has more variables, he or she will use a small threshold of p-value. In another word, by varying the threshold of p-value, one can vary the number of variables in a prediction model. More details about statistical hypothesis and p-value can be found in [68]. The stepwise regression procedures end up with the identification of a single "best" model. However it is often criticized that this single "best" model may hide the fact that several other models may explain the data equally well. This is especially true in our application because lots of reflection coefficients may be correlated with each other. The best model cannot be decided until all candidate models have been tested by another set of data.

8.1.2 Akaike's Information Criterion

Akaike's information criterion (AIC) is a tool of model selection, which is developed by Hirotsugu Akaike in 1974. It is a widely used method for model selection [68]. It measures how well a statistical model fits the data. AIC penalizes models with large numbers of predictors and it determines the best size of the model when it reaches the minimum. AIC is defined in Eq. 8-1.

$$AIC = -2\ln(L_p) + 2p \tag{8-1}$$

where n is the number of data sets used to build the regression model, p is the number of predictors, and in the first term, $\ln(L_p)$ is the sample log-likelihood calculated for the case when p predictors are used in the model. The second term can be viewed as a penalty for overfitting. If the residuals are assumed to be normally distributed with homogeneous variance, the log-likelihood can be calculated as [73]:

$$\ln\left(L_p\right) = -\frac{1}{2}n(\ln(2\pi) + \ln\left(\frac{SSE}{n}\right) + 1) \tag{8-2}$$

where SSE is sum of square error. Substitute Eq. 8-2 in to Eq. 8-1 and we can get:

$$AIC = n\ln(2\pi) + n\ln\left(\frac{SSE}{n}\right) + n + 2p \tag{8-3}$$

Since the first term and the third term on the right hand side of the equation do not change with the analysis for different models, they can be omitted from the equation. Eq. 8-3 becomes Eq. 8-4.

$$AIC = n\ln\left(\frac{SSE}{n}\right) + 2p \tag{8-4}$$

In Eq. 8-4, n is given and remains constant for a model selection problem. As more predictors are added into the model, the first term decreases as SSE drops because of a better fit of the data but the second term increases as p increases. It will eventually reach the point when the decrease of the first term cannot compensate the increase of the second term in Eq. 8-4. The best size of the model is determined when AIC reaches the minimum. The Corrected Akaike's Information Criterion (AICc) is a corrected version of AIC, and it is defined in Eq. 8-5.

$$AICc = n\ln\left(\frac{SSE}{n}\right) + \frac{2np}{n-p-1} \tag{8-5}$$

The only difference between AIC and AICc is the second term in the equations. AIC can be viewed as a limit case of AICc when n is infinitely large. Burnham and Anderson [74] suggested that if sample size, n, is not significantly greater than the number of predictor, p, the corrected version should be used. Since in our case, the number of sample used for model development is 81, and the number of predictors used could potentially be very large, the AICc is used in this research.

It is also informative to compare the use of the AICc and Mean Squared Error (MSE) criterion for model selection. The mean square error can be defined as in Eq. 8-6

$$MSE = \frac{1}{n-p-1}\sum_{i=1}^{n}\left(\widehat{Y_i} - Y_i\right)^2 \tag{8-5}$$

where i is the running index for each data point, $\hat{Y}_i$ is the predicted value, and Y_i is the actual value. The factor of n-p-1 is the degree of freedom. It provides normalization for the number of data points and model complexity. The MSE takes account of the number of predictors in the regression model. The main disadvantage of using MSE is that when the number of data sets is large, the MSE become less sensitive to the penalty induced by the increase of number of predictors in the regression model.

8.1.3 Determination of form of Regression Models

Many researchers have investigated the relationship between reflection coefficients of Lamb wave modes and geometry of notches with varying width or depth in thin plates. Jin et al. [70] used the boundary element method and Lowe and Diligent [71] used the finite element method to study reflection coefficients of fundamental A0 and S0 Lamb wave modes from a notch. They have shown that reflection coefficients of Lamb waves are not only dependent on the geometry of the notches, but also the wavelengths of Lamb waves.

Marical et al. [72] investigated guided waves traveling in elastic plates with Gaussian section variation and showed that waves can be trapped in the Gaussian domain depending on the incident mode and on the Gaussian maximum height.

The geometry of a butt weld can be approximated as a plate with Gaussian section variation and a notch. No analytical solutions or models can be found in the literature to describe how Lamb waves propagate in this kind of structures. The problem is even further complicated by the existence of the material interfaces between the weld bead and the base material. The only thing that is for certain is that the reflected waves contain information regarding weld dimensions.

Regression analysis is used here to develop an empirical model(s) to relate weld dimensions to reflection coefficients of Lamb waves. Since there is no theory that can be followed to determine the form of the regression models, polynomial regression models are chosen because when the true curvilinear response function is unknown or too complex, it is very common to use a polynomial to approximate the true function.

A main danger in using polynomial regression models is that extrapolations may be hazardous with these models, especially those with higher-order terms. Polynomial regression models may provide good fits for the data at hand, but may turn in unexpected directions when extrapolated beyond the range of the data.

Polynomial models with the predictor variable present in higher powers than the third should be employed with special caution. The models may be highly erratic for interpolations and even small extrapolations.

In this research, the dependent variable is each of the weld dimensions and the independent variables are 20 reflection coefficients. They are named as A0Wx and S0Wx, which denote the reflection coefficients of A0 and S0 Lamb wave modes of the xth wavelength. The correspondence between x and the actual wavelength can be found in Table 8-1. A cubic polynomial with second order cross-product interaction terms are chosen for the regression analysis. Cubic polynomials have 251 coefficients to be determined. These coefficients include one intercept, 20 coefficients for the linear terms, 20 coefficients for the quadratic terms, 20 coefficients for the cubic terms, and 190 coefficients for the second order cross-product interaction terms. Of course, most of these parameters can be omitted because they are insignificant.

Since weld joints have very complex geometry, and different reflection coefficients may be sensitive to different dimensions of a weld joint. There were no guidelines for determining what reflection coefficients should be used in the analysis. The statistical approach is used to determine the important reflection coefficients that should be included in prediction models.

Table 8-1: Variables used in regression model

x	Wavelength (mm)	Mode: A0	Mode: S0
1	1.75	A0W1	S0W1
2	2	A0W2	S0W2
3	2.25	A0W3	S0W3
4	2.5	A0W4	S0W4
5	2.75	A0W5	S0W5
6	3	A0W6	S0W6
7	3.25	A0W7	S0W7
8	3.5	A0W8	S0W8
9	3.75	A0W9	S0W9
10	4	A0W10	S0W10

8.1.4 Model Development and Validation for PD

The stepwise regression is first used to find a model. A very lenient criterion, threshold of p-value = 0.2, is used to include more than necessary predictors into the model with the understanding that the model may overfit the data. Twenty-one terms are selected and their indices are shown in the first two columns of Table 8-2. The commercial software JMP 8.0 is then used to calculate AICc values for all the possible regression models that can be constructed using these 21 terms. There are 2,097,151 possible models that can be constructed. For each case, a regression model is made and the AICc value is calculated. The software identifies the model that gives the lowest AICc value for each corresponding number of predictors, p, used. The AICc analysis is a computationally intensive process. Therefore, in order to save computational time, the total number of terms that is selected by the stepwise regression needs to be smaller than a certain limit. According to the computational power of the computer that does the analysis, the total number of terms cannot be greater than 23. In practice, the threshold of p-value is changed to make sure fewer than 23 terms are selected in the stepwise regression. The information of these models that give lowest AICc values is also shown in column 3 to 6 in Table 8-2. The third column denotes the number of predictors, p, included in the model. The fourth column shows the terms corresponding to a p which are used in the model that gives the lowest AICc values. The fifth column shows the AICc values. The sixth column shows the root mean square errors (RMSE) when these models are validated with the validation data, which will be discussed in the next section. The RMSE is defined as in Eq. 8-1.

$$\sqrt{\frac{\sum_{i=1}^{N}(\widehat{Y_i} - Y_i)^2}{N}} \tag{8-1}$$

where N is the total number of data points, i is the running index for each data point, Ŷ is the predicted value, and Y is the actual value. Since all weld dimensions are normalized by the plate thickness in this research, RMSE is also dimensionless. RMSE is used for validating prediction models and to compare models developed by different methods. If replicate experiments were performed, the weighted least square error could have been used to take into consideration that unequal error variance may happen.

For example, for p = 2, the model that is constructed using term 7 and term 18, or equivalently S0W6 and S0W5*S0W6, gives the lowest AICc value, -338.43. By the same fashion, when p = 4, the model that is constructed using A0W2, S0W4, S0W4*S0W5, and S0W7*S0W8 would give the lowest AICc value, -378.317. The plot of AICc with respect to p, or the number of predictors in the model is shown in Fig. 8-1. Also shown in the figure is RMSE. For each p, the AICc value is the smallest value among all the possible values obtained from the models with the same number of predictors. The AICc value reaches a minimum when p is around 12.

Table 8-2: Summary of model development using AICc and validation using RMSE for PD

Index	Term	p	Indices of terms in model	AICc	RMSE
1	A0W2	1	7	-317.942	0.1252
2	A0W5	2	7,18	-338.43	0.1118
3	A0W7	3	7,17,18	-365.773	0.1094
4	A0W8	4	1,6,17,19	-378.317	0.1110
5	S0W1	5	1,6,11,14,16	-402.061	0.1108
6	S0W4	6	1,6,7,11,14,16	-411.761	0.1080
7	S0W6	7	5,6,7,10,16,18,19	-416.513	0.1067
8	A0W1*A0W2	8	2,7,10,11,12,17,19,21	-420.696	0.1043
9	A0W1*A0W10	9	2,5,7,10,11,12,16,17,19	-430.719	0.0983
10	A0W2*A0W5	10	2,4,5,7,10,11,12,16,17,19	-435.98	0.0941
11	A0W2*S0W4	11	4,5,6,7,9,10,16,17,18,19,21	-434.091	0.0952
12	A0W2*S0W6	12	5,7,8,9,10,11,12,13,17,19,20,21	-434.404	0.0914
13	A0W5*A0W10	13	2,5,7,8,9,10,11,12,13,16,17,19,20	-421.64	0.0955
14	A0W7*A0W10	14	4,5,6,7,8,9,10,13,16,17,18,19,20,21	-424.204	0.0976
15	A0W9*S0W4	15	4,5,6,7,8,9,10,13,14,16,17,18,19,20,21	-423.206	0.1029
16	S0W1*S0W5	16	2,4,5,7,8,9,10,11,12,13,15,16,17,19,20,21	-421.91	0.0912
17	S0W4*S0W5	17	2,4,5,7,8,9,10,11,12,13,15,16,17,18,19,20,21	-419.627	0.0966
18	S0W5*S0W6	18	2,4,5,7,8,9,10,11,12,13,14,15,16,17,18,19,20,21	-416.686	0.0948
19	S0W7*S0W8	19	2,4,5,6,7,8,9,10,11,12,13,14,15,16,17,18,19,20,21	-413.325	0.0998
20	A0W9^3	20	2,3,4,5,6,7,8,9,10,11,12,13,14,15,16,17,18,19,20,21	-408.807	0.0973
21	S0W5^3	21	ALL	-403.877	0.1006

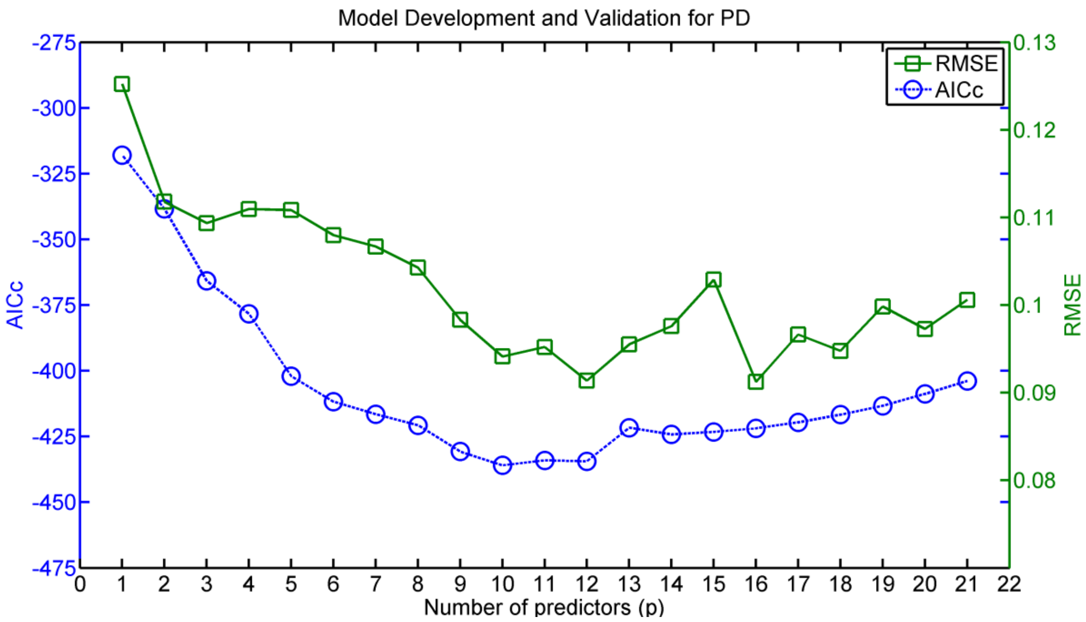

Fig. 8-1: AICc and RMSE vs. p for model development and validation for PD

In order to find the model that can make most accurate prediction, these 21 models are built, and error analysis and model validation are further carried out using the validation data. The RMSE with respect to p is also shown in Fig. 8-1. The RMSE reaches a minimum value, 0.0912, when p = 16. The second minimum value, 0.0914 is reached when p = 12. According to the parsimony principle as pointed out by Wu [69], the model with p = 12 is chosen since it has fewer predictors. The model for predicting PD can be expresses as PD = $\mathbf{k}^T\mathbf{X}$, where $\mathbf{k}^T$ is the transpose of the coefficient vector and **X** is the predictor vector. The coefficients associated with the predictors in the predictor model are listed in Table 8-3. The relationship between actual PD and predicted PD from the model development data is shown in Fig. 8-2(a). The residual plot is shown in Fig. 8-2(b). Most of the errors are within ±0.1. The RMSE is 0.0552. No systematic errors are observed, which indicates the adequacy of the model. Fig. 8-3(a) shows the relationship between actual PD and predicted PD from the model validation data and Fig. 8-3(b) shows actual and predicted PD versus test locations. The predicted PD follows the actual PD very well.

Table 8-3: Coefficients of the prediction model for PD

Term, **X**	Coefficient, **k**
Intercept	1.182
S0W1	0.668
S0W6	-2.686
A0W1*A0W2	2.185
A0W1*A0W10	-2.653
A0W2*A0W5	-2.443
A0W2*S0W4	-7.577
A0W2*S0W6	4.870
A0W5*A0W10	1.982
S0W4*S0W5	6.187
S0W7*S0W8	-0.249
A0W9^3	0.550
S0W5^3	-2.500

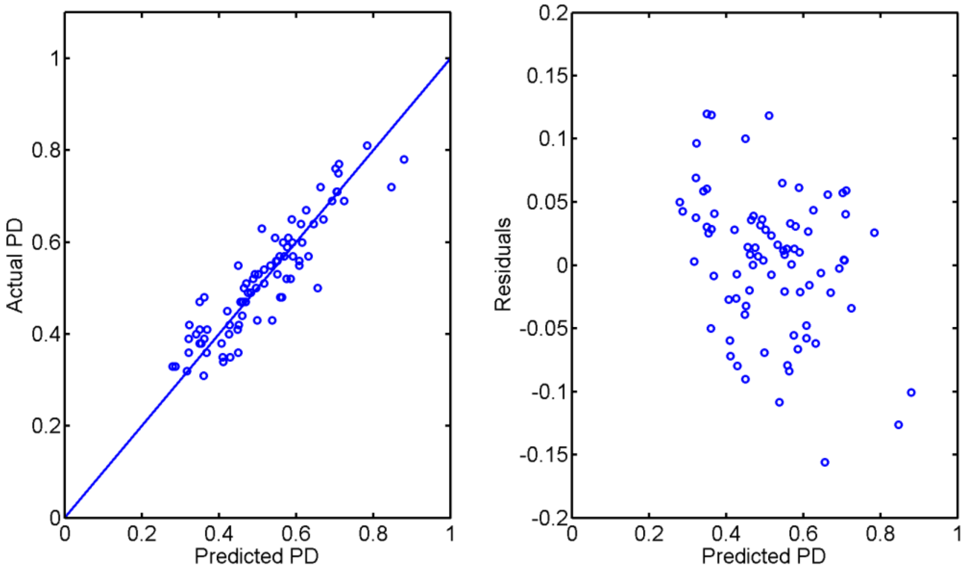

Fig. 8-2: (a) Predicted PD vs. Actual PD (b) residual plot for model development using direct method

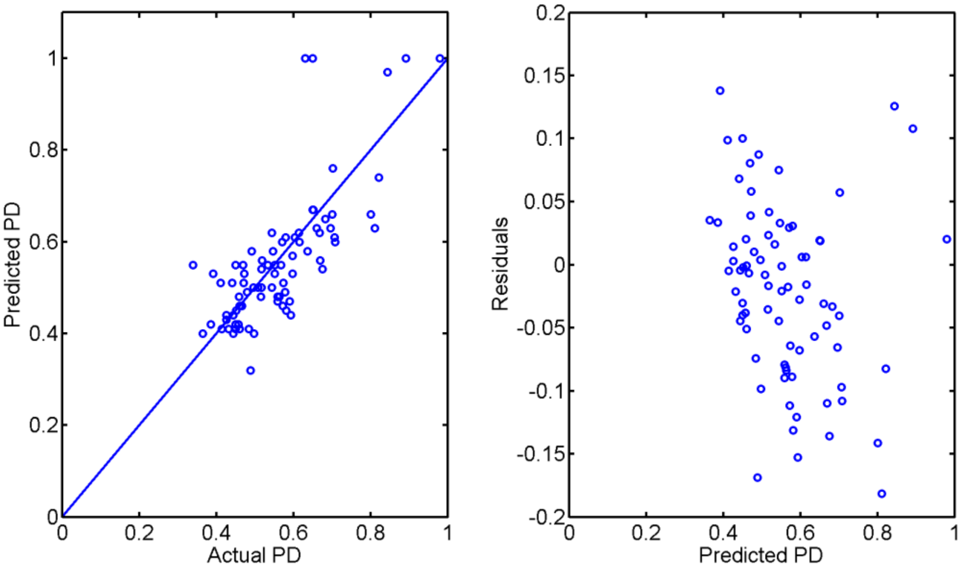

Fig. 8-3: (a) Predicted PD vs. Actual PD (b) residual plot for model validation using direct method

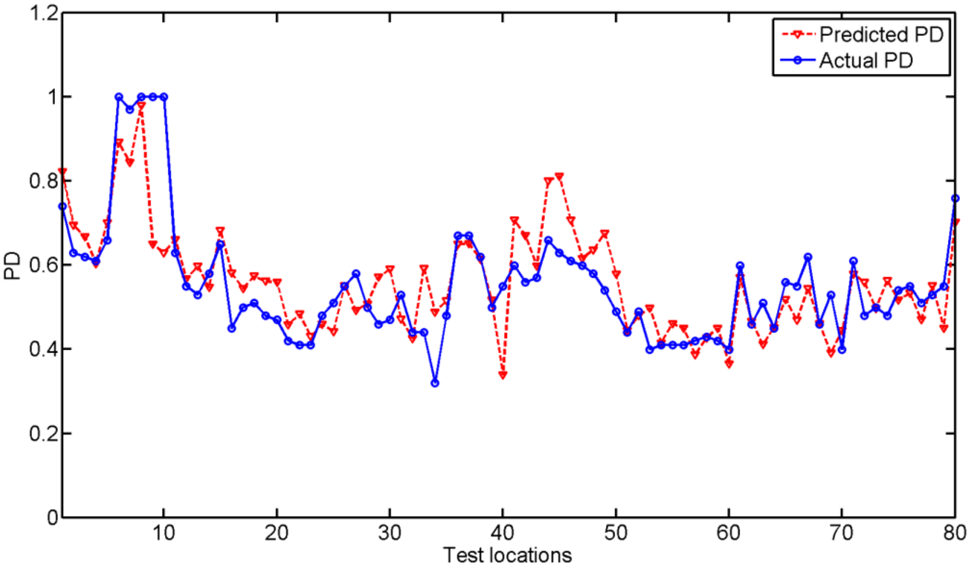

Fig. 8-4: PD vs. Test locations for model validation using direct method

8.1.5 Model Development and Validation for PD with Addition of RH and BW as Predictors

Sometimes laser profilometer is used to measure RH and BW of a butt weld. The same model development procedure discussed previously can be applied to build the prediction model for PD with two additional dimensions (RH and BW) as predictors. Here the threshold of p-value = 0.2 is chosen for the stepwise regression. The indices and the sixteen terms selected by the stepwise regression using the development data are shown in the first two columns of Table 8-4. Sixteen models are built with increasing number of predictors as described in the earlier section and they are shown in the fourth columns of Table 8-4. Fig. 8-5 shows AICc values with respect to p. These models are then validated by the validation data and the RMSE values of each model are also listed in Table 8-4 and plotted in the Fig. 8-5. The AICc reaches the local minimum -362.06 when p = 8. The RMSE follows the trend of AICc and reaches the minimum value, 0.0774, when p = 7. In this case, the best model is not the one indicated by the AICc value. For comparison, the RMSE values calculated from the model without including RH and BW as predictors is 0.0912. It clearly shows that with the addition of RH and BW as predictors, the developed model can predict PD more accurately with fewer predictors. Therefore, if RH and BW measurements are available, it is better to include them into the prediction model. The model for predicting PD can be expresses as PD = $\mathbf{k}^T\mathbf{X}$, where $\mathbf{k}^T$ is the transpose of the coefficient vector and $\mathbf{X}$ is the predictor vector. The coefficients and associated statistical data of the model are shown in Table 8-5. The results also show that the prediction power of the model cannot always be determined by the AICc values. It is always desirable to validate the model by using another set of data and calculate the RMSE values to determine the best model. The relationship between actual PD and predicted PD from the model development data is shown in Fig. 8-6(a). The residual plot is shown in Fig. 8-6(b). Fig. 8-7(a) shows the relationship between actual PD and predicted PD from the model validation data and Fig. 8-7(b) shows actual and predicted PD versus test locations of the validation data. Except for the test locations that have actual PDs very close to one, the predicted PD follows the actual PD even better than it does in Fig. 8-3.

Table 8-4: Summary of model development using AICc and validation using RMSE for PD (with RH and BW as predictors)

Index	Term	p	Terms in model	AICc	RMSE
1	BW*A0W9	1	7	-271.59	0.1043
2	BW*S0W4	2	3,7	-301.95	0.1008
3	BW*S0W7	3	3,4,8	-323.90	0.0856
4	RH*A0W6	4	3,4,7,8	-336.39	0.0904
5	RH*A0W10	5	3,4,7,8,14	-340.79	0.0839
6	RH*S0W3	6	3,4,7,8,9,14	-352.09	0.0804
7	RH*S0W9	7	3,4,7,8,9,12,14	-357.11	0.0774
8	RH*S0W10	8	2,3,4,7,8,9,12,14	-362.06	0.0811
9	A0W1*S0W6	9	2,3,4,7,8,9,12,14,16	-360.87	0.0790
10	A0W2*A0W7	10	3,4,7,8,9,10,11,13,15,16	-358.76	0.0837
11	A0W2*S0W3	11	2,4,7,8,9,10,11,12,13,15,16	-359.29	0.0833
12	A0W3*A0W10	12	2,3,4,7,8,9,10,11,12,13,15,16	-361.32	0.0798
13	A0W6*S0W3	13	2,3,4,6,7,8,9,10,11,12,13,15,16	-358.88	0.0793
14	A0W6*S0W10	14	2,3,4,6,7,8,9,10,11,12,13,14,15,16	-355.41	0.0842
15	A0W7*S0W4	15	2,3,4,5,6,7,8,9,10,11,12,13,14,15,16	-353.52	0.0850
16	S0W4^3	16	ALL	-347.41	0.0837

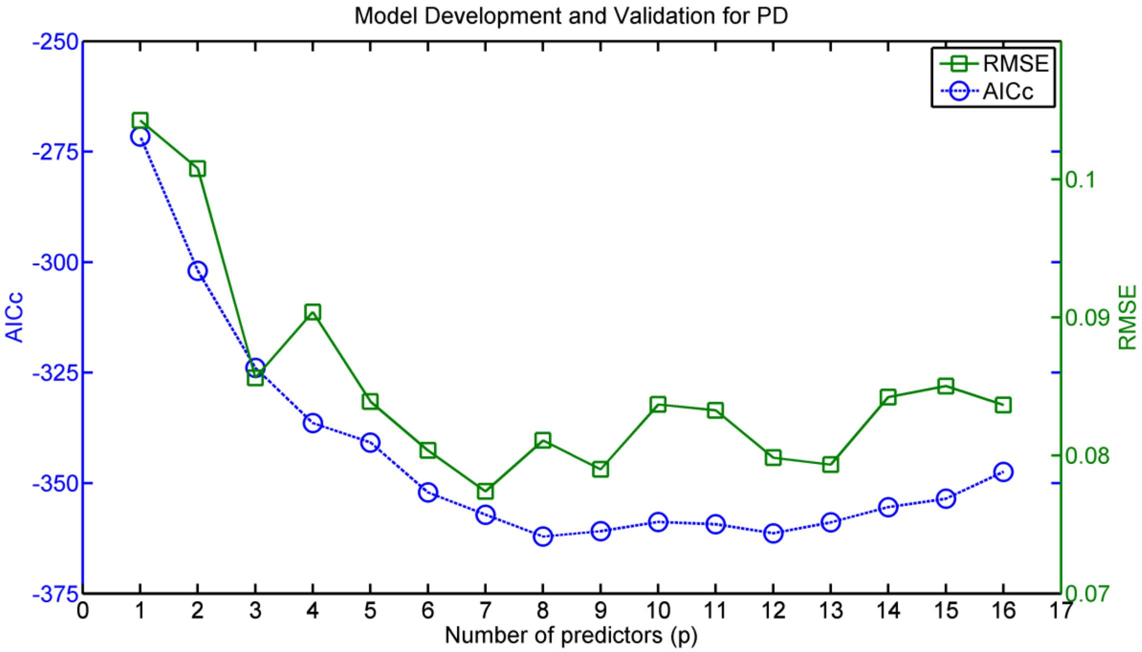

Fig. 8-5: AICc and RMSE vs. p for model development and validation for PD (with RH and BW as predictors)

Table 8-5: Coefficients of the prediction model for PD (with RH and BW as predictors)

Term, **X**	Coefficient, **k**
Intercept	1.074
BW*S0W7	-0.120
RH*A0W6	-0.638
RH*S0W9	-0.216
RH*S0W10	-0.787
A0W1*S0W6	-0.240
A0W3*A0W10	-0.264
A0W6*S0W10	0.730

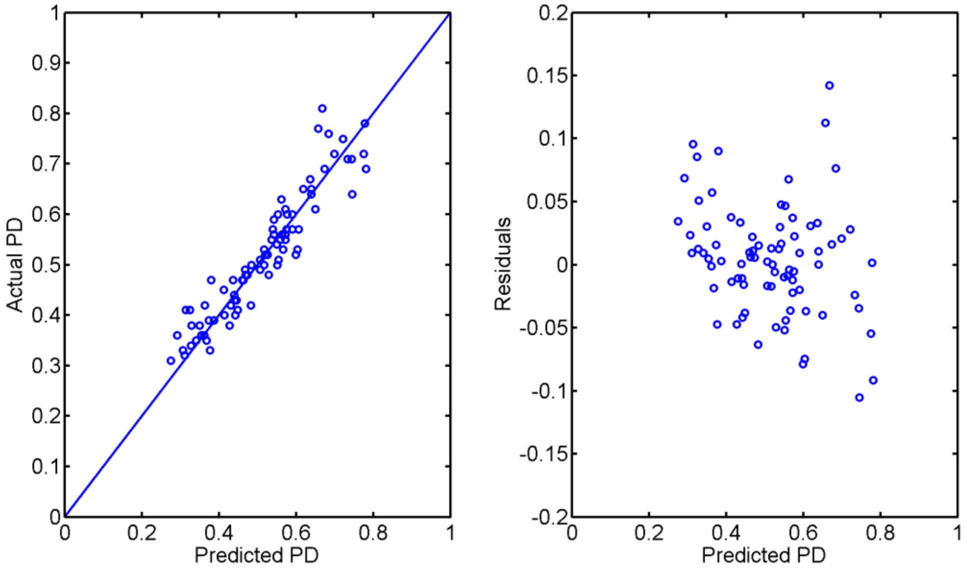

Fig. 8-6: (a) Predicted PD vs. Actual PD (b) residual plot for model development using direct method (with RH and BW as predictors)

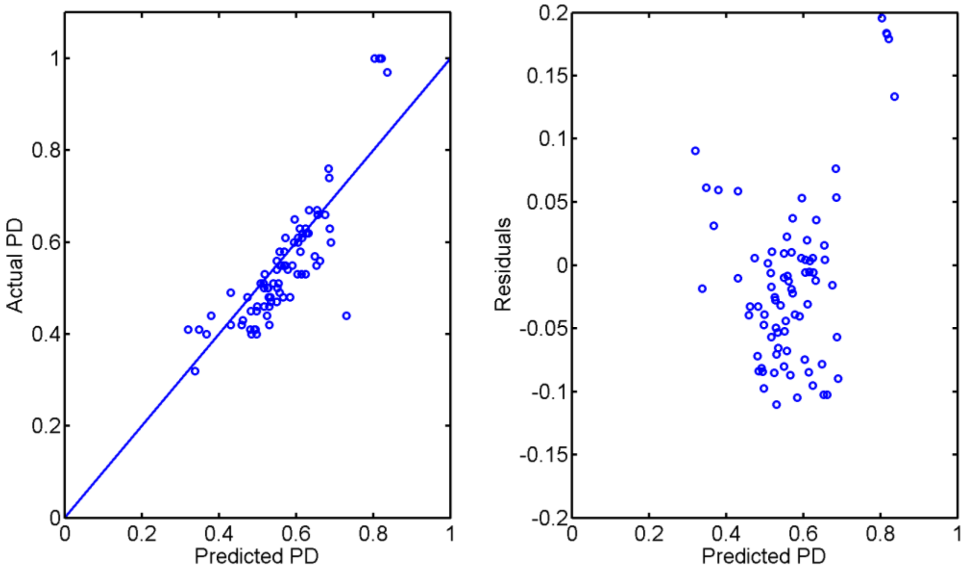

Fig. 8-7: (a) Predicted PD vs. Actual PD (b) residual plot for model validation using direct method (with RH and BW as predictors)

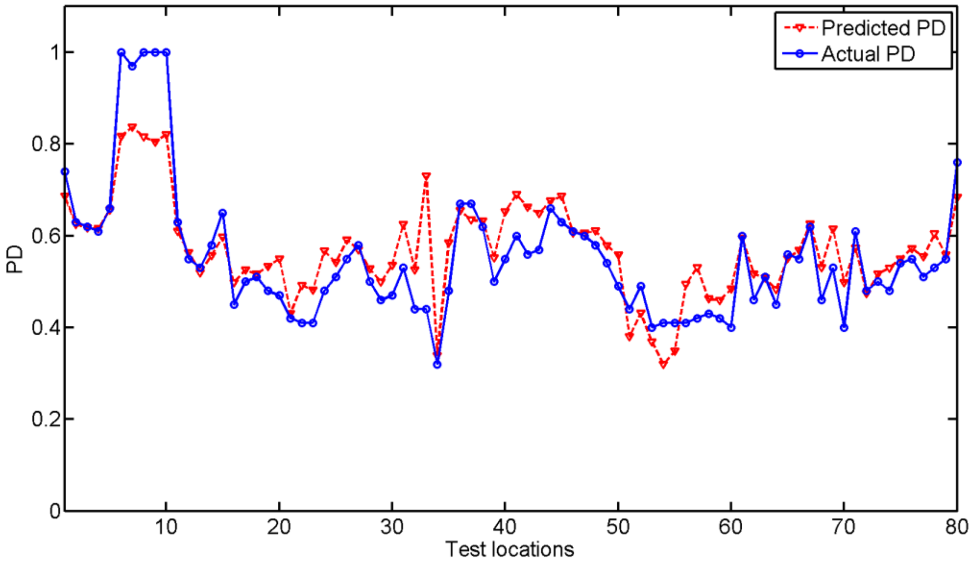

Fig. 8- 8: PD vs. Test locations for model validation using direct method (with RH and BW as predictors)

8.1.6 Model Development and Validation for RH

For reinforcement height (RH), the p-value for the stepwise regression is chosen to be 0.2. The 20 terms selected and their indices are shown in the first two columns of Table 8-6. The AICc values are calculated for all possible models that can be constructed using these 20 terms and the model that gives the lowest AICc for each number of predictors, p, is identified. These models that give lowest AICc values are also shown in Table 8-6. The detailed description of each column can be found in Chapter 8.1.4. The sixth column shows the root mean square errors (RMSE) when these models are validated by the validation data. The AICc and RMSE values with respect to p are shown in Fig. 8-9. The AICc starts to level off when p = 9 and reaches the minimum value, -311.636 when p = 14. The RMSE reaches the minimum value, 0.1037 when p = 17. In this case, the lowest values for AICc and RMSE do not happen at the same number of predictors. The best model for predicting the reinforcement height of a butt weld is determined after validation, which is the model with p = 17. The model for predicting PD can be expresses as RH = $\mathbf{k}^T\mathbf{X}$, where $\mathbf{k}^T$ is the transpose of the coefficient vector and **X** is the predictor vector. The coefficients and associated statistical data of the model are shown in Table 8-7. The relationship between actual RH and predicted RH of the data used for model development is shown in Fig. 8-10(a). The residual plot is shown in Fig. 8-10(b). Most of the errors are within ±0.1. No serious systematic errors can be observed, which indicates the adequacy of the model. Fig. 8-11(a) shows the relationship between actual RH and predicted RH of the data used for model validation and Fig. 8-11(b) shows actual and predicted RH versus test locations of the validation data. The RMSE values calculated for the development data and validation data are 0.0588 and 0.1037 respectively. For reference, among two data sets, the maximum and minimum of the RH are 0.95 and 0.39, respectively. The range of the RH is 0.56.

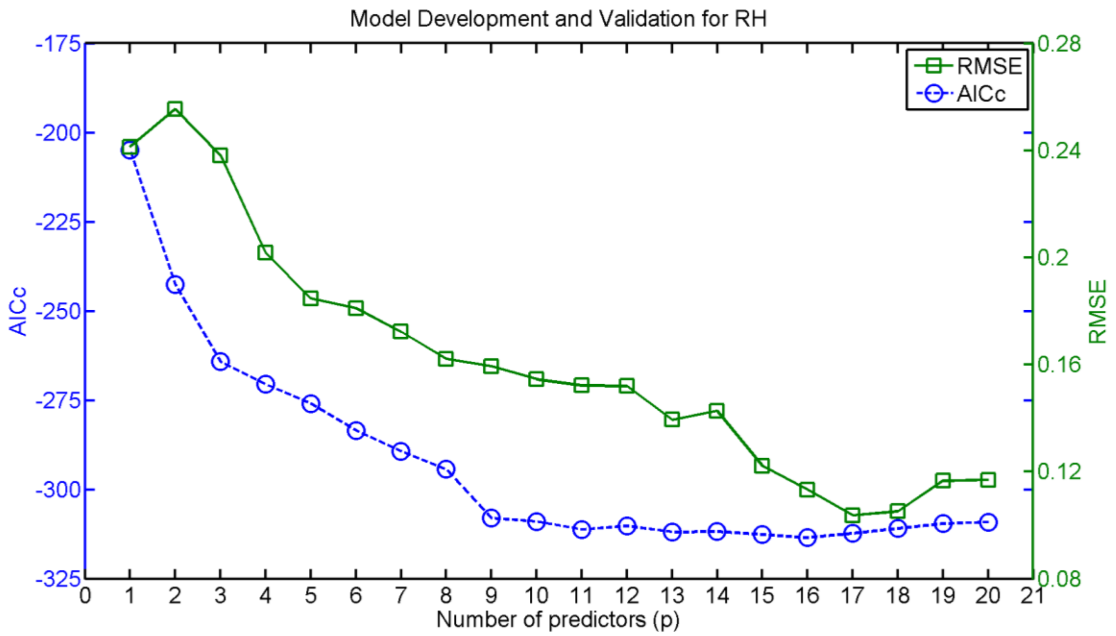

Fig. 8-9: AICc and RMSE vs. p for model development and validation for RH

Table 8-6: Summary of model development using AICc and validation using RMSE for RH

Index	Term	p	Indices of terms in model	AICc	RMSE
1	S0W4	1	5	-210.390	0.2414
2	S0W9	2	5,19	-247.552	0.2556
3	A0W2*A0W3	3	2,13,18	-267.632	0.2381
4	A0W2*A0W8	4	1,2,6,13	-289.812	0.2018
5	A0W2*A0W9	5	1,2,5,6,13	-295.062	0.1848
6	A0W3*S0W9	6	1,2,5,6,13,15	-295.401	0.1811
7	A0W6*S0W6	7	1,2,6,9,12,16,20	-303.912	0.1723
8	A0W7*A0W10	8	1,2,4,10,12,13,15,17	-301.147	0.1622
9	A0W8*S0W5	9	1,2,4,10,12,13,15,17,20	-309.855	0.1594
10	A0W8*S0W9	10	2,4,10,11,12,13,15,17,18,20	-318.221	0.1545
11	S0W1*S0W8	11	2,4,7,10,11,12,13,15,17,18,20	-321.336	0.1522
12	S0W2*S0W3	12	2,4,7,8,10,11,12,13,15,17,18,20	-311.982	0.1520
13	S0W4*S0W5	13	2,4,5,7,8,10,11,12,13,15,17,18,20	-322.462	0.1394
14	S0W4*S0W9	14	2,4,5,7,8,9,10,11,12,13,15,17,18,20	-331.636	0.1427
15	A0W2^3	15	2,3,4,5,6,7,8,9,11,12,1315,16,18,20	-320.522	0.1222
16	A0W3^3	16	1,2,3,4,5,6,7,8,9, 11,12,13,14,15,16,20	-320.156	0.1133
17	A0W8^3	17	1,2,3,4,5,6,7,8,9, 11,12,13,14,15,16,17,20	-328.406	0.1037
18	S0W4^2	18	1,2,3,4,5,6,7,8,9,10,11,12,13,14,15,16,17 ,20	-326.028	0.1051
19	S0W4^3	19	1,2,3,4,5,6,7,8,9,11,12,13,14,15,16,17,18,19,20	-315.817	0.1166
20	S0W9^3	20	ALL	-321.782	0.1169

Table 8-7: Coefficients of the prediction model for RH

Term, **X**	Coefficient, **k**
Intercept	0.8037
S0W4	1.8290
S0W9	-3.1423
A0W2*A0W3	2.2231
A0W2*A0W8	-4.5299
A0W2*A0W9	-0.8204
A0W3*S0W9	5.5908
A0W6*S0W6	0.4634
A0W7*A0W10	0.7392
A0W8*S0W5	4.0893
S0W1*S0W8	-0.5225
S0W2*S0W3	0.8110
S0W4*S0W5	-5.4686
S0W4*S0W9	3.3341
A0W2^3	1.6988
A0W3^3	-6.8854
A0W8^3	-0.5786
S0W9^3	-0.9792

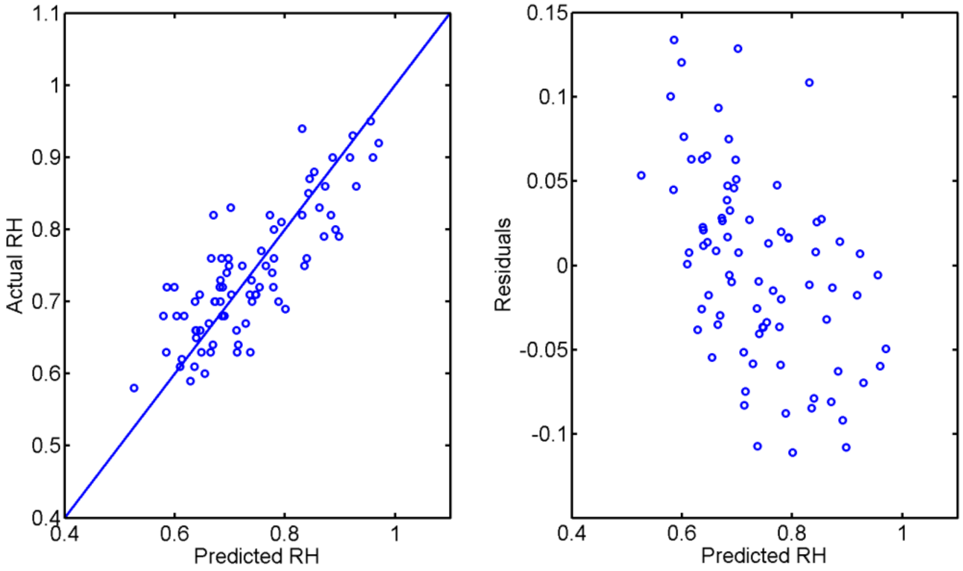

Fig. 8-10: (a) Predicted RH vs. Actual RH (b) residual plot for model development using direct method

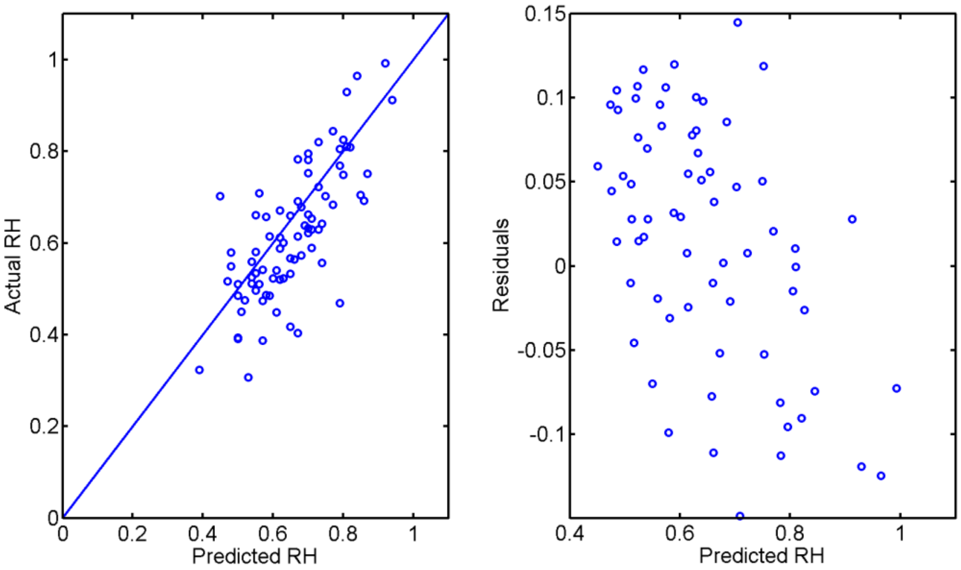

Fig. 8-11: (a) Predicted RH vs. Actual RH (b) residual plot for model validation using direct method

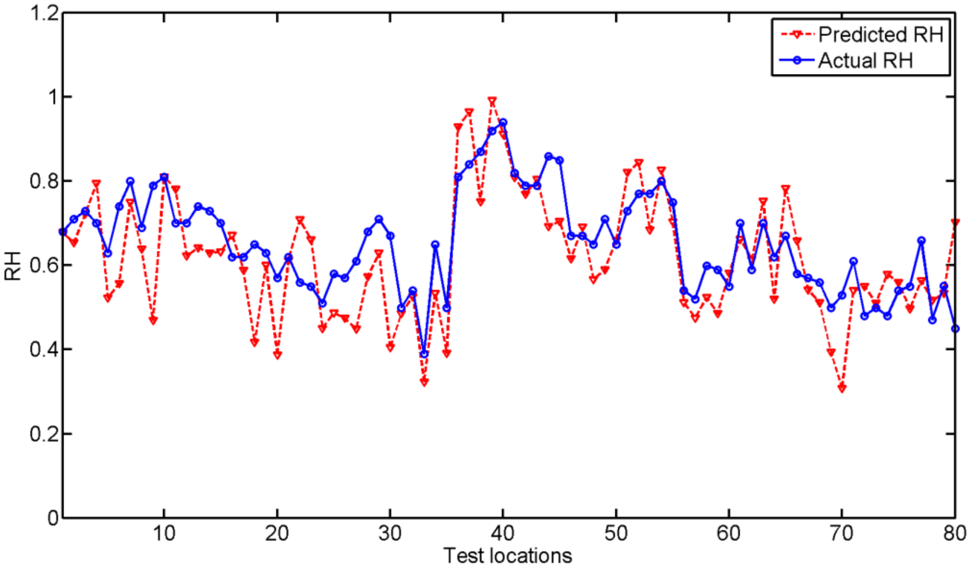

Fig. 8-12: RH vs. Test locations for model validation using direct method

8.1.7 Model Development and Validation for BW

Follow the same procedure, the model for bead width (BW) can also be developed. The threshold of p-value for the stepwise regression is chosen to be 0.3. The

16 terms are selected. They and their indices are shown in the first two columns in Table 8-8. Again, the AICc values are calculated for all possible models that can be constructed using these 16 terms and the model that gives the lowest AICc for each corresponding number of predictors, p, is identified. These models that give lowest AICc values are also shown in Table 8-8. The AICc and RMSE values for model development and validation are shown in Table 8-8 and Fig. 8-13. The AICc and RMSE both reach minimum when p = 15. The smallest AICc is -288.901 and the smallest RMSE is 0.2075. The best model for predicting the bead width of a butt weld is determined, which is the model when p = 15. The model for predicting PD can be expresses as BW = $\mathbf{k}^T\mathbf{X}$, where $\mathbf{k}^T$ is the transpose of the coefficient vector and **X** is the predictor vector. The coefficients and associated statistical data of the model are shown in Table 8-9. The relationship between actual BW and predicted BW of the data used for model development is shown in Fig. 8-14(a) and the residual plot is shown in Fig. 8-14(b). Most of the errors are within ±0.3. Fig. 8-15(a) shows the relationship between actual BW and predicted BW of the data used for model validation and Fig. 8-15(b) shows actual and predicted BW versus test locations of the validation data. The RMSE values calculated for the development data and validation data are 0.1329 and 0.2129 respectively. For reference, among two data sets, the maximum and minimum of the BW are 2.53 and 1.21, respectively. The range of the BW is 1.32.

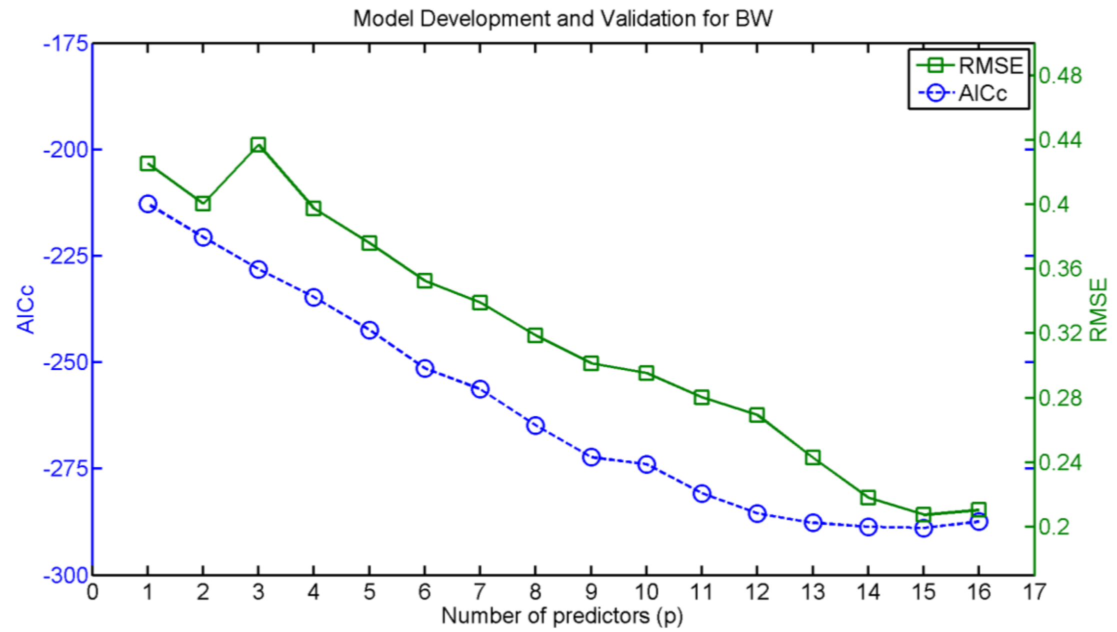

Fig. 8-13: AICc and RMSE vs. p for model development and validation for BW

Table 8-8: Summary of model development using AICc and validation using RMSE for BW

Index	Term	p	Indices of terms in model	AICc	RMSE
1	A0W2	1	12	-212.773	0.4254
2	S0W2	2	12,13	-220.531	0.4004
3	S0W3	3	2,12,13	-228.143	0.4370
4	A0W1*A0W2	4	1,6,7,12	-234.654	0.3974
5	A0W1*S0W2	5	2,4,6,7,12	-242.358	0.3759
6	A0W3*S0W1	6	2,4,6,7,11,12	-251.342	0.3526
7	A0W3*S0W8	7	2,4,6,7,11,12,13	-256.309	0.3389
8	A0W4*S0W9	8	2,3,4,5,6,7,11,14	-264.817	0.3187
9	A0W5*A0W8	9	1,2,3,4,5,6,7,11,13	-272.27	0.3014
10	A0W7*A0W10	10	1,2,3,4,5,6,7,11,12,13	-273.911	0.2954
11	A0W8*S0W9	11	1,2,3,4,5,6,7,9,11,13,16	-280.779	0.2803
12	S0W3*S0W5	12	1,2,3,4,5,6,7,9,11,12,13,16	-285.456	0.2694
13	S0W3*S0W9	13	1,2,3,4,5,6,7,9,10,11,12,13,16	-287.662	0.2427
14	A0W2^2	14	2,3,5,6,7,8,9,10,11,12,13,14,15,16	-288.633	0.2181
15	A0W2^3	15	1,2,3,5,6,7,8,9,10,11,12,13,14,15,16	-288.901	0.2075
16	A0W5^3	16	ALL	-287.383	0.2105

Table 8-9: Coefficients of the prediction model for BW

Term, **X**	Coefficient, **k**
Intercept	3.1907
A0W2	-3.8103
S0W2	-1.0746
S0W3	-2.8904
A0W1*S0W2	1.0734
A0W3*S0W1	-4.0420
A0W3*S0W8	1.3039
A0W4*S0W9	-0.6276
A0W5*A0W8	4.3269
A0W7*A0W10	0.8328
A0W8*S0W9	-4.9762
S0W3*S0W5	-1.4998
S0W3*S0W9	5.8077
A0W2^2	14.0308
A0W2^3	-13.8294
A0W5^3	-4.7824

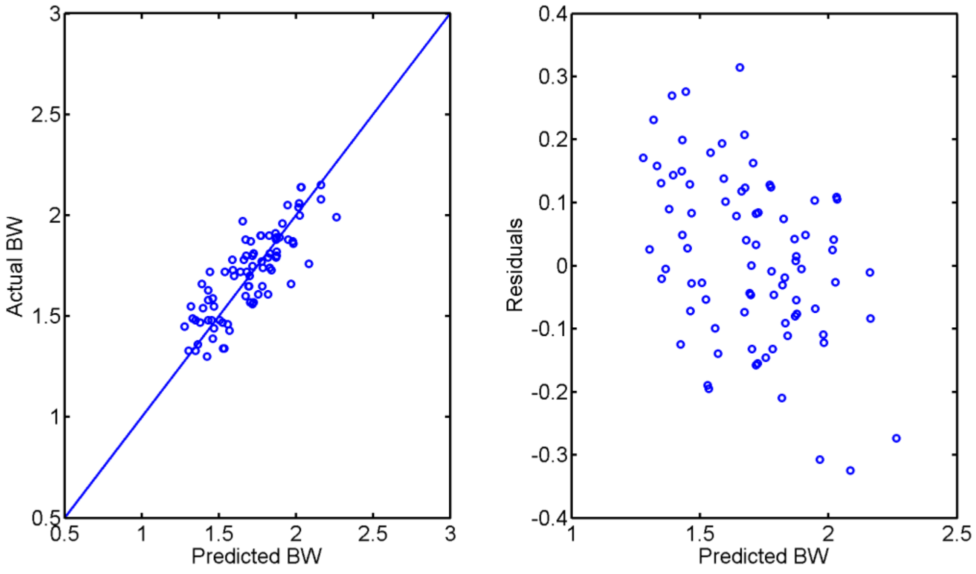

Fig. 8-14: (a) Predicted BW vs. Actual BW (b) residual plot for model development using direct method

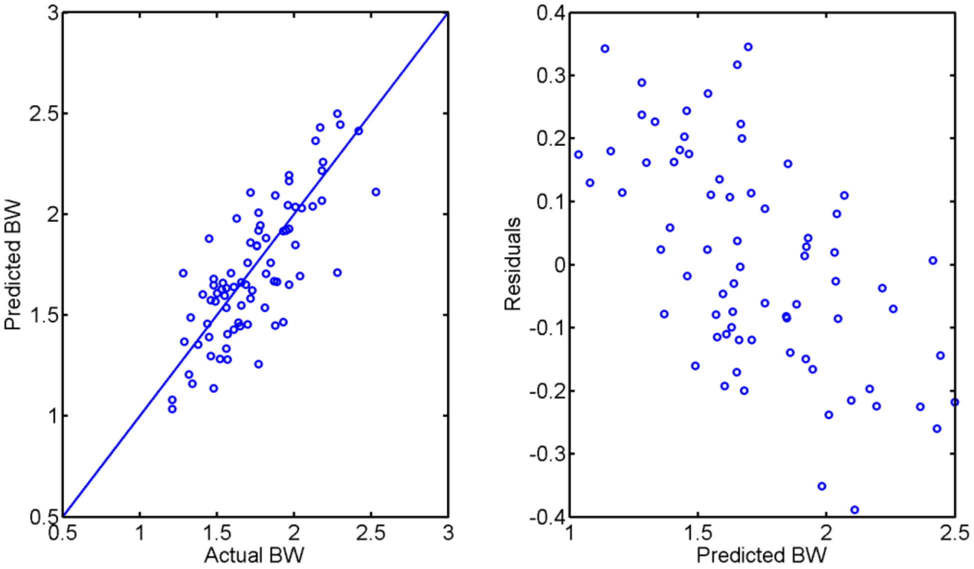

Fig. 8-15: (a) Predicted BW vs. Actual BW (b) residual plot for model validation using direct method

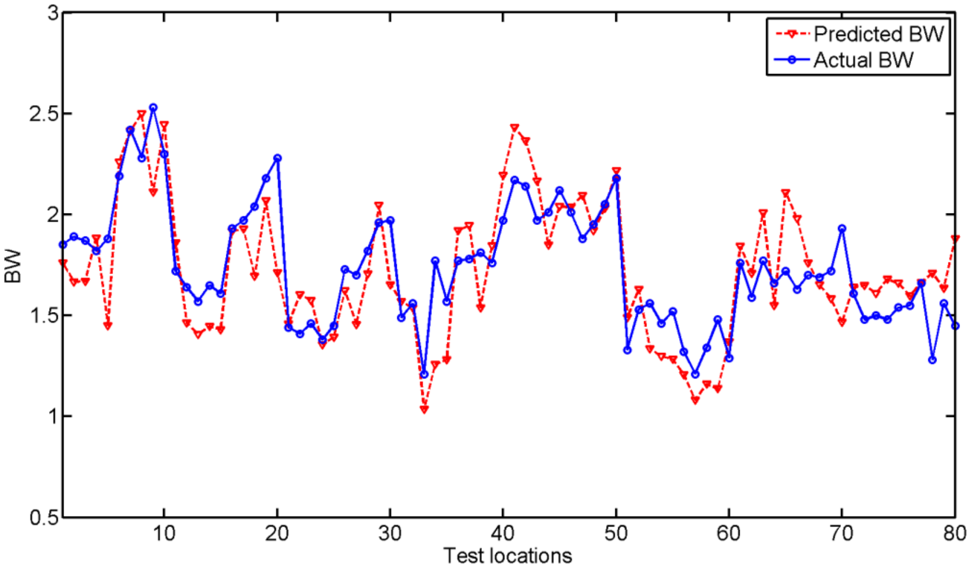

Fig. 8-16: RH vs. Test locations for model validation using direct method

8.2 The Indirect Method

8.2.1 Introduction

An alternative method is proposed to measure weld dimensions. Unlike the previous method in which the weld dimensions are assumed to be functions of the reflection coefficients of different Lamb wave modes. In this alternative method, each reflection coefficient is assumed to be a function of the weld dimensions. For example, a regression model for A0W1, which is the reflection coefficient of 1.75 mm A0 mode according to Table 8-1, can be developed with the weld dimensions as predictors. It can be expressed as in Eq. 8-2.

$$\begin{aligned} A0W1 = C_{1,0} + C_{1,1}PD + C_{1,2}RH + C_{1,3}BW + C_{1,4}PD^2 + C_{1,5}RH^2 + C_{1,6}BW^2 \\ + C_{1,7}PD \cdot RH + C_{1,8}PD \cdot BW + C_{1,9}RH \cdot BW + C_{1,10}PD^3 \\ + C_{1,11}RH^3 + C_{1,12}BW^3 + \cdots + C_{1,N}(some\ higher\ order\ term) \end{aligned} \tag{8-2}$$

where $C_{1,0}$ is the intercept and $C_{1,1}$, $C_{1,2}$,…,$C_{1,N}$ are regression coefficients associated with the terms shown in the equation. There are N terms used as predictors in the regression analysis. In the same fashion, regression models for all other reflection coefficients can be derived. A matrix equation can be formulated as in Eq. 8-3.

$$\boldsymbol{R} = \boldsymbol{K} \cdot \boldsymbol{D} \tag{8-3}$$

where **R** is the reflection coefficients matrix, **K** is the regression coefficients matrix and **D** is the weld dimensions matrix. They can be explicitly expressed in Eq. 8-4.

$$\boldsymbol{R}=\begin{bmatrix} A0W1 \\ A0W2 \\ A0W3 \\ A0W4 \\ A0W5 \\ A0W6 \\ A0W7 \\ A0W8 \\ A0W9 \\ A0W10 \\ S0W1 \\ S0W2 \\ S0W3 \\ S0W4 \\ S0W5 \\ S0W6 \\ S0W7 \\ S0W8 \\ S0W9 \\ S0W10 \end{bmatrix}_{20\times 1} \quad \boldsymbol{K}=\begin{bmatrix} C_{1.0} & C_{1.1} & \cdots & C_{1.N} \\ C_{2.0} & C_{2.1} & \cdots & C_{2.N} \\ \vdots & \vdots & & \vdots \\ C_{10.0} & C_{10.1} & \cdots & C_{10.N} \\ C_{11.0} & C_{11.1} & \cdots & C_{11.N} \\ C_{12.0} & C_{12.1} & \cdots & C_{12.N} \\ \vdots & \vdots & & \vdots \\ C_{20.0} & C_{20.1} & \cdots & C_{20.N} \end{bmatrix}_{20\times(N+1)} \quad \boldsymbol{D}=\begin{bmatrix} 1 \\ PD \\ RH \\ BW \\ PD^2 \\ RH^2 \\ BW^2 \\ PD\cdot RH \\ PD\cdot BW \\ RH\cdot BW \\ PD^3 \\ RH^3 \\ BW^3 \\ \vdots \end{bmatrix}_{(N+1)\times 1} \tag{8-4}$$

In the example shown here, twenty reflection coefficients are used. The matrix **K** defines the relationship between the reflection coefficients and the weld dimensions and their interactions. If the regression models are well constructed and they can nicely explain the relationship between each of the reflection coefficients and the weld dimensions, then the matrix K is well constructed. For the weld dimension prediction purposes, if one wants to predict weld dimensions of an unknown sample, one can use the nondestructive testing procedure that is described in this research to measure reflection coefficients and use the inverse of the matrix K to find the weld dimensions. The mathematic expression is shown in Eq. 8-5.

$$\boldsymbol{D}=\boldsymbol{K}^{-1}\cdot\boldsymbol{R} \tag{8-5}$$

If K matrix is not square, or the number of equations is not equal to the number of variables, inverse of K cannot be derived. In this case, the system of matrix can be further classified into two categories. If the number of equations is greater than the number of variables, the system is called overdetermined. For an overdetermined system, there is no exact solution, but it is still possible to find the least square solution by using the Eq. 8-6.

$$\boldsymbol{D} = (\boldsymbol{K}^{\boldsymbol{T}}\boldsymbol{K})^{-\boldsymbol{1}}\boldsymbol{K}^{\boldsymbol{T}} \cdot \boldsymbol{R} \tag{8-6}$$

On the other hand, if the number of equations is fewer than the number of variables, the system is called underdetermined. For an underdetermined system, there are infinite numbers of solutions. Unless there are other constraints, this type of system should be avoided.

8.2.2 Predictor Selection Procedure

As in the direct method, when constructing regression models, the balance between data fitting and prediction needs to be maintained. If too many predictors are included in a regression model, they may end up with modeling noises and losing the prediction capability. The questions that need to be answered are how many predictors are needed to model the reflection coefficients as in Eq. 8-2 and what those are. Here, a predictor selection procedure is proposed and used in this research. The procedure is similar to the backward elimination procedure in the stepwise regression. It first includes all predictors into the model and then eliminates some of them if they are not significant. The method described here is different from the backward elimination procedure in the stepwise regression. Instead of using the p-value to evaluate the significance of each predictor, our method evaluates the significance of each predictor through error analysis. The idea is that the more significant a predictor is, the more the error increases when that predictor is eliminated from the model.

The procedure begins with using all potential predictors to construct regression models for all reflection coefficients of model development data. Assume there are N potential predictors. After all the regression models have been found, the K matrix can be determined. The predicted weld dimensions can be calculated by plugging reflection coefficient matrices and inverse of K matrix into Eq. 8-5 or Eq. 8-6 if K matrix is not square. The predicted weld dimensions are compared with the actual weld dimensions and the errors can then be calculated.

The second step is to eliminate one of the predictors so that the number of predictors becomes N-1. There are N different combinations of predictors when the number of predictors is N-1. For each combination, the K matrix can be determined and the errors can be calculated. If an unnecessary predictor is eliminated, the errors should decrease and it should be less than the errors when all predictors are used. On the other hand, if an important predictor is eliminated, the errors should increase. By examining these errors, one can identify the K matrix that gives the lowest error. It indicates that the eliminated term is not in favor of the accuracy of prediction and should be eliminated.

The third step is to eliminate one more predictor from the N-1 predictors that are obtained from the second step. There are N-1 different combinations of predictors when the number of predictors is N-2. Following the same procedure as described in the second step, N-1 RMSE values can be calculated and the predictor to be eliminated can be identified.

This new set of predictors is used for the next iteration of the procedure until the elimination of any predictor would no longer reduce error. And the best model is found. Here the sum of normalized RMSEs of PD, RH and BW is used to test if a predictor is significant or not. The RMSEs of PD, RH and BW are normalized with their data range respectively.

8.2.3 Implementation of Predictor Selection Procedure

In this research, all the reflection coefficients are assumed to be functions of weld dimensions: PD, RH, and BW. From section 8.2.1, we know that the largest number of predictors that can be used to model reflection coefficients is twenty because there are twenty reflection coefficients in the reflection coefficient matrix in Eq. 8-3. Initially, a third order polynomial with second order interaction terms are chosen for the regression analysis between each of reflection coefficient and three weld dimensions: PD, RH, and BW. For such a regression model, the total number of predictors that can be used is twelve. They are PD, RH, BW, PD^2, RH^2, BW^2, $PD \cdot RH$, $PD \cdot BW$, $RH \cdot BW$, PD^3, RH^3, and BW^3. Since we can have up to 20 predictors, we can include more predictors by increasing the order of regression model to the fourth order. Three more predictors are also included for the regression analysis, and they are PD^4, RH^4, and BW^4, giving the total number of predictors to fifteen. Table 8-10 shows the details of the predictor selection process in this research. The first column is iteration. In each iteration, one more predictor is eliminated than in the previous iteration. Iteration 0 denotes the initial condition where all the predictors are included in the regression models. The second column is analysis run order. The run order increments by one in each iteration. For each run order, one predictor is eliminated. The third column lists the number of predictors that are included in the model and the fourth column lists the number of predictors that are eliminated from the model. The sum of the numbers in the third and fourth column should add up to fifteen. The fifth column explicitly shows the eliminated predictors. The sixth shows the sum of normalized RMSEs of BW, RH and PD.

Initially, fifteen predictors are used to model twenty reflection coefficients. From the first row of Table 8-10, the sum of RMSEs is 0.5281. In the first iteration, the lowest sum of normalized RMSEs is 0.5033 which happens when BW^4 is eliminated. In the second iteration, the lowest sum of normalized RMSEs is 0.4914 which happens when BW^4 and BW^2 are eliminated. In the third iteration, the sum of normalized RMSEs improves to 0.4906 when BW^4, BW^2 and RH^4 are eliminated. The procedure continues until the sum of normalized RMSEs does not improve anymore in the sixth iteration. Hence, ten predictors that construct the regression models are found. The selected predictors are PD, RH, BW, PD^2, RH^2, PD·RH, RH·BW, PD^3, BW^3 and PD^4. Fig. 8-17 shows the sum of normalized RMSEs in this procedure, in which the X axis shows iteration and run order. The first and second numbers denote iteration and run order respectively.

Table 8-10: Summary of predictor selection procedure for indirect method

Iteration	Run order	number of predictors	number of eliminated predictor(s)	Eliminated predictor(s)	Sum of normalized RMSEs
0	1	15	0	N/A	0.5281
1	**1**	**14**	**1**	**BW^4**	0.5033
1	2	14	1	RH^4	0.5151
1	3	14	1	PD^4	0.5163
1	4	14	1	BW^3	0.5053
1	5	14	1	RH^3	0.5149
1	6	14	1	PD^3	0.5164
1	7	14	1	RH·BW	0.5219
1	8	14	1	PD·BW	0.5046
1	9	14	1	PD·RH	0.5261
1	10	14	1	BW^2	0.5067
1	11	14	1	RH^2	0.5146
1	12	14	1	PD^2	0.5173
2	1	13	2	BW^4,RH^4	0.5013
2	2	13	2	BW^4,PD^4	0.4958
2	3	13	2	BW^4,BW^3	0.4927
2	4	13	2	BW^4,RH^3	0.5020
2	5	13	2	BW^4,PD^3	0.4964
2	6	13	2	BW^4,RH·BW	0.5138
2	7	13	2	BW^4,PD·BW	0.5014
2	8	13	2	BW^4,PD·RH	0.5158
2	**9**	**13**	**2**	**BW^4,BW^2**	0.4914
2	10	13	2	BW^4,RH^2	0.5027
2	11	13	2	BW^4,PD^2	0.4971
3	**1**	**12**	**3**	**BW^4,BW^2,RH^4**	0.4906
3	2	12	3	BW^4,BW^2,PD^4	0.5022
3	3	12	3	BW^4,BW^2,BW^3	0.4938
3	4	12	3	BW^4,BW^2,RH^3	0.4912
3	5	12	3	BW^4,BW^2,PD^3	0.5030
3	6	12	3	BW^4,BW^2,RH·BW	0.4970
3	7	12	3	BW^4,BW^2,PD·BW	0.4948
3	8	12	3	BW^4,BW^2,PD·RH	0.5059
3	9	12	3	BW^4,BW^2,RH^2	0.4919
3	10	12	3	BW^4,BW^2,PD^2	0.5036
4	1	11	4	BW^4,BW^2,RH^4,PD^4	0.4997
4	2	11	4	BW^4,BW^2,RH^4,BW^3	0.4868
4	**3**	**11**	**4**	**BW^4,BW^2,RH^4,RH^3**	0.4774
4	4	11	4	BW^4,BW^2,RH^4,PD^3	0.5004

4	5	11	4	BW^4,BW^2,RH^4,RH·BW	0.4906
4	6	11	4	BW^4,BW^2,RH^4,PD·BW	0.4845
4	7	11	4	BW^4,BW^2,RH^4,PD·RH	0.4998
4	8	11	4	BW^4,BW^2,RH^4,RH^2	0.4785
4	9	11	4	BW^4,BW^2,RH^4,PD^2	0.5011
5	1	10	5	BW^4,BW^2,RH^4,RH^3,PD^4	0.5088
5	2	10	5	BW^4,BW^2,RH^4,RH^3,BW^3	0.4819
5	3	10	5	BW^4,BW^2,RH^4,RH^3,PD^3	0.5098
5	4	10	5	BW^4,BW^2,RH^4,RH^3,RH·BW	0.4863
5	**5**	**10**	**5**	**BW^4,BW^2,RH^4,RH^3,PD·BW**	0.4767
5	6	10	5	BW^4,BW^2,RH^4,RH^3,PD·RH	0.4952
5	7	10	5	BW^4,BW^2,RH^4,RH^3,RH^2	0.4920
5	8	10	5	BW^4,BW^2,RH^4,RH^3,PD^2	0.5113
6	1	9	6	BW^4,BW^2,RH^4,RH^3,PD·BW,PD^4	0.5117
6	2	9	6	BW^4,BW^2,RH^4,RH^3,PD·BW,BW^3	0.4854
6	3	9	6	BW^4,BW^2,RH^4,RH^3,PD·BW,PD^3	0.5128
6	4	9	6	BW^4,BW^2,RH^4,RH^3,PD·BW,RH·BW	0.4779
6	5	9	6	BW^4,BW^2,RH^4,RH^3,PD·BW,PD·RH	0.4943
6	6	9	6	BW^4,BW^2,RH^4,RH^3,PD·BW,RH^2	0.4905
6	7	9	6	BW^4,BW^2,RH^4,RH^3,PD·BW,PD^2	0.5139

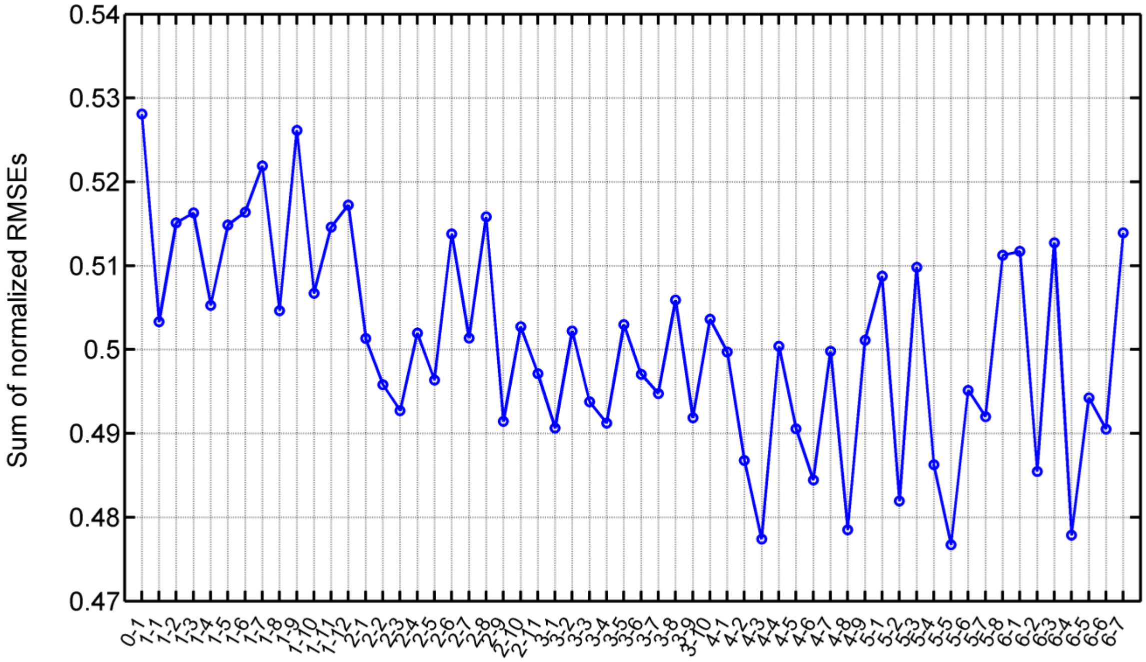

Fig. 8-17: Summary of predictor selection procedure for indirect method

The weld dimension matrix D in Eq. 8-3 can be expressed as:

$$\boldsymbol{D} = [PD\ \ RH\ \ BW\ \ PD^2\ \ RH^2\ \ PD \cdot RH\ \ RH \cdot BW\ \ PD^3\ \ BW^3\ \ PD^4]^T \tag{8-6}$$

The coefficient matrix K can also be expressed explicitly as:

$$\begin{bmatrix}
0.886 & -4.552 & 2.374 & -0.043 & 6.960 & -1.129 & 0.179 & -0.598 & -3.792 & 0.033 & 0.075 \\
-1.113 & 7.440 & 1.265 & 0.018 & -14.046 & -0.314 & -0.683 & -0.308 & 11.221 & 0.013 & -3.298 \\
0.239 & 1.121 & 1.095 & 0.046 & -4.500 & -0.462 & 1.091 & -0.627 & 3.794 & 0.017 & -1.147 \\
-0.566 & 2.594 & 1.868 & -0.046 & -4.002 & -0.357 & -1.946 & -0.234 & 5.676 & 0.013 & -2.953 \\
-0.804 & 2.035 & 2.186 & 0.088 & -0.375 & -0.114 & -3.445 & -0.183 & 1.974 & -0.011 & -1.395 \\
-0.571 & 4.810 & 0.823 & -0.019 & -8.773 & -0.092 & -1.338 & -0.060 & 8.103 & -0.004 & -2.786 \\
0.737 & -0.432 & 0.891 & 0.045 & -3.915 & -0.321 & 1.017 & -0.661 & 6.455 & 0.031 & -3.273 \\
2.343 & -4.379 & -1.320 & 0.034 & 3.141 & 0.204 & 1.784 & -0.290 & -0.521 & 0.004 & -0.495 \\
1.937 & -2.007 & -1.157 & -0.024 & -1.531 & 0.141 & 1.486 & -0.239 & 3.771 & 0.007 & -1.928 \\
1.971 & -3.360 & -0.880 & 0.020 & 2.330 & 0.053 & 1.336 & -0.237 & -0.929 & 0.006 & 0.128 \\
0.512 & 0.233 & 0.333 & -0.082 & -2.119 & -0.244 & 0.024 & -0.079 & 3.571 & 0.001 & -1.869 \\
0.029 & -3.260 & 3.476 & -0.035 & 4.363 & -0.699 & -1.067 & -0.880 & 1.377 & 0.045 & -2.709 \\
1.239 & -6.141 & 1.227 & -0.045 & 13.077 & -0.219 & 0.719 & -0.683 & -13.285 & 0.029 & 4.795 \\
0.914 & 0.806 & -1.137 & 0.012 & -4.495 & 0.233 & 1.487 & 0.012 & 3.174 & -0.012 & -0.540 \\
0.239 & 2.757 & 0.250 & 0.133 & -6.152 & 0.084 & 0.845 & -0.659 & 3.524 & 0.012 & -0.346 \\
0.982 & 0.761 & -0.274 & 0.059 & -5.277 & -0.165 & 1.953 & -0.376 & 3.159 & 0.003 & -0.140 \\
1.555 & 0.682 & -0.573 & -0.018 & -9.859 & -0.069 & 0.790 & -0.151 & 14.352 & -0.002 & -6.380 \\
2.934 & -5.130 & -0.901 & -0.068 & 1.251 & -0.037 & 2.375 & -0.557 & 2.884 & 0.026 & -2.090 \\
1.069 & 3.740 & -0.606 & 0.142 & -15.557 & -0.018 & 1.345 & -0.557 & 17.227 & 0.017 & -6.411 \\
1.409 & 3.579 & -1.135 & 0.048 & -17.367 & 0.009 & 1.929 & -0.370 & 20.637 & 0.010 & -8.299
\end{bmatrix}$$

8.2.4 Evaluation of Weld Dimensions

After the best set of predictors is determined, we need to investigate how well the model fits both the model development data and validation data. The scatter plot between actual PDs and predicted PDs of the model development data is shown in Fig. 8-18(a) and the residual plot is shown in Fig. 8-18(b). From Fig. 8-18(a), although a positive correlation can be seen between actual and predicted PDs, the accuracy of fitting is not very good. From the residual plot, most errors fall between ±0.3 and a systematic error pattern can be observed. Roughly speaking, the error linearly increases as the predicted PD increases. A simple linear regression trend line is also shown in the plot to show the trend clearly. This overall error can be mitigated by adjusting the predicted PD to compensate the systematic error. The compensated amount can be calculated by plugging the predicted PD into the equation of the regressed trend line in the residual plot and the corrected predicted PD can be derived by subtracting the compensated amount from the old predicted PD. The corrected scatter plot between actual PDs and predicted PDs of the model development data is shown in Fig. 8-19(a) and the corrected residual plot is shown in Fig. 8-19(b). From the residual plot, the error distributes randomly around zero indicating there is no systematic error. The RMSE reduces from 0.1235 to 0.0930 after the correction.

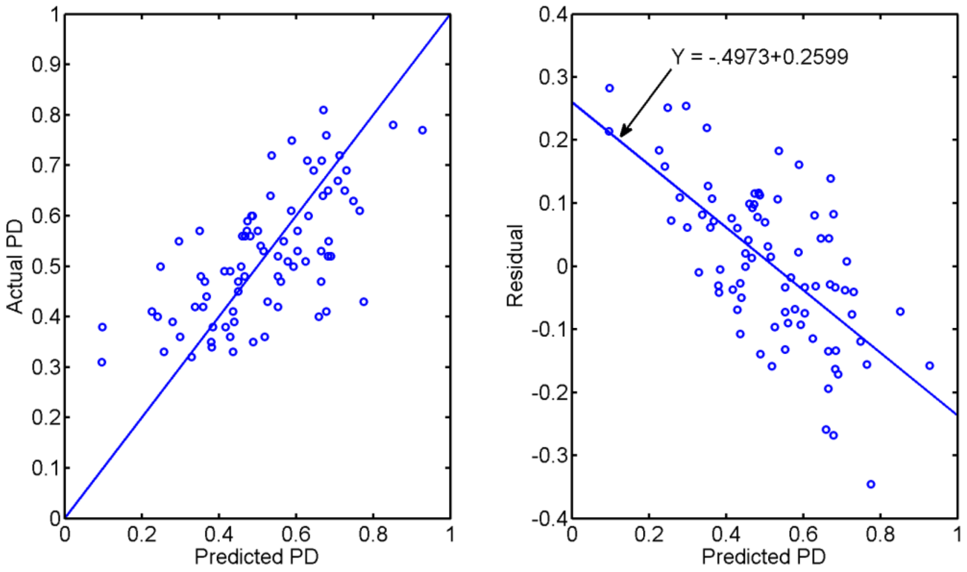

Fig. 8-18: (a) Predicted PD vs. Actual PD (b) residual plot for model development using indirect method before correction

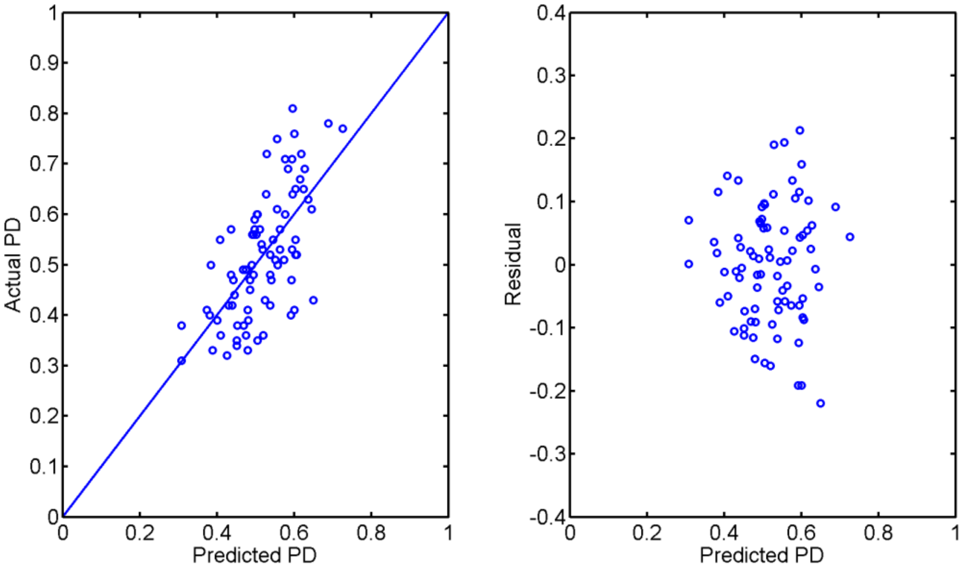

Fig. 8-19: (a) Predicted PD vs. Actual PD (b) residual plot for model development using indirect method after correction

The corrected model is then used on the validation data. The scatter plot between actual PDs and predicted PDs of the validation data is shown in Fig. 8-20(a) and the actual and predicted PDs are plotted together vs. test locations in Fig. 8-20(b). Except for the five data points that have actual PD close to one, the accuracy of prediction for other data points is very high. The RMSE of PDs of the validation data is 0.1094.

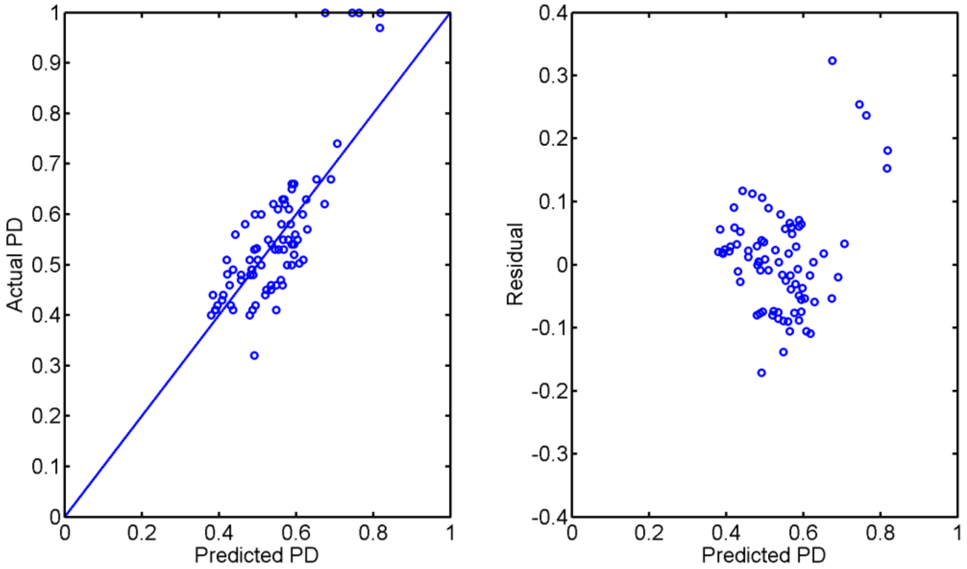

Fig. 8-20: (a) Predicted PD vs. Actual PD (b) residual plot for model validation using indirect method

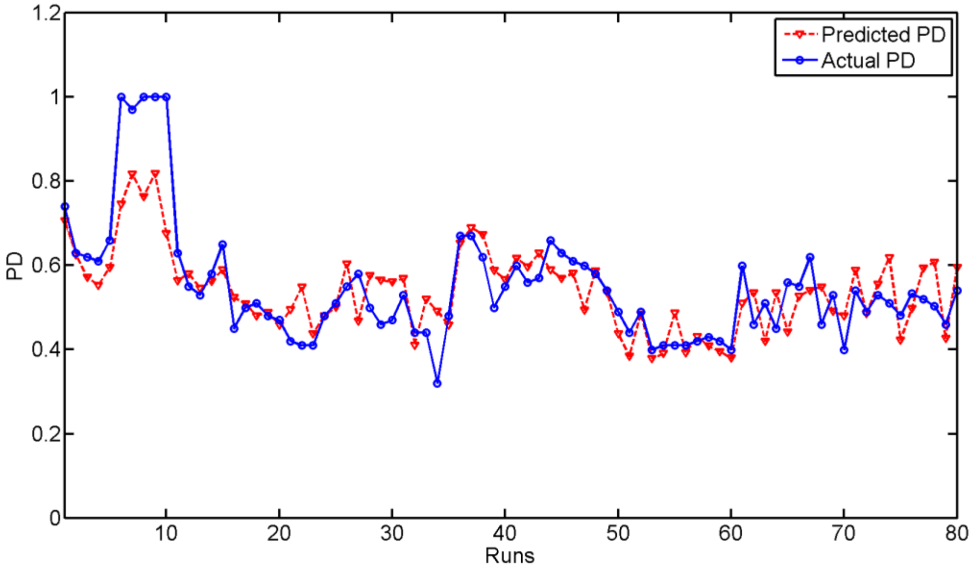

Fig. 8-21: PD vs. Test locations for model validation using indirect method

In addition to PD, RH and BW can also be calculated from both the model development data and validation data. Fig. 8-22(a) shows the scatter plot of predicted RHs vs. actual RHs and Fig. 8-22(b) shows the residual plot for the model development data. No serious systematic error is present so no correction procedure is needed. Fig. 8-23(a) shows the predicted RHs vs. actual RHs for the model validation data and Fig. 8-23(b) shows both actual and predicted RH at each test locations along the welds. The predicted RH follows the actual RH very well. The RMSEs of RHs for both the model development and validation data are 0.0863 and 0.1992 respectively.

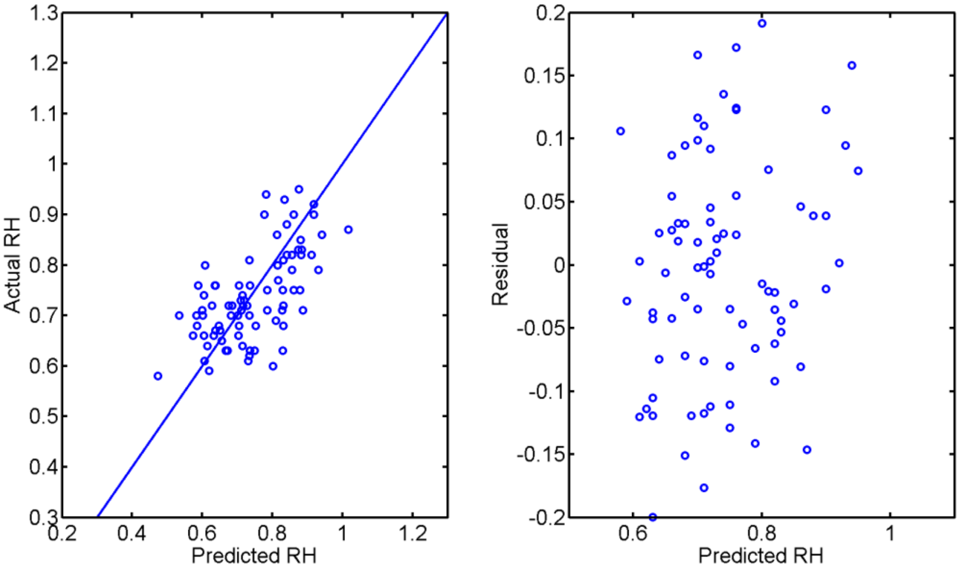

Fig. 8-22: (a) Predicted RH vs. Actual RH (b) residual plot for model development using indirect method

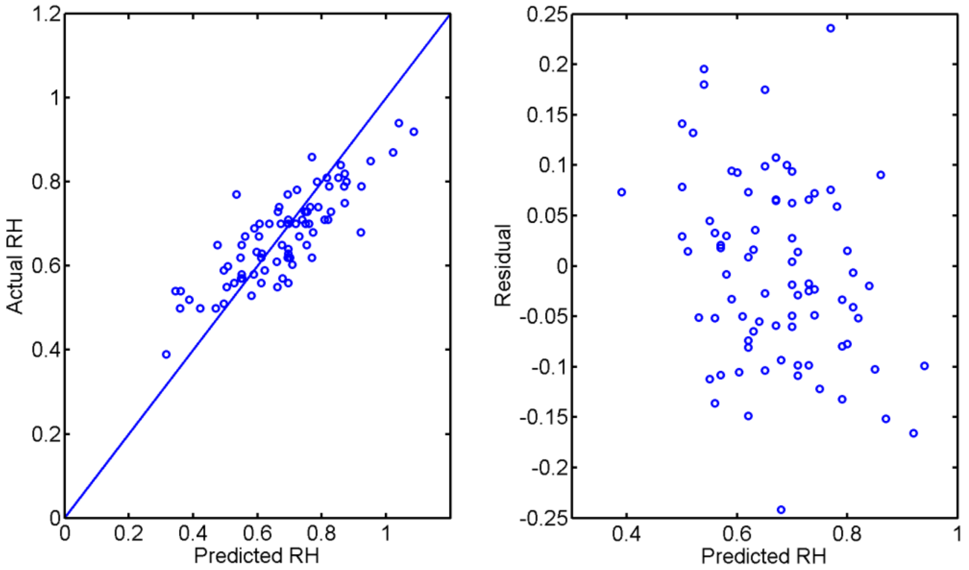

Fig. 8-23: (a) Predicted RH vs. Actual RH (b) residual plot for model validation using indirect method

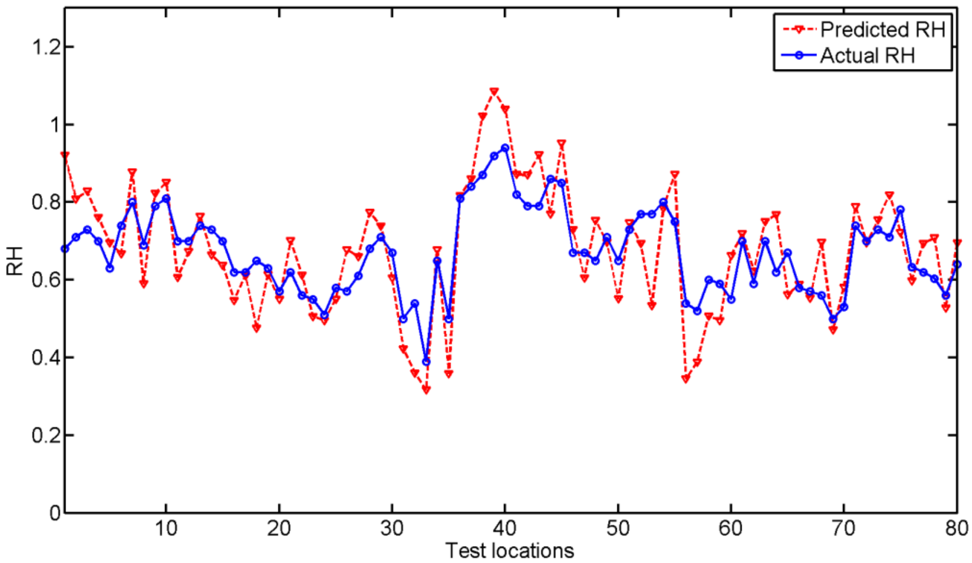

Fig. 8-24: RH vs. Test locations for model validation using indirect method

Likewise, Fig. 8-25(a) shows the scatter plot of predicted BWs vs. actual BWs and Fig. 8-25(b) shows the residual plot for the model development data. Again, serious systematic error is present. The correction procedure as described before must be taken to mitigate the systematic error. The corrected scatter plot between actual BWs and predicted BWs of the model development data is shown in Fig. 8-26(a) and the corrected residual plot is shown in Fig. 8-26(b). Fig. 8-27(a) shows the predicted BWs vs. actual BWs for the model validation data and Fig. 8-27(b) shows both actual and predicted BW at each test locations along the welds after the correction procedure is taken. The RMSEs of BWs for both the model development and validation data after correction are 0.1606 and 0.2439 respectively.

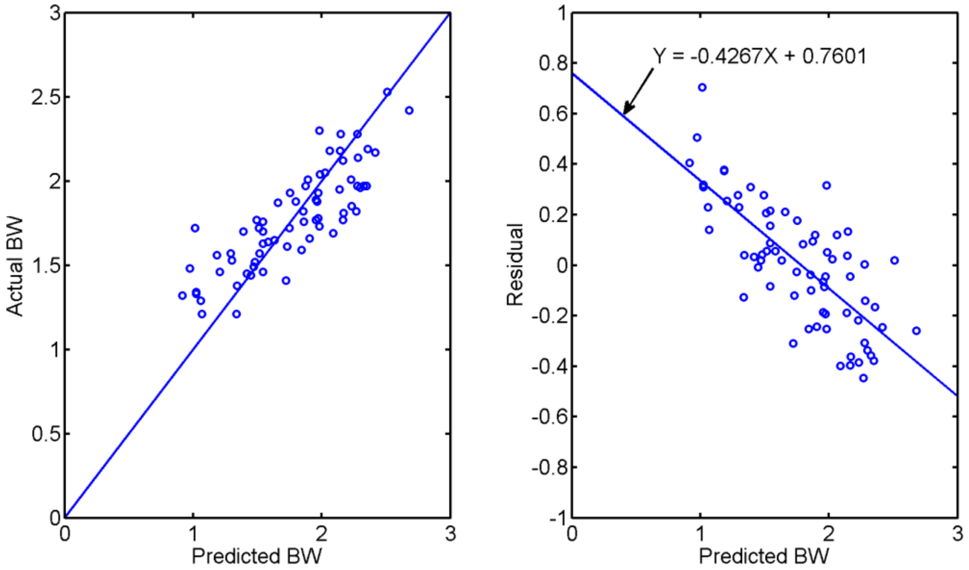

Fig. 8-25: (a) Predicted BW vs. Actual BW (b) residual plot for model development using indirect method before correction procedure

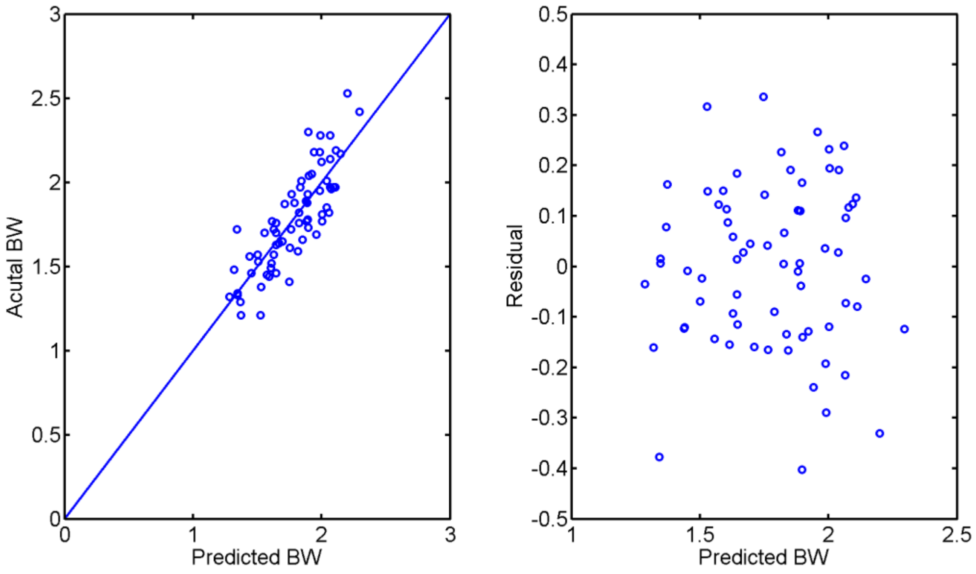

Fig. 8-26: (a) Predicted BW vs. Actual BW (b) residual plot for model development using indirect method after correction procedure

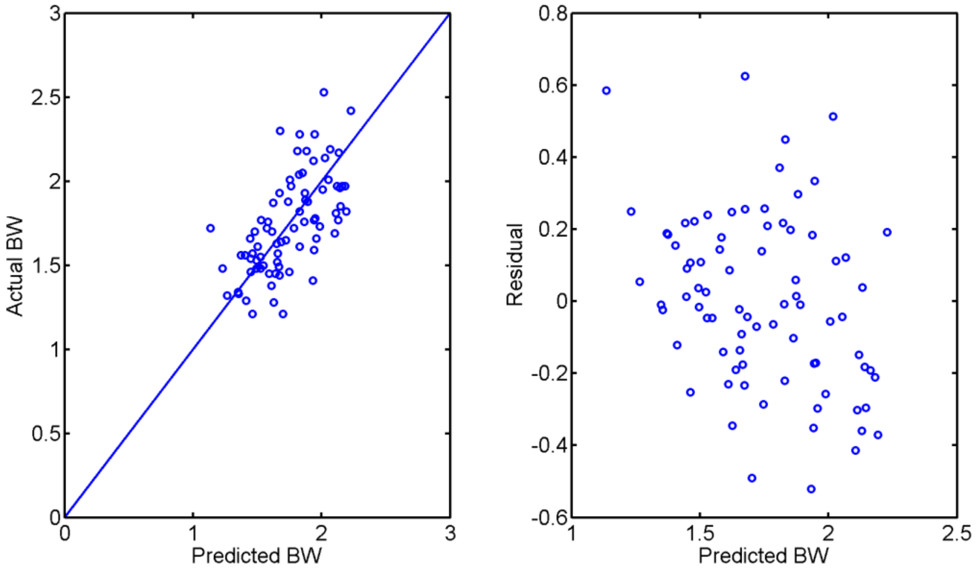

Fig. 8-27: (a) Predicted BW vs. Actual BW (b) residual plot for model validation using indirect method

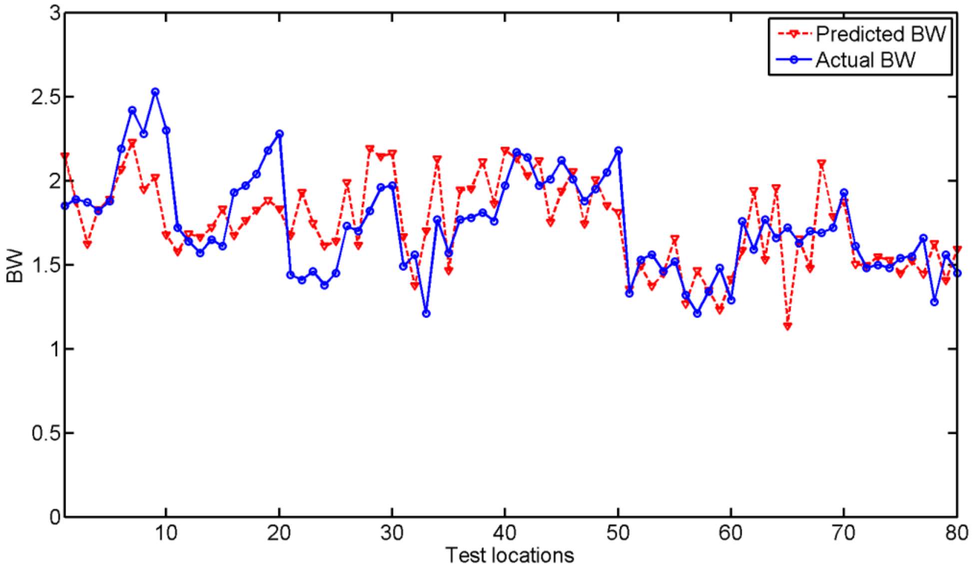

Fig. 8-28: BW vs. Test locations for model validation using indirect method

8.2.5 Reflection Coefficients vs. Weld Dimensions of Butt Welds

In the indirect method, the coefficient matrix K defines the relationship between the weld dimensions and 20 reflection coefficients. In this section, we will study how each reflection coefficient changes with respect to the changes of penetration depth, reinforcement height and bead width.

8.2.5.1 Penetration Depth

In order to know how these reflection coefficients change with PD, the value of PD is set to range from 0.3 to 0.8 in an increment of 0.01 and the values of RH and BW are fixed to be 0.70 and 1.73, which are their median values among all data. The weld dimension matrix in Eq. 8-3 can be obtained for each value of PD. By plugging the K matrix and D matrix into Eq. 8-3, the reflection coefficient matrix R can be calculated for each PD and the relationship between each reflection coefficient with PD can be plotted. The plots between the reflection coefficients of A0 modes and PD are shown in Fig. 8-29: Reflection coefficients of Lamb waves A0 mode vs. PD and the plots between the reflection coefficients of S0 modes and PD are shown in Fig. 8-30. From Fig. 8-29, these reflection coefficients show different characteristics with respect to different PDs. For example, reflection coefficients for A0W4 and A0W5 do not show much sensitivity to the change of PD while A0W8, A0W9 and A0W10 share a lot of similarities and are more sensitive to the change of PD. Likewise, each curve for the reflection coefficients of S0 mode has their own characteristic. From the information that can be obtained from these plots, it is possible to refine our prediction models to increase their accuracy. The indirect method that has been described in this chapter offers a great tool to visualize how the reflection coefficient of a particular wavelength and/or wave mode change with weld dimensions.

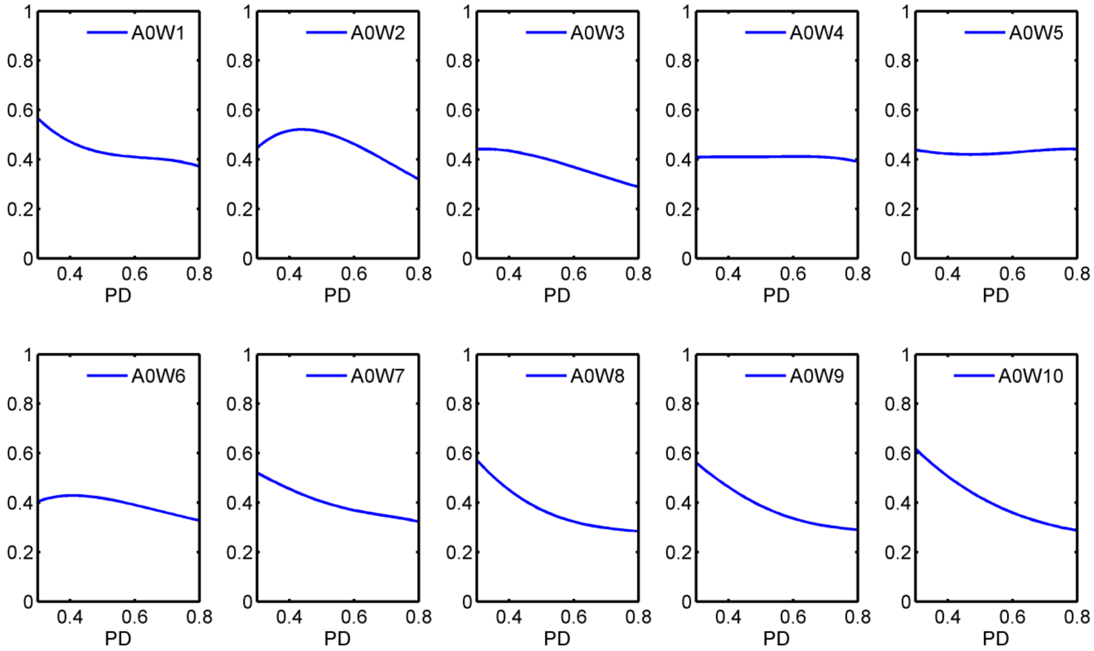

Fig. 8-29: Reflection coefficients of Lamb waves A0 mode vs. PD

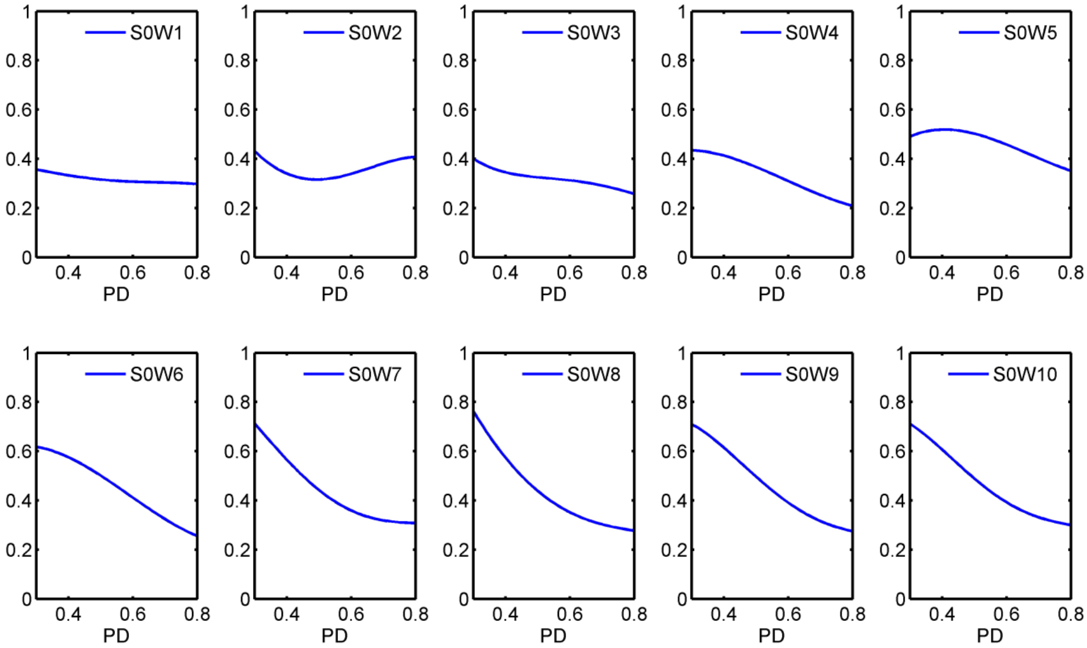

Fig. 8-30: Reflection coefficients of Lamb waves S0 mode vs. PD

8.2.5.2 Reinforcement Height

In the same fashion, the relationship between the reflection coefficients and reinforcement height can be plotted. The plots for A0 modes and S0 modes are plotted in Fig. 8-31 and Fig. 8-32 respectively. In these plots, the value of RH ranges from 0.4 to 0.9 in an increment of 0.01 and the values of PD and BW are fixed to be 0.52 and 1.73, which are their median values among all data. It is interesting that for A0 modes, except for A0W8, A0W9 and A0W10, all the other wavelengths are not very sensitive to the change of RH. For S0 modes, there are more variations in the plots but the waves with larger wavelengths are more sensitive to the change of reinforcement height as well. For most cases in both A0 and S0 modes, as the reinforcement height increases, the reflection coefficients decrease, indicating more waves transmitting through the weld joint.

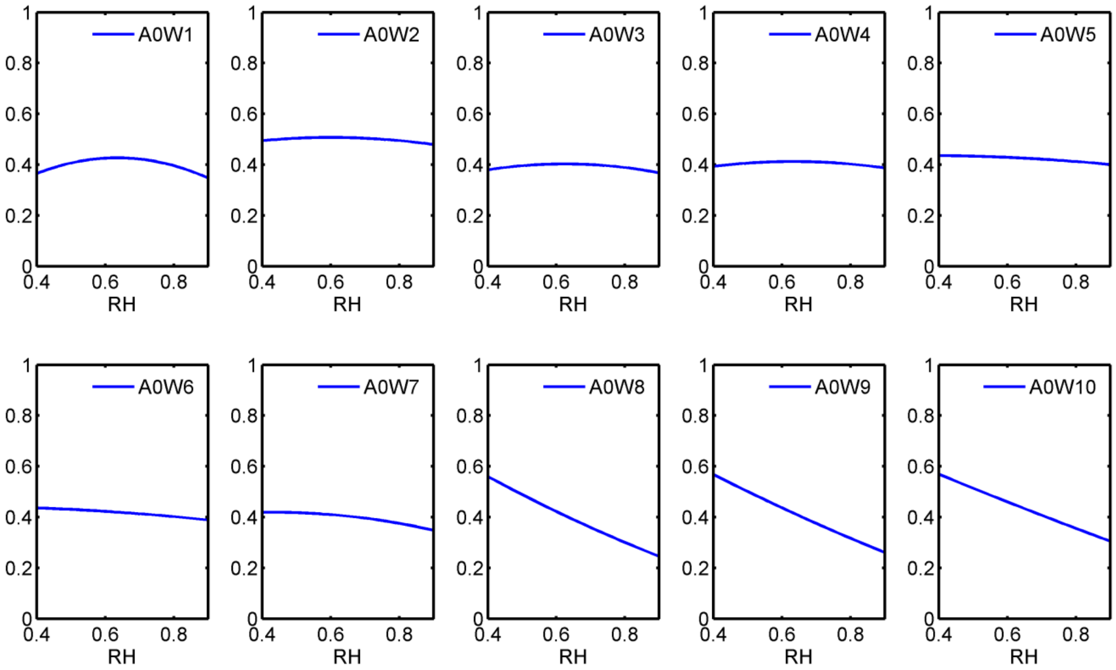

Fig. 8-31: Reflection coefficients of Lamb waves A0 mode vs. RH

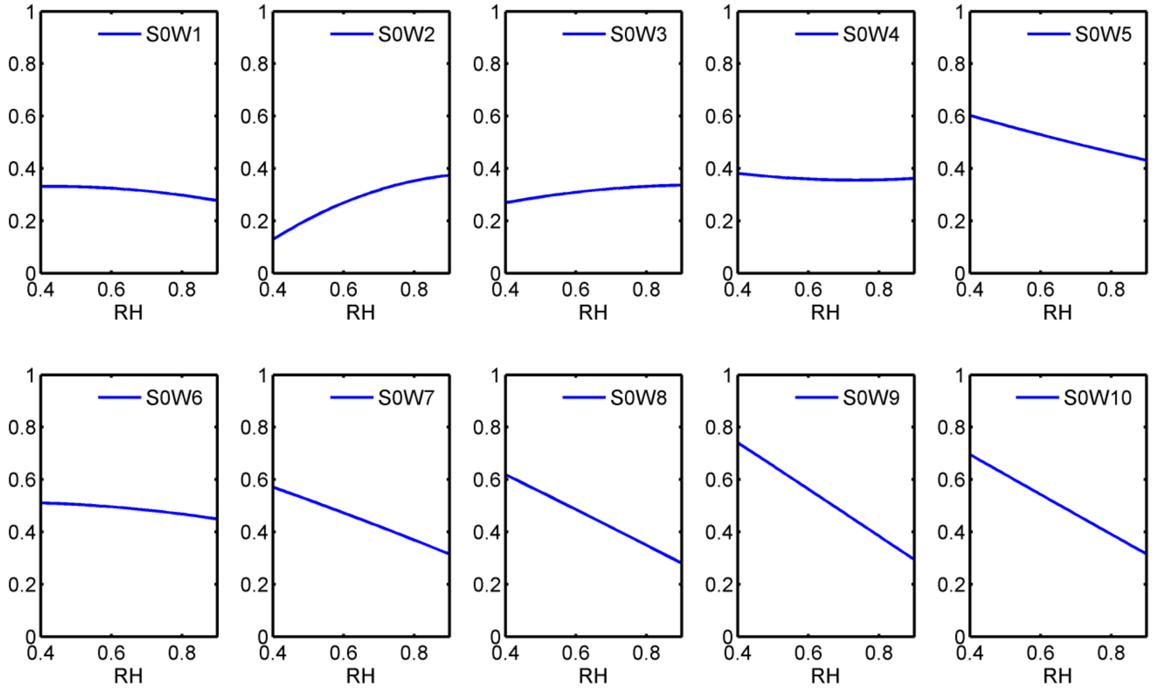

Fig. 8-32: Reflection coefficients of Lamb waves S0 mode vs. RH

8.2.5.3 Bead Width

The relationship between the reflection coefficients and bead width can also be plotted. The plots for A0 modes and S0 modes are shown in Fig. 8-33 and Fig. 8-34 respectively. In these plots, the value of BW ranges from 1.20 to 2.50 in an increment of 0.01 and the values of PD and RH are fixed to be 0.52 and 0.70, which are their median values among all data. Although each reflection coefficient shows different characteristic, the general trend of these reflection coefficients is that as the bead width increases, the reflection coefficients decrease.

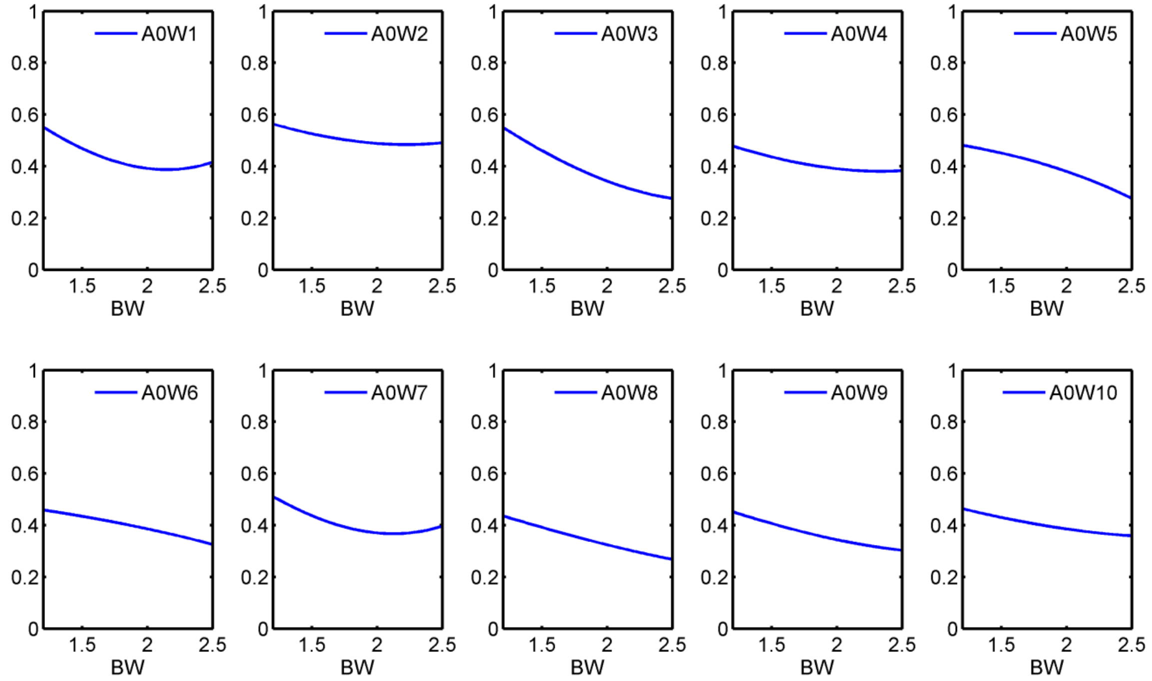

Fig. 8-33: Reflection coefficients of Lamb waves A0 mode vs. BW

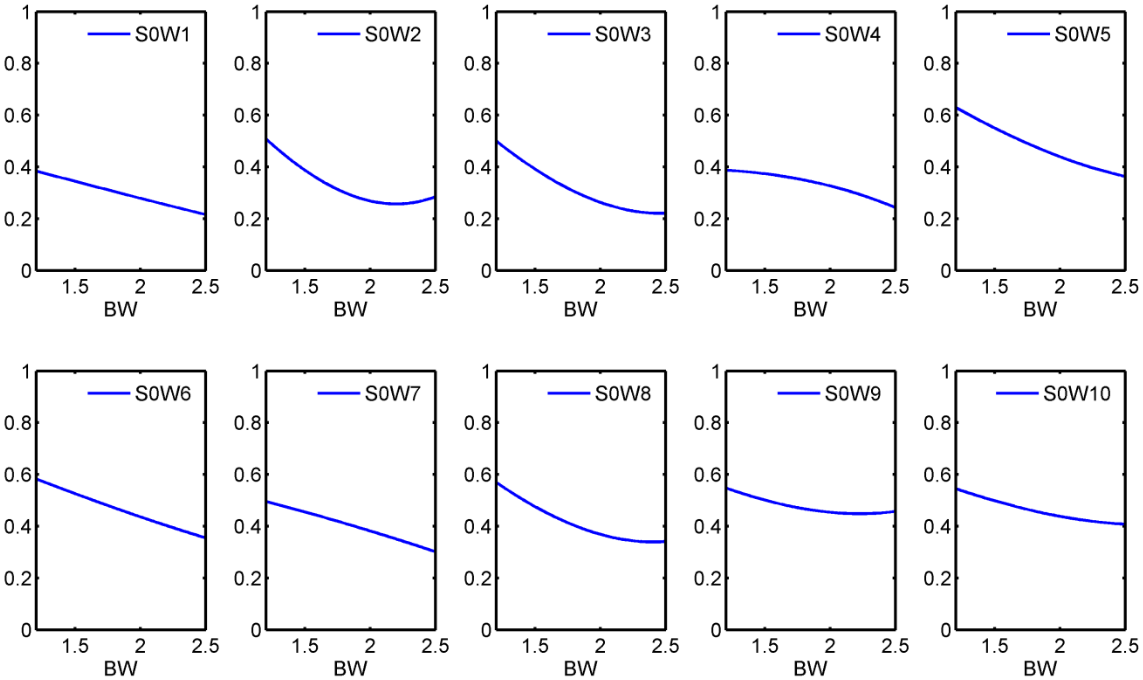

Fig. 8-34: Reflection coefficients of Lamb waves S0 mode vs. BW

8.3 Discussion

Two systematic ways to develop models that relate the reflection coefficients of Lamb wave modes to the weld dimensions in butt welds have been presented. The RMSE values for predicting PD, RH and BW using both methods on both development and validation data are shown in Table 8-11. The accuracy of the direct method is higher than that of the indirect method. In this section, the sources of the modeling errors and the advantages and disadvantages of both methods will be discussed.

Table 8-11: Comparison of RMSEs of models developed by both methods

			Direct Method	Indirect Method
Butt Weld	Penetration Depth (w/o RH and BW)	Development	0.0552	0.0930
		Validation	0.0914	0.1094
	Penetration Depth (with RH and BW)	Development	0.0443	N/A
		Validation	0.0774	N/A
	Reinforcement Height	Development	0.0588	0.0863
		Validation	0.1037	0.1992
	Bead Width	Development	0.1329	0.1606
		Validation	0.2129	0.2439

8.3.1 Sources of Modeling Errors

The sources of modeling errors can come from welding process, inspection, cutcheck, operator error and variations of the laser energy or EMAT gain. The first error source could be from sample preparation. As the sample is being welded, the portion that is first welded shrinks as the weld cools down. The shrinkage would cause the other end of the sample to open up; therefore, on one end of the sample, two metal pieces may be touching, but on the other end, there could be a small gap. This causes reflection coefficients to be inconsistent because when the plates touch, waves may transmit more to the other plate. The second error source could be from material properties mismatch. The raw materials are cold rolled, so the material properties may not be isotropic. Also, when the welding is done, the shrinkage of the weld would cause the sample to warp in the direction of the path of the weld. When the sample is mounted on the inspection stage, since the distance between the cylindrical lens and the surface of the sample is kept constant, bending moment must be exerted on the sample to keep it flat. The stress built in the sample would cause the speeds and frequencies of Lamb waves to deviate from the theoretical prediction, which will cause errors because when using synthetic phase tuning, the shifting of waves is based on their phase theoretical phase velocities. The third source of error comes from the welding process. As indicated in Fig. 7-5 to Fig. 7-7, the weld dimensions have different variations depending on the welding parameters. When the inspection is performed, multiple line sources are used. The measured reflection coefficients are affected by not only one cross section; instead they are affected by an averaging effect over all the cross sections. The fourth source of error source is introduced when the cutcheck locations and inspection locations do not coincide because of the thickness of the saw that cuts samples and/or because of the operator error. Sometimes the offset can be more than 2 mm. This source of error is mitigated by the averaging effect mentioned earlier. The fifth error occurs when the dimensions of the cross section of a weld is measured. Since the measurements are done manually on 1200 dpi scan of cross sections, an operator error can be introduced when measuring weld dimensions. The sixth source of error comes from the variations in laser power and EMAT gain during the measurement process. When the EMAT is used for a long time, the heat generated by the circuit inside the preamplifier could introduce some low frequency noises in the signals.

8.3.2 Discussion on the Direct Method

In the direct method, the weld dimensions are assumed to be functions of the reflection coefficients of Lamb wave modes. The procedures for the model development optimize the number of predictors. Different models have been built for PD, RH and BW. For predicting PD, if RH and BW dimensions are included in the model, the number of the predictors in the model can be reduced and the accuracy of the model can be improved. The advantage of the direct method is that it is intuitive and effective to assume that the weld dimensions are functions of reflection coefficients. From Table 8-11, it shows that the direct method can predict weld dimensions more accurately. It is easy to find enough predictors to fit the model very well, even though overfitting is possible when there are too many predictors and limited number of development data sets. Therefore, validation data are always needed to validate the proposed models. On the other hand, the disadvantage of this method is that it may lack physical meaning to assume that weld dimensions are functions of all reflection coefficients. In the literature, it is more common to express reflection or transmission coefficients as functions of geometry features of the structures.

The models that are developed in this chapter may not be the only ones that can be used to predict weld dimensions for the following reasons: When conducting the

AICc analysis, for each p, or the number of predictors in the model, only the model that gives the lowest AICc value is identified and validated by the validation data. It is possible that there may be another model that does not have the lowest AICc value but can predict the weld dimension of interest equally accurately. Therefore, if time and resources permit, it will be desirable to analyze more models that have the second or third lowest AICc values for the corresponding p, or the number of predictors. If all these models can predict weld dimensions equally well, then another criterion may be introduced to decide which model is the best. For example, a model that uses reflection coefficients of fewer wavelengths is better than the one that uses those of more wavelengths because this will save experimental and signal processing time. Another example is that if S0W9 is a predictor in a model, it does not mean that S0W8, S0W10 or reflection coefficients of other similar wavelengths cannot be used to quantify the weld dimension of interest. It is very possible that S0W8 or S0W10 have relatively similar behavior as S0W9 does so that once S0W9 is included in the model, the addition of S0W8 or S0W10 will not improve the model much. The same explanation applies to all other reflection coefficients. Therefore there could be more than one model with accurate prediction power.

8.3.3 Discussion on the Indirect Method

In the indirect method, instead of assuming that the weld dimensions are functions of the reflection coefficients of Lamb wave modes, it is assumed that the reflection coefficients are functions of the weld dimensions. The predictor selection procedures determine the predictors that are used in the regression analysis. A system of equations can be derived from the regression analysis to relate weld dimensions to all the reflection coefficients and can be represented in the matrix form. For the prediction purposes, one would measure reflection coefficients and solve the system of equations to predict the weld dimensions. The indirect method has many advantages. It has more physical meaning. It conforms to the practices that are usually found in the literature in which reflection coefficients are usually expressed as functions of dimensions of a structure. In addition, the indirect method can predict PD, RH and BW at the same time using the same system of equations. Unlike the direct method, three separate models need to be developed for PD, RH and BW. One particular advantage over the direct method is shown in Chapter 8.2.5. It is possible to study how a particular reflection coefficient responds to the change of a weld dimension. This provides us the information about the sensitivity of each reflection coefficient to the weld dimensions. This information can be used to design better models for both the direct and indirect methods. We can only use the reflection coefficients that are sensitive to the change of weld dimensions to build new models. One of the disadvantages of the indirect method is that the accuracy is slightly worse than the direct method because when solving for the weld dimension matrix, we need to calculate the inverse of the coefficient matrix as in Eq. 8-5. On top of all the sources of errors, additional errors can come from this matrix inversion operation. Another disadvantage of this method is that in order to have a solution, it is required that the number of equations must be greater than the number of variables. Since twenty reflection coefficients are used to build twenty regression models, the maximal number of variables we can have is twenty. Therefore, if the relationship between regression coefficients and weld dimensions are so complicated that it needs more than 20 terms for the regression model, more reflection coefficients need to be included into the analysis or this method cannot work. To include more reflection coefficients, we can either calculate reflection coefficients for more wavelengths or more wave modes such as A1 or S1 modes.

CHAPTER 9

PREDICTION AND EXPEIMENTAL VALIDATION OF DIMENSIONS OF LAP WELDS IN THIN PLATES

In this chapter, the same method and procedure as described in the earlier chapters will be used to measure dimensions of lap welds in thin plates using laser generated ultrasound. To refresh the memory, the schematic of cross section of a lap weld is shown in Fig. 9-1. The important dimensions of a lap weld are shown in the figure. The important dimensions of a lap weld are leg lengths, throat thickness, and penetration depth. The legs of a lap weld are shown as S1 and S2 in Fig. 9-1. They are defined as the projected lengths of the interfaces between the weld bead and the base materials on the material edges. The throat thickness is shown as TH in Fig. 9-1. To measure the TH, a line is drawn from the root of the joint to the surface of the weld bead in a 45 degree angle with respect to the edge of the base materials. The length of the line represents the TH of the weld. The penetration depth is defined as the depth at which the fusion portion extends into the base material.

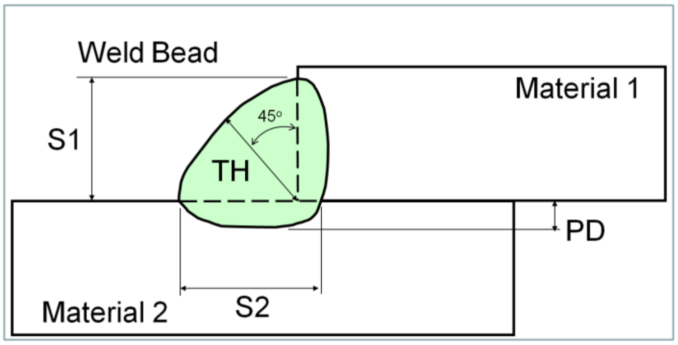

Fig. 9-1: Schematic of the cross section of a lap joint

9.1 Experimental Methods

9.1.1 Experimental Procedure

The experimental procedures, model development and validation can be described in the following steps: 1. Prepare samples. 2. Inspect these samples using the SLS technique. 3. Perform cutcheck inspections on the samples and measure dimensions of the weld joints. 4. Follow the signal processing procedure and calculate the reflection coefficients of Lamb wave modes A0 and S0 for different wavelengths. 5. Develop regression models that correlate the reflection coefficients to weld dimensions with data from one set of samples. 6. Use reflection coefficients from the other set of samples to predict weld dimensions using the regression models. These predicted weld dimensions are validated with cutcheck results. From the validated prediction results, the best prediction model can be chosen.

9.1.2 Sample Preparation

The samples used in this research are made by lap welding two pieces of steel plates together. The plate measures 254 x 130 x 2.5 mm. The overlapped portion measures 10 mm wide. The weld seam is 228.6 mm long. During welding, the torch is fixed and pointed to the root of the lap joint with a 45 degree angle as depicted in Fig. 3-2(a). The samples are moved by a linear stage with a programmable speed. The samples are prepared by varying two welding parameters which are welding speed and WFR. A two-factor three-level full factorial design is implemented. There are nine runs. The levels are shown in Table 9-1 and the design matrix is shown in Table 9-2. The CTWD and Arc voltage are held constant as 0.625 inch and 18V respectively. The CTWD is measured from the root of the lap joint to the contact tip.

Table 9-1: Welding parameters for lap weld samples

Factor	-	0	+
A. CTWD (inch)	0.625		
B. Welding speed (in/min)	15	20	25
C. Arc voltage (Volt)	18		
D. Wire feed rate (in/min)	160	180	200

Table 9-2: Design matrix for lap weld samples

Run	Welding speed	WFR
1	-	-
2	-	0
3	-	+
4	0	-
5	0	0
6	0	+
7	+	-
8	+	0
9	+	+

9.1.3 Experimental Setup

The experimental setup is the same as the one used to measure weld dimensions in butt welds. For more information, please see Chapter 7.1.3 for more details.

9.1.4 Nondestructive testing using the SLS technique

Totally nine samples are made, and for each sample, 14 locations along the weld seam are inspected, giving a total number of 126 test locations. During the inspection of a particular location, the laser beam is fixed while the samples and the EMAT are moved by the linear stage at 0.25 mm increments. At each laser incident location, 32 signals are acquired and averaged to increase signal-to-noise ratio. A total number of 140 averaged signals are stored for each test location.

9.1.5 Cutcheck Inspection

After the samples are inspected nondestructively, cutchecks are performed to measure the dimensions of the welds. The details of the cutcheck procedure have been described in Chapter 7.1.5. The cross sections of some lap welds are shown in Fig. 9-2. There are 126 cutcheck locations (14 locations on each of the 9 samples). The box plot for S1, S2, TH, and PD versus test location number is shown in Fig. 9-3. The values of weld dimensions in this paper are all normalized with the plate thickness. For the welding parameters that have been used to produce the lap welds, they do not have large effects on the leg length 1 (S1). Most of the values fall between 0.9 and 1. The main effects plots for S1, S2, TH, and PD, and their standard deviations are shown in Fig. 9-4 to Fig. 9-7 in which the solid line plots represent weld dimensions and the dashed plots represent their standard deviations. From the main effects plots for S1, as expected, S1 does not change a lot with respect to either welding speed or WFR in our experiments. For S2, to increase S2, welding speed should be small while WFR should be large. But there is not a clear trend for the variation of S2. For TH, welding speed should decrease to increase TH but WFR does not have large effects on TH. Again, there is not a clear trend for the variation of TH. To increase PD, welding speed should be minimized while WFR should be increased. As for the variation of PD, to our surprise, the variation of PD increases as welding speed decreases. On the other hand, WFR does not have large effects on the variation of PD. According to the discussion in Chapter 7.6, these erratic trends of the variation of the weld dimensions are likely due to the error associated with the welder itself.

Fig. 9-2: cutcheck cross sections of lap welds

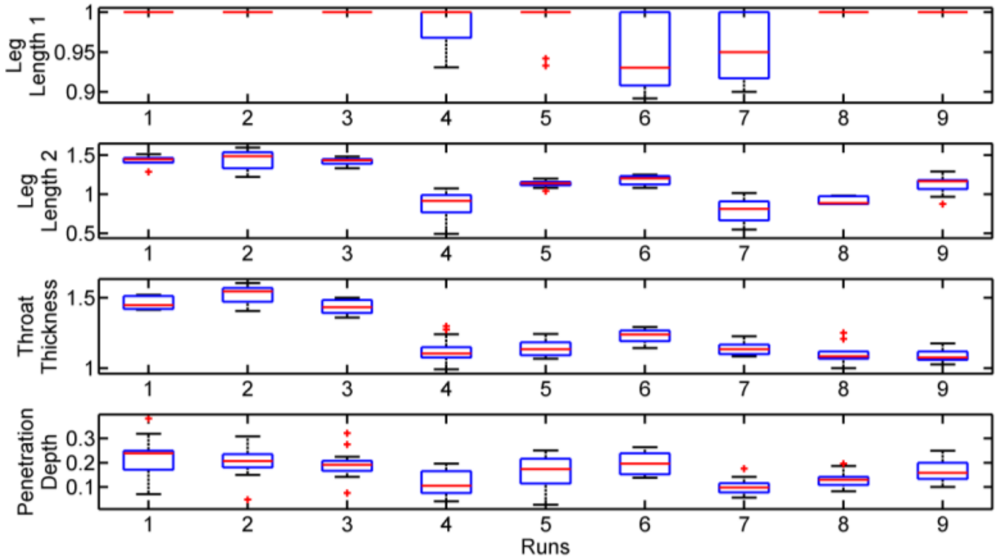

Fig. 9-3: Box plots of S1, S2, TH and PD of lap welds

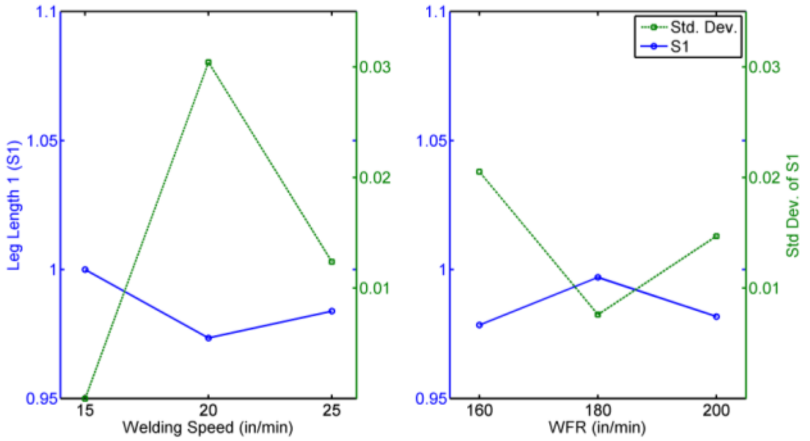

Fig. 9-4: Main effects plots of S1 and its standard deviation

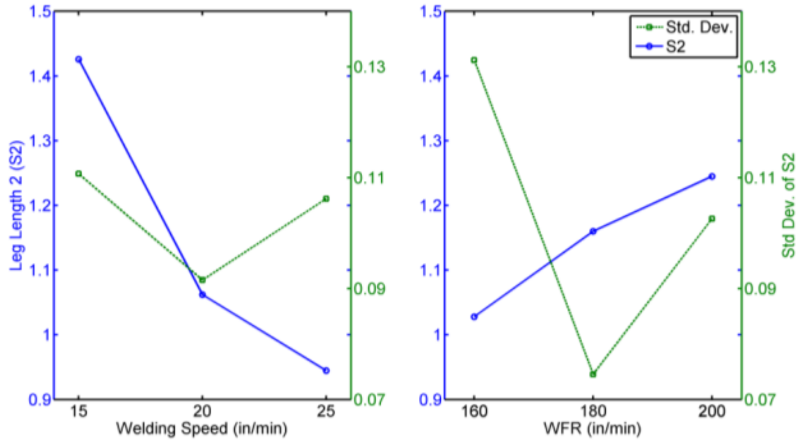

Fig. 9-5: Main effects plots of S2 and its standard deviation

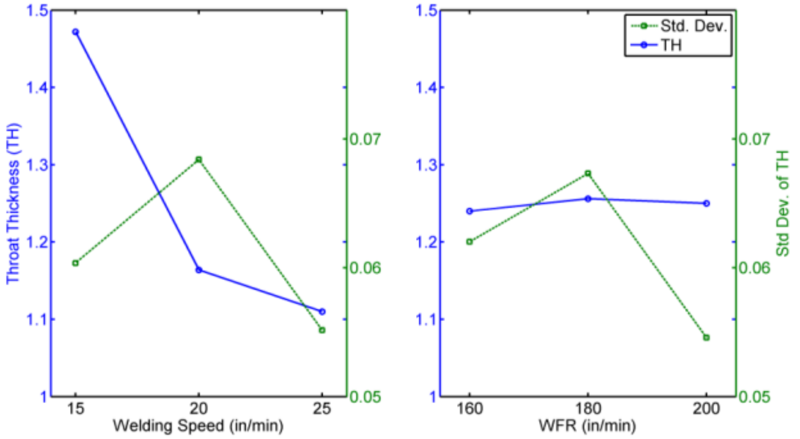

Fig. 9-6: Main effects plots of TH and its standard deviation

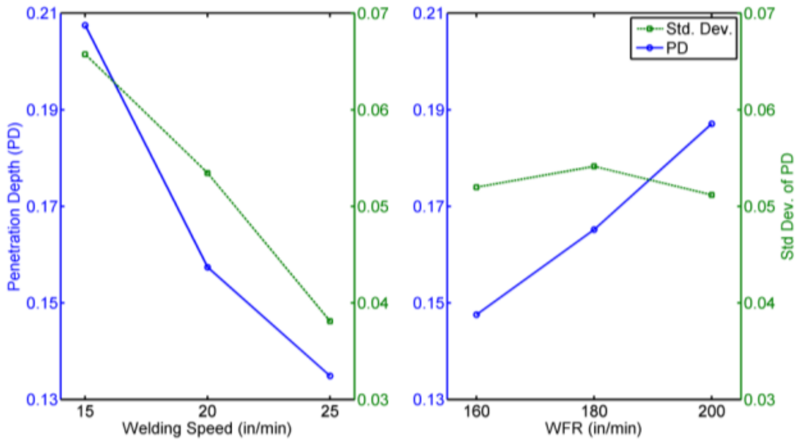

Fig. 9-7: Main effects plots of PD and its standard deviation

9.1.6 Signal Processing

The signal processing procedure is the same as the one used to measure weld dimensions in butt welds. The SLS technique is used to produce narrowband ultrasound. Every seven signals are superimposed to form the desired wavelengths. Ten wavelengths from 1.75 to 4 mm at the step of 0.25 mm are generated. The k-ω domain filtering is used to filter out unwanted waves in the signals and the synthetic phase tuning technique is then used to isolate a particular Lamb wave mode. Finally, the reflection coefficients for both Lamb wave modes for each wavelength that is of interest can be calculated. For each test location, 20 reflection coefficients can be calculated for ten wavelengths and two Lamb wave modes.

9.2 Analysis, Model Development and Validation

There are 14 test locations on each of the nine samples. One hundred and twenty six sets of data are available for model development and validation. Here, the first nine sets of data on each sample are used as model development data and the last five sets of data are used as model validation data. Hence, we have 81 and 45 sets of data for model development and validation respectively. The same model development procedure is used here again. Both the direct method and indirect method are used to build prediction models for throat thickness, leg length 2, and penetration depth. The prediction model for leg length 1 cannot be built because among the samples that have been made, most of the samples have this dimension very close to one. There are simply not enough data points for model development.

9.2.1 The Direct Method

The detailed description of the direct method can be found in Section 8.1. The stepwise regression is first used to find a model that includes more than necessary predictors. Different models that are developed using the combinations of these predictors are then analyzed using AICc criterion and validated by the validation data. After validation, the best model that gives the smallest error can be selected.

9.2.1.1 Throat Thickness

For throat thickness (TH), the p-value for the stepwise regression is chosen to be 0.2. The 21 terms selected and their indices are shown in the first two columns in Table 9-3. Most of the selected terms are interaction terms. The AICc values are calculated for all the possible models that can be constructed using these 21 terms. The model that gives the lowest AICc values for each corresponding number of predictors, p, is also identified. These models that give lowest AICc values are also shown in Table 9-3. The third column in Table 9-3 denotes the number of predictors included in the model, p. The fourth column shows the terms selected in the model that gives the lowest AICc values for the corresponding p. The fifth column shows the AICc values. The sixth column shows the root mean square errors (RMSE) when these models are validated by the validation data. The AICc and RMSE values with respect to p are shown in Fig. 9-8. The AICc decreases gradually and reaches the minimum value, -455.498, when p = 19. The RMSE suddenly drops when p is greater than 14 and it reaches the minimum value, 0.0928, when p = 17. Although the lowest values for AICc and RMSE do not happen with the same number of predictors, the AICc analysis does provide valuable information regarding the best size of the model. The best model for predicting the throat thickness of a lap weld is determined after validation, which is the model with p = 17. The coefficients and their standard error of the model are shown in Table 9-4. The relationship between actual TH and predicted TH from model development data is shown in Fig. 9-9(a). The residual plot is shown in Fig. 9-9(b). Most of the errors are within ±0.2. Fig. 9-10(a) shows the relationship between actual TH and predicted TH of the data used for model validation and Fig. 9-10(b) shows actual and predicted TH versus test locations of the validation data. The RMSE values calculated for the development data and validation data are 0.0879 and 0.0928 respectively. For reference, among two data sets, the maximum and minimum of the TH are 1.603 and 0.992, respectively. The range of the TH is 0.611.

Table 9-3: Summary of model development using AICc and validation using RMSE for TH

Index	Term	P	Indices of terms in model	AICc	RMSE
1	A0W1*A0W7	1	7	-167.024	0.2901
2	A0W1*A0W9	2	3,12	-280.615	0.2871
3	A0W1*S0W6	3	3,7,12	-354.129	0.2598
4	A0W2*S0W1	4	2,3,7,20	-366.988	0.2448
5	A0W3*A0W10	5	2,3,7,12,20	-391.843	0.2199
6	A0W4*S0W10	6	2,3,5,7,12,20	-397.007	0.2238
7	A0W5*S0W1	7	2,3,6,7,8,13,20	-409.191	0.2011
8	A0W5*S0W4	8	2,3,6,7,8,13,15,20	-414.977	0.1924
9	A0W5*S0W10	9	2,3,5,6,7,8,13,15,20	-422.598	0.1888
10	A0W6*A0W7	10	2,3,5,7,8,11,13,15,18,20	-428.003	0.2642
11	A0W6*S0W5	11	2,3,5,6,7,8,11,13,15,16,20	-434.81	0.2318
12	A0W9*S0W5	12	2,3,5,6,7,8,11,13,15,16,17,20	-435.785	0.2056
13	A0W10*S0W6	13	2,3,5,6,7,8,11,13,14,15,16,17,20	-438.997	0.2160
14	A0W10*S0W7	14	2,3,5,7,8,9,12,13,14,15,16,17,20,21	-441.015	0.2782
15	S0W2*S0W9	15	1,2,3,6,7,8,9,12,14,15,16,17,19,20,21	-446.635	0.1013
16	S0W4*S0W8	16	1,2,3,5,6,7,8,9,12,13,14,15,16,17,20,21	-449.815	0.0955
17	S0W6*S0W10	17	1,2,3, 5,6,7,8,9,10,12,13,14,15,16,17,20,21	-454.764	0.0928
18	S0W8*S0W10	18	1,2,3,4,5,6,7,8,9,10,12,13,14,15,16,17,20,21	-455.151	0.0937
19	A0W1^3	19	1,2,3,4,5,6,7,8,9,10,11,12,13,14,15,16,17,20,21	-455.498	0.0959
20	S0W5^2	20	1,2,3,4,5,6,7,8,9,10,11,12,13,14,15,16,17,18,20,21	-451.904	0.0958
21	S0W7^3	21	ALL	-448.094	0.0956

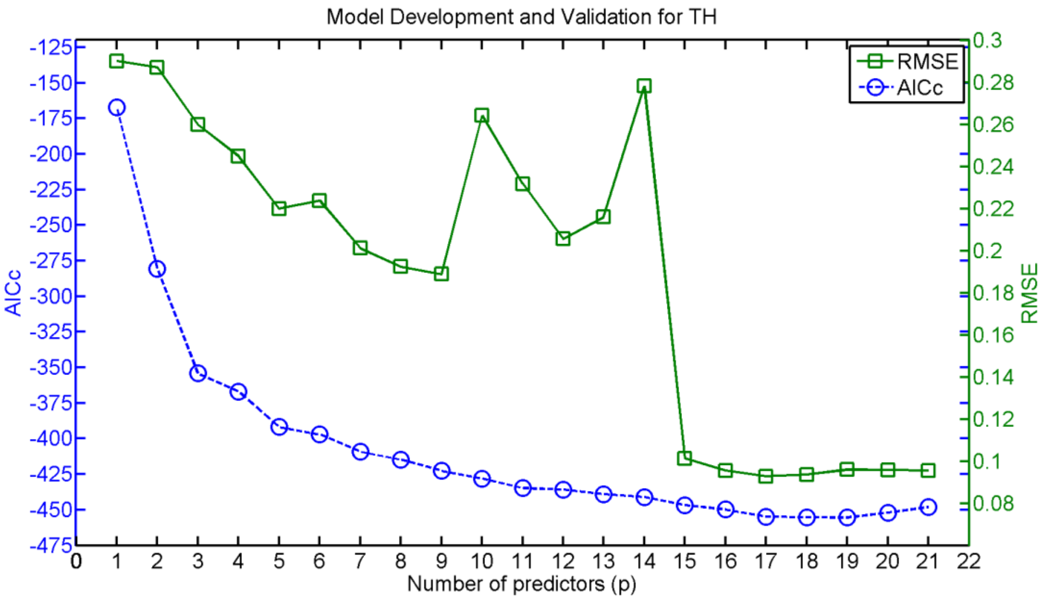

Fig. 9-8: AICc and RMSE vs. p for model development and validation for TH

Table 9-4: Coefficients of the prediction model for TH

Term	Estimate
Intercept	1.0492
A0W1*A0W7	-1.5589
A0W1*A0W9	3.9019
A0W1*S0W6	-5.4813
A0W3*A0W10	-0.6920
A0W4*S0W10	-1.7619
A0W5*S0W1	-1.1377
A0W5*S0W4	2.1284
A0W5*S0W10	-2.2457
A0W6*A0W7	0.6790
A0W9*S0W5	-4.2128
A0W10*S0W6	2.5014
A0W10*S0W7	3.5159
S0W2*S0W9	1.0280
S0W4*S0W8	-1.7866
S0W6*S0W10	6.8006
S0W5^2	5.0654
S0W7^3	-11.6965

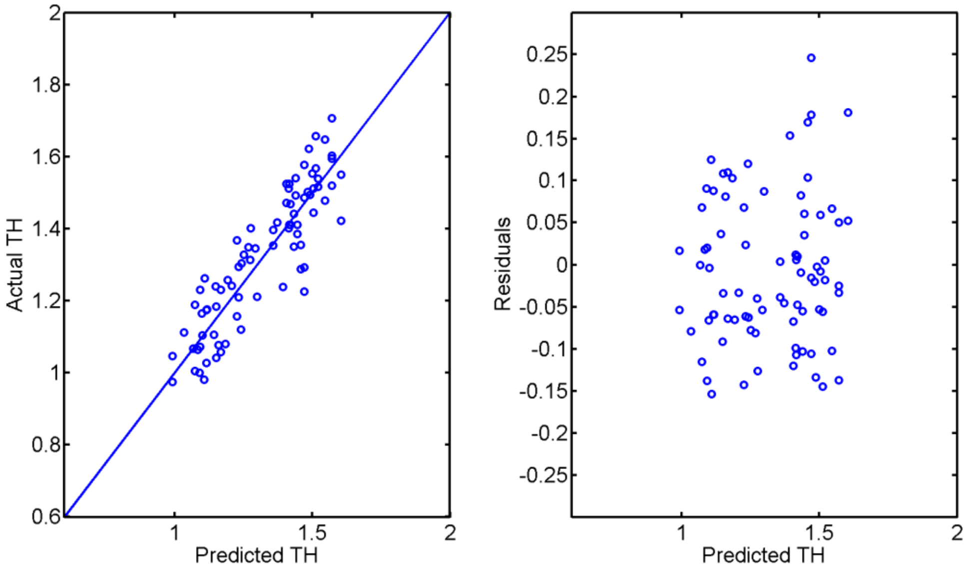

Fig. 9-9: (a) Predicted TH vs. Actual TH (b) residual plot for model development using direct method

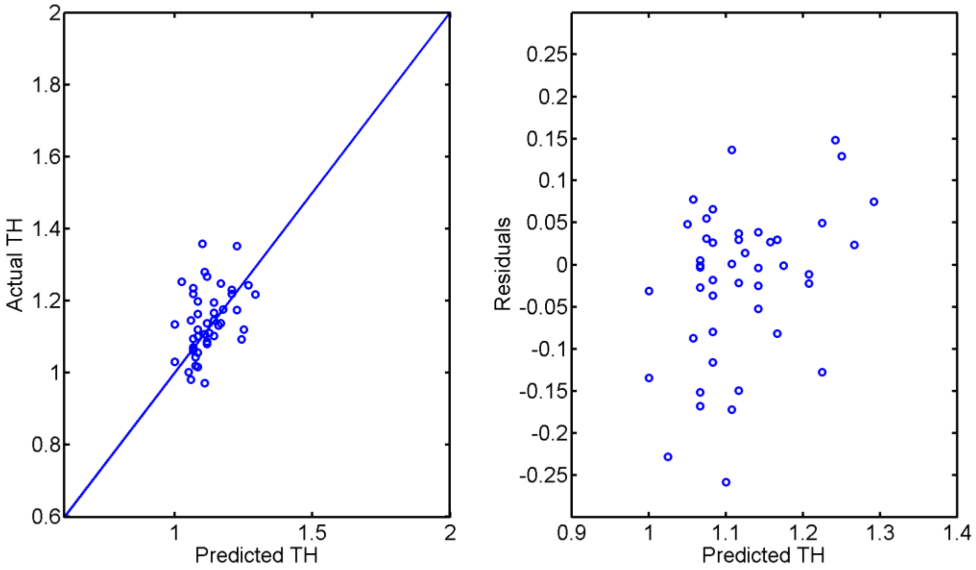

Fig. 9-10: (a) Predicted TH vs. Actual TH (b) residual plot for model validation using direct method

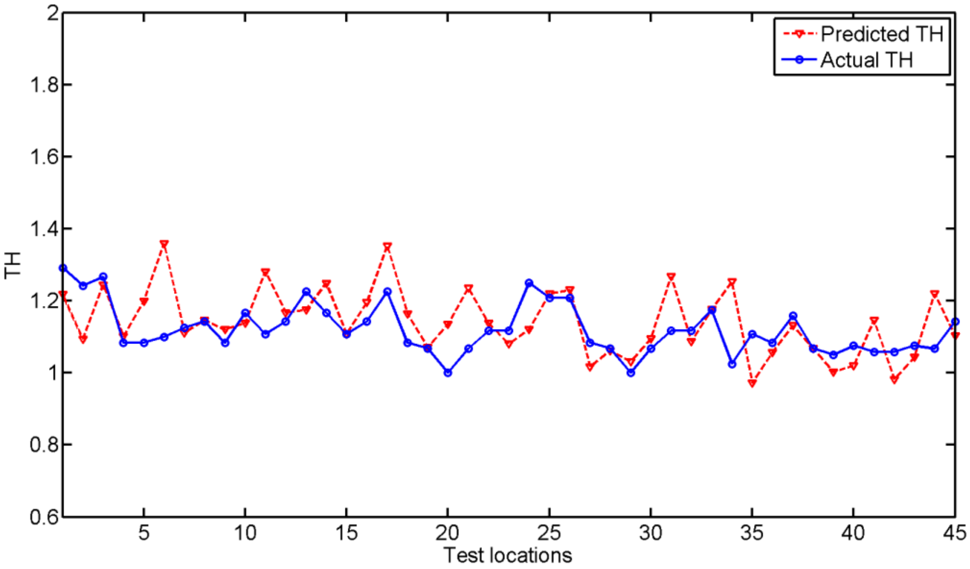

Fig. 9- 11: TH vs. Test locations for model validation using direct method

9.2.1.2 Leg Length 2

The model development and validation procedures for leg length 2 (S2) is the same. The p-value for the stepwise regression is chosen to be 0.2. The 22 terms selected and their indices are shown in the first two columns in Table 9-5. The AICc and RMSE values for model development and validation are shown in Table 9-5 and Fig. 9-12. The AICc decreases gradually and reaches the minimum value, -365.296 when p = 21. The RMSE decreases with fluctuations and reaches the minimum value, 0.1465 when p = 18. The best model for predicting the leg length 2 of a lap weld is determined, which is the model when p = 18. The coefficients and their standard error of the model are shown in Table 9-6. The relationship between actual S2 and predicted S2 from model development data is shown in Fig. 9-13(a) and the residual plot is shown in Fig. 9-13(b). No systematic errors can be observed and most of the errors are within ±0.3. Fig. 9-

14(a) shows the relationship between actual TH and predicted TH from model validation data and Fig. 9-14(b) shows actual and predicted S2 versus test locations of the validation data. The RMSE values calculated for the development data and validation data are 0.1417 and 0.1465 respectively. For reference, among two data sets, the maximum and minimum of the S2 are 1.595 and 0.496, respectively. The range of the S2 is 1.099.

Table 9-5: Summary of model development using AICc and validation using RMSE for S2

Index	Term	P	Indices of terms in model	AICc	RMSE
1	S0W6	1	3	-112.968	0.3001
2	A0W1*A0W10	2	3,14	-162.766	0.2767
3	A0W1*S0W1	3	14,18,21	-219.154	0.2732
4	A0W2*A0W4	4	13,16,18,21	-242.388	0.2678
5	A0W2*S0W7	5	3,6,13,18,21	-256.785	0.2612
6	A0W3*S0W9	6	2,7,12,13,15,18	-269.435	0.2507
7	A0W4*S0W10	7	2,3,8,12,15,16,18	-284.552	0.2444
8	A0W8*A0W10	8	2,3,8,12,14,15,19,22	-297.828	0.2312
9	A0W8*S0W7	9	1,2,3,8,12,14,15,19,22	-303.490	0.2224
10	A0W9*S0W3	10	1,2,3,5,8,12,14,15,18,22	-310.226	0.1953
11	A0W9*S0W10	11	1,2,3,5,8,9,12,14,1518,22	-321.332	0.1818
12	A0W10*S0W10	12	1,2,3,5,8,9,12,13,14,15,18,22	-328.224	0.1680
13	S0W1*S0W5	13	2,3,4,5,7,8,9,12,15,17,18,19,22	-333.53	0.1750
14	S0W1*S0W6	14	1,2,3,4,5,6,8,9,12,14,15,16,18,22	-348.902	0.1602
15	S0W5*S0W10	15	1,2,3,4,5,6,8,9,12,14,15,16,18,19,22	-350.934	0.1714
16	S0W6*S0W9	16	1,2,3,4,5,6,8,9,12,13,14,15,16,18,21,22	-353.817	0.1481
17	S0W6*S0W10	17	1,2,3,4,5,7,8,9,12,13,14,1718,19,20,21,22	-361.293	0.1481
18	A0W1^3	18	1,2,3,4,5,7,8,9,10,11,12,13,14,17,18,19,21,22	-363.795	0.1465
19	S0W1^3	19	1,2,3,4,5,7,8,9,10,11,12,13,14,15,17,18,19,21,22	-363.073	0.1528
20	S0W3^3	20	1,2,3,4,5,6,8,9,10,11,12,13,14,16,17,18,19,20,21,22	-365.178	0.1566
21	S0W5^3	21	1,2,3,4,5,6,7,8,9,10,11,12,13,14,16,17,18,19,20,21,22	-365.296	0.1497
22	S0W6^3	22	ALL	-363.586	0.1564

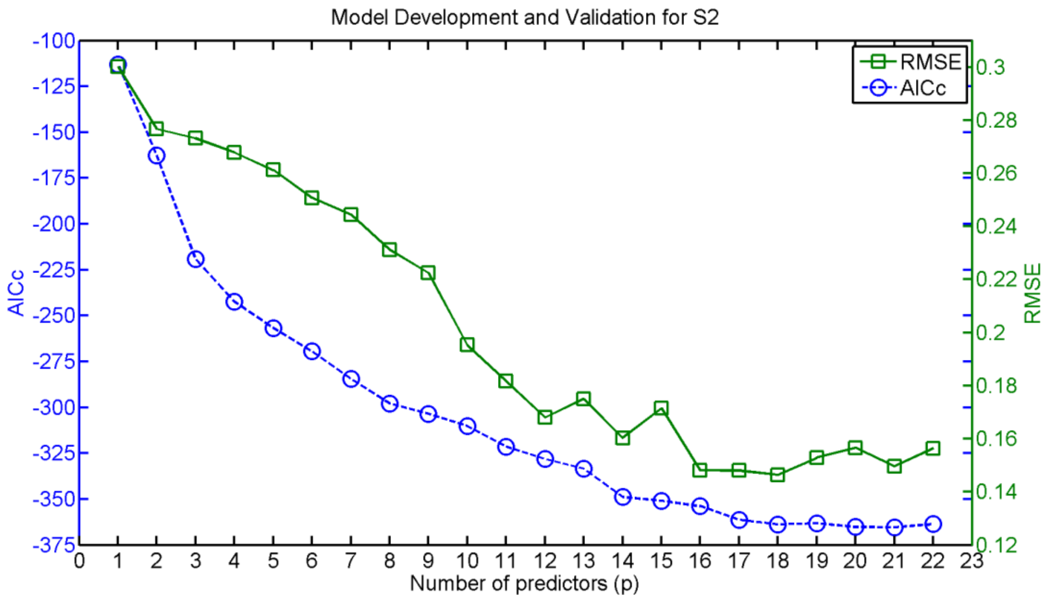

Fig. 9-12: AICc and RMSE vs. p for model development and validation for S2

Table 9-6: Coefficients of the prediction model for S2

Term	Estimate
Intercept	3.2896
S0W6	-6.8793
A0W1*A0W10	10.4874
A0W1*S0W1	-8.5769
A0W2*A0W4	1.6672
A0W2*S0W7	-8.8480
A0W4*S0W10	-4.6204
A0W8*A0W10	-5.4577
A0W8*S0W7	8.7505
A0W9*S0W3	-1.8124
A0W9*S0W10	4.6925
A0W10*S0W10	-10.2872
S0W1*S0W5	-8.8933
S0W1*S0W6	13.8770
S0W6*S0W10	17.5072
A0W1^3	-1.8880
S0W1^3	3.7379
S0W5^3	16.7547
S0W6^3	-16.0008

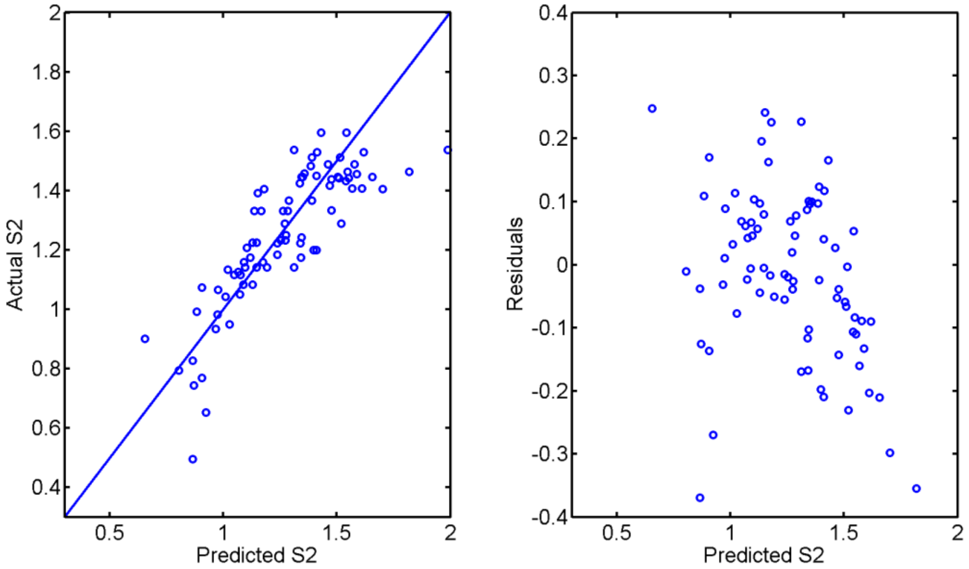

Fig. 9-13: (a) Predicted S2 vs. Actual S2 (b) residual plot for model development using direct method

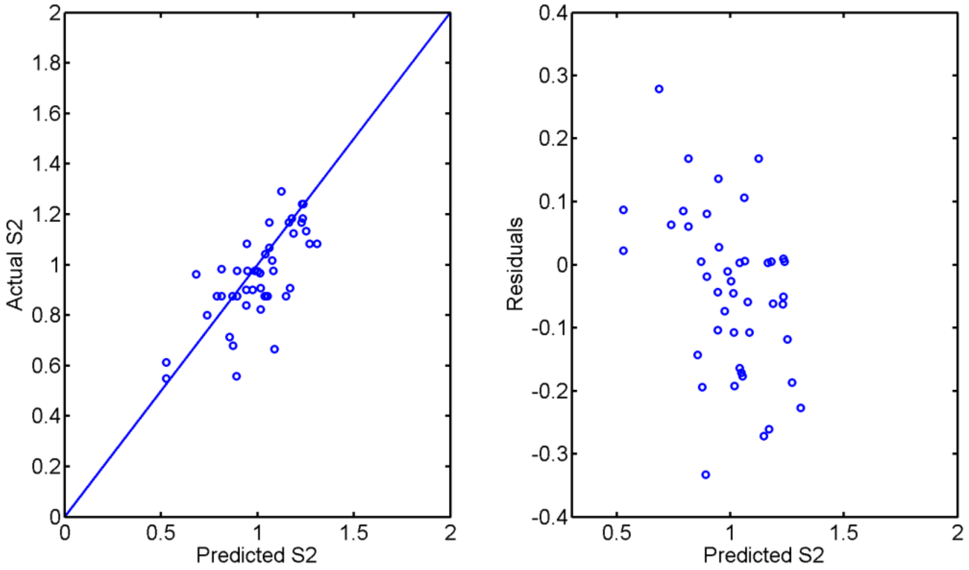

Fig. 9-14: (a) Predicted S2 vs. Actual S2 (b) residual plot for model validation using direct method

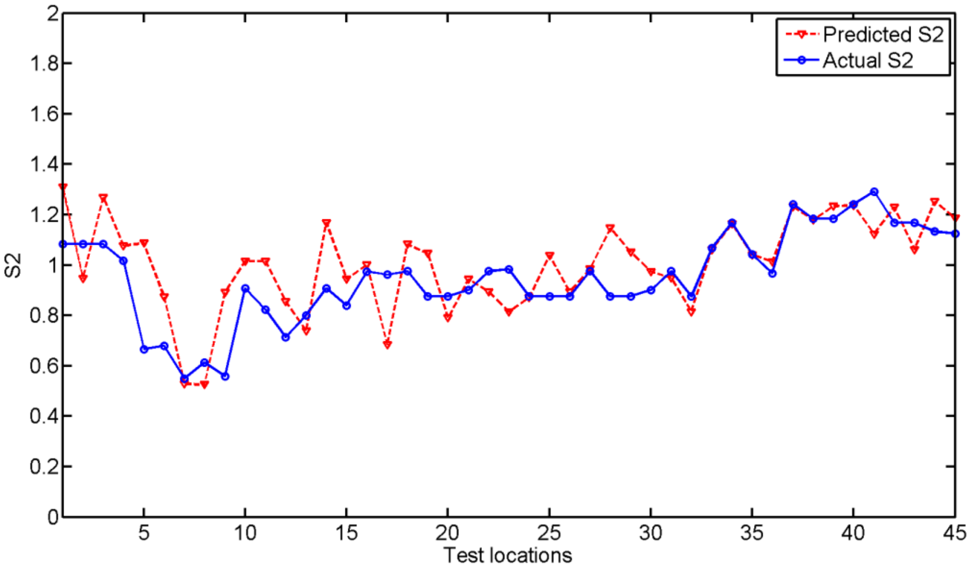

Fig. 9- 15: S2 vs. Test locations for model validation using direct method

9.2.1.3 Penetration Depth

Follow the same fashion, the model for penetration depth (PD) can be developed. The p-value for the stepwise regression is chosen to be 0.15. The 21 terms selected and their indices are shown in the first two columns in Table 9-7. The AICc and RMSE values for model development and validation are shown in Table 9-7 and Fig. 9-16. The AICc decreases gradually and reaches the minimum value, -426.277 when p = 20. The RMSE reaches the minimum value, 0.0473 when p = 16. The best model for predicting the penetration depth of a lap weld is determined, which is the model when p = 16. The coefficients and their standard error of the model are shown in Table 8-9. The relationship between actual PD and predicted PD from model development data is shown in Fig. 9-17(a) and the residual plot is shown in Fig. 9-17(b). Most of the errors are within ±0.1. Fig. 9-18(a) shows the relationship between actual PD and predicted PD from model validation data and Fig. 9-18(b) shows actual and predicted PD versus test locations of the validation data. The RMSE values calculated for the development data and validation data are 0.0524 and 0.0473 respectively. For reference, among two data sets, the maximum and minimum of the PD are 0.3815 and 0.0276, respectively. The range of the PD is 0.3539.

Table 9-7: Summary of model development using AICc and validation using RMSE for PD

Index	Term	P	Indices of terms in model	AICc	RMSE
1	A0W7	1	11	-273.561	0.0612
2	S0W2	2	15,16	-282.213	0.0590
3	A0W1*A0W6	3	8,10,21	-295.315	0.0588
4	A0W3*A0W10	4	2,13,14,19	-312.617	0.0572
5	A0W4*S0W4	5	2,10,14,19,21	-319.700	0.0567
6	A0W4*S0W10	6	2,7,10,14,19,21	-331.965	0.0539
7	A0W5*S0W3	7	1,2,8,9,13,20,21	-344.160	0.0523
8	A0W6*A0W9	8	2,8,9,13,14,19,20,21	-357.574	0.0519
9	A0W6*S0W2	9	2,8,9,12,13,14,19,20,21	-365.647	0.0511
10	A0W6*S0W10	10	2,8,9,10,12,13,14,16,17,19	-379.297	0.0521
11	A0W7*S0W1	11	2,8,9,10,12,13,14,16,17,18,19	-385.271	0.0514
12	A0W8*S0W1	12	2,8,9,10,12,13,14,16,17, 19,20,21	-396.146	0.0501
13	A0W9*S0W10	13	2,8,9,10,12,13,14,16,17, 18,19,20,21	-402.787	0.0504
14	S0W1*S0W2	14	1,2,8,9,10,12,13,14,16,17, 18,19,20,21	-408.074	0.0498
15	S0W4*S0W8	15	1,2,8,9,10,11,12,13,14,16,17, 18,19,20,21	-416.930	0.0480
16	A0W1^2	16	1,2,8,9,10,11,12,13,14,15,16,17, 18,19,20,21	-420.200	0.0473
17	A0W1^3	17	1,2,3,8,9,10,11,12,13,14,15,16,17, 18,19,20,21	-424.033	0.0493
18	A0W8^3	18	1,2,3,4,8,9,10,11,12,13,14,15,16,17,18,19,20,21	-424.133	0.0475
19	S0W1^2	19	1,2,3,4,5,8,9,10,11,12,13,14,15,16,17,18,19,20,21	-426.277	0.0494
20	S0W10^2	20	1,2,3,4,5,7,8,9,10,11,12,13,14,15,16,17,18,19,20,21	-425.466	0.0506
21	S0W10^3	21	ALL	-422.530	0.0555

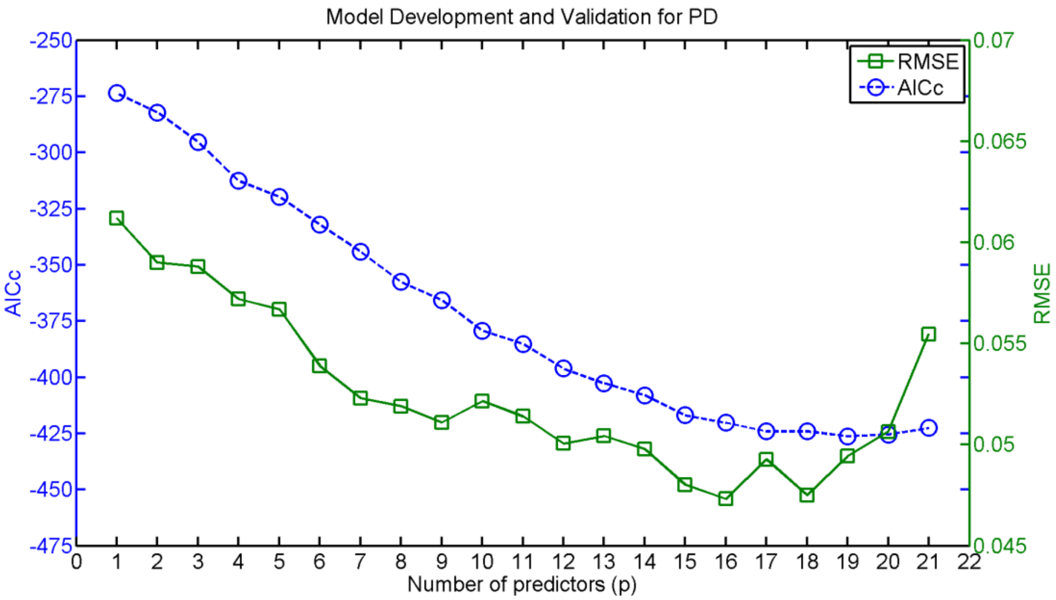

Fig. 9-16: AICc and RMSE vs. p for model development and validation for PD

Table 9-8: Coefficients of the prediction model for PD

Term	Estimate
Intercept	-3.2589
A0W7	-5.0153
S0W2	21.4342
A0W6*A0W9	7.3018
A0W6*S0W2	-13.0097
A0W6*S0W10	9.2599
A0W7*S0W1	8.6143
A0W8*S0W1	-9.7267
A0W9*S0W10	-19.9073
S0W1*S0W2	-25.0738
S0W4*S0W8	-1.6093
A0W1^2	4.1360
A0W1^3	-4.3407
A0W8^3	4.0860
S0W1^2	11.2603
S0W10^2	32.6389
S0W10^3	-64.0077

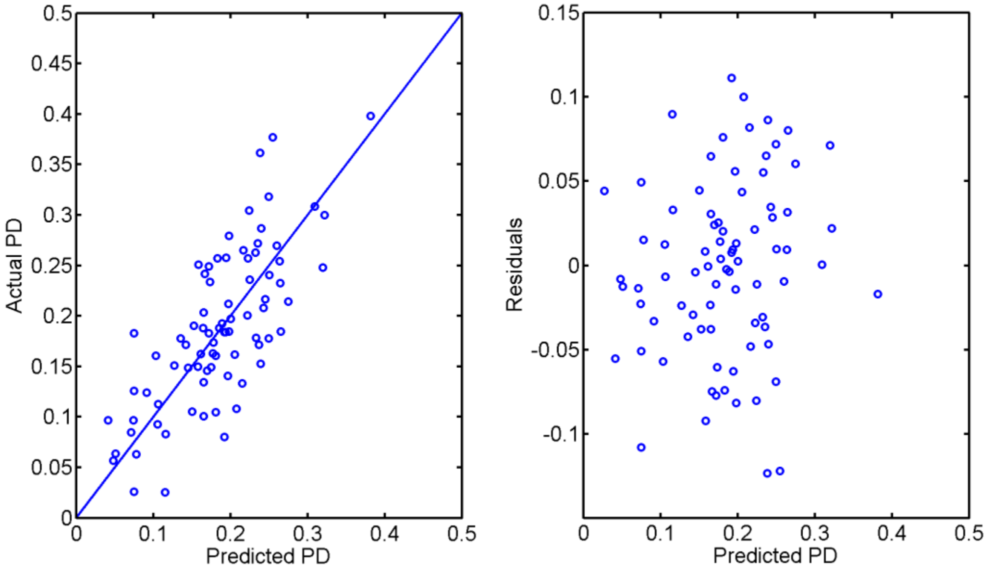

Fig. 9-17: (a) Predicted PD vs. Actual PD (b) residual plot for model development using direct method

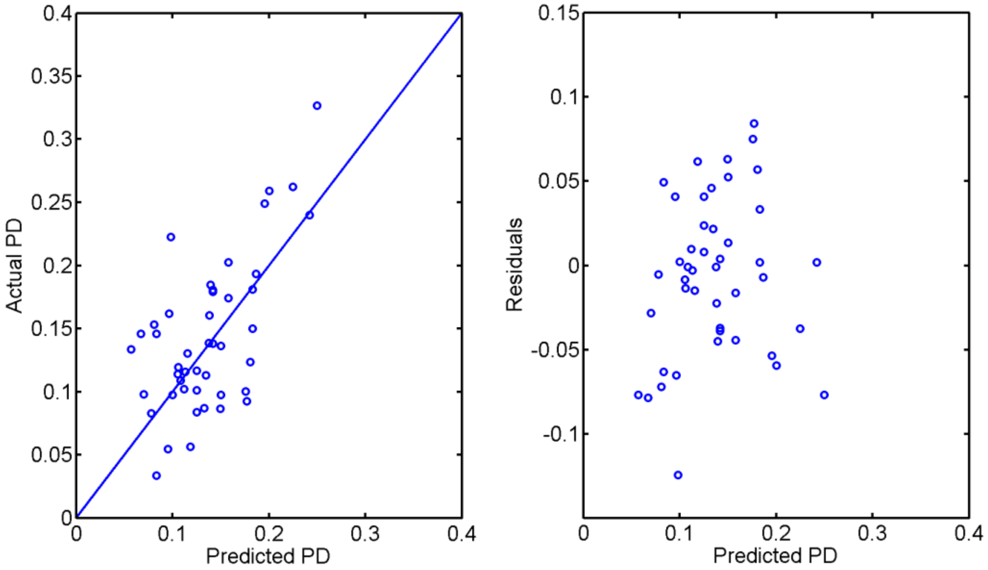

Fig. 9-18: (a) Predicted PD vs. Actual PD (b) PD vs. Test locations for model validation using direct method

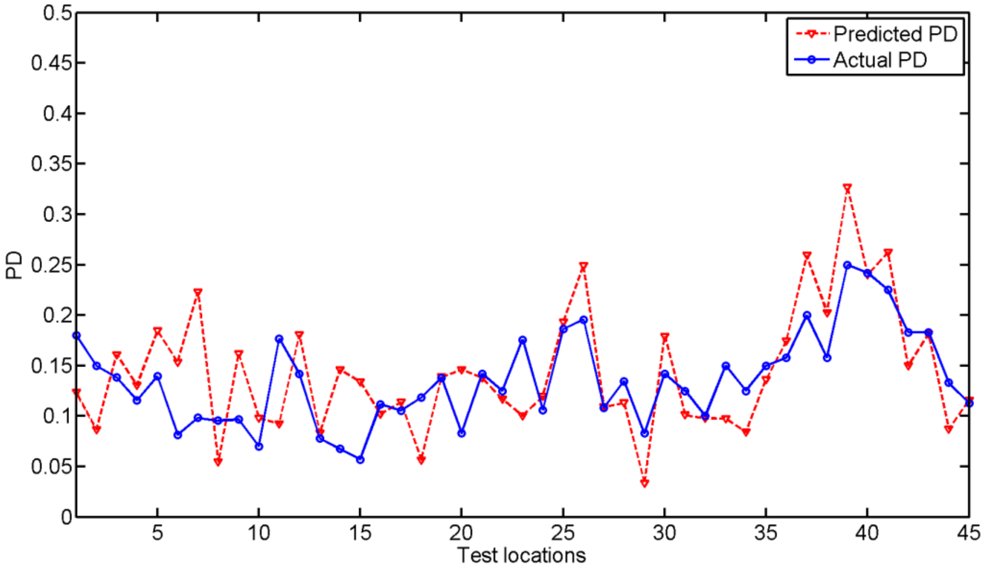

Fig. 9- 19: (a) Predicted PD vs. Actual PD (b) PD vs. Test locations for model validation using direct method

9.2.2 The Indirect Method

Here, it is assumed that all the reflection coefficients are functions of weld dimensions: PD, TH, and S2. A fourth order polynomial with second order interaction terms are chosen for the regression analysis. There are fifteen terms in the regression model. They are PD, TH, S2, PD^2, TH^2, $S2^2$, PD·TH, PD·S2, TH·S2, PD^3, TH^3, $S2^3$, PD^4, TH^4, and $S2^4$. The detailed predictor selection procedure can found in section 8.2.3. Here, the sum of normalized RMSEs of S2, TH and PD is used to determine the significance of a predictor. Table 9-9 shows the details of the predictor selection process.

Initially, fifteen predictors are used to model twenty reflection coefficients. From the first row of Table 9-9, the sum of RMSEs is 1.2400. In the first iteration, the lowest sum of normalized RMSEs is 1.1836 when PD·S2 is eliminated. In the second iteration, the lowest sum of normalized RMSEs is 1.0587 which happens when PD·S2 and TH·S2 are eliminated. In the third iteration, the sum of normalized RMSEs improves to 1.0399 when PD·S2, TH·S2 and PD^4 are eliminated. In the fourth iteration, the sum of normalized RMSEs does not improve anymore. Hence, ten predictors that construct the regression models are found. The selected predictors are PD, TH, S2, PD^2, TH^2, S2^2, PD·TH, PD^3, TH^3, S2^3, TH^4, and S2^4. Fig. 9-20 shows the sum of normalized RMSEs in this procedure, in which the X axis shows iteration and run order. The first and second numbers denote iteration and run order respectively.

Table 9-9: Summary of predictor selection procedure for indirect method

Iteration	Run order	Number of predictors	Number of eliminated predictor(s)	Eliminated predictor(s)	Sum of normalized RMSEs
0	1	15	0	N/A	1.2400
1	1	14	1	S2^4	1.2268
1	2	14	1	TH^4	1.2042
1	3	14	1	PD^4	1.2045
1	4	14	1	S2^3	1.2243
1	5	14	1	TH^3	1.2042
1	6	14	1	PD^3	1.2228
1	7	14	1	TH·S2	1.2063
1	**8**	**14**	**1**	**PD·S2**	1.1836
1	9	14	1	PD·TH	1.2500
1	10	14	1	S2^2	1.2207
1	11	14	1	TH^2	1.2042
1	12	14	1	PD^2	1.2425
2	1	13	2	PD·S2,S2^4	1.1090
2	2	13	2	PD·S2,TH^4	1.1143
2	3	13	2	PD·S2,PD^4	1.1840
2	4	13	2	PD·S2,S2^3	1.1040
2	5	13	2	PD·S2,TH^3	1.1167
2	6	13	2	PD·S2, PD^3	1.1955
2	**7**	**13**	**2**	**PD·S2,TH·S2**	1.0587
2	8	13	2	PD·S2,PD·TH	1.1125

2	9	13	2	PD·S2,S2^{2}	1.0993
2	10	13	2	PD·S2,TH^{2}	1.1192
2	11	13	2	PD·S2,PD^{2}	1.2040
3	1	12	3	PD·S2,TH·S2,S2^{4}	1.0875
3	2	12	3	PD·S2,TH·S2,TH^{4}	1.0460
3	**3**	**12**	**3**	**PD·S2,TH·S2,PD^{4}**	1.0399
3	4	12	3	PD·S2,TH·S2,S2^{3}	1.0911
3	5	12	3	PD·S2,TH·S2,TH^{3}	1.0475
3	6	12	3	PD·S2,TH·S2, PD^{3}	1.0535
3	7	12	3	PD·S2,TH·S2,PD·TH	1.0978
3	8	12	3	PD·S2,TH·S2, S2^{2}	1.0587
3	9	12	3	PD·S2,TH·S2,TH^{2}	1.0587
3	10	12	3	PD·S2,TH·S2,PD^{2}	1.0587
4	1	11	4	PD·S2,TH·S2,PD^{4},S2^{4}	1.0870
4	2	11	4	PD·S2,TH·S2,PD^{4},TH^{4}	1.0465
4	3	11	4	PD·S2,TH·S2,PD^{4},S2^{3}	1.0887
4	4	11	4	PD·S2,TH·S2,PD^{4},TH^{3}	1.0479
4	5	11	4	PD·S2,TH·S2,PD^{4}, PD^{3}	1.0764
4	6	11	4	PD·S2,TH·S2,PD^{4},PD·TH	1.1760
4	7	11	4	PD·S2,TH·S2,PD^{4}, S2^{2}	1.0905
4	8	11	4	PD·S2,TH·S2,PD^{4},TH^{2}	1.0498
4	9	11	4	PD·S2,TH·S2,PD^{4},PD^{2}	1.0811

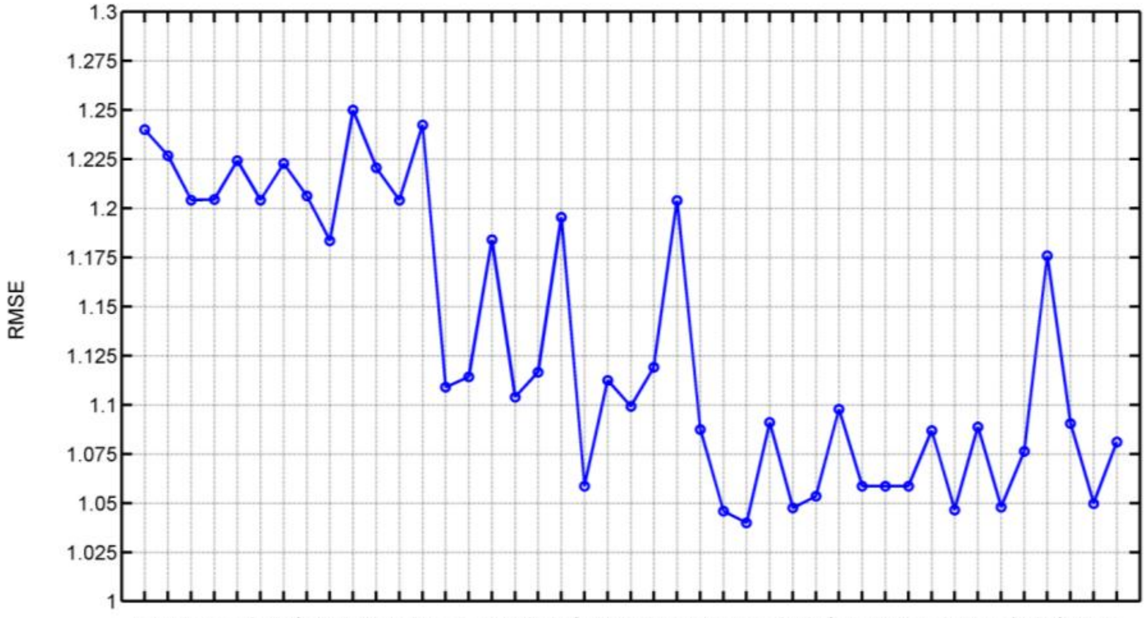

Fig. 9-20: Summary of predictor selection procedure for indirect method

9.2.2.1 Evaluation of Weld Dimensions

After the best set of predictors is determined, the performance of the model is investigated to see how well the model fits both the model development data and validation data. Fig. 9-21(a) shows the scatter plot of predicted TH vs. actual TH and Fig. 9-9(b) shows the residual plot for the model development data. No serious systematic error is present so no correction procedure is needed. Fig. 9-22(a) shows the predicted TH vs. actual TH for the model validation data and Fig. 9-22(b) shows both actual and predicted TH at each test locations along the welds. The predicted TH follows the actual TH very well. The RMSEs of THs for both the model development and validation data are 0.0929 and 0.1001 respectively.

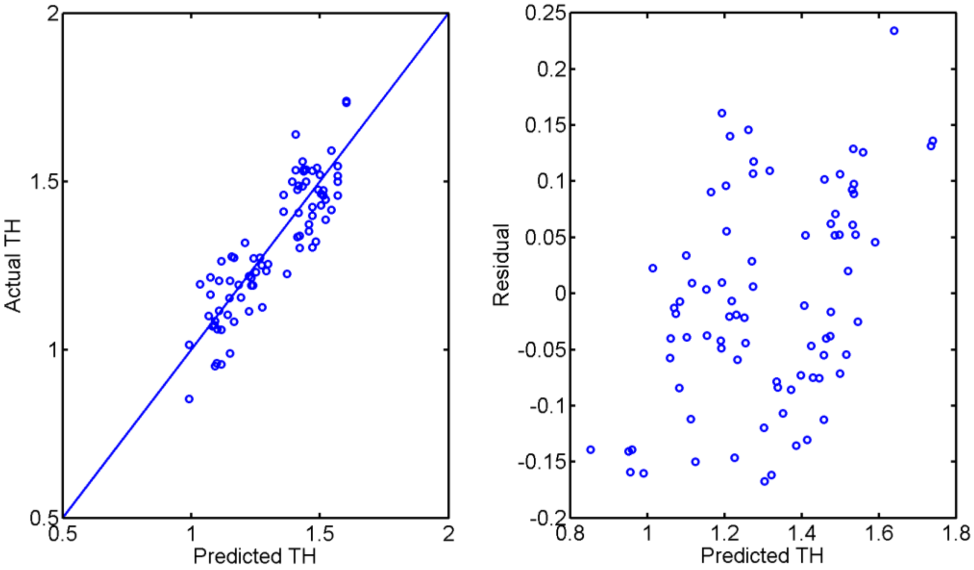

Fig. 9-21: (a) Predicted TH vs. Actual TH (b) residual plot for model development using indirect method

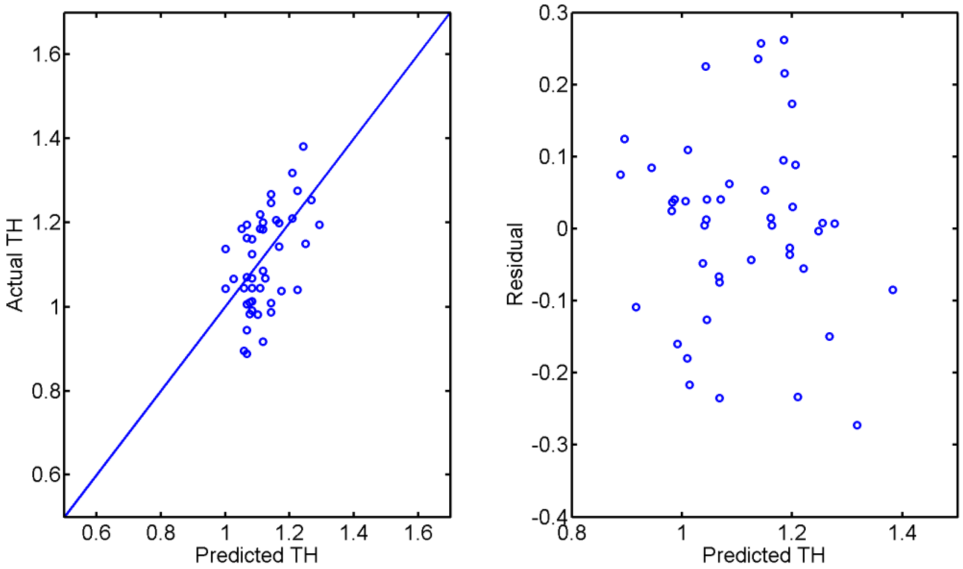

Fig. 9-22: (a) Predicted TH vs. Actual TH (b) residual plot for model validation using indirect method

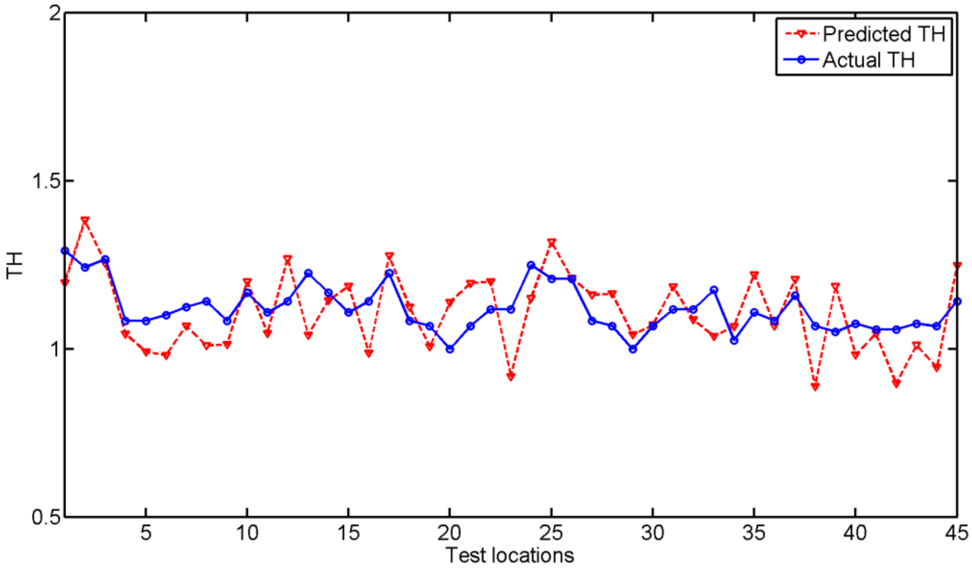

Fig. 9- 23: TH vs. Test locations for model validation using indirect method

Fig. 9-24(a) shows the scatter plot of predicted S2 vs. actual S2 and Fig. 9-24(b) shows the residual plot for the model development data. No serious systematic error is present so no correction procedure is needed. Fig. 9-25(a) shows the predicted S2 vs. actual S2 for the model validation data and Fig. 9-25(b) shows both actual and predicted S2 at each test locations along the welds. The predicted S2 follows the actual S2 very well. The RMSEs of S2s for both the model development and validation data are 0.1418 and 0.1447 respectively.

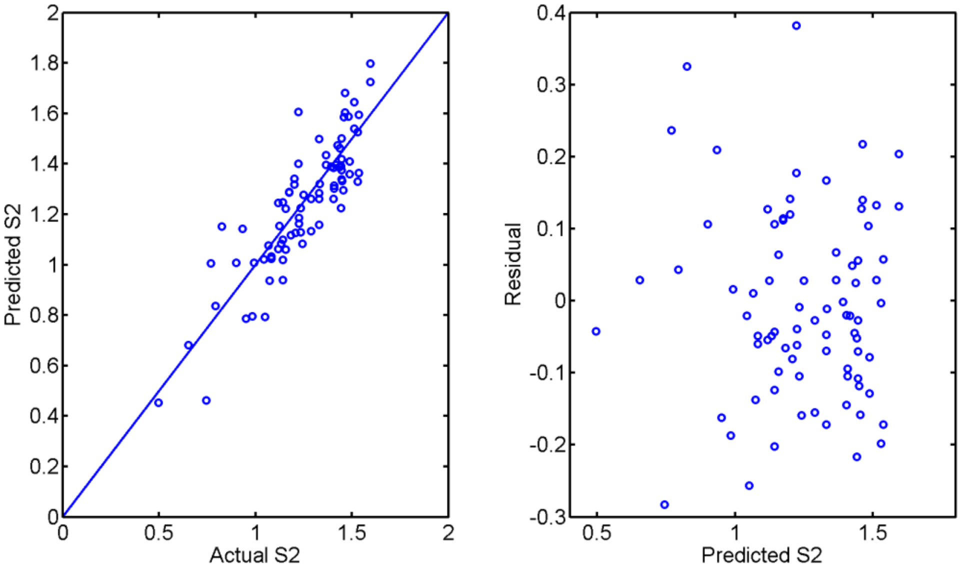

Fig. 9-24: (a)Predicted S2 vs. Actual S2 (b) residual plot for model development using indirect method

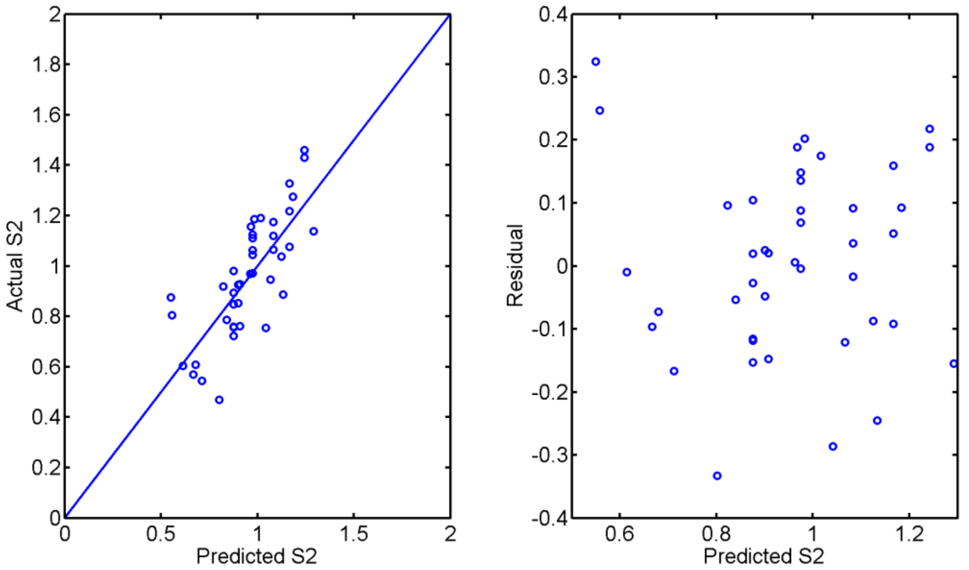

Fig. 9-25: (a) Predicted S2 vs. Actual S2 (b) residual plot for model validation using indirect method

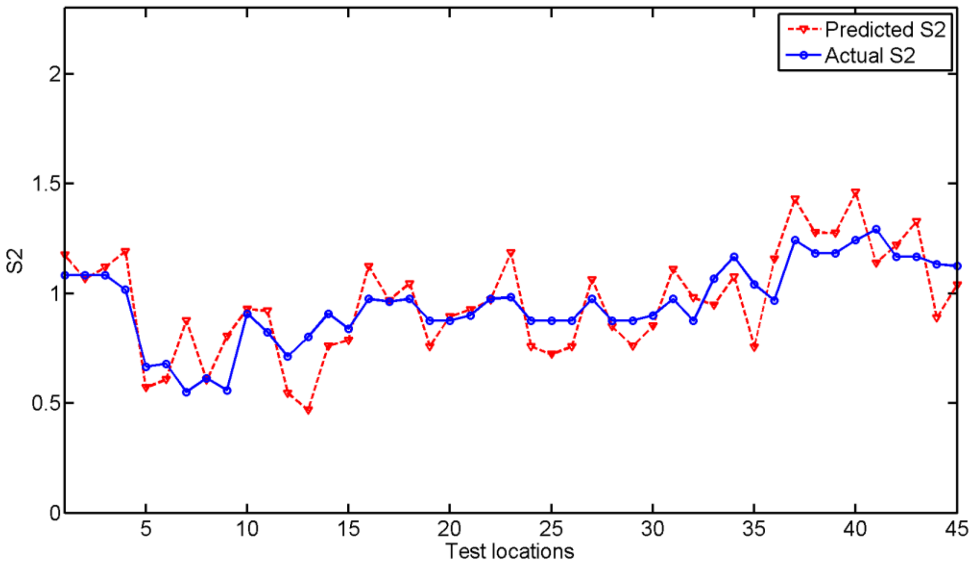

Fig. 9- 26: S2 vs. Test locations for model validation using indirect method

The scatter plot between actual PDs and predicted PDs of the model development data is shown in Fig. 9-27(a) and the residual plot is shown in Fig. 9-27(b).

Serious systematic error can be observed. The correction procedure is also described in Chapter 8.2.4. After correction, the corrected scatter plot between actual PDs and predicted PDs of the model development data is shown in Fig. 9-28(a) and the corrected residual plot is shown in Fig. 9-28(b). From the residual plot, the error distributes randomly around zero indicating there is no systematic error. The RMSE reduces from 0.0680 to 0.0564 after the correction.

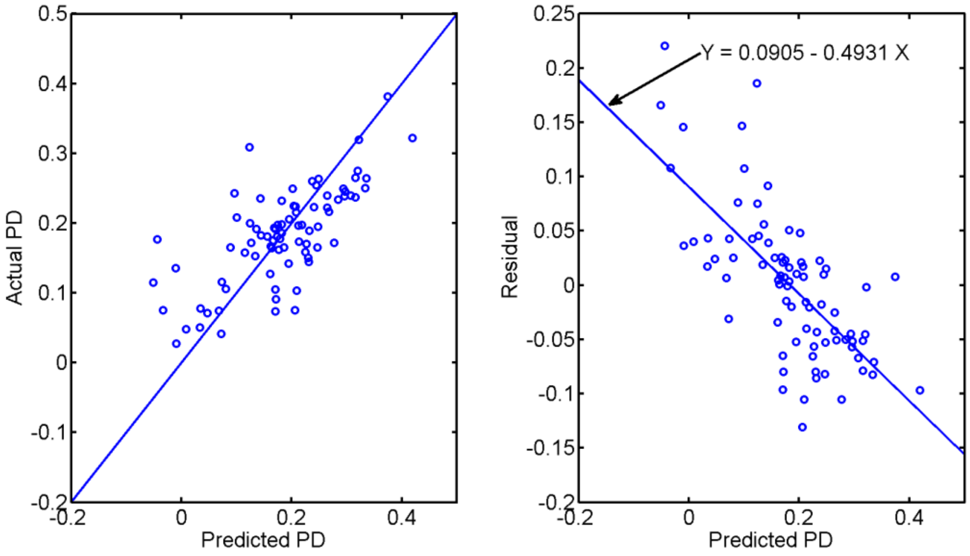

Fig. 9-27: (a) Predicted PD vs. Actual PD (b) residual plot for model development using indirect method before correction

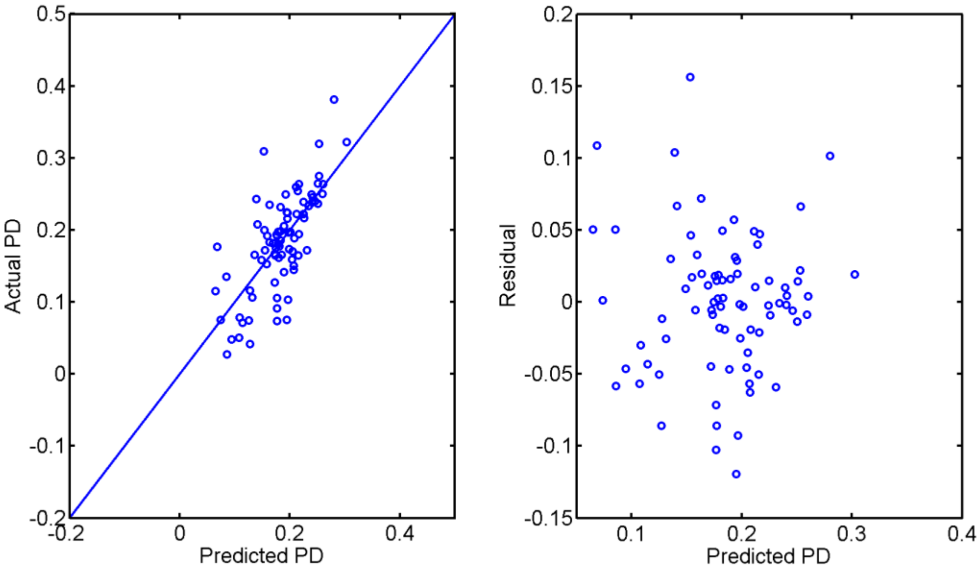

Fig. 9-28: (a) Predicted PD vs. Actual PD (b) residual plot for model development using indirect method after correction

The corrected model is then used on the validation data. The scatter plot between actual PDs and predicted PDs of the validation data is shown in Fig. 9-29(a) and the actual and predicted PDs are plotted together with respect to test locations in Fig. 9-29(b). The accuracy of the prediction is not very high. Big discrepancy between the predicted and actual PDs can be found when the test location is around 15. The RMSE of PDs of the validation data is 0.0771. The possible reasons for the inaccuracy will be discussed in the later sections.

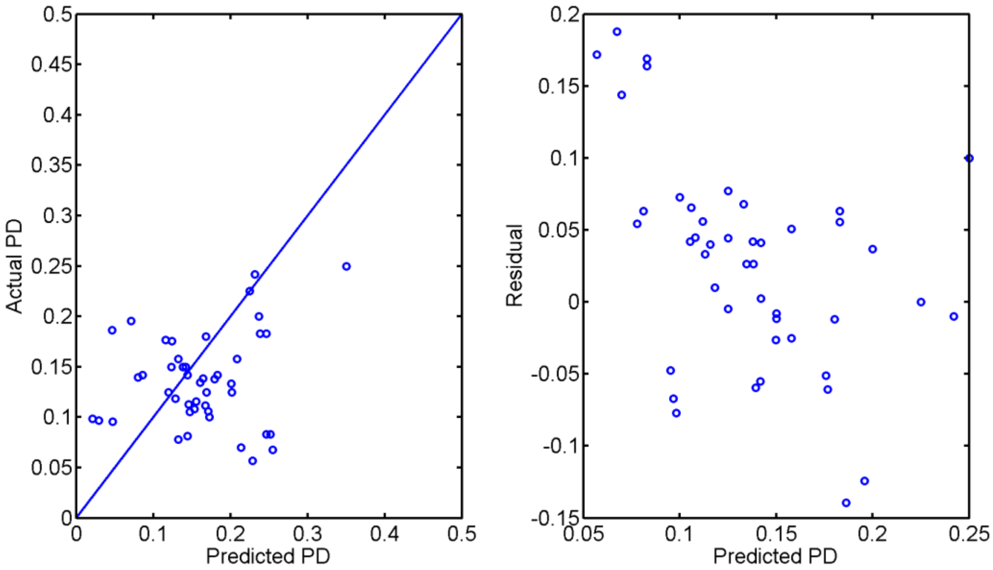

Fig. 9-29: (a) Predicted PD vs. Actual PD (b) residual plot for model validation using indirect method

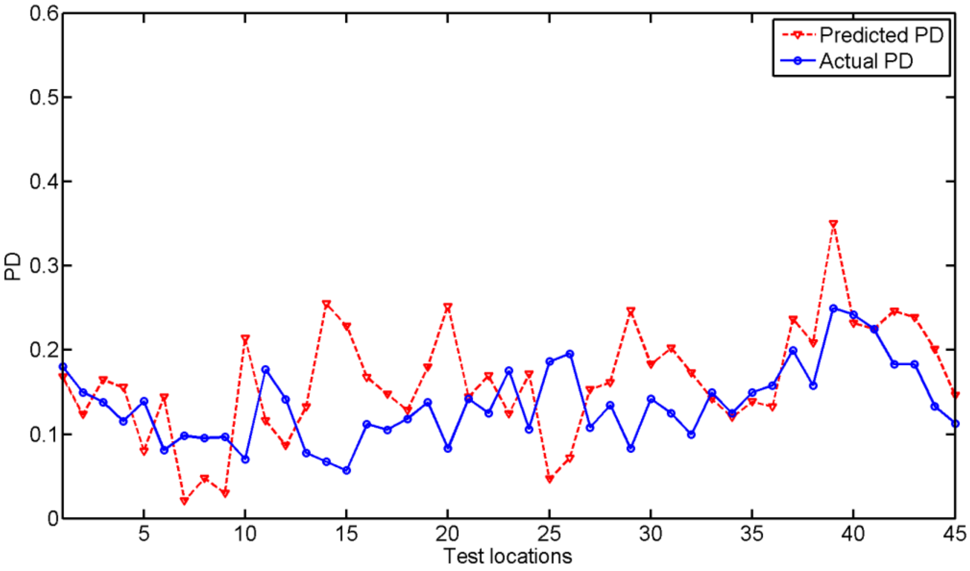

Fig. 9- 30: (a) Predicted PD vs. Actual PD (b) residual plot for model validation using indirect method

9.2.2.2 Reflection Coefficients vs. Weld Dimensions of Lap Welds

In the indirect method, the coefficient matrix K defines the relationship between the weld dimensions and 20 reflection coefficients. In this section, how each reflection coefficient changes with respect to the changes of throat thickness, leg length 2 and penetration depth is studied.

(1) Throat Thickness

In order to know how these reflection coefficients change with TH, the value of TH is set to range from 1.0 to 1.6 in an increment of 0.01 and the values of S2 and PD are fixed to be 1.16 and 0.17, which are their median values among all data. By the same procedure as described in Chapter 8.2.5, the relationship between the reflection coefficients of A0 and S0 modes and TH can be plotted in Fig. 9-31 and Fig. 9-32. For A0 modes, except for A0W8, A0W9 and A0W10, most of the reflection coefficients show very complex responses with respect to TH. For S0 modes, the reflection coefficients of S0W1 to S0W5 do not show much sensitivity to the change of TH. Only the reflection coefficient of S0W6 shows roughly monotonic decreasing trend. The plots reveal the complex effects that the throat thickness has on the behavior of the Lamb waves of different modes and wavelengths.

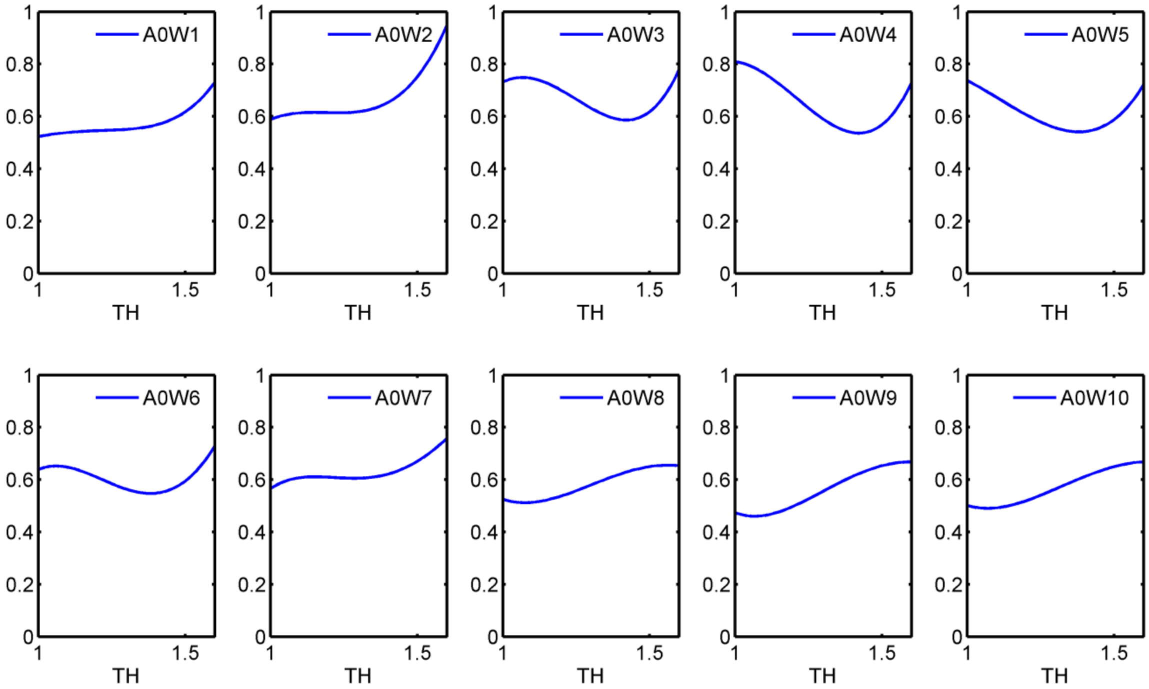

Fig. 9-31: Reflection coefficients of Lamb waves A0 mode vs. TH

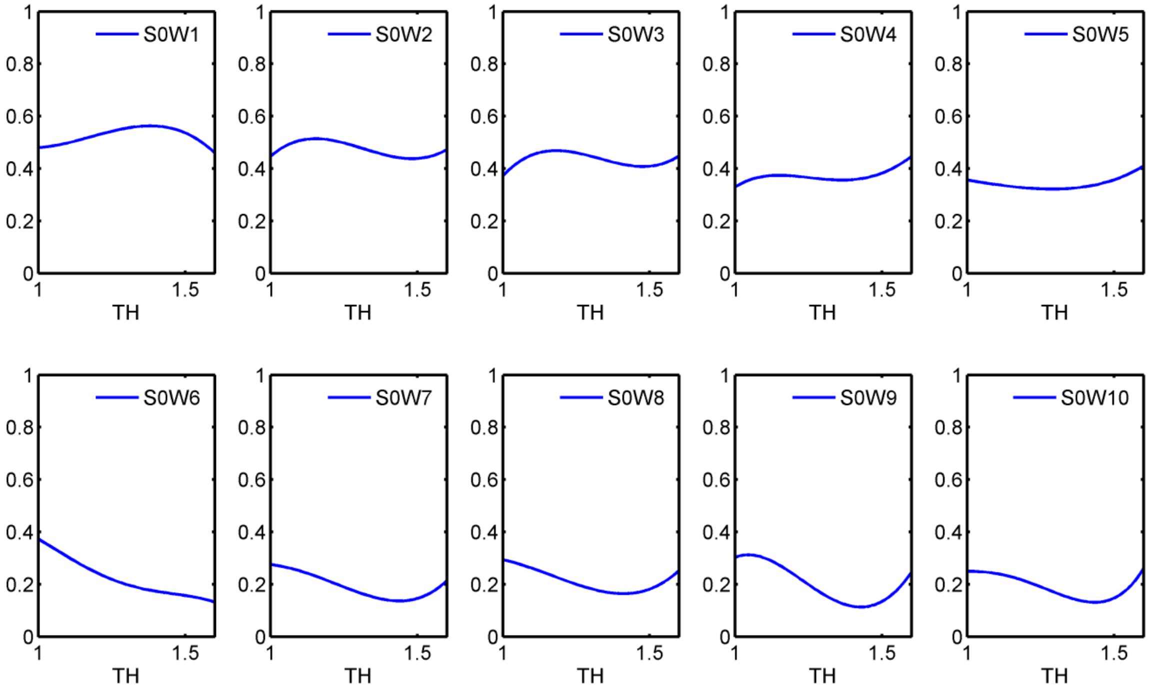

Fig. 9-32: Reflection coefficients of Lamb waves S0 mode vs. TH

(2) Leg Length 2

In the same fashion, the relationship between the reflection coefficients and leg length 2 can be plotted. The plots for A0 modes and S0 modes are plotted in Fig. 9-33 and Fig. 9-34 respectively. In these plots, the value of S2 ranges from 0.5 to 1.5 in an increment of 0.01 and the values of TH and PD are fixed to be 1.20 and 0.17, which are their median values among all data. For A0 mode, most of them show decreasing trend with increasing S2. This is predictable because if we examine the cross section of a lap weld, the dimension S2 represents window size at which the waves can propagate from the top plate to the bottom plate through the weld. As S2 increases, the open area increases so that more waves can pass through. For S0 mode, similar trend can be observed for most of them.

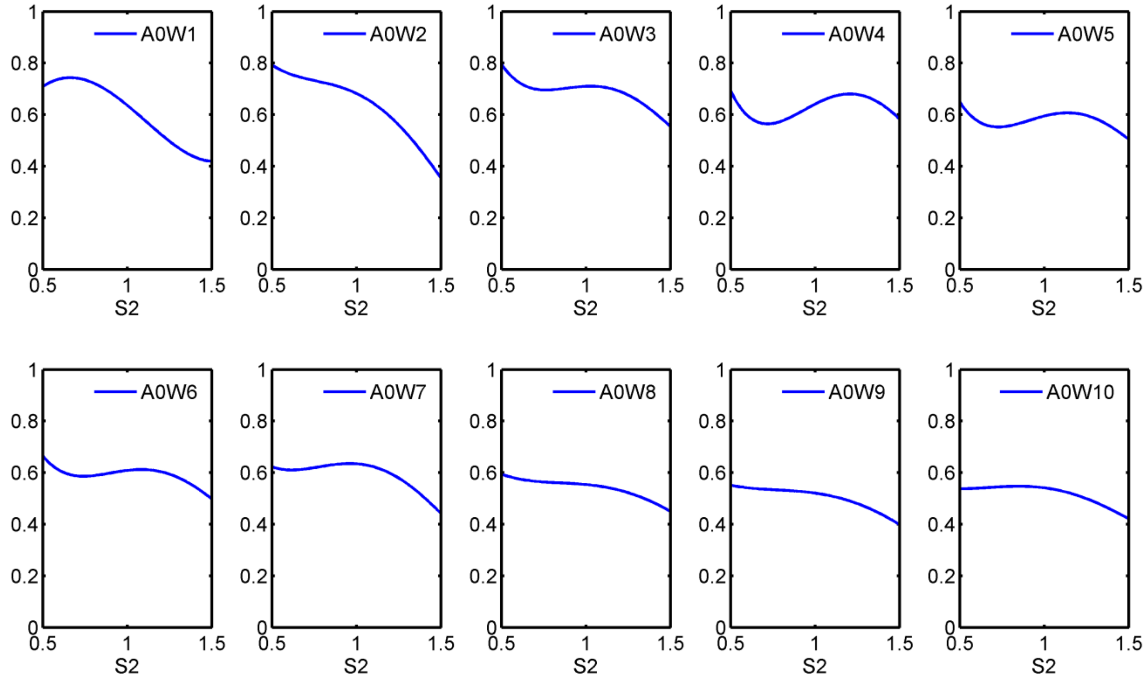

Fig. 9-33: Reflection coefficients of Lamb waves A0 mode vs. S2

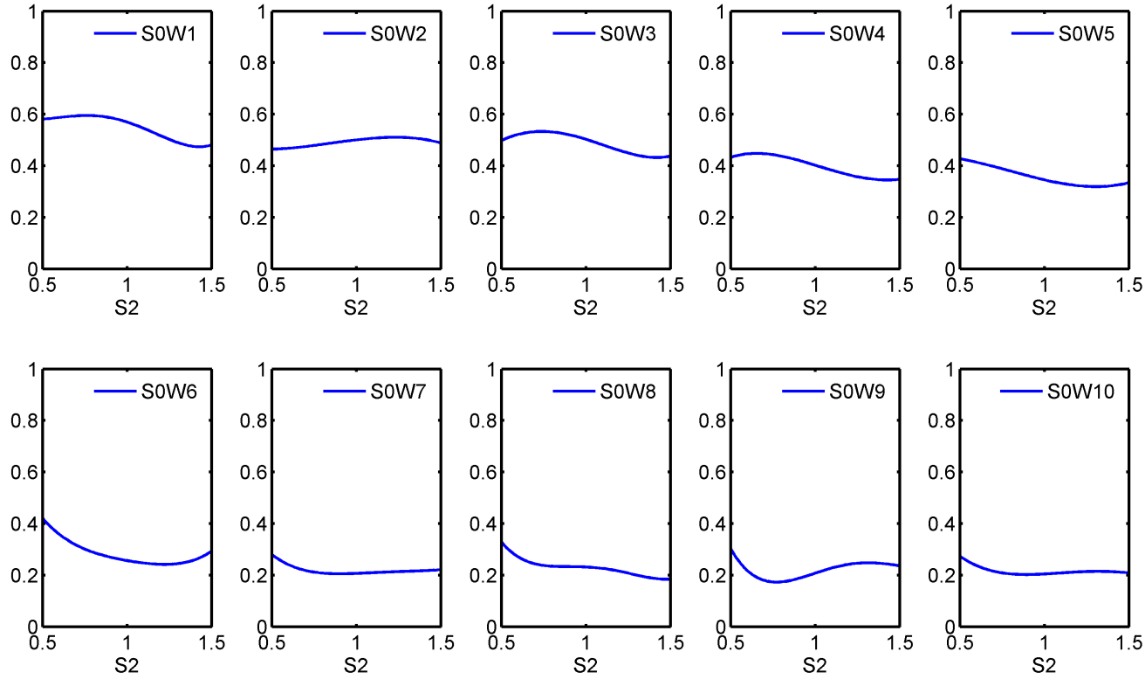

Fig. 9-34: Reflection coefficients of Lamb waves S0 mode vs. S2

(3) Penetration Depth

The relationship between the reflection coefficients and bead width can also be plotted. The plots for A0 modes and S0 modes are shown in Fig. 9-35 and Fig. 9-36 respectively. In these plots, the value of PD ranges from 0.03 to 0.35 in an increment of 0.01 and the values of TH and S2 are fixed to be 1.20 and 1.16, which are their median values among all data. The reflection coefficients of both A0 and S0 modes do not show much sensitivity to the change of penetration depth. Unlike the penetration depth in a butt weld which actually controls the window size for the waves to propagate through the weld, the penetration depth is a lap weld is not a critical dimension that affects the path that waves travel through the weld. As long as the weld and the base materials are fused well together, waves can travel from the top plate to the bottom. As the result, even when the penetration depth varies, the reflection coefficients do not change much.

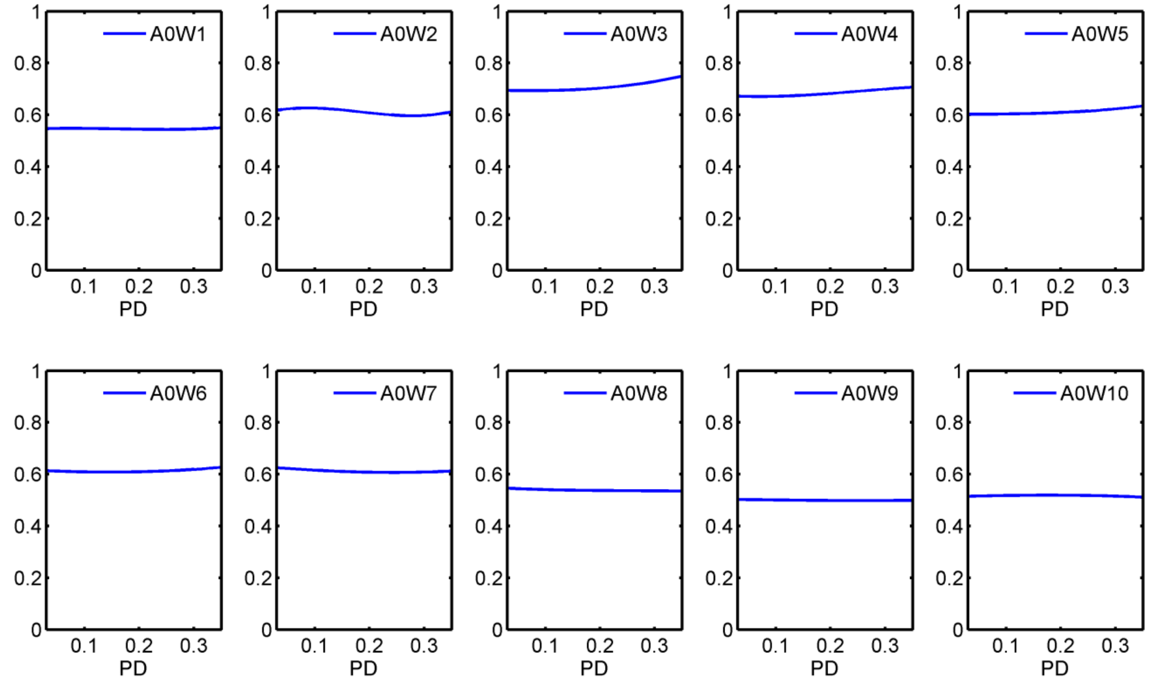

Fig. 9-35: Reflection coefficients of Lamb waves A0 mode vs. PD

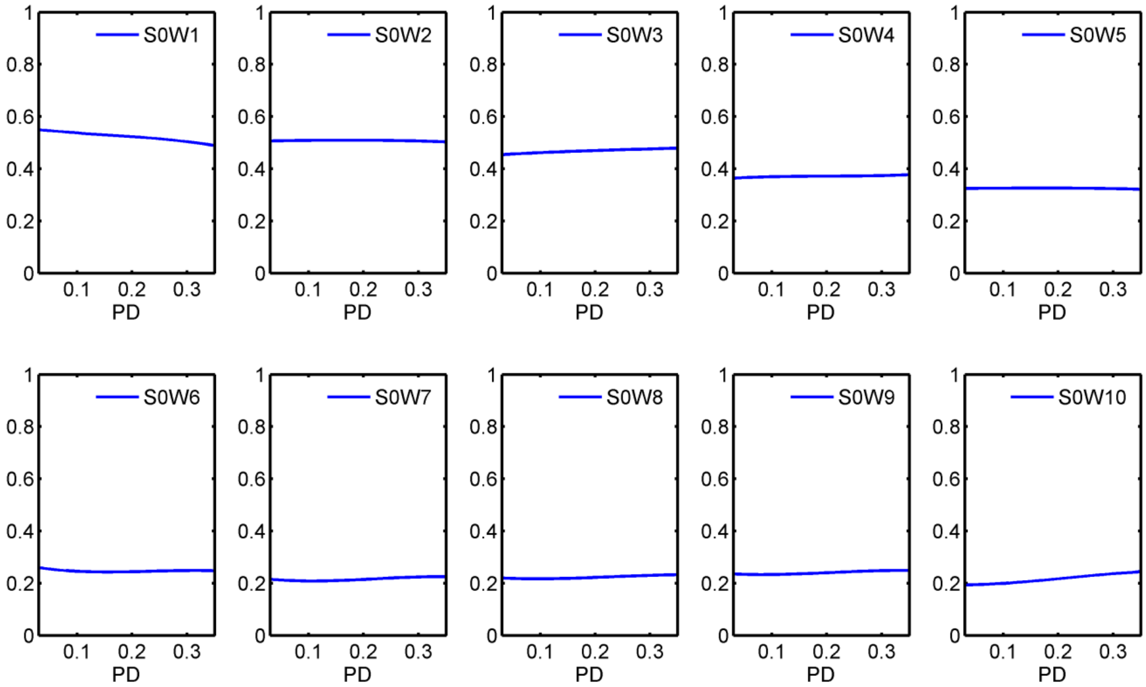

Fig. 9-36: Reflection coefficients of Lamb waves S0 mode vs. PD

9.3 Discussion

Two systematic ways to develop models that relate the reflection coefficients of Lamb wave modes to the weld dimensions in lap welds have been presented. The RMSE values for predicting TH, S2 and PD using both methods on both the development and validation data are shown in Table 9-10. Similar to the models developed for the butt welds, the accuracy of the direct method is higher than that of the indirect method. The sources of modeling errors and advantages and disadvantages of both methods have been described in Chapter 8.3.

Table 9-10: Comparison of RMSEs of models developed by both methods

			Direct Method	Indirect Method
Lap Weld	Throat Thickness	Development	0.0879	0.0929
		Validation	0.0928	0.1001
	Leg Length 2	Development	0.1417	0.1418
		Validation	0.1465	0.1447
	Penetration Depth	Development	0.0524	0.0564
		Validation	0.0473	0.0771

In a lot of applications of lap welds, penetration depth is the most critical dimension. However, according to the findings revealed in this research, it is also the most difficult dimension in a lap weld to be measured. From Table 9-10, the RMSE for predicting penetration depth ranges from 0.0473 to 0.0771 depending on which data set and model developing method are used. At the first glance, this RMSE values do not look unsatisfactory given that they are only 4.7% to 7.7% of the plate thickness. However if considering that the range of PD among two sets of data is just 0.354, the

RMSE values are actually 13.36% to 21.77% of the data range of PD. The large RMSE values can be explained by the geometry of a lap weld.

The geometry of a lap weld is more complex and is not as symmetric as the geometry in a butt weld. By looking at Fig. 9-1 carefully, it can be observed that it is the leg lengths, S1 and S2, which control the window size of the path for the ultrasound to travel from one of the plates to another. If the weld bead is well bonded to the base materials, then the size of penetration depth may not have a big effect on the reflection coefficients of Lamb waves. If the reflection coefficients do not respond to the change of penetration depth, it is hard to develop a model with high accuracy. On the contrary, in the butt weld, it is the penetration depth and the reinforcement height that control the window size of the path that waves travel. Therefore we can expect that the reflection coefficients must be strongly correlated to their dimensions.

However, from Fig. 9-18 and Fig. 9-29, the predicted PD still follows the actual PD to some degree. This indicates the models developed by both methods can still be used to predict the penetration depth of lap welds. The prediction power of the models comes from the correlation between penetration depth and other weld dimensions. When other weld dimensions have higher effect on the reflection coefficients, the relationship between penetration depth and the reflection coefficients can be established through other weld dimensions. Therefore, to increase the accuracy of the prediction of the penetration depth, it is imperative to understand the correlation between the weld dimensions in lap welds.

CHAPTER 10

Conclusion, Contributions and Recommendations

10.1 Conclusion

The overall objective of this research is to develop a technique to measure important weld dimensions in thin plates by using laser generated ultrasound. This research consists of three aspects: First, to develop a technique that can generate narrowband Lamb waves in thin plates using a laser source. Secondly, to develop a signal processing procedure to extract useful information out of ultrasonic signals to quantify weld dimensions. Thirdly, to develop a methodology for developing prediction models to predict weld dimensions by using the reflection coefficients of narrowband Lamb waves. The laser generation technique and signal processing procedure developed in this research have proven to be very effective. The prediction models have shown the great potential to predict weld dimensions in both butt welds and lap welds. The objective of this research is successfully accomplished. Some of the important aspects of this research are recapped in the following.

The superimposed laser sources (SLS) technique is applied to generate narrowband Lamb waves with fixed wavelengths in thin plates. To generate narrowband Lamb waves with a dominant wavelength, the signals that are generated by the laser line sources at the interval corresponding to the desired wavelength are superimposed together. The superposition is performed in software so that it permits the flexibility of selecting desired wavelength afterwards. By generating narrowband signals with fixed wavelengths using the SLS technique, the complexity of signals can be reduced and the speeds and frequency can be estimated from the dispersion curves. The knowledge of speeds and frequencies of narrowband Lamb wave modes permits identification and time-of-flight analysis of each Lamb wave mode.

The signal processing procedure that combines wavenumber-frequency (k-ω) domain filtering and synthetic phase tuning (SPT) is used to further reduce the complexity of Lamb waves. The k-ω domain filtering technique helps to filter out the unwanted wave components traveling at the direction that is not of interest to us and the SPT technique is applied to amplify and isolate a particular Lamb wave mode. The signal processing procedure facilitates the calculation of reflection coefficients of Lamb waves that result from the presence of defects or weld joints.

In order to validate the feasibility of the proposed research, a series of finite element simulations and experiments are conducted on aluminum thin plates with surface breaking defects with varying depths. Reflection coefficients are calculated for fundamental A0 and S0 Lamb wave modes. Good agreement is found between the results of simulations and experiments, which gives us a strong confidence to use reflection coefficients to evaluate severity of defects and weld dimensions.

The SLS technique and the signal processing procedure are then applied to measure reflection coefficients in butt welds and lap welds. The important weld dimensions in butt welds are penetration depth (PD), reinforcement height (RH) and bead width (BW). And the important weld dimensions in lap welds are throat thickness (TH), leg lengths (S1, S2), and penetration depth (PD). Reflection coefficients that result from the welds can be calculated for A0 and S0 Lamb wave modes for ten discrete wavelengths of interest.

Two methodologies, the direct method and the indirect method, are used to develop models that use reflection coefficients as predictors to measure these weld dimensions. In the direct method, weld dimensions are assumed to be functions of the reflection coefficients. The geometry and material composition of butt welds and lap welds are very complicated. No theory or guideline exists to determine the form of relationship between reflection coefficients of Lamb waves and weld dimensions. Polynomial regression models are chosen for the development of prediction models. A methodology is used to determine important predictors to be included in the prediction models. The methodology includes the stepwise regression method and the Corrected Akaike's Information Criterion (AICc). It selects significant predictors to formulate the prediction models by the statistical approach.

In the indirect method, instead of assuming that the weld dimensions are functions of the reflection coefficients of Lamb wave modes, we have assumed that the reflection coefficients are functions of the weld dimensions. The predictor selection procedures determine the predictors that are used in the regression analysis. A system of equations can be derived from the regression analysis to relate weld dimensions to all the reflection coefficients and can be represented in the matrix form. For the prediction purposes, one will measure reflection coefficients and solve the system of equations to predict the weld dimensions. The prediction models have shown the great potential to predict weld dimensions in both butt welds and lap welds. Furthermore, from the model developed by the indirect method, we are able to show how each reflection coefficient responds to the change of weld dimensions. This is the first time one is able to plot the relationship between the reflection coefficients of Lamb waves and the weld dimensions in both butt welds and lap welds. The results provide us a way to investigate the interaction between Lamb waves and geometry of welds. Both models are shown to effectively predict weld dimensions in thin plate and they are complementary to each other. The advantages and disadvantages of these two methods have been discussed, and the detailed discussion about the sources of errors has also been presented.

The model development procedure used in this research is a data driven approach. It is efficient and effective but the prediction models may suffer from some disadvantages. One of them is that these models may lack physical senses. Another is that there is a possibility that these models may not be robust enough to be extended to predict weld dimensions in other types of steels or when the ranges of weld dimensions are beyond those used in model development. However, in industry, the materials used in the welding process in a manufacturing plant are usually fixed. For example, in the automobile industry, the type and the thickness of the steel used for a certain part in a car model is usually identical. One manufacturing line is usually dedicated to one type of material, one thickness and one type of welding process. The welding robot arm performs one task in one cell and the samples are transported to the next cell for another task. The process is simple and always repeated without many changes. Because of the special conditions of the manufacturing process used in the industry, the data driven approach is very efficient, effective and valuable.

In general, the laser generation technique, signal processing procedures and the models developed by both the direct and indirect methods in this thesis can readily be applied and used for commercial applications.

10.2 Contributions

The contributions of this research can be summarized as the following.

1. Developed and implemented the superimposed laser sources technique to generate narrowband Lamb waves in thin plates.
2. Developed a signal processing procedure and algorithm that combine the wavenumber-frequency domain filtering and the synthetic phase tuning techniques to simplify ultrasonic signals in thin plates. The wavenumber-frequency domain filtering transform signals which are complicated in space-time domain to wavenumber-frequency domain. In wavenumber-frequency domain, signals traveling in different directions will have different signs in wavenumber. By removing components that have positive or negative wavenumbers, and inversely transforming signals back to space-time domain, one can separate wave traveling in different directions. In synthetic phase tuning technique, a particular wave component can be isolated and amplified if the

phase velocity of it is known. It helps to reduce complexity of ultrasonic signals in thin plate and facilitate the calculation of reflection coefficients of wave modes.

3. Developed a finite element model to simulate the laser generation of Lamb waves in thin plates. The simulation is approached as a sequentially solved transient thermomechanical problem. The temperature field induced by laser input is first solved and the temperature distribution is taken as a thermal nodal load in the transient structural analysis in each time step and then the transient displacement field is solved sequentially.
4. Conducted a series of finite element simulations and experiments on aluminum plates with surface breaking defects of varying depths and showed that we can use the SLS technique and the proposed signal processing procedure to quantify severity of defects by using reflection coefficients of narrowband Lamb waves.
5. Systematically fabricated samples of butt welds and lap welds and studied the effects of the welding parameters: contact tip-to-workpiece-distance, wire feed rate, welding speed, and arc voltage on the weld dimensions.
6. Developed two methodologies for developing prediction models for predicting weld dimensions in butt welds and lap welds. The models developed by the direct method have shown to accurately predict weld dimensions in thin plates. The models developed by the indirect method can also predict weld dimensions fairly accurately and provide us a means to understand how reflection coefficients respond to the change in weld dimensions.

10.3 Recommendations

The superimposed laser sources technique, the signal processing procedure and the prediction models developed by both the direct and indirect methods in this research have shown to be very effective and promising. However, there are still many challenging research areas to be explored. Some recommendations for future work are listed below.

1. More experiments and analyses can be conducted on the welded samples with different thicknesses. If possible, it would be very useful to develop a universal prediction model(s) that can be used to predict weld dimensions in welded samples with different thicknesses.
2. Extensibility studies need to be conducted to see whether the prediction models are robust enough to be extended to predict weld dimensions in different steels or other materials. One needs to determine how much percentage different material properties can vary before the prediction models cannot make good predictions.
3. The placement of the sensor and laser line sources can be properly adjusted so that the mode converted waves can be easily observed. In the current setup, the sensor is placed close to the weld. The distance from the weld to the sensor is not large enough to separate the mode converted waves from the reflection waves using the time-of-flight method.

4. It is possible to include reflection, transmission and mode conversion coefficients into prediction models to increase accuracy of prediction.
5. For future research, it is recommended to use the finite element simulation to investigate the interaction between different weld dimensions and Lamb wave modes of different wavelengths. From the simulations, one may be able to identify wavelengths that are more sensitive to a certain wave dimension. Different wavelengths may be sensitive to different weld dimensions. One can build separate prediction models for different weld dimensions using different sets of sensitive waves. By doing this, one may be able reduced the number of predictors in the prediction models and make the prediction model development procedure more efficient and effective.
6. In this research, the polynomial regression model is used for developing prediction models. A better form of regression model may be found through more literature survey.
7. The technique can be expanded to quantify other types of defect in weld joints such as the length of cracks or the size of voids and porosity.
8. The hardware of the inspection system can be improved to reduce experimental time. While the superimposed laser sources technique is effective and flexible to generate narrowband Lamb waves in thin plates, it takes more time to inspect one test location. If the stability of the laser and the sensor can be improved,

then the number of averages can be reduced, which will decrease the inspection time greatly. The linear screw can also be upgraded to have higher speed.

9. A system that can scan the entire weld seam can be developed. The system can monitor the change of weld dimensions along the weld and can identify the location of the weld seam that may have issues.

REFERENCES

1. Raj B, Shankar V, and Bhaduri AK, Welding Technology for Engineers. 2006, New Delhi: Narosa Publishing House.
2. Cornu J, Advanced Welding Systems: Consumable Electrode Processes. 1988: IFS Publications.
3. Raj B, Subramanian CV, and Jayakumar T, Non-destructive Testing of Welds. 2000, New Delhi: Narosa Publishing House.
4. Lankalapalli K, Tu J, and Gartner M, A model for estimating penetration depth of laser welding processes. Journal of Physics D: Applied Physics 1996; 29: 1831-1837.
5. Menaka M, Vasudevan M, Venkatraman B, and Raj B, Estimating bead width and depth of penetration during welding by infrared thermal imaging. Insight: Non-Destructive Testing & Condition Monitoring 2005; 47(9): 564-568.
6. Tawfik D, Mutton PJ, and Chiu WK, Experimental and numerical investigations: Alleviating tensile residual stresses in flash-butt welds by localised rapid post-weld heat treatment. Journal of Materials Processing Technology 2008; 196(1-3): 279-291.
7. Moreira PMGP, et al., Temperature field acquisition during gas metal arc welding using thermocouples, thermography and fibre Bragg grating sensors. Measurement Science and Technology 2007; 18(3): 877-883.

8. Matteï S, Grevey D, Mathieu A, and Kirchner L, Using infrared thermography in order to compare laser and hybrid (laser+MIG) welding processes. Optics & Laser Technology 2009; 41(6): 665-670.

9. Huang RS, Liu LM, and Song G, Infrared temperature measurement and interference analysis of magnesium alloys in hybrid laser-TIG welding process. Materials Science and Engineering: A 2007; 447(1-2): 239-243.

10. Wu T-Y, Ume IC, and Rogge M. Detection of defects in welded structures with complex geometry using statistical method based on descrete wavelet transform. in Proceedings of the ASME 2009 IMECE. 2009. Lake Buena Vista, FL: ASME.

11. Takagi T, Benchmark models of eddy current testing for steam generator tube: experiment and numerical anlysis. International Journal of Applied Electromagnetics and Mechanics 1994; 5(3): 149-162.

12. Hoshikawa H, Koyama K, and Kawate Y. Electromagnetic surface testing of weld over painting by uniform eddy current probe. in Review of Progress in Quantitative Nondestructive Evaluation, 30 July-4 Aug 2006. 2007. USA: AIP.

13. Rao BPC, Raj B, Jayakumar T, and Kalyanasundaram P, An artificial neural network for eddy current testing of austenitic stainless steel welds. NDT&E International 2002; 35(Copyright 2002, IEE): 393-8.

14. Vasudevan M, et al., Artificial neural network modelling for evaluating austenitic stainless steel and Zircaloy-2 welds. Journal of Materials Processing Technology 2005; 169(Copyright 2006, IEE): 396-400.

15. Yusa N, et al., Detection of embedded fatigue cracks in Inconel weld overlay and the evaluation of the minimum thickness of the weld overlay using eddy current testing. Nuclear Engineering and Design 2006; 236(Copyright 2006, The Institution of Engineering and Technology): 1852-9.

16. Dutli J, Gerhold W, and Tenney H, A preliminary Investigation of the Radiographic Visualisation of Cracks. NDT&E International 1994; 12(2).

17. Souza MP, Almeida RM, Rebello JMA, and Soares SD, Detection of lack of fusion weld defects by radiography. AIP Conference Proceedings 2009; 1096(1): 1174-1181.

18. Deschepper P, Computed radiography in weld inspection applications. Welding in the World 2007; 51(Compendex): 457-464.

19. Alleyne DN and Cawley P, Optimization of Lamb wave inspection techniques. NDT&E International 1992; 25: 11-22.

20. Fromme P, Wilcox PD, Lowe MJS, and Cawley P, On the development and testing of a guided ultrasonic wave array for structural integrity monitoring. IEEE transactions on Ultrasonics, Ferroelectrics, and Frequency Control 2006; 53: 777-785.

21. White RM, Generation of elastic waves by transient surface heating. Journal of Applied Physics 1963; 34: 3559-3567.

22. Kita A, *Measurement of Weld Penetration Depth Using Non-contact Ultrasound Methods*. 2005, PhD Thesis, Georgia Institute of Technology.

23. Kita A and Ume IC, Measuring on-line and off-line noncontact ultrasound iime of flight weld penetration depth. Welding Journal 2007; 86: 9-17.

24. Mi B, *Implementation of Fiber Phased Array Ultrasound Generation System and Signal Analysis for Weld Penetration Control*. 2003, PhD Thesis, Georgia Institute of Technology.

25. Mi B and Ume IC, Real-time weld penetration depth monitoring with laser ultrasonic sensing system. Journal of Manufacturing Science and Engineering 2006; 128: 280-286.

26. Mi B and Ume IC, Parametric studies of laser generated ultrasonic signals in ablative regime: time and frequency domains. Journal of Nondestructive Evaluation 2002; 21: 23-33.

27. Rogge M, *In-Process Sensing of Weld Penetration Depth Using Non-Contact Laser Ultrasound System*. 2009, PhD Thesis, Georgia Institute of Technology.

28. Rogge M, Li R, Wu T-Y, and Ume IC, *Laser ultrasound system for weld defect detection and measurement in thin structures*, in *International Symposium on Flexible Automation*. 2008: Atlanta, GA.

29. Graham G, *On-Line Laser Ultrasonic Sensing for Control of Robotic Welding Quality*. 1995, PhD Thesis, Georgia Insitute of Technology.

30. Hopko S, *Laser Ultrasonic Probe for Industrial or High Temperature Applications*. 1998, PhD Thesis, Georgia Institute of Technology.

31. Rogge M and Ume IC, *Investigation of laser generated rayleigh waves in elastic plates*, in *Review of Progress in Quantitative Nondestructive Evaluation*. 2009: Kingston, RI.

32. Sanderson T and Ume IC, Experimental and numerical results for intensity modulated laser ultrasonics. The Journal of the Acoustical Society of America 1998; 104: 2207-2212.

33. Wu T-Y and Ume IC, *Study on laser generation of narrowband Lamb waves using superimposed line sources technique*, in *Review of Progress in Quantitative Nondestructive Evaluation*. 2009: Kingston, RI.

34. Wu T-Y and Ume IC, Fundamental study of laser generation of narrowband Lamb waves using superimposed line sources technique. NDT & E International 2011; 44: 315-323.

35. Achenbach AD, Wave Propagation in Elastic Solids. 1999, Amsterdam: North-Holland.

36. Graff KF, Wave Motion in Elastic Solids. 1991, New York: Dover Publications.

37. Rose JL, Ultrasonic Waves in Solid Media. 2004: Cambridge University Press.

38. Kim H, Jhang K, Shin M, and Kim J, A noncontact NDE method using a laser generated focused-Lamb wave with enhanced defect-detection ability and spatial resolution. NDT&E International 2006; 39: 312-319.

39. Jhang K, Shin M, and Lim BO, Application of the laser generated focused-Lamb wave for non-contact imaging of defects in plate. Ultrasonics 2006; 44(1): 1265-1268.

40. Baldwin KC, Berndt TP, and Ehrlich MJ, Narrowband laser generation/air-coupled detection: ultrasonic system for on-line process control of composites. Ultrasonics 1999; 37: 329-334.

41. Huang J, Krishnaswamy S, and Achenbach JD, Laser generation of narrow-band surface waves. The Journal of the Acoustical Society of America 1992; 92: 2527-2531.

42. Murray TW, Beaton JB, and Wagner JW, Experimental evaluation of enhanced generation of ultrasonic waves using an array of laser sources. Ultrasonics 1996; 34: 69-77.

43. Harata A, Nishimura N, and Sawada T, Laser-induced surface acoustic-waves and photothermal surface gratings generated by crossing 2 pulsed laser-beams. Applied Physics Letter 1990; 57: 132-134.

44. Edwards C, Bushell AC, Palmer SB, and Nakano H, Laser interference grating for surface wave generation. Nondestructive Testing and Evaluation 1992; 10(1): 15-23.

45. Cosenza C, Kenderian S, and Djordjevic B, Generation of narrowband antisymmetric Lamb waves using a formed laser source in the ablative regime. IEEE transactions on Ultrasonics, Ferroelectrics, and Frequency Control 2007; 54: 147-156.

46. Kenderian S, Djordjevic B, and Green JR, Narrowband laser-generated surface acoustic waves using a formed source in the ablative regime. The Journal of the Acoustical Society of America 2003; 113(1): 261-266.

47. McKie ADW, Wagner JW, Spicer JB, and Penney CM, Laser generation of narrow-band and directed ultrasound. Ultrasonics 1989; 27(6): 323-330.

48. Scruby C and Drain L, Laser Ultrasonics: Techniques and Applications. 1990: Taylor and Francis.

49. Shi Y, Wooh S, and Orwat M, Laser-ultrasonic generation of Lamb waves in the reaction force range. Ultrasonics 2003; 41(8): 623-633.

50. Ogi H, Hirao M, and Ohtani T, Line-focusing electromagnetic acoustic transducers for the detection of slit defects. IEEE transactions on Ultrasonics, Ferroelectrics, and Frequency Control 1999; 46(2): 341-346.

51. Yamasaki T, Tamai S, and Hirao M. Arrayed-coil EMAT for longitudinal wave in steel wires. in Proceedings of Ultrasonics Symposium. 1998.

52. Alleyne DN and Cawley P, The interaction of Lamb waves with defects. IEEE transactions on Ultrasonics, Ferroelectrics, and Frequency Control 1992; 39(3): 381-397.

53. Michaels TE, Michaels JE, and Ruzzene M, Frequency-wavenumber domain analysis of guided wavefields. Ultrasonics 2011; 51(4): 452-466.

54. Ruzzene M, Frequency-wavenumber domain filtering for improved damage visualization. Smart Materials & Structures 2007; 16: 2116-2129.

55. Gao W, Glorieux C, and Thoen J, Laser ultrasonic study of Lamb waves: determination of the thickness and velocities of a thin plate. International Journal of Engineering Science 2003; 41: 219-228.

56. Sadler J and Maev RG, Experimental and theoretical basis of Lamb waves and their applications in material sciences. Canadian Journal of Physics 2007; 85: 707-731.

57. Su Z, Ye L, and Lu Y, Guided Lamb waves for identification of damage in composite structures: A review. Journal of Sound and vibration 2006; 295: 753-780.

58. Alleyne DN and Cawley P, A two-dimensional Fourier transform method for the measurement of propagating multimode signals. The Journal of the Acoustical Society of America 1991; 89(3): 1159-1168.

59. Wooh S and Shi Y, Synthetic phase tuning of guided waves. IEEE transactions on Ultrasonics, Ferroelectrics, and Frequency Control 2001; 48(1): 209-223.

60. Daubechies I, Ten Lectures on Wavelets. 1992: SIAM.

61. Mallat S, A Wavelet Tour of Signal Processing. 1999: Academic Press.

62. Lu Y, Ye L, Su Z, and Yang C, Quantitative assessment of through-thickness crack size based on Lamb wave scattering in aluminum plates. NDT&E International 2008; 41: 59-68.

63. Staszewski WJ, Boller C, and Tomlinson GR, Health monitoring of aerospace structures: smart sensor technologies and signal processing. 2004, New York: Wiley.

64. Xu B, Shen Z, Ni X, and Lu J, Numerical simulation of laser-generation ultrasound by the finite element method. Journal of Applied Physics 2004; 95: 2116-2122.

65. Shen Z, Xu B, Ni X, and Lu J, Numerical simulation of laser-generated ultrasonic waves in layered plates. Journal of Physics D: Applied Physics 2004; 37: 2364-2370.

66. Benmeddour F, Grondel S, Assaad J, and Moulin E, Study of the fundamental Lamb modes interaction with asymmetrical discontinuities. NDT&E International 2008; 41: 330-340.

67. Benmeddour F, Grondel S, Assaad J, and Moulin E, Study of the fundamental Lamb modes interaction with symmetrical notches. NDT&E International 2008; 41: 1-9.

68. Kutner MH, Nachtsheim CJ, Neter J, and Li W, Applied Linear Statistical Models. 2005: McGraw-Hill Education.

69. Wu CFJ and Hamada M, Experiments: Planning, Analysis, and Parameter Design Optimization. 2000: John Wiley & Sons, Inc.

70. Jin J, Quek ST, and Wang Q, Wave boundary element to study Lamb wave propagation in plates. Journal of Sound and vibration 2005; 288: 195-213.

71. Lowe MJS and Diligent O, Low-frequency reflection characteristics of the s_0 Lamb wave from a rectangular notch in a plate. The Journal of the Acoustical Society of America 2002; 111(1): 64-74.

72. Marical P, Ech-Cherif El-Kettani M, and Predoi MV, Guided waves in elastic plates with Gaussian section variation: Experimental and numerical results. Ultrasonics 2007; 47(1-4): 1-9.

73. Gagne P, and Dayton CM, Best Regression Model Using Information Criteria. Journal of Modern Applied Statistical Methods 2002; 1(2): 479-488.

74. Burnham KP, and Anderson DR, Multimodel inference: Understanding AIC and BIC in Model Selection. Sociological Methods and Research 2004; 33: 261-304.